Laser Produced Plasmas in Liquid Environments

Nichola Walsh
B. Sc. Hons.

A thesis submitted for the degree of:
DOCTOR OF PHILOSOPHY

Presented To:
The School of Physical Sciences, Faculty of Science and Health,
Dublin City University

Research Supervisor
Prof. John T Costello

Co-Supervisors
Lampros Nikolopoulos
Stephen Daniels

September 2016

Declaration

I hereby certify that this material, which I now submit for assessment on the programme of study leading to the award of Doctor of Philosophy is entirely my own work, that I have exercised reasonable care to ensure that the work is original, and does not to the best of my knowledge breach any law of copyright, and has not been taken from the work of others save and to the extent that such work has been cited and acknowledged within the text of my work.

Signed: _____

ID No.: 56379656

Date: _____

For James

Acknowledgements

Firstly, I would like to thank my supervisor Prof. John Costello for giving me the opportunity to carry out this research. Thank you for your help, support and guidance over the years. My thanks also to Dr. Lampros Nikolopoulos, Dr. Stephen Daniels and Prof. Eugene Kennedy for their assistance and advice.

I would like to thank all the members of the physics department who have helped me along the way. Thanks in particular to Dr. Mossy Kelly who has contributed greatly to this work and has helped me throughout. Thanks also to Dr. Paddy Hayden for his help and advice. Thanks to all past members - Conor, Colm, Jiang Xi, Éanna and Séamus for making my time here a pleasant and entertaining experience. Thanks to current group members - Stephen, Ben, Ares, Hu Lu, Mo, Will, Syedah, Get and Pramod. It has been a pleasure to work with you all and I wish you all the best in the future.

I would like to express my appreciation for all the staff in the physics department and the NCPST, in particular Des Lavelle, Pat Wogan, Lisa Peyton and Sheila Boughton. Thank you all for your time and for always being happy to help.

I would like to express my sincerest thanks to my friends and family for their support. A special mention to my brothers Christopher and Dean, and to my friends Michelle and Sarah for making me laugh when times were tough. Finally, a very special thanks to Justin for all your help and for being there for me throughout. I could not have done it without you.

Contents

List of Figures

List of Tables

List of Abbreviations

LIBS	Laser-Induced Breakdown Spectroscopy, page xxvi
PLA	Pulsed Laser Ablation, page 1
Nd:YAG	Neodymium-Doped Yttrium Aluminium Garnet, page 18
IB	Inverse-Bremsstrahlung, page 20
B-B	Bound-Bound, page 24
B-F	Bound-Free, page 24
F-F	Free-Free, page 24
CTE	Complete Thermodynamic Equilibrium, page 29
LTE	Local Thermodynamic Equilibrium, page 30
CE	Coronal Equilibrium, page 31
CRE	Collisional Radiative Equilibrium, page 32
CCD	Charge-Coupled Device, page 32
ICCD	Intensified Charge-Coupled Device, page 32
FWHM	Full Width at Half Maximum, page 35
SEM	Scanning Electron Microscope, page 62
OPO	Optical Parametric Oscillator, page 64
PC	Pockels Cell, page 66
BBO	Beta-Barium Borate, page 69
MCP	Microchannel Plate, page 71
NIST	National Institute of Standards and Technology, page 75
CMOS	Complementary Metal-Oxide-Semiconductor, page 78
AlO	Aluminium Monoxide, page 119

Abstract

Nichola Walsh

Laser Produced Plasmas in Liquid Environments

During the interaction of an intense laser pulse with a solid metal target, a high temperature, high density plasma is formed. Pulsed laser ablation has attracted much interest over the past fifty years with experimental and theoretical work largely focussed on the study of laser produced plasmas in vacuum. The study of pulsed laser ablation has been largely motivated from a materials processing perspective, with the characterisation of thin films using pulsed laser deposition of particular interest. Another application resulting from the study of laser produced plasmas is the use of laser-induced breakdown spectroscopy (LIBS) for elemental composition and quantitative analysis of samples. LIBS is now a widely used technique employed in various fields including environmental analysis, forensics and biomedical applications.

While much work has been carried out on pulsed ablation of materials in vacuum and gas ambient, comparatively little research has been done on ablation in liquid media. As a result, the fundamental understanding of laser produced plasmas in liquids remains insufficient. Using techniques such as time resolved imaging and spectroscopy, a thorough characterisation of the plasma formed in air was undertaken as a comparison to the subsequent investigation of the plasma formed in water ambient. Single pulse studies revealed information on the dynamic evolution of a laser plasma formed in the liquid phase where strong confinement and broadband emission were the main observations. Shadowgraphy measurements were performed to examine the dynamic behaviour of the cavitation bubble that eventually forms post plasma ignition. The results of time resolved optical emission measurements from within the cavitation bubble using a second laser pulse reveal for the first time the full dynamic evolution of the plasma formed in such an environment.

Chapter 1

Introduction

1.1 Laser Produced Plasmas

A laser produced plasma is formed when a high power laser is focussed onto a solid target. In the initial interaction seed electrons are formed and material is ablated from the surface to form a dilute vapour. On a picosecond timescale the electrons are heated up by inverse Bremsstrahlung and ionize both the vapour and the target to create further ablation and ionisation. The degree of ionisation of the plasma plume so formed will depend on the target irradiance (in Wcm^{-2}) and laser wavelength [1]. Pulsed laser ablation (PLA) has attracted considerable interest since the invention of the ruby laser in the 1960's [2], [3], [4]. Since that time research in the area of PLA has been motivated mostly from a materials-processing point of view. One major application has been in thin-films where pulsed laser deposition has developed into a widely used technique [5]. In a laser produced plasma, the ablated atoms and ions comprising the plume emit characteristic line radiation which forms the basic principle of laser-induced breakdown spectroscopy (LIBS). Initially, the application of LIBS for analytical classification and quantification of elements had limited capability due to low laser pulse repetition rates and the inaccessibility of time resolved measurements [6]. With the

arrival of improved pulsed laser sources offering high quality beams and short (nanosecond) pulses via electro-optical Q-switching, the impact of LIBS has risen significantly in succeeding decades since the invention of the ruby laser [7]. LIBS in now a widely used technique employed in a variety of different applications such as environmental analysis, forensics, industrial, pharmaceutical and biomedical applications [8]. Pulsed laser ablation has also attracted much interest as a route to nanoparticle generation offering several advantages over conventional methods due to purity and variety of available materials [9].

1.2 Review of Laser Produced Plasmas in Liquid

The main interest to date in laser produced plasmas in liquid environments has been related to the colloidal suspension of nanoparticles that form as a by-product of the laser ablation of a submerged target. Laser produced plasmas in liquids have been relatively unexplored in comparison to the numerous studies which have been carried out in vacuum or gas backgrounds. Of these studies, fewer again are concerned with the fundamental interactions occurring when a plasma is formed in a liquid. While an increased effort to study laser ablation in liquids in greater detail has taken place during the last decade, much work remains to be done to improve the fundamental understanding [10]. In particular, the reactions that occur between plasma species and liquid molecules are complex and still under investigation [11]. In an effort to summarise the current status of research in this area, an overview of the major findings available to date in the literature is presented in this chapter.

Patil *et al.* were the first to study the interaction of a pulsed laser at a solid-liquid interface [12]. They reported in 1987 on their findings on the chemical composition of iron samples irradiated via a pulsed ruby laser and the subsequent aqueous oxidation of the iron samples.

Ogale *et al.* investigated the potential of laser ablation in liquids as a means of surface modification with the formation of oxides, nitrides and carbides being observed [13]. Subsequent studies by Ogale *et al.* in 1992 reported the formation of diamond structures by irradiating graphite targets immersed in liquid [14]. This pioneering work was the first demonstration of laser produced plasma generation in liquids as a method of materials processing. The use of pulsed lasers for the production of nanostructures in liquid environments began to attract interest in the 2000's [3]. Since that time much work has been done on the synthesis of these nanostructures. By manipulating the many variables involved in their production, such as laser wavelength, intensity and materials used, it has been possible to achieve excellent control and reproducibility of a vast array of complex nanostructures. Zeng *et al.* provide an excellent review article on studies carried out to date on nanomaterials fabricated by laser ablation in liquids [15]. Some of the most exotic nanostructures fabricated include carbon nanocubes [4], hollow nanoparticles [16], nanorods, 2D and 3D nanoflowers [17] to name a select few. Nanoparticles of diamond are of particular interest to researchers owning to their unique properties of physical hardness, optical transparency and high thermal conductivity [18].

PLA is defined as the removal of material from the surface of a target by a laser pulse. Depending on the intensity and duration of the laser pulse the liberation of material from the target sample may be brought about by different mechanisms. Which mechanism occurs is largely dictated by the temporal duration of the ablating laser pulse with respect to the electron-phonon coupling time constant of the material [19]. For the case of metals, the laser pulse energy is transferred to the free electrons in the material on a timescale on the order of 100 fs. This energy is then transferred to the lattice via electron-phonon coupling [19]. The electron-phonon coupling time for many metals occurs on a timescale of approximately 1-10 ps. For nanosecond duration laser pulses, the electron-phonon coupling time will be much less than the temporal duration of the laser pulse and hence the main outcome of the laser-material interaction process will be the thermal heating and surface melting with subsequent vaporisation. On the other hand, for ultrashort pulses at low fluence, there is no transfer of energy to thermal

heating. Laser energy is transferred to the free electrons in the metal which in turn couple to the lattice phonons resulting in strong excitation of the phonon state spectrum. These strong lattice vibrations lead to the breakup and subsequent Coulomb explosion of the lattice leading in turn to the formation of an ablation plume consisting initially of ions and electrons and subsequently of nanoparticles, and so that the ablation mechanism here can be considered to be a sort of sublimation process [19] in which the liquid phase is bypassed.

A description of the process of laser ablation in a solid-liquid environment is provided by Dell'Aglio *et al.* [10]. In this report three distinct phases are identified which are illustrated in figure 1.1:

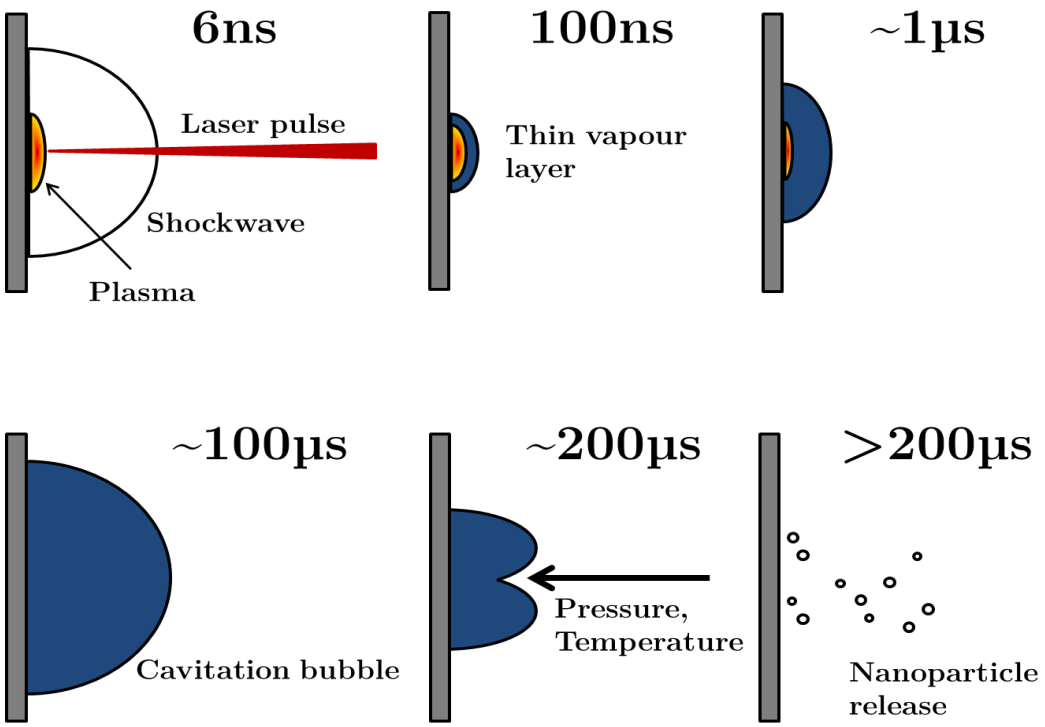

Figure 1.1: Adapted from Dell'Aglio *et al.* [10]. Time sequence of the processes involved during pulsed laser ablation in a liquid.

The three unique phases identified are (i) plasma production and cooling, (ii) cavitation bubble evolution and (iii) nanoparticle diffusion in the cavitation bubble and subsequent release into solution. The initial interaction takes place with the arrival of the laser

pulse at the target surface submerged in liquid. During this interaction a plasma will be formed at the surface, provided that the laser pulse energy is above the ablation threshold for that material [19]. Laser-induced breakdown occurs and a plasma is created when the leading edge of the laser pulse makes contact with the target at the solid-liquid interface. This is followed by the expansion of the plasma into the liquid brought about by absorption of the trailing edge of the laser pulse by the nascent plasma. Shockwaves are formed when a sudden change in the environment occurs creating a high pressure wave-front that travels faster than the speed of sound in that medium [4]. The plasma then expands and cools, followed by the formation of a cavitation bubble several microseconds after the initial laser-matter interaction. The cavitation bubble consists of a vapour layer at high temperature and pressure that expands in all directions. After the collapse of the cavitation bubble, the nanoparticles which have been produced via condensation of the plasma during the plasma cooling phase are released into the surrounding liquid forming a colloidal suspension [20], [21], [22]. The nanoparticles that are released into solution exhibit a large size distribution and spherical shape, an example of which can be seen in figure 1.2 for nanoparticles created during the present work by laser ablation of a gold target submerged in deionised water.

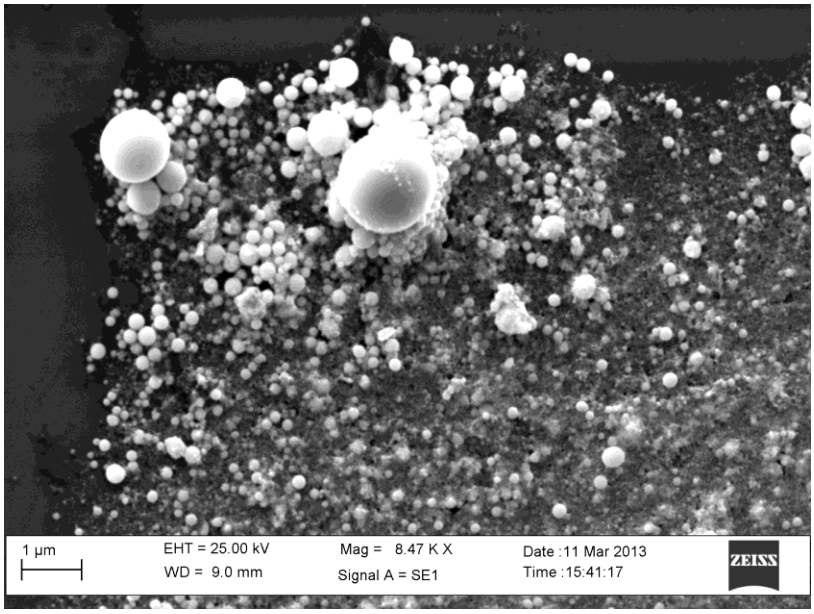

Figure 1.2: SEM image of gold nanoparticles formed in colloidal suspension of water using 120 mJ, 1064 nm pulses. Figure illustrates an array of nanoparticles of various size distributions observed during this work.

Research in the area of laser ablation in liquids has grown in recent times [3]. Of particular interest is the generation of nanostructures by pulsed laser ablation in liquids and their subsequent applications in fields such as biomedicine and sensors [23], [24], [25], [26]. These suspensions of nanoparticles have a great many applications in the biomedical field in particular for in vivo applications [19]. A host of other applications of nanoparticles exists in a range of areas owing to their unique properties (optical, magnetic, surface area etc.) which differ from bulk material.

There are multiple "advantages" associated with nanoparticle formation via pulsed laser sources. There is no need for a catalyst in their creation [4] which is often a requirement when fabricating nanoparticles by chemical means. The technique is considered "clean" in that no pre-cursor chemicals or surfactants are required. This is particularly useful in biomedicine where pure noble metallic nanoparticles are used for in-vivo research and applications. Nanoparticles formed by PLA are unique in terms of their tunability of size and shape [15], [19]. Characteristics of nanoparticles formed are susceptible to various laser parameters such as laser fluence, pulse duration and wavelength. By varying these laser parameters, the morphology of the nanoparticle distribution may be

modified. In interactions of nanoparticles with laser pulses of wavelength close to the plasmon resonance of the material, strong absorption will take place [19].

During production, nanoparticles formed by the "leading edge" of the laser pulse will interact with the "trailing edge" of the laser pulse causing fragmentation to occur and a narrowing of the size distribution, termed an intra-pulse interaction [19]. Irradiation post-production is another method in which to "tune" the size distribution of the suspension [15]. During laser-matter interaction in a liquid, nanoparticles are easily captured by the solution forming colloidal suspensions. The high pressure, high density liquid environment allows unique nanostructures to form, the size and shape of which can be varied by appropriate choice of laser pulse and environmental parameters [15], [27]. Additionally, the type of liquid in which the nanoparticles are being created will have an effect on the size distributions within a colloidal suspension [28], [29], [30].

The plasma created in a liquid environment experiences increased levels of confinement due to compression from the dense surrounding medium. In a study comparing the expansion of a laser produced aluminium plasma in air and water using time resolved imaging, Kumar *et al.* reported that the expansion rate is comparable only at the early plasma lifetimes [20]. In their investigations they have found that the plume expansion reaches a plateau level in water much earlier than in air using the same laser pulse energy. From spectroscopic measurements, electron densities were estimated from Stark broadened Al^0 transitions to be roughly an order of magnitude greater in a background of water than in air ambient with densities of 3×10^{18} cm^{-3} and 2×10^{19} cm^{-3} respectively being deduced at early plasma lifetimes. The densities recorded at later times were found to tend towards the same value of approximately 2×10^{18} cm^{-3} after roughly 1 µs. During related work using a copper target, a similar trend was observed for the temporal evolution of the electron densities calculated in air and water ambient with a more rapid decay occurring again in the case of water [31]. The electron temperatures were also calculated as a function of time in this study with a higher temperature determined in the air plasma, roughly 2× that observed in water. Similar to the results on electron densities, a more rapid cooling is found in the case of water ambient.

Exhibiting higher electron densities, an increased rate of collisional events is proposed in liquid ambient. This produces a high rate of heat transfer which contributes to the rapid decrease in temperature observed. This is also apparent from the rapid quenching of emission times observed in the water background during the study.

The plasma that forms on a submerged target is accompanied by the production of an energetic shockwave that expands radially from the target surface. The shock-front consists of a layer of compressed gas that develops due to the rapid explosive delivery of energy to the target. In addition to the shockwave that forms, a stress wave is also induced in the target material. These two laser-induced shock processes have been studied simultaneously in the works of Nguyen *et al.* using the technique of photoelasticity [32], [33]. Using this approach, several waves are discerned both inside and outside of the target material. The laser-induced stress wave produces a series of waves which expand radially into the target material. The formation of a longitudinal, compressive wave front termed a "P-wave" front is apparent from photoelastic images within the solid phase which is followed by several fringes. In addition to the shockwave and cavitation bubble, an inverted "V-shaped" wave is observed approximately 200 ns after the laser pulse arrives at the target surface. The v-shaped wave is thought to be a shockwave that travels horizontally along the target interface [33]. Photoelastic images in air and water observed using the same laser conditions show that a much stronger amplitude stress wave is generated in the liquid environment. A possible explanation for this phenomenon is the confining effect of the water, which prohibits the expansion of the plasma thereby creating a stress wave of greater amplitude.

In addition to the shockwave that is generated in a liquid, a "cavitation bubble" forms several microseconds after the initial laser pulse is fired. After plasma ignition, a bubble of heated gas is created as energy is transferred from the plasma to the surrounding liquid molecules. This heating results in the production of a layer of water vapour which grows into a cavitation bubble as the plasma cools. Shadowgraphy has been the most commonly employed technique in the study of the laser produced shockwave and the cavitation bubble. This is a relatively simple technique which allows the evolution of the

bubble to be examined dynamically. The bubble expands until a maximum radius is reached on the order of millimetres, depending on the initial energy of the laser pulse, with a larger radius formed at higher pulse energies [34], [35]. The collapse of the bubble may be followed by the growth and collapse of secondary, and tertiary bubbles of increasingly smaller radius [35], [36]. This period of growth and collapse cycles of subsequent cavitation bubbles continues until the energy of the induced cavitation bubble has been dissipated. The cavitation bubble consists of liquid vapour and is formed approximately one microsecond after the creation of the plasma in liquid. A second laser pulse directed onto a submerged target and coincident with the cavitation bubble will generate a plasma in a very different environment to that of the bulk liquid. In this gaseous-like surrounding, the appearance of atomic spectra may be observed much more readily than in the bulk liquid itself where emission is rapidly quenched by electron-ion recombination.

While many studies are available from the literature relating to PLA in liquids the majority of this work involves characterisation of colloidal suspensions. As yet, the processes involved in laser ablation of solid targets in liquids are not well understood [3], [20] and research carried out to date is limited compared to those studies carried out in air [3], [4]. Much work remains to be done on the fundamental understanding of the interactions taking place during plasma formation in liquid ambient which constitutes the main motivation of the current work. By studying submerged plasmas using the diagnostics commonly applied in plasma studies under vacuum, it can be expected that new information would be learned to complement studies performed in other areas such as material processing. Another field for which these studies may be of relevance is in the area of LIBS for elemental composition analysis of liquids and in limit of detection[1] studies [20], [38]. An excellent review on the current status and findings in the literature on LIBS under water is found in the paper by De Giacomo *et al.* [10]. For submerged samples, the poor emission associated with laser produced plasmas in liquids is overcome by the double-pulse method which was first applied in liquids by Pichahchy *et*

[1] Limit of detection is the lowest concentration of a substance that the analytical process can reliably detect [37]

al. [39], although good quality atomic spectra have been reported using relatively long laser pulses also [40]. Laser ablation in liquids has many applications such as the monitoring of corrosion in nuclear power plant [38], tissue identification in biology [41], laser surgery [42], underwater geological and oceanographic studies [43] and marine research [44]. In particular for medical applications, the understanding of these processes is of fundamental importance due to the high water content present in human tissue.

Many methods exist for the study of laser-produced plasmas. Using techniques such as time resolved imaging and spectroscopy, useful information related to plasma parameters may be extracted. In this way processes taking place can be tracked as the plasma evolves and important information is revealed. Using a range of analysis techniques the results on an in-depth study of the plasma-liquid interaction are presented in this thesis. Each of the experiments performed served to provide a better understanding of the fundamental processes taking place forming the motivation for the present work.

1.3 Thesis Structure

This thesis is divided into eight chapters. This chapter has introduced the topic of laser produced plasmas in liquids and provided an overview of the relevant up-to-date findings available in the literature. A brief description of the contents of each of the remaining chapters is provided for ease of reference.

In chapter 2 the relevant theoretical background related to laser produced plasmas is presented. Plasma evolution, atomic processes and applicable equilibrium models related to plasmas are described. The concepts underlying the experimental techniques employed and methods used in the analysis of experimental data are also discussed.

The different experimental systems and equipment used are described in chapter 3. During the course of this work a range of diagnostic techniques were utilised in the

study of laser produced plasma in both air and water ambient. An outline of the operational methods associated with experimental systems that were used is provided in this chapter.

The results of studies performed under atmospheric conditions in air are presented in chapter 4. For plasma emission studies, time resolved imaging and spectroscopy were employed to study the physical evolution of the plasma and its spectroscopic emission in the visible wavelength range. Shadowgraphy measurements were also carried out to investigate the shockwave expansion associated with the laser produced plasma. Electron density and temperature calculations are also presented and discussed.

Chapter 5 outlines the findings on aluminium oxide formation in air. Using an optical parametric oscillator, a series wavelength-tuned pump-probe experiments were performed. By varying the time delay between the pump and probe beams, a series of experiments were carried out to study the effect on the emission observed by delaying the delivery of the probe pulse to the molecule.

The results of laser produced plasmas in a liquid environment are detailed in chapter 6. A series of single pulse and double pulse studies were performed, the results of which are presented in this chapter. The shockwave formation and cavitation bubble evolution are studied in liquid using shadowgraphy.

Chapter 7 provides a comparative study of laser produced plasmas in air and water using a range of experimental techniques. Different plasma expansion models are applied for plasmas created in air and water environments and the results discussed. An overview of the main findings and unique features associated with plasma formation in a background of air and liquid is presented.

Finally, chapter 8 concludes the work carried out and summarises the main findings presented in this thesis. Suggestions for potential future work are also outlined.

References

[1] D. Colombant and G. F. Tonon, "X-ray emission in laser-produced plasmas," *J. Appl. Phys.*, vol. 44, no. 8, p. 3524, 1973.

[2] H. M. Smith and A. F. Turner, "Vacuum Deposited Thin Films Using a Ruby Laser," *Appl. Opt.*, vol. 4, no. 1, p. 147, Jan. 1965.

[3] Z. Yan and D. B. Chrisey, "Pulsed laser ablation in liquid for micro-/nanostructure generation," *J. Photochem. Photobiol. C Photochem. Rev.*, vol. 13, no. 3, pp. 204–223, Sep. 2012.

[4] G. Yang, "Laser ablation in liquids: Applications in the synthesis of nanocrystals," *Prog. Mater. Sci.*, vol. 52, no. 4, pp. 648–698, May 2007.

[5] D. B. Chrisey and G. K. Hubler, Eds., *Pulsed laser deposition of thin films*. New York: Wiley, 1994.

[6] E. F. Runge, R. W. Minck, and F. R. Bryan, "Spectrochemical analysis using a pulsed laser source," *Spectrochim. Acta*, vol. 20, no. 4, pp. 733–736, Apr. 1964.

[7] R. Noll, *Laser-Induced Breakdown Spectroscopy*. Berlin, Heidelberg: Springer Berlin Heidelberg, 2012.

[8] D. W. Hahn and N. Omenetto, "Laser-Induced Breakdown Spectroscopy (LIBS), Part I: Review of Basic Diagnostics and Plasma–Particle Interactions: Still-Challenging Issues Within the Analytical Plasma Community," *Appl. Spectrosc.*, vol. 64, no. 12, pp. 335–366, Dec. 2010.

[9] A. Hahn, "Influences on Nanoparticle Production during Pulsed Laser Ablation," *J. Laser MicroNanoengineering*, vol. 3, no. 2, pp. 73–77, Apr. 2008.

[10] M. Dell′Aglio, R. Gaudiuso, O. De Pascale, and A. De Giacomo, "Mechanisms and processes of pulsed laser ablation in liquids during nanoparticle production," *Appl. Surf. Sci.*, vol. 348, pp. 4–9, Sep. 2015.

[11] T. Sakka, S. Iwanaga, Y. H. Ogata, A. Matsunawa, and T. Takemoto, "Laser ablation at solid–liquid interfaces: An approach from optical emission spectra," *J. Chem. Phys.*, vol. 112, no. 19, p. 8645, 2000.

[12] P. P. Patil, D. M. Phase, S. A. Kulkarni, S. V. Ghaisas, S. K. Kulkarni, S. M. Kanetkar, S. B. Ogale, and V. G. Bhide, "Pulsed-laser-induced reactive quenching at liquid-solid interface: Aqueous oxidation of iron," *Phys. Rev. Lett.*, vol. 58, no. 3, pp. 238–241, Jan. 1987.

[13] S. B. Ogale, "Pulsed-laser-induced and ion-beam-induced surface synthesis and modification of oxides, nitrides and carbides," *Thin Solid Films*, vol. 163, pp. 215–227, Sep. 1988.

[14] S. . Ogale, A. . Malshe, S. . Kanetkar, and S. . Kshirsagar, "Formation of diamond particulates by pulsed ruby laser irradiation of graphite immersed in benzene," *Solid State Commun.*, vol. 84, no. 4, pp. 371–373, Oct. 1992.

[15] H. Zeng, X.-W. Du, S. C. Singh, S. A. Kulinich, S. Yang, J. He, and W. Cai, "Nanomaterials via Laser Ablation/Irradiation in Liquid: A Review," *Adv. Funct. Mater.*, vol. 22, no. 7, pp. 1333–1353, Apr. 2012.

[16] K. Y. Niu, J. Yang, S. A. Kulinich, J. Sun, H. Li, and X. W. Du, "Morphology Control of Nanostructures via Surface Reaction of Metal Nanodroplets," *J. Am. Chem. Soc.*, vol. 132, no. 28, pp. 9814–9819, Jul. 2010.

[17] S. C. Singh and R. Gopal, "Nanoarchitectural Evolution from Laser-Produced Colloidal Solution: Growth of Various Complex Cadmium Hydroxide Architectures from Simple Particles," *J. Phys. Chem. C*, vol. 114, no. 20, pp. 9277–9289, May 2010.

[18] G.-W. Yang, J.-B. Wang, and Q.-X. Liu, "Preparation of nano-crystalline diamonds using pulsed laser induced reactive quenching," *J. Phys. Condens. Matter*, vol. 10, no. 35, pp. 7923–7927, Sep. 1998.

[19] N. G. Semaltianos, "Nanoparticles by Laser Ablation," *Crit. Rev. Solid State Mater. Sci.*, vol. 35, no. 2, pp. 105–124, May 2010.

[20] B. Kumar and R. K. Thareja, "Synthesis of nanoparticles in laser ablation of aluminum in liquid," *J. Appl. Phys.*, vol. 108, no. 6, p. 64906, 2010.

[21] C. X. Wang, P. Liu, H. Cui, and G. W. Yang, "Nucleation and growth kinetics of nanocrystals formed upon pulsed-laser ablation in liquid," *Appl. Phys. Lett.*, vol. 87, no. 20, p. 201913, 2005.

[22] T. Tsuji, S. Ozono, T. Mizuki, M. Tsuji, T. Doi, and J. Yamaki, "Injection of Laser Ablation Products into a Liquid in Evacuated Environment: An Alternative Laser Ablation Technique for Fabrication of Colloidal Nanoparticles," *Jpn. J. Appl. Phys.*, vol. 48, no. 9, p. 95006, Sep. 2009.

[23] M. Hu, J. Chen, Z.-Y. Li, L. Au, G. V. Hartland, X. Li, M. Marquez, and Y. Xia, "Gold nanostructures: engineering their plasmonic properties for biomedical applications," *Chem. Soc. Rev.*, vol. 35, no. 11, p. 1084, 2006.

[24] J. Z. Zhang, "Biomedical Applications of Shape-Controlled Plasmonic Nanostructures: A Case Study of Hollow Gold Nanospheres for Photothermal Ablation Therapy of Cancer," *J. Phys. Chem. Lett.*, vol. 1, no. 4, pp. 686–695, Feb. 2010.

[25] K. An and T. Hyeon, "Synthesis and biomedical applications of hollow nanostructures," *Nano Today*, vol. 4, no. 4, pp. 359–373, Aug. 2009.

[26] A. N. Shipway, E. Katz, and I. Willner, "Nanoparticle Arrays on Surfaces for Electronic, Optical, and Sensor Applications," *ChemPhysChem*, vol. 1, no. 1, pp. 18–52, Aug. 2000.

[27] A. R. Tao, S. Habas, and P. Yang, "Shape Control of Colloidal Metal Nanocrystals," *Small*, vol. 4, no. 3, pp. 310–325, Mar. 2008.

[28] P. V. Kazakevich, A. V. Simakin, V. V. Voronov, and G. A. Shafeev, "Laser induced synthesis of nanoparticles in liquids," *Appl. Surf. Sci.*, vol. 252, no. 13, pp. 4373–4380, Apr. 2006.

[29] R. M. Tilaki, A. Iraji zad, and S. M. Mahdavi, "Size, composition and optical properties of copper nanoparticles prepared by laser ablation in liquids," *Appl. Phys. A*, vol. 88, no. 2, pp. 415–419, Jun. 2007.

[30] A. V. Simakin, V. V. Voronov, N. A. Kirichenko, and G. A. Shafeev, "Nanoparticles produced by laser ablation of solids in liquid environment," *Appl. Phys. A*, vol. 79, no. 4–6, Sep. 2004.

[31] B. Kumar and R. K. Thareja, "Laser ablated copper plasmas in liquid and gas ambient," *Phys. Plasmas*, vol. 20, no. 5, p. 53503, 2013.

[32] T. T. P. Nguyen, R. Tanabe, and Y. Ito, "Laser-induced shock process in under-liquid regime studied by time-resolved photoelasticity imaging technique," *Appl. Phys. Lett.*, vol. 102, no. 12, p. 124103, 2013.

[33] T. T. P. Nguyen, R. Tanabe, and Y. Ito, "Effects of an absorptive coating on the dynamics of underwater laser-induced shock process," *Appl. Phys. A*, vol. 116, no. 3, pp. 1109–1117, Sep. 2014.

[34] T. Tsuji, Y. Tsuboi, N. Kitamura, and M. Tsuji, "Microsecond-resolved imaging of laser ablation at solid–liquid interface: investigation of formation process of nano-size metal colloids," *Appl. Surf. Sci.*, vol. 229, no. 1–4, pp. 365–371, May 2004.

[35] R. Tanabe, T. T. P. Nguyen, T. Sugiura, and Y. Ito, "Bubble dynamics in metal nanoparticle formation by laser ablation in liquid studied through high-speed laser stroboscopic videography," *Appl. Surf. Sci.*, vol. 351, pp. 327–331, Oct. 2015.

[36] V. Lazic, J. J. Laserna, and S. Jovicevic, "Insights in the laser-induced breakdown spectroscopy signal generation underwater using dual pulse excitation — Part I: Vapor bubble, shockwaves and plasma," *Spectrochim. Acta Part B At. Spectrosc.*, vol. 82, pp. 42–49, Apr. 2013.

[37] D. MacDougall, W. B. Crummett, and . et al., "Guidelines for data acquisition and data quality evaluation in environmental chemistry," *Anal. Chem.*, vol. 52, no. 14, pp. 2242–2249, Dec. 1980.

[38] V. Lazic, F. Colao, R. Fantoni, and V. Spizzicchino, "Laser-induced breakdown spectroscopy in water: Improvement of the detection threshold by signal processing," *Spectrochim. Acta Part B At. Spectrosc.*, vol. 60, no. 7–8, pp. 1002–1013, Aug. 2005.

[39] A. E. Pichahchy, D. A. Cremers, and M. J. Ferris, "Elemental analysis of metals under water using laser-induced breakdown spectroscopy," *Spectrochim. Acta Part B At. Spectrosc.*, vol. 52, no. 1, pp. 25–39, Jan. 1997.

[40] T. Sakka, H. Oguchi, S. Masai, K. Hirata, Y. H. Ogata, M. Saeki, and H. Ohba, "Use of a long-duration ns pulse for efficient emission of spectral lines from the laser ablation plume in water," *Appl. Phys. Lett.*, vol. 88, no. 6, p. 61120, 2006.

[41] A. Assion, M. Wollenhaupt, L. Haag, F. Mayorov, C. Sarpe-Tudoran, M. Winter, U. Kutschera, and T. Baumert, "Femtosecond laser-induced-breakdown spectrometry for Ca 2+ analysis of biological samples with high spatial resolution," *Appl. Phys. B Lasers Opt.*, vol. 77, no. 4, pp. 391–397, Oct. 2003.

[42] A. Vogel, "Shock wave emission and cavitation bubble generation by picosecond and nanosecond optical breakdown in water," *J. Acoust. Soc. Am.*, vol. 100, no. 1, p. 148, 1996.

[43] B. Thornton, T. Sakka, T. Takahashi, A. Tamura, T. Masamura, and A. Matsumoto, "Spectroscopic Measurements of Solids Immersed in Water at High Pressure Using a Long-Duration Nanosecond Laser Pulse," *Appl. Phys. Express*, vol. 6, no. 8, p. 82401, Aug. 2013.

[44] C. Fabre, M.-C. Boiron, J. Dubessy, M. Cathelineau, and D. A. Banks, "Palaeofluid chemistry of a single fluid event: a bulk and in-situ multi-technique analysis (LIBS,

Raman Spectroscopy) of an Alpine fluid (Mont-Blanc)," *Chem. Geol.*, vol. 182, no. 2–4, pp. 249–264, Feb. 2002.

Chapter 2

Theoretical Background

This chapter will introduce the fundamental properties of laser produced plasmas. The principal atomic processes occurring within the plasma will be discussed in addition to the relevant plasma expansion and equilibrium models. The principles of plasma diagnostic techniques applied in this work will be described as well as the physical properties of the plasma that may be extracted using these methods. Finally, the unique processes associated with a laser produced plasma in a liquid will be detailed.

2.1 Plasma Definition

A plasma is essentially a gas of charged particles consisting of a mixture of positive ions and negative electrons and is considered to be a unique state of matter. Plasma is fundamentally distinct from all other states of matter in that plasma formation requires the stripping of electrons from atoms and not the breaking of atomic bonds (albeit molecular dissociation can occur in a plasma). A laser produced plasma is formed when an intense laser pulse is focused onto a target material to an irradiance in excess of the threshold value of the material which is typically ~0.1 GW/cm^2. In this instance, atoms will become ionised due to the absorption of photons and an assembly of electrons, ions and neutral atoms will result in the creation of a plasma provided certain criteria are

met. The first important criterion is that the plasma must exhibit overall charge neutrality during its lifetime meaning that:

$$n_e = \sum_Z n_Z Z \tag{2.1}$$

where n_e is the electron density and n_Z is the ion density in charge state Z [1].

Charged particles can interact over significantly larger distances than uncharged particles. The distance over which a charged particles can influence neighbouring particles is known as the Debye length (λ_D) and is defined as [1]:

$$\lambda_D = \left(\frac{\varepsilon_0 k_B T_e}{n_e e^2}\right)^{\frac{1}{2}} \tag{2.2}$$

where ε_0 is the permittivity of free space, k_B is the Boltzman constant, T_e is the plasma temperature in Kelvin and e is the charge on the electron.

The Debye length is a measure of the charge seperation present in the plasma and also the distance over which the electric field of the charge penetrates into the plasma. The plasma electrically shields the volume surrounding the charged particle over a distance equal to the Debye length. If this is the case then the plasma is said to be quasineutral meaning charge neutrality holds over the physical extent of the plasma. The dimensions of the plasma must be greater than the Debye length for the definition of a plasma to hold, that is $L >> \lambda_D$ [2]. Outside of the plasma the potential of the charged particles will fall with a $1/r$ dependance.

Within the assembly of charged particles any perturbation of one charged particle will influence the surrounding neighbours. The collective response of the neighbouring particles is contained within the concept of the Debye sphere and is another important criterion in the defining of a plasma. The Debye sphere is characterised by the expression [2]:

$$N_D = \frac{4}{3} n_e \pi \lambda_D^3 \tag{2.3}$$

The Debye sphere (having units of number of charges) is also known as the "plasma parameter" and must have a value greater than unity.

When disturbed from equilibrium the system will exhibit electrostatic restoring forces which effectuate an oscillation about the equilibrium position. The displacement of charge will result in the collective oscillation of the charged particles. The electron oscillation will be the most significant contribution in comparison to the more slowly moving ions. The sinusoidal motion of the electron oscillation is defined by the electron frequency ω_e:

$$\omega_e = \left(\frac{n_e e^2}{m_e \varepsilon_0}\right)^{\frac{1}{2}} \tag{2.4}$$

where m_e is the mass of the electron [2].

Taking into account ion motion an expression to define the so-called plasma frequency ω_p is given by:

$$\omega_p = {\omega_e}^2 + \omega_i^2 \tag{2.5}$$

where ω_i is the ion frequency. As the ion mass is much greater than the electron mass, the ion frequency is much less than the electron frequency and so the palsma frequency is usually taken to be approximately equal to the electron frequency.

A plasma which is subject to an electromagnetic wave at a frequency greater than the plasma frequency will not be capable of responding to the field. This means that the plasma is transparent to frequencies above the plasma frequency and opaque to those below it. By using equation 2.4 and setting $\omega = \omega_p$ the electron density at which an electromagnetic wave can no longer propogate through the plasma can be ascertained which is given by [1]:

$$n_c = \frac{\varepsilon_0 m_e \omega^2}{e^2} \tag{2.6}$$

This is known as the critical density which for an neodymium-doped yttrium aluminium garnet (Nd:YAG) laser of wavelength 1064 nm is 10^{21} cm^{-3} and so, for n_e above this

density, Nd:YAG laser radiation will be reflected by the plasma. The electromagnetic wave is reflected off the so-called "critical density layer" of the plasma and undergoes an exponential decay as a function of distance into the plasma.

2.2 Plasma Evolution

When an intense laser is focussed onto a material, an interaction takes place with the target surface and a plasma is formed. The plasma that forms depends greatly on the parameters of the laser pulse including the wavelength, intensity and pulse shape and duration. For 50 mJ pulses of 6 ns duration focussed to a spot size of diameter 100 µm, typical irradiances achieved during the current work were on the order 10^{10}-10^{11} Wcm^{-2}. The properties of the plasma that is produced will depend also on the properties of the material target used such as atomic weight, density, surface reflectivity, conductivity, etc. The evolution of a laser produced plasma can be classified into three stages:

(i) The interaction of the laser pulse with the target material produces heating of the target surface and subsequent melting and evaporation

(ii) Interaction of the laser pulse with the ablated material (and isothermal expansion)

(iii) Expansion of the plume into the surrounding medium after the laser pulse (adiabatic expansion)

When the laser pulse reaches the target surface, radiation will penetrate into the material up to a thin layer (several nm) referred to as the optical skin depth which is defined as:

$$\delta = \sqrt{\frac{2}{\omega\mu\sigma}} \tag{2.7}$$

where ω is the angular frequency (s^{-1}) of the incident laser radiation, $\mu$is the magnetic permeability of free space ($kgms^{-2}A^{-2}$) and σ is the conductivity ($kg^{-1}m^{-3}s^{3}A^{2}$) of the

target material [3], [4]. The optical skin depth using 1064 nm radiation is < 10 nm for an aluminium target.

Radiation is absorbed by electrons within the skin depth through various processes (e.g. photoexcitation, single photoionization and multi-photon ionization) resulting in the release of electrons. Energy can be transferred into the bulk material by energetic electrons which have been promoted to the conduction band. This energy transfer can take place up to a depth given by the heat penetration depth L_{th}:

$$L_{th} \approx \sqrt{2D\tau_L} \tag{2.8}$$

where D is the heat diffusion coefficient ($D = k/\rho C$ (k thermal conductivity (W/(mK)), ρ mass density (kg/m^3) and C is the specific heat capacity (J/kgK) and τ_L is the pulse duration of the laser [3].

The heat penetration depth is typically on the order of ~1 µm. Being several times larger than the optical skin depth, the energy delivered by the laser pulse is largely transferred by heat conduction several microns into the bulk material which acts to melt the material. For nanosecond laser pulses the phase transitions of the laser-matter interaction process are solid → liquid → vapour. As metals require more energy to undergo vaporisation than melting, vaporisation of the molten material occurs when the energy absorbed by the skin depth becomes larger than the latent heat of evaporation. The ablation depth ΔZ (cm) can be determined from:

$$\Delta Z \approx \frac{A_s(F_L - F_{th})}{\rho L_v} \tag{2.9}$$

where A_s is the surface absorbance, F_L is the laser fluence (J/cm^2), F_{th} is the threshold fluence and L_v is the latent heat per unit mass [3].

The majority of electrons and ions released from the target surface are restricted to a distance of a few nanometers forming the so-called "deflagration layer". The free electrons in this layer interact with the laser pulse via the inverse-Bremsstrahlung (IB) process [3]. In the IB process, an electron absorbs a laser photon in the field of an ion of

charge Z. Absorption of photons by the IB process is greatly dependent upon electron and ion densities and also on the laser pulse wavelength. The IB absorption coefficient is defined as [5], [6]:

$$\alpha_{IB} = \sigma_{IB} N_e = \frac{4}{3}\left(\frac{2\pi}{3k_B T_e}\right)^{\frac{1}{2}} \frac{Z^2 e^6}{hcm_e^{\frac{3}{2}}\nu^3} N_i g_{ff}\left(1 - exp\left(\frac{-h\nu}{k_B T_e}\right)\right) N_e \qquad (2.10)$$

where α_{IB} is the IB cross section, N_i and N_e the number density of ions and electrons, ν is the laser frequency, Z the ionic charge, h Planck's constant. The Gaunt factor g_{ff} is included in a more exact theory of the absorption coefficient and is taken as unity by Kramer's rule [3], [7].

The IB process is less efficient at lower wavelength which means short wavelength lasers are preferable in probing the dense regions of a plasma which are opaque to infrared radiation. The absorption of radiation by the IB process imparts kinetic energy to the liberated electrons. These energetic electrons cause further ionisation and the electron density increases. As this process continues a point arises at which the electron density has increased to critical density (see equation 2.6) which for an Nd:YAG operating at the fundamental frequency is 10^{21} cm^{-3}. When the critical density is reached the laser pulse is reflected from the critical density layer. As the plasma expands the electron density decreases below the critical density and radiation from the laser can be absorbed once more. This process repeats until the laser pulse has terminated. While the majority of the laser pulse energy is absorbed in the thin layer around the critical density boundary (the deflagration zone), a low density plasma exists in front of this zone which can expand isothermally away from the target surface. This stage in the evolution of the plasma can be considered isothermal as the heating cycle time is much less than the expansion time. Hence although the plasma volume is increasing, the plasma temperature will remain constant.

2.3 Plasma Expansion

During the temporal interval of the laser pulse the plasma is classified as isothermal, meaning the rate of thermal radiation produced via IB and collisional excitation is greater than or equal to the rate of heat loss to the surroundings by radiative processes. A dynamic equilibrium exists between the absorption of laser radiation by the electrons and the rapid conversion of thermal energy to kinetic energy.

After the termination of the pulse the plume evolution proceeds via an adiabatic expansion (for the case in vacuum). Here no further evaporation of particles occurs and the plasma plume cools upon expansion. The plume evolution in this regime is described by the adiabatic expansion model of Singh and Narayan [8]. In this model the plasma is treated as an ideal gas at high pressure, temperature and fixed volume which expands abruptly into a vacuum. The model does not differentiate between the motion of different species present in the plasma. The expansion velocities of the plasma plume constituents are related to the initial temperature, dimension and atomic mass of the species present. The expansion for all species is expressed by the equation of adiabatic expansion as follows:

$$X(t)\left[\frac{d^2X}{dt^2}\right] = Y(t)\left[\frac{d^2Y}{dt^2}\right] = Z(t)\left[\frac{d^2Z}{dt^2}\right] = \frac{k_B T_0}{m}\left[\frac{X_0 Y_0 Z_0}{X(t)Y(t)Z(t)}\right]^{\gamma-1} \tag{2.11}$$

where X_0, Y_0 and Z_0 are the initial values of X, Y and Z which are the plume dimensions at time t. T_0 is the isothermal temperature of the plasma, m is the mass of the atomic species and γ is the adiabatic parameter which is the ratio of the specific heat capacities at constant pressure and volume.

Looking at equation 2.11 it is evident that if the initial dimensions of the plasma are large, then the acceleration in that direction is small. As the velocity of ablated species is determined by the pressure gradient experienced, the expansion is anisotropic in the Z direction perpendicular to the target [8] where the gradient is greatest. Since $X_0$and Y_0 are on the order of the spot size (i.e. $\approx$ 100 µm) and Z_0 is on the order of the

physical plasma dimensions ($\approx$ 2 µm), it is clear that the plasma expands much more rapidly in a direction normal to the target surface than in the lateral direction.

As it expands most of the thermal energy is converted into kinetic energy and velocities of roughly 10^6 cm/s in vacuum are typical for the type of laser irradiances of concern here [9]. The expansion velocities are determined by the pressure gradients that exist in the plasma. As was the case in the isothermal regime, the initial transverse expansion dimensions are much larger than the perpendicular dimension. Having the largest pressure gradient, the predominant expansion will be in the perpendicular direction [8], leading to an elliptical shape of the plasma plume. As the plasma expands, the velocity of the electrons greatly exceeds that of the heavier ions. The electrons will travel at the outer region of the plasma with the ions trailing behind. The Coulombic force that exists between the oppositely charged species will act to accelerate the ions and slow the electrons which may result in the occurrence of charge-separation within the plasma at early expansion times [9], [10], [11].

2.4 Atomic Processes in Plasmas

The processes that occur within a laser produced plasma may be classified as radiative processes (those relating to the laser radiation delivered) and collisional processes (those related to the transferring of energy between species within the system). In any laser-matter interaction a number of processes can take place:

(i) Absorption of photons by atoms or ions resulting in an excitation of plasma atoms and ions into more highly excited bound states (photoabsorption)

(ii) Absorption of photons by atoms or ions resulting in liberation of electrons into the free-electron continuum (photoionization)

(iii) Absorption of photons by free-electrons in the vicinity of ions resulting in an increase of kinetic energy of the electrons (inverse-Bremsstrahlung)

During the lifetime of the plasma collisional processes between electrons, ions and neutrals will dominate energy transfer within the system and also the radiative emission that takes place. Radiative and collisional processes are however linked throughout the plasma lifetime. The main processes occurring between species in a laser produced plasma are summarised in table 2.1. These can be categorised into three main classes which are bound-bound (B-B), bound-free (B-F) and free-free (F-F) interactions.

Process	Excitation	De-excitation	Type
B-B	Impact Excitation	Impact De-excitation	Collisional
B-B	Photoabsorption	Spontaneous Decay	Radiative
B-F	Impact Ionisation	3-Body Recombination	Collisional
B-F	Photoionisation	Radiative Recombination	Radiative
F-F	Bremsstrahlung	-	Collisional
F-F	-	Inverse Bremsstrahlung	Radiative

Table 2.1: The main atomic processes that occur within a laser produced plasma [12].

2.4.1 Bound-Bound Pathways

Collisional Processes.

A bound electron may gain or lose energy through collision with another electron. The bound electron may become excited by energy transfer from the free-electron to the bound electron, promoting it to a higher energy level. This process is referred to as *electron-impact excitation*. The inverse situation may occur wherein the bound electron may be demoted to a lower energy level within the atom upon collision of the atom with another electron. This process is known as *electron-impact de-excitation*. In this case the second electron which is causing the de-excitation will experience a gain in kinetic energy equal to the difference between the initial and final states of the first electron.

The following balance equation describes these collisional processes [12]:

$$A + e(\epsilon_1) \rightleftharpoons A^* + e(\epsilon_2) \qquad (where\ \epsilon_2 < \epsilon_1) \tag{2.12}$$

where A is the atom/ion under consideration in a relaxed state and A^* is the atom/ion in an excited state. ϵ_1 and ϵ_2 are the free electron kinetic energies before and after collision. Electron-impact excitation proceeds left-to-right in the balance equation with electron-impact de-excitation occurring right-to-left.

Radiative Processes.

Photoabsorption is the process of promotion of an electron to an excited energy state by absorption of a photon. *Spontaneous decay* is the inverse process whereby an electron is demoted to a lower energy level by emission of a photon. These processes are described by equation 2.13. Photoabsorption occurs left-to-right and spontaneous decay occurs from right-to-left in the balance equation.

$$A + h\nu \rightleftharpoons A^* \tag{2.13}$$

A schematic of the bound-bound processes described is given in figure 2.1.

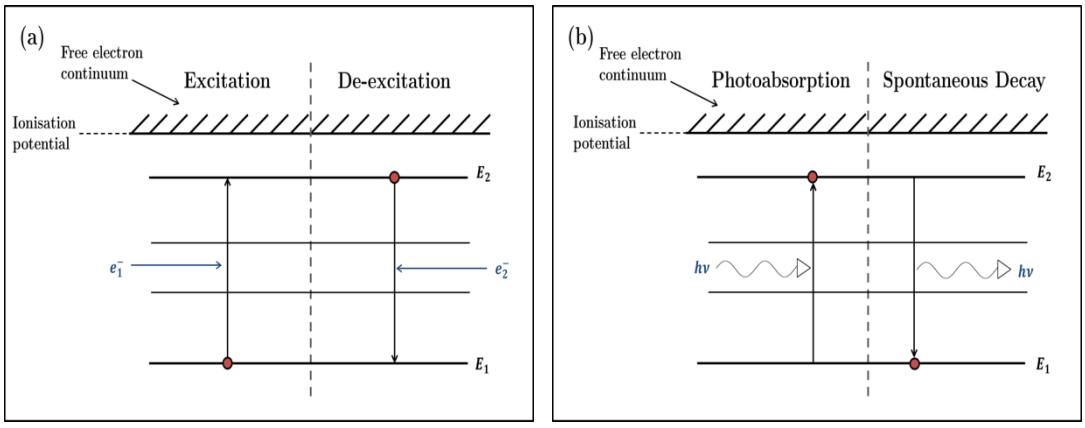

Figure 2.1: Schematic of (a) collisional and (b) radiative bound-bound processes occurring in a laser produced plasma [12] where $E_2 > E_1$.

These bound-bound collisional and radiative processes are the principal interactions that take place. In a laboratory plasma where electron densities are typically between 10^{16} cm^{-3} - 10^{21} cm^{-3}, collisional interactions play a vital role in plasma interactions. The

competition between collision and radiative processes are key factors in plasma equilibrium models which will be discussed in section 2.5.

2.4.2 Bound-Free Pathways

Bound-free processes occur between discrete (bound) states and continuum (free) states. When an ion receives enough energy, an electron may be promoted to the continuum. A free electron may also lose energy and be captured by an ion of charge "z+1" into a discrete energy level of an ion of charge "z". These types of processes are ionization and recombination transitions respectively.

Collisional Processes.

Ionisation occurs when a free electron collides with a bound electron and imparts enough energy to promote the bound electron into a continuum state. This process is known as *electron-impact ionisation* and results in ionisation of the target atom (or ion). The inverse process is known as *3-body recombination* and occurs in relatively high density plasmas in which a high probability exists to find two free electrons entering the Debye sphere of an ion. The first electron may be captured by the ion (reducing the ionization stage by one) while the second electron may absorb this surplus energy and experience a gain in kinetic energy. Since this process involves the interaction of an ion and two free electrons it is termed a "3-body" recombination. The first electron can now transition (by potentially multiple steps) to a lower bound state of the atom/ion. The two processes are described by the following balance equation:

$$A^Z + e_1(\epsilon_1) \rightleftharpoons A^{Z+1} + e_1'(\epsilon_1') + e_2(\epsilon_2) \qquad (\epsilon_1 > \epsilon_1') \qquad (2.14)$$

where Z represents the charge state, ϵ_1 is the energy of the incoming electron, ϵ_1' denotes its energy post interaction and ϵ_2 is the energy of the liberated free electron. Ionisation proceeds left-to-right in equation 2.14 and 3-body recombination proceeds from right-to-left.

Radiative Processes.

When a bound electron absorbs a photon of energy greater than the binding energy of the atom, an electron will be liberated into the continuum and the parent atom will become ionised. This process is referred to as *photoionization*. In cases of very high photon energy more than one electron may be liberated known as single photon, multi-electron ionization. This process can only occur where strong electron-electron correlation prevails [13]. Conversely, an electron existing in a continuum state may combine with an ion emitting a photon in the process. This interaction is known as *radiative recombination*. Both processes are described by equation 2.15 with photoionization proceeding from left-to-right and radiative recombination from right-to-left.

$$A^Z + h\nu \rightleftharpoons A^{Z+1} + e \tag{2.15}$$

Bound-free radiative processes are of particular importance in low density plasmas where competing collisional processes are of reduced significance. A schematic to represent the bound-free processes taking place within the laser produced plasma are shown in figure 2.2.

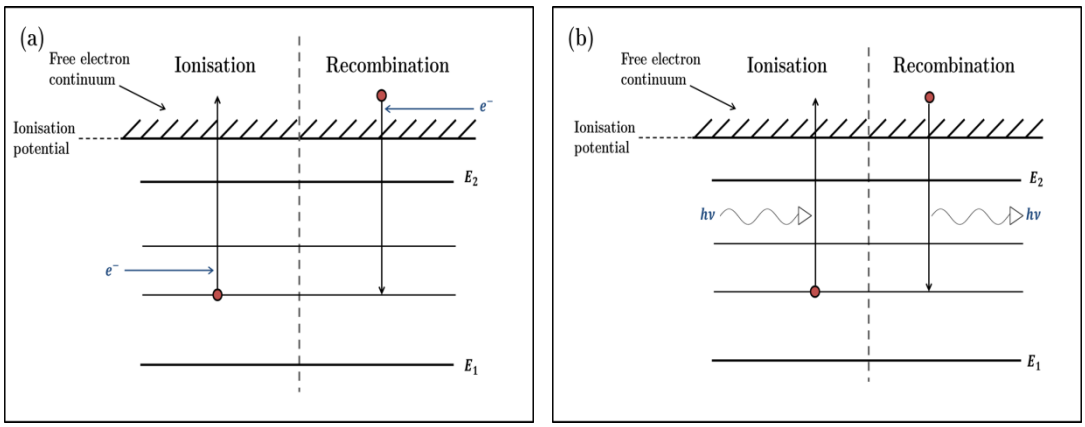

Figure 2.2: Bound-free transitions occurring in a laser produced plasma. Figure (a) demonstrates the collisional processes and (b) shows the radiative processes which may occur [12] where $E_2 > E_1$.

2.4.3 Free-Free Pathways

Only two mechanisms account for free-free transition possibilities within the plasma, namely the collisional process of *Bremsstrahlung* and the radiative process of *inverse-Bremsstrahlung* (IB). These free-free interactions are of particular importance in the laser produced plasma. The Bremsstrahlung process is the dominant feature of early lifetime plasma emission ($<$ 100 ns typically) and IB is the primary mechanism through which laser radiation is absorbed and heating occurs [6]. Both processes involve the scattering of a free electron from a nearby ion.

Collisional Processes.

An electron passing near an ion will feel the force of the Coulombic field and may decelerate resulting in the emission of a photon during this process. The emission of many multiples of these photons produces the familiar "braking radiation" observed in the early stages of a laser produced plasma. This continuum radiation is incoherent in nature and can provide meaningful information on the temperature of the plasma formed [14].

Radiative Processes.

The inverse-Bremsstrahlung process occurs when a free electron passing near the vicinity of an ion absorbs a photon and experiences an increase in kinetic energy. This interaction may only take place in the vicinity of an ion where any additional momentum occurring by this process may be transferred to the heavier ion. The two free-free processes described are represented in equation 2.16 where the Bremsstrahlung processes proceeds from left-to-right and the IB process *vice-versa*.

$$A^Z + e(\epsilon) \rightleftharpoons A^Z + e'(\epsilon') + h\nu \qquad (\epsilon > \epsilon') \tag{2.16}$$

The free-free interactions are demonstrated in figure 2.3.

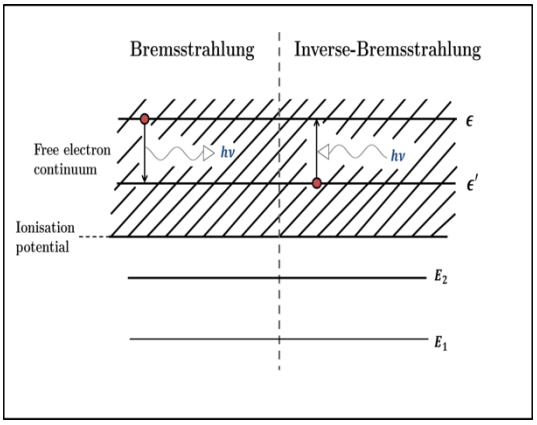

Figure 2.3: Schematic illustration of free-free processes of collisional Bremsstrahlung and radiative inverse-Bremsstrahlung occurring within the laser produced plasma [12] where the energy of continuum states $\epsilon > \epsilon'$.

2.5 Equilibrium in Plasmas

A plasma which exists in a state of *complete thermodynamic equilibrium* (CTE) must meet the following criteria [1]:

(i) All plasma species (electron, ions and atoms) exhibit a Maxwell velocity distribution [15].

(ii) The population distributions over the states of any atom or ion are given by the Boltzmann relation [16].

(iii) The ratio of ions having charge Z to those of charge (Z-1) is given by the Saha equation [17].

(iv) The intensity distribution of the emitted radiation can be described by the Planck radiation distribution function [18].

All atomic processes occurring in an ideal CTE plasma are balanced by an equal and opposite process. This ideal case is not feasible in laboratory plasmas due to energy losses brought about by the emission of radiation. As a result, a model with more flexible criteria must be employed for the description of the laboratory plasma which is transient in nature. The three thermodynamic models most frequently employed for laboratory plasmas are:

(i) Local Thermodynamic Equilibrium (LTE)

(ii) Coronal Equilibrium (CE)

(iii) Collisional Radiative Equilibrium (CR)

The applicability of each model is largely dictated by the electron density present in the plasma. Figure 2.4 is a phase diagram in which the limits of applicability of the various plasma equilibrium models are shown as a function of plasma temperature [19].

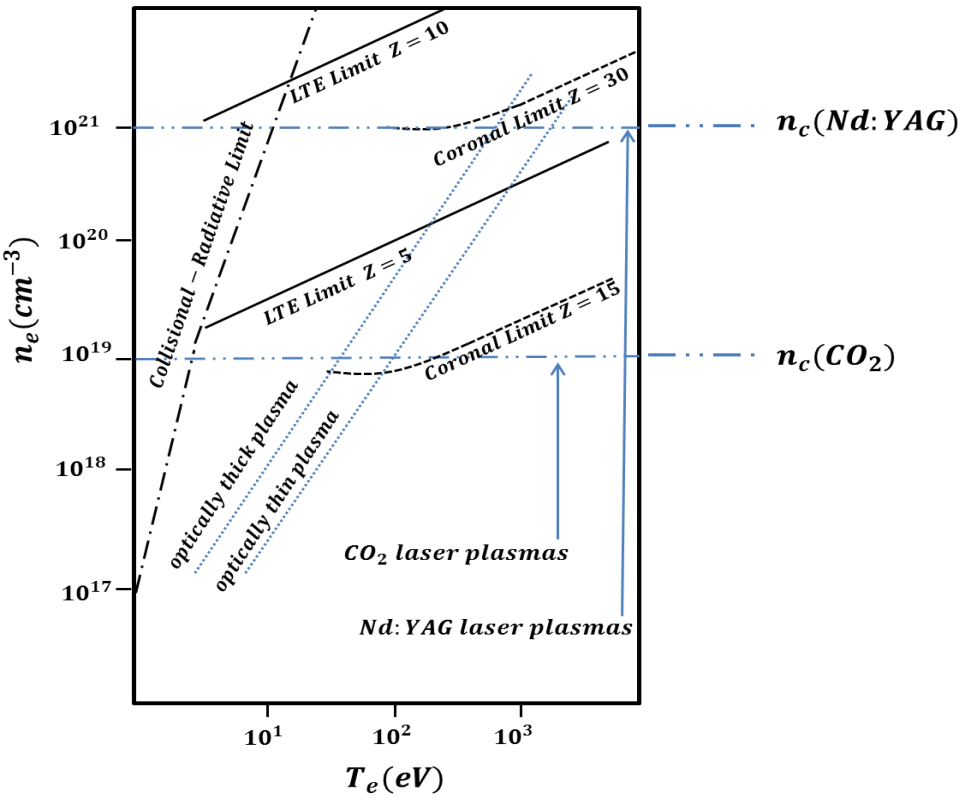

Figure 2.4: Criteria for applicability of different plasma equilibrium models. Taken from [19].

2.5.1 Local Thermodynamic Equilibrium (LTE)

The LTE model describes a system in which collisional processes dominate over radiative processes. For this to occur, a high electron density must exist in the plasma such that the collision frequency is high. The plasma is considered to be in a state of equilibrium when the rate of collisional excitation and ionisation is equal to the rate of collisional de-excitation and three-body recombination [19]. The electron density must

be high enough that an ion in an excited state has a greater probability of returning to the ground state via collisional de-excitation than by spontaneous emission which puts a lower limit on the electron density given by the McWhirter criterion [20]:

$$n_e \geq 1.6 \times 10^{12} T_e^{\frac{1}{2}} (\Delta E)^3 \tag{2.17}$$

where n_e is in units of cm^{-3}, T_e is the electron temperature in Kelvin and ΔE in eV is the transition energy for the emission line used to diagnose the plasma. The electron density requirements are higher in the case of optically thin plasmas where re-absorption of radiation is not significant.

Contrary to the case of CTE, the temperature is not necessarily uniform throughout the plasma. The electron and ion velocity distributions must however obey a Maxwell-Boltzmann distribution. This criterion is satisfied when the electron-electron relaxation time is small compared to the electron heating time. This condition is characteristic of all plasma radiation models [19].

2.5.2 Coronal Equilibrium (CE)

The CE model describes low density, optically thin plasmas such as those typically found in solar coronas. In these low density, high temperature (typically $n_e < 10^{12}$ cm^{-3}) plasmas the rate of radiative de-excitation processes becomes comparable, or even greater than the rate of collisional de-excitation processes. Collisional excitation rates are low in the CE plasma due to the low electron density, meaning that excited electrons will have sufficient time to relax to the ground state before another collisional excitation incident can occur. The significance of this is that the majority of ions within the plasma will be found in the ground state.

2.5.3 Collisional Radiative Equilibrium (CRE)

For plasmas with a moderate electron density (in the range 10^{19} cm^{-3} – 10^{21} cm^{-3}) the CRE model is appropriate. In this regime, the rate of collisional recombination and radiative recombination processes are comparable in the plasma. In order for the CRE model to be valid the population density of ions having charge $(Z+1)$ must not change significantly during the period when the quasi steady-state population distribution is being established among the ions of charge Z [19]. The plasma must also be optically thin to its radiation.

2.6 Fast Imaging

A number of different plasma diagnostic techniques were employed during the course of this work on the study of laser produced plasmas in liquid and air. Imaging and spectroscopy experiments were used to track the expansion dynamics of the plasma and to extract information on plasma parameters such as electron temperature and density. Laser interferometry and shadowgraphy can be employed to study the spatial distribution of electron densities or regions of non-uniformity such as shockwave expansion. All of these techniques can be applied to laser produced plasmas to build a full picture of the plasma properties. This section will detail the theory of each diagnostic technique and the methods by which useful plasma parameters can be extracted.

Broadband emission imaging is a technique widely employed in the study of laser produced plasmas. By applying a fast electronic shutter to gate the charge-coupled device (CCD), the spatial and temporal evolution of the excited emission plume can be tracked. Gate widths on the order of ten nanoseconds were typically used throughout this work allowing the plasma emission to be observed with good temporal resolution. An increasingly higher voltage can be applied to the intensified charge-coupled device (ICCD) array to yield a higher gain for a sufficiently bright image to be obtained at late

times when plasma emission is weakening. The operation of the ICCD is discussed in further detail in section 3.4. From imaging data the physical dimensions of the plasma as well as plume velocities can by ascertained for the entirety of the excited plasma emission lifetime. During this work plume front was defined as the position at which the ICCD count had dropped to $1/e$ (~0.37) of its maximum value in the expansion direction normal to the target surface.

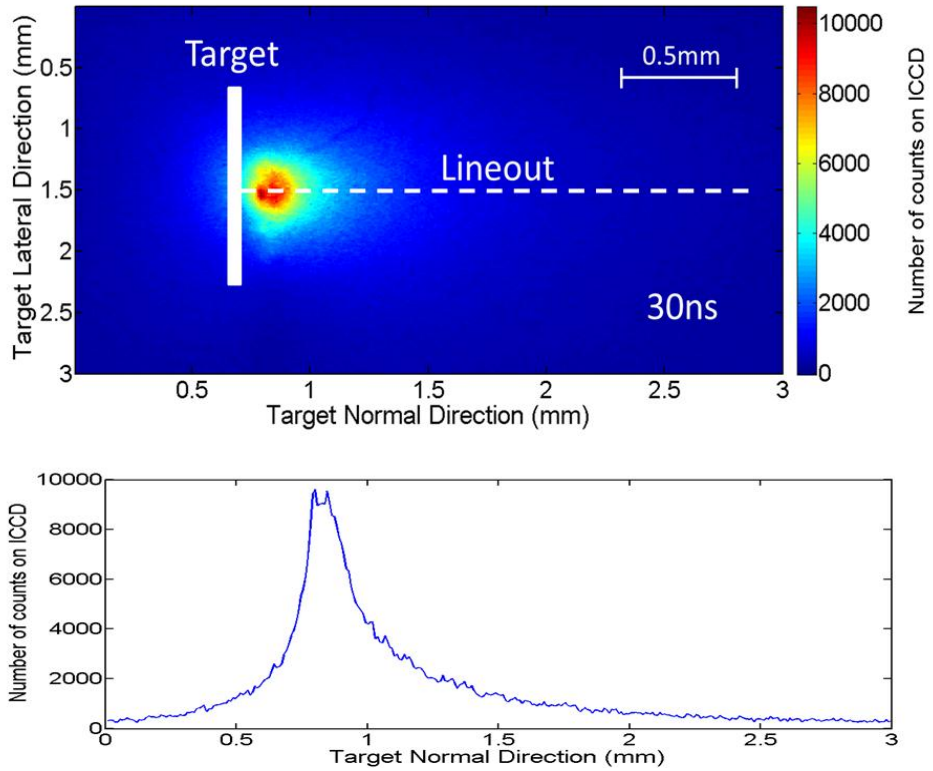

Figure 2.5: Image of aluminium plasma formed in air using a 1064 nm, 52 mJ pulse with corresponding lineout beneath. Plume front positions were extracted from image lineouts. Image recorded at a delay time of 30 ns using a 10 ns gate width.

Spectral filtering of the plasma emission allows specific charge states of interest to be imaged. Narrow bandpass filters may be inserted into the setup which will allow selection of a particular spectral transition of interest. For example, the singly charged aluminium ion at 466.6 nm may be isolated from the broadband emission by means of a filter whose central wavelength corresponds to the transition of interest. This most simplistic of diagnostic tools can provide information on spatial and spectral distribution maps of emitting species as a function of time. The imaging of plume

dynamics is however limited to the excited emitting species and does not represent those non-emitting species in the cold outer regions of the plasma.

2.7 Optical Emission Spectroscopy

Arguably the most informative diagnostic tool is emission spectroscopy. The spectral radiation emitted by the laser produced plasma contains information relating to the constituent emitting species within the plasma. Analysis of this spectral radiation provides knowledge of important plasma parameters.

Two types of radiation are emitted by the plasma. Continuous or broadband radiation is emitted by bound-free and free-free interactions and is the dominant radiation type in the first ~100 ns of the plasma lifetime. At mid to late plasma lifetimes, line radiation is observed due to bound-bound interactions. The profile of an emitted spectral line will be determined by the local plasma conditions and different broadening mechanisms will have an effect. The three main mechanisms taking place in the plasma are natural, Doppler and pressure broadening. Each of these potential broadening mechanisms are related to different properties of the plasma, namely transition probability, thermal velocity and collision frequency for each mechanism respectively.

In this section the spectral line profiles will be discussed as well as the different broadening mechanisms that may occur. The methods in which electron densities and temperatures have been extracted from spectroscopy measurements will also be discussed.

2.7.1 Natural Broadening

The angular frequency of radiation emitted or absorbed in a transition between two discrete energy levels is given by:

$$\omega_{21} = \frac{E_2 - E_1}{\hbar} \tag{2.18}$$

where $E_2 > E_1$, ω_{21} is the angular frequency of the photon emitted and $\hbar$ is the Planck constant divided by 2π.

According to this relation an infinitely sharp line is emitted (or absorbed). From the Uncertainty Principle the exact knowledge of the energy of such levels is forbidden leading to a spread of possible energies on the order of $\hbar/\tau$ where τ is the lifetime of the state. This means that a finite probability exists for a photon to be emitted in some finite energy interval centred about (E_2 - E_1). This is the minimum possible spectral line width that may be measured which results in a Lorentzian intensity distribution function of the form:

$$\mathcal{L}(\omega) = \frac{\Gamma}{2\pi} \frac{1}{(\omega - \omega_0)^2 + (\Gamma/2)^2} \tag{2.19}$$

where $\Gamma/2$ is the Full Width at Half Maximum (FWHM) of a normalised Lorentzian line [12]. In general the natural line width of an atomic transition is beyond the resolution of most laboratory scale grating spectrometers and is usually probed using actively stabilised narrow linewidth lasers or Fabry-Perot interferometers.

2.7.2 Doppler Broadening

Doppler broadening is a shift in the observed wavelength of a line caused by the motion of the emitter with respect to the observer. A shift to shorter wavelength (blueshift) is observed if the emitting atom is moving towards the observer and the opposite (redshift) for an emitter moving away from the observer. The observed wavelength is given by:

$$\lambda_{observed} = \lambda_0 \left(1 \pm \frac{v_x}{c}\right) \tag{2.20}$$

where v_x is the non-relativistic velocity of the emitter and λ_0 is the emitted wavelength.

The Doppler effect creates a spread of observed wavelength and is related to the velocity distribution of the emitters. Assuming a Maxwellian velocity distribution this results in a Gaussian profile for the observed spectral line of the form:

$$\mathcal{G}(\omega) = \frac{1}{\sqrt{2\pi\sigma}} exp\left(-\frac{1}{2}\left(\frac{\omega - \omega_0}{\sigma}\right)^2\right) \tag{2.21}$$

where σ is the FWHM of the Gaussian line [12].

The Doppler broadening contribution plays a significant role in high temperature plasma and in low-Z elements where the velocities of the emitting species are greatest. The FWHM (nm) of such a line is given by [21]:

$$\Delta\lambda_{D_{\frac{1}{2}}} = 7.16 \times 10^{-6}\lambda_0\sqrt{\frac{T}{m}} \tag{2.22}$$

where m is the atomic weight of the emitting atom or ion, λ_0 is the centre wavelength (nm) and T is the temperature (K) of the Maxwellian velocity distribution of the emitters.

2.7.3 Pressure Broadening

Interactions occurring between the emitter and the surrounding species will induce pressure broadening. Three classifications exist which are (i) resonance, (ii) Van der Waals and (iii) Stark broadening depending on whether the interaction taking place with the emitter is with (i) the same type of atom, (ii) a different type of atom or (iii) a charged particle.

The class of broadening of greatest concern in the work reported here is Stark broadening as the majority of particles comprising the plasma are by definition charged. There are two components that contribute to the Stark broadened line width, electron-emitter collisions and ion-emitter collisions. Electron-emitter collisions occur on a very short timescale, much shorter than the natural lifetime of the state. Electron-emitter collisions dominate the line broadening in dense laser plasmas. The ion-emitter collisions

take place over a much longer timescale. The FWHM (nm) of a Stark-broadened spectral line is given by the expression [22]:

$$\Delta\lambda_{width} = 2w\left(\frac{n_e}{10^{16}}\right) + 3.5A_i\left(\frac{n_e}{10^{16}}\right)^{\frac{1}{4}}\left(1 - 1.2N_D^{-\frac{1}{3}}\right)w\left(\frac{n_e}{10^{16}}\right) \quad (2.23)$$

where w is the electron-impact parameter. The first term on the right-hand side of the equation describes the contribution due to the electron-emitter collisions. The second term on the right-hand side of the expression is the ion-emitter contribution which is determined by A_i, the ion broadening parameter. In the case of relatively low temperature, high density ($n_e > 10^{14}\,\mathrm{cm}^{-3}$) plasmas Stark broadening is dominated by electron-emitter collisions meaning the ion broadening term may be omitted in these cases reducing the electron density (cm^{-3}) expression to [23]:

$$n_e = \left(\frac{\Delta\lambda_{FWHM}}{2w}\right) \times 10^{16} \quad (2.24)$$

In a hot dense plasma, the Stark-shift of the energy levels may also act to broaden the emission lines. The electric fields from neighbouring particles perturbs the energy levels of the emitter, causing a shift in the observed wavelength of the emitted photons given by:

$$\Delta\lambda_{shift} = d\left(\frac{n_e}{10^{16}}\right) + 2A_i\left(\frac{n_e}{10^{16}}\right)^{\frac{1}{4}}\left(1 - 1.2N_D^{-\frac{1}{3}}\right)w\left(\frac{n_e}{10^{16}}\right) \quad (2.25)$$

where d is the calculated shift parameter [24] i.e. the amount by which a spectral line is shifted by the plasma field experienced by the emitted atom or ion. Equations 2.24 and 2.25 may only be applied if the number of particles within the Debye sphere is greater than 2 and if the parameter A_i is less than 0.5 [25].

2.7.4 Gaussian, Lorentzian and Voigt Profiles

As a consequence of the different broadening effects the resulting profile of the emitted line is in general best approximated by a Voigt profile which takes the form:

$$\mathcal{V}(\omega) = \mathcal{L}(\omega_0 - \omega) \otimes \mathcal{G}(\omega_0 - \omega) \tag{2.26}$$

where $\otimes$ corresponds to convolution. A Voigt profile is the result of the convolution of a Gaussian and a Lorentzian profile.

In any real spectral measurement instrument broadening must also be accounted for which may take many forms (e.g. trapezoidal, Gaussian etc.). The instrument broadening imposes a limitation on the resolution achievable for the spectra recorded and should be experimentally determined prior to analysis.

The instrument function was experimentally determined for the spectrometer employed in this work using a low pressure Mercury lamp (~567 nm line). A FWHM of 0.45 nm was obtained for a 50 µm slit width which was used for all recorded spectra measured in this work. The measured linewidth was best approximated by a Gaussian function. An instrument function of 0.26 nm was achievable using a narrower slit width of 10 µm, however this had the effect of reducing significantly the amount of light collected by the CCD. Further details on the spectrometer are presented in section 3.5.

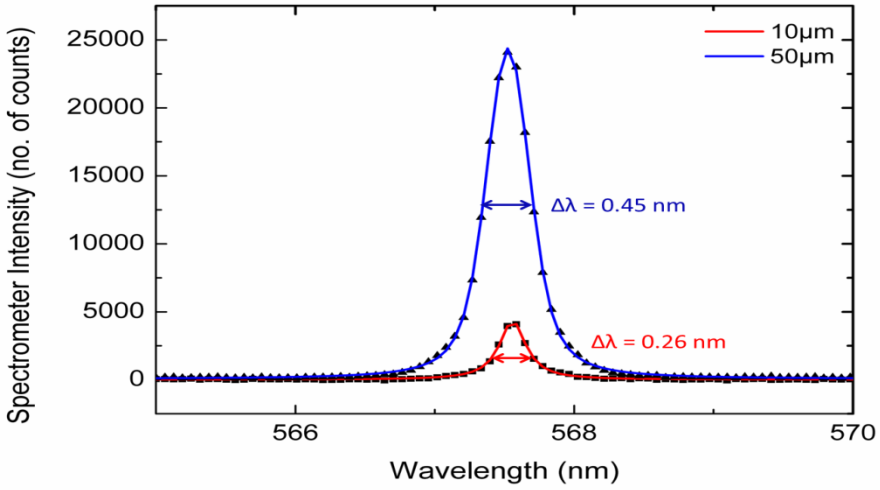

Figure 2.6: Mercury spectral line measured using a 10 µm slit width and a 50 µm slit width. Number of spectrometer counts measured ~6× increased using 50 µm slit width.

2.7.5 Electron Density

Many spectroscopic methods exist for the determination of electron densities in plasmas. Electron densities may be extracted by analysis of Stark widths, Stark shifts, relative line intensities and absolute continuum intensities [24]. An approximate knowledge of the plasma temperature is required for each of these methods. For a laser produced plasma in collisional-radiative equilibrium, Colombant and Tonon have shown that this temperature can be approximately known by the expression [19]:

$$T(eV) \approx 5 \times 10^{-6} Z^{\frac{1}{5}} (I\lambda^2)^{\frac{3}{5}} \tag{2.27}$$

where Z is the atomic mas, λ is the laser wavelength (in µm) and I is the on-target irradiance (in Wcm^{-2}). This estimate for the plasma temperature assumes a state of collisional radiative equilibrium for the plasma and is considered valid during the laser pulse [19]. For the laser irradiances used during this work (10^{10} - 10^{11} Wcm^{-2}), initial plasma temperatures in the range of ~10 to 40 eV should be expected for plasmas generated using a 1064 nm laser pulse.

In order to determine electron temperature and densities the plasma was assumed to exist in a state of LTE. This assumption requires the condition that transitions occurring within the plasma are dominated by collisional processes as opposed to competing radiative processes [19]. For the validity of this assumption the electron density must be sufficiently high, the minimum value being determined from the McWhirter criterion given in equation 2.17. This places a lower limit of n_e~10^{15} cm^{-3} for transitions studied during the work reported here (from equation 2.17) making LTE a valid assumption since the measured plasma densities exceeded ~10^{16} cm^{-3} in all cases.

2.7.6 Electron Temperature

There are many techniques which are used to evaluate electron temperatures in plasmas. An approximate knowledge of the plasma temperature is indicated by observation of the maximum ion stage present in the plasma [26]. Bremsstrahlung

radiation can also be used to calculate the electron temperature in plasmas where no bound-bound or bound-free interactions occur [1]. As previously mentioned, by equation 2.22 the Doppler broadening of atomic transitions can also be used to calculate electron temperatures. However the most frequently used techniques are related to line intensity ratios. The three principal methods are (i) line-to-line ratios from the same charge state, (ii) line-to-line ratios from successive charge states and (iii) line-to-continuum ratios.

Line-to-Line Ratios from the Same Charge State

In optically thin plasmas of length l along the line of sight, the integrated intensity of a line is given by [27]:

$$I_{nm} \approx \frac{\hbar\omega_{mn}}{4\pi} A_{nm} N_m l \tag{2.28}$$

where I_{nm} is the integrated intensity of the line, ω_{mn} is the emission frequency of the line, A_{nm} is the atomic transition probability and N_m is the excited state population distribution. Assuming a state of LTE the population distribution of any two states can be related by the Boltzmann factor [27]:

$$\frac{N_m}{N_n} = \frac{g_m}{g_n} \exp\left(-\frac{E_m - E_n}{k_B T}\right) \tag{2.29}$$

Expressing the ratio of the integrated intensities of the two populations in the same manner gives:

$$\frac{I_m}{I_n} \approx \left(\frac{\omega_m A_m g_m}{\omega_n A_n g_n}\right) exp\left(\frac{E_m - E_n}{k_B T}\right) \tag{2.30}$$

where m and n refer to the two individual spectral lines. Plasma temperatures calculated by this method will in general produce errors of at least 10% [27], [28]. The accuracy of the method can be improved by using the relative intensities of several lines originating from (or to) the same atomic states of different excitation energies of the same species. Plotting the logarithm of the intensity ratios against the excitation energies of the upper levels should produce a straight line [21]. This is known as the

Boltzmann plot method. The reciprocal of this straight line will provide a more accurate value for the electron temperature with typical uncertainties in the range of 5-10% as noted by Griem [24] and observed during this work.

Line-to-Line Ratios from Successive Charge Stages

Due to the relatively small energy differences between excitation energies, line ratios within a given ion normally do not lend themselves to very precise temperature measurements [27]. This situation can be improved by measuring the ratios from successive charge states. This introduces a further energy separation by E_∞, the ionisation energy, which usually leads to an energy separation of the levels larger than $k_B T$. Using the Saha equation, Griem has shown that the intensity ratios are given by [27]:

$$\frac{I_1}{I_2} = \frac{f_1 g_1 \lambda_2^3}{f_2 g_2 \lambda_1'^3} (4\pi^{\frac{3}{2}} a_0^3 n_e)^{-1} \left(\frac{k_B T_e}{E_H}\right)^{\frac{3}{2}} exp\left(\frac{-E_1 + E_2 - E_\infty + \Delta E_\infty}{k_B T_e}\right) \qquad (2.31)$$

where I, f, g and λ are the total integrated intensity of the line, the oscillator strength, the statistical weight of the transition and the wavelength respectively. a_0 and E_H represent the Bohr radius and the ionisation energy of the hydrogen atom. E_1 and E_2 are the excitation energies of the successive ion stages. E_∞ and ΔE_∞ are the ionisation energy of the lower ionic stage and the high density correction factor which accounts for the shift of the ionisation energy due to a strong electric field. The higher ion stage is denoted by the subscript 1.

Since the error on the slope is usually greater than the error associated with the line ratio, the successive ion stage method will provide better precision on the electron temperature than the Boltzmann plot method.

Line-to-Continuum Ratios

The background continuum emission is due to free-bound interactions (interactions of free electrons with ions resulting in recombination) and Bremsstrahlung emission due to free-free transitions. The relative line-to-continuum method uses the ratio of integrated line profiles relative to the underlying continuum emission in the same wavelength interval. This technique is useful at early plasma lifetimes where a strong continuum emission creates difficulties in accurately measuring the intensity of line emission. The expression for the evaluation of the electron temperature by this technique has been derived by Griem [24] and is given by:

$$\frac{\epsilon_l}{\epsilon_c}(\lambda) = C_r \frac{A_{21}}{U_i} \frac{\lambda_c^2}{\lambda_l T_e} exp\left(\frac{E_\infty - E_2 - \Delta E_\infty}{k_B T_e}\right)$$

$$\times \left[\xi\left(1 - exp\left(\frac{-hc}{\lambda k_B T_e}\right)\right) + G\left(exp\left(\frac{-hc}{\lambda k_B T_e}\right)\right)\right]^{-1} \quad (2.32)$$

where $C_r = 2\times10^{-5}$ (sK), A_{21} is the transition probability for the discrete line emission. ϵ_c is the continuum emission coefficient over the line profile and ϵ_l is the integrated emission coefficient over the line profile. λ_c and λ_l are the continuum centre wavelength and line centre wavelength. E_∞, E_2 and ΔE_∞ are the ionisation potential, upper level energy and the correction to the ionisation potential in the field of the ions. U_i is the partition function of the ion of interest. G is the free-free Gaunt factor and ξ is the free-bound continuum correction factor [14], [29].

The line-to-continuum method will only yield accurate results when the intensity of the continuum and line emission are comparable. For laser-produced plasmas this corresponds to a timescale of roughly 30-100 ns after the creation of the plasma [14]. The determination of the electron temperature using this method is complicated by the inclusion of the partition function U_i which has a non-negligible temperature dependence. In addition, the continuum correction factor ξ is unknown for most situations and must be determined by comparing the line-to-continuum ratios of the two lines, resulting in simultaneous equations.

2.7.7 Data Analysis

Analysis of the spectral lines was carried out using the commercial peak fitting software AAnalyzer [30]. From these fits, measurements of Stark broadened line-widths and integrated line intensities could be extracted. The parameters acquired from the peak fitting operation were then exported to MATLAB where electron temperature and density calculations were carried out. Figure 2.7 shows an example of the fitting procedure carried out using the AAnalyzer program. The measured Gaussian instrument function was then used in the AAnalyzer deconvolution software to extract the Lorentzian component for Stark width analysis.

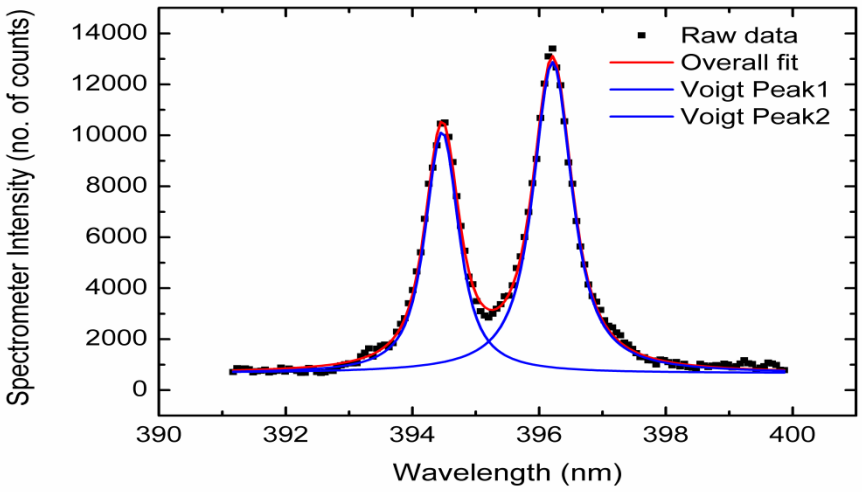

Figure 2.7: Aluminium neutral doublet and corresponding fit carried out in AAnalyzer [30]. Parameters obtained from fitting procedure include the Stark broadened FWHM and integrated line intensities.

From the Stark broadened line profiles the electron densities could be deduced using equation 2.24. Knowing the electron density, the electron temperature could be subsequently obtained by solving equation 2.31 By comparing the ratio of integrated line intensities from the spectral line data with the solution on the right-hand-side of equation 2.31 the temperature may be determined. The process is demonstrated graphically for ease of representation in figure 2.8.

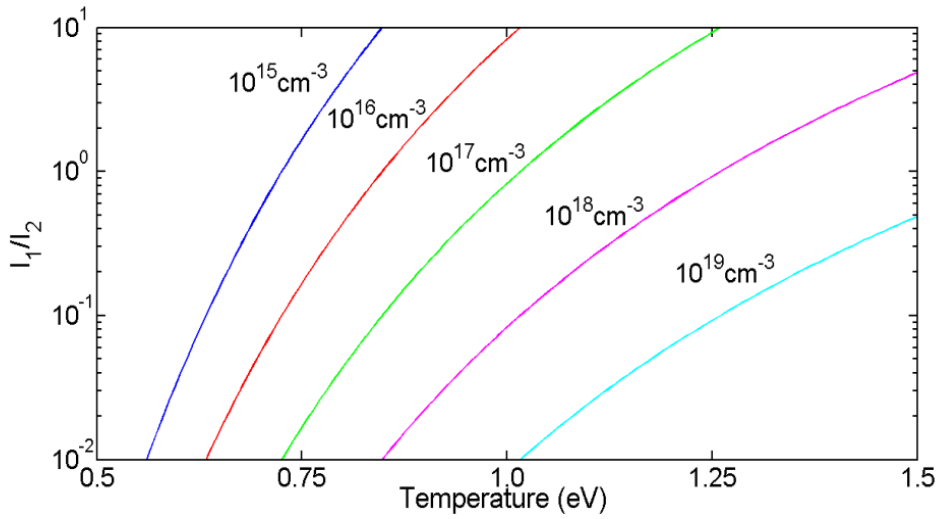

Figure 2.8: Theoretical solution to equation 2.31 for a range of electron densities calculated from the ratio of Al^+ 466.15 nm and Al^0 396.15 nm transitions.

The electron density n_e is first determined using the Stark broadening method described in section 2.7.3. For a given value of n_e, equation 2.31 is solved over a suitable temperature range which produces a solution for the transitions of interest such as those demonstrated in figure 2.8 for the transitions Al^+ 466.3 nm and Al^0 396.15 nm. The experimentally calculated line intensity ratio is then compared to this solution and the temperature is deduced. As the electron density is changing with time, the temperature is evaluated at each point in time by this procedure.

2.8 Shadowgraphy

Shadowgraphy is a technique used to measure variations in transmitted intensity of light which passes through a non-uniform medium such as a laser produced plasma. The non-uniform electron density distribution of the plasma corresponds to a change in refractive index for the collimated probe beam. The refractive index of the medium will result in a deflection of the collimated light probe beam [31]. This is represented schematically in figure 2.9.

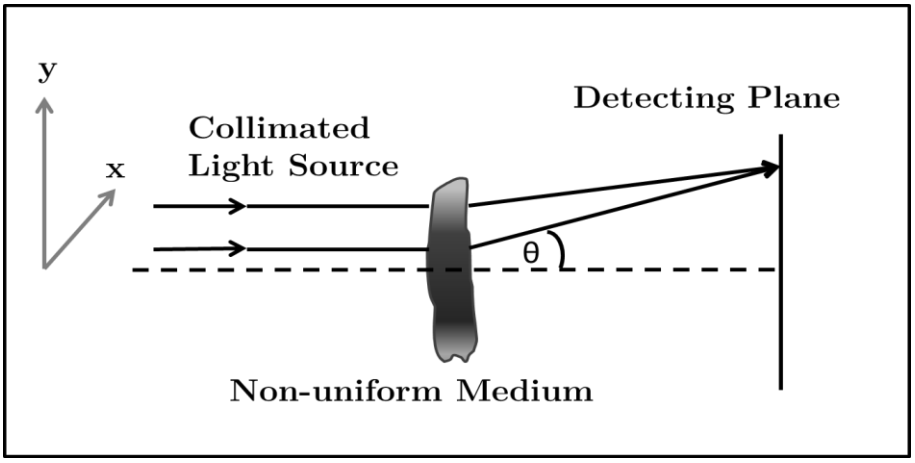

Figure 2.9: Schematic diagram of the deflection of a collimated light source passing through a non-uniform medium. Deflection occurs in the position y-direction for a plasma density gradient along the x-direction.

The phase shift induced by the plasma is given by [32]:

$$\phi = \int n \frac{\omega}{c} . dl \tag{2.33}$$

After passing through the plasma the emerging beam is subtended by an angle θ with respect to the incident beam given by [32]:

$$\theta(y) = \frac{d\phi}{dy} \frac{\lambda}{2\pi} = \frac{d}{dy} \int ndl \tag{2.34}$$

On passage through the plasma the beam is deflected through an angle proportional to the density gradient. If the position of the beam in the absence of the plasma is denoted by y, then the new position of the beam in the presence of the plasma y' is given by:

$$y' = y + L\theta(y) \tag{2.35}$$

where L is the distance from the non-uniform medium to the detecting plane.

The same deflection occurs in the orthogonal direction i.e. along the target plane denoted by the x coordinate. A beam incident on a point (x, y) at the detection plane will be displaced to a position (x', y') on the observation plane in the presence of the plasma where:

$$(x', y') = \left(x + L\frac{d}{dx}\int ndl\, , y + L\frac{d}{dy}\int ndl\right) \tag{2.36}$$

Denoting the incident beam intensity by I_i and the detected intensity I_d gives:

$$I_d dx' dy' = I_i dx dy \tag{2.37}$$

From equation 2.36 and 2.37:

$$\frac{I_i}{I_d} = 1 + L\left(\frac{d^2}{dx^2} + \frac{d^2}{dy^2}\right)\int ndl \tag{2.38}$$

From this expression and assuming relatively small fractional intensity variations one retrieves:

$$\frac{\Delta I_{dl}}{I} = L\left(\frac{d^2}{dx^2} + \frac{d^2}{dy^2}\right)\int ndl \tag{2.39}$$

Thus the recorded shadowgram signal is proportional to the second derivative of the refractive index of the medium.

Shadowgraphy is a particularly useful technique for studying the dynamic expansion of the laser produced shock-front [33], [34]. Details of the experimental setup used for shadowgraphy measurements during the current work are provided in section 3.6. The compression arising at the shock-front causes a variation in refractive index which is discernible from the shadowgrams. By differentiating the images, the discontinuities at the shock-front become more apparent.

2.9 Laser Interferometry

As previously stated, the determination of plasma temperatures and densities at early plasma lifetimes may be achieved using the line-to-continuum ratios provided by emission spectroscopy. This method however is more complicated than those available at mid to late plasma lifetimes. An alternative or complementary technique is provided by laser interferometry where the electron density distribution at early plasma lifetimes <

100 ns may be determined [35], [36]. The underlying concept of the interferometer is described by Hutchinson [32].

According to standard plasma theory the refractive index of the plasma is due to contribution from free electrons only [32]. The phase shift induced by the plasma is then related to the number density of free electrons contained in the plasma by:

$$\Delta\phi = \frac{-\omega}{2cn_c}\int n_e dl \tag{2.40}$$

The negative sign denotes a retarding of the probe beam as it passes through the density gradient of the plasma. Using the mathematical Abel inversion technique [37] a solution can be obtained which gives the electron density as [38]:

$$n_e \cong -\frac{\lambda_{\mu m} n_c}{\pi}\int_r^{rmax}\frac{d\Delta\phi}{dx}(x^2 - r^2)^{-\frac{1}{2}}dx \tag{2.41}$$

where r is the radial distance from the centre of the plasma to the light path passing through the plasma and x is the propagation distance of the light [37].

The interferometry setup used during this work is detailed in section 3.6. Figure 2.10 shows an example of an interferogram of an aluminium plasma recorded using a 38 mJ, 1064 nm laser pulse in air and the corresponding background interferogram where no plasma is present. The interferograms were recorded at a time delay of 50 ns. Hemispherical fringes corresponding to plasma shockwave expansion from the point of laser focus on the target can be discerned from the image.

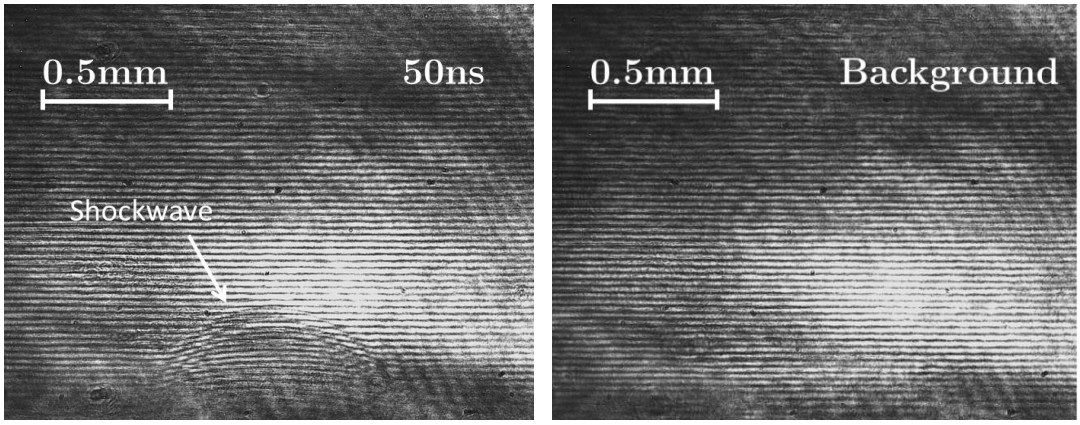

Figure 2.10: Interferogram showing shockwave expansion after 50 ns in air (left) and background interferogram where no plasma is present (right). Interference fringes can be seen in the presence of the plasma.

2.10 Laser Produced Plasmas in Liquid

A laser produced plasma created in a liquid environment exhibits some very unique behaviours compared to that of a plasma formed in gas or vacuum. The expanding plasma is heavily restricted by the density of the surrounding background. Owing to this, the high-pressure plasma that is created drives a shockwave into the surrounding liquid. The high density liquid acts to constrain the plasma during expansion which creates a stronger shock in comparison to ablation under atmospheric conditions [39]. Another unique feature of the laser produced plasma in liquid is the cavitation bubble that forms by vapour generated by the plasma some microseconds after the laser pulse.

2.10.1 Laser-Matter-Liquid Interactions

When a laser pulse is focussed onto a target material submerged in liquid a series of interactions may occur [40]. The initial interaction takes place between the laser pulse and the liquid. Following this, the laser-matter interaction occurs. At sufficient laser pulse energy, this will result in the liberation of target material forming a suspension in the liquid. The liquid medium may contain various ionic/molecular elements (surfactants, electrolyte) which can potentially interact with the target material. The

material released from the target surface may also interact with the trailing edge of the laser pulse. All of these interactions are strongly coupled, and the unique particle bonding reactions taking place have had particular significance in the area of nanoparticle generation [40].

2.10.2 Expansion Models

A laser plasma created in a vacuum will undergo free adiabatic expansion at a constant velocity [41]. On the other hand, for a plasma expanding into a background gas, the abrupt release of energy from the target surface into the background ambient results in a "blast wave" which emanates radially outwards from the interaction area. The shock front position of such a blast wave is described by the Sedov-Taylor theory or the point explosion model as it is sometimes referred to [42]:

$$R = \xi_0 \left(\frac{E_0}{\rho_0}\right)^{\frac{1}{(2+\upsilon)}} t^{\frac{2}{(2+\upsilon)}} \tag{2.42}$$

where t is the time delay with respect to plasma ignition, E_0 is the amount of energy released in the explosion, ρ_0 is the ambient gas density, and ξ_0 is a constant given by $\xi_0 = \left[1.08\left(\frac{\gamma+1}{2}\right)\right]^{\frac{2}{(2+\upsilon)}}$ [43]. The parameter υ will have a value of 1, 2 or 3 for planar, cylindrical or spherical symmetry. A general equation can be used for freely expanding plasmas where the plume front position is given by:

$$R = \alpha t^n \tag{2.43}$$

Here R is the plume front position, t is time and α and n are fitting parameters. α is a constant and n will have a value of 0.4 for a perfectly spherical shock wave [41]. This shock wave (or point explosion) model is applied in this report to describe the expansion of the plume front in air. As the volume of the plasma increases, the pressure exerted by the surrounding medium makes a larger contribution to the plasma confinement. Pressure is exerted on the plume front by the surrounding medium which causes a deceleration of the plume front that is not accounted for in the shock-wave

model. Therefore in high pressure backgrounds a classic drag-force model is usually employed to account for this deceleration [41], [44]:

$$R = R_0\left(1 - e^{-\beta t}\right) \tag{2.44}$$

where R_0 is the stopping distance of the plasma and β is the drag coefficient. In the present work, both expansion models were employed to describe the observed behaviour of plasma expansion in a liquid environment.

2.11 Shockwave Formation

After the laser impinges on the submerged solid target, the absorption of the laser pulse at the target surface causes the emission of a shockwave which acts to dissipate the energy. By definition this shockwave is the formation of discontinuities in flow variables such as density [6]. Two distinct compressive waves are emitted, one is transmitted into the bulk material and the other propagates into the liquid [39], [45]. The pressure associated with the stress wave induced in the bulk material can exceed several GPa due to the confining effects of the liquid on the plasma expansion [46]. In the liquid a change in refractive index occurs at the shock-front which is observable at ~50 ns [47], [48]. The shockwave carried energy is defined as the energy flux across an area where a shockwave front arrives given by [49]:

$$E_s = \frac{4\pi r_s^2}{\rho_\infty}\int_0^{t'} \frac{(P - P_\infty)^2}{U_s - \left((P - P_\infty)/\rho_\infty U_s\right)}\,dt \tag{2.45}$$

where r_s is the radial distance of the shock-front from the origin, P is the shockwave pressure, P_∞ is the ambient liquid pressure, ρ_∞ is the liquid density, U_s is the shock-front velocity and time t is taken as zero at the shock-front and t' at the tail of the shockwave.

The shockwave emitted in a liquid environment has been observed in many studies to consist of two temporal regimes. During the first several nanoseconds the shockwave

expands rapidly with decreasing velocity as time proceeds. A report by Tsuji *et al.* [47] demonstrates this non-linear behaviour at early shockwave expansion times. In their study shadowgraphy measurements carried out using the fundamental wavelength 1064 nm on a silver target show the evolution of the shockwave as a function of time shown in figure 2.11.

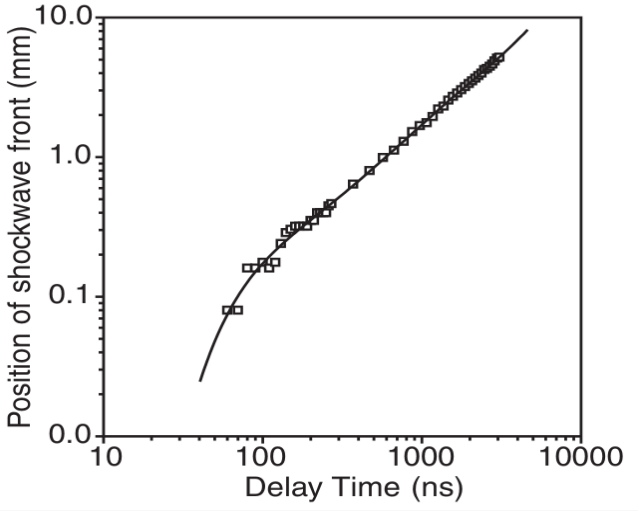

Figure 2.11: Time profile of the propagation of the shockwave observed from shadowgraph images of a silver plate in water using 20 mJ, 1064 nm laser pulses. Taken from [47].

Supersonic velocities have been reported for this initial expansion occurring in the first ~100 ns [45], [47], [48]. The expansion velocity of the shockwave is then reported to transition to an approximately linear behaviour after ~300 ns as can be seen in figure 2.11. This transition from a strong wave to a weak wave is consistent with early findings on the dynamic behaviour of spherical shockwaves in water first reported by Vogel *et al.* [50].

2.11.1 Cavitation Bubble

A unique feature of the laser produced plasma in liquid environments is the cavitation bubbles that are generated at the solid-liquid interface. When the liquid pressure falls below the tension strength of the liquid by ΔP_c (equation 2.47) at roughly constant

liquid temperature, a cavitation bubble is formed. The internal pressure and temperature of the bubble is much greater than that of the surrounding medium [51]. The interior pressure of a bubble P_B with radius R is given by:

$$P_B = P_\infty + \frac{2\sigma}{R} \tag{2.46}$$

Where P_∞ is the liquid pressure at infinity i.e. atmospheric pressure [52]. Nucleation of cavitation occurs at the critical nucleation size R_c, therefore

$$\Delta P_c = \frac{2\sigma}{R_c} \tag{2.47}$$

The cavitation bubble grows to a maximum radius and then collapses. After the collapse of the bubble, the residual water vapour is compressed forming a second, smaller bubble through rarefaction. The secondary bubble that forms will have a smaller radius than the initial primary bubble. This cycle continues for a period of several hundred microseconds depending on the pulse energy delivered to the target.

Under the assumption of an incompressible liquid, for a spherical bubble growth the bubble boundary $R(t)$ can be described by the Rayleigh-Plesset equation [52], [53]:

$$R\frac{d^2R}{dt^2} + \frac{3}{2}\left(\frac{dR}{dt}\right)^2 = \frac{1}{\rho_l}\left(P_B - P_\infty - \frac{2\sigma}{R} - \frac{4\mu}{R}\frac{dR}{dt}\right) \tag{2.48}$$

where μ is the viscosity coefficient. The equation does not take into account the stability of the bubble interface, thermal effects or physical conditions within the bubble. However the oscillatory nature of the bubble dynamics is described by this expression. During the expansion phase, the pressure and temperature inside the bubble are decreasing. During the collapsing phase, the pressure and temperature increase up to their original values. The collapse of the bubble induces a shockwave to be emitted. The internal energy of the spherical bubble is given by [49]:

$$E_B \cong \frac{4\pi}{3} R_{max}^3 (P_\infty - P_B) \tag{2.49}$$

where R_{max} is the maximum radius of the bubble.

The cycle of growth and collapse of the cavitation bubble occurs several times until energy is finally dissipated. Energy losses occur due to shockwave emission, heat conduction and damping caused by the viscosity of the liquid. Subsequent bubbles formed will exhibit a decreased radius and reduced lifetime at each oscillation. From equation 2.49 an expression can be derived to calculate the time required for complete collapse of the bubble t_c given by the Rayleigh model for a cavitation bubble collapsing in an infinite liquid (i.e. a liquid volume which is large compared to the bubble volume) [52], [53], [54]:

$$t_c \simeq 0.915 \sqrt{\frac{\rho_l}{P_\infty - P_B}} R_{max} \tag{2.50}$$

Increasing the liquid viscosity will decrease the rate of bubble growth and collapse meaning the bubble oscillation undergoes less damping in the liquid and exhibits a longer lifetime as a result [55], [56].

2.12 Summary

In this chapter the basic theory of the laser produced plasma is outlined. The fundamental atomic processes that occur within the plasma have been described as well as the thermodynamic equilibrium models that apply. The underlying concepts of the different experimental techniques applied during this work have been outlined and the methods of extracting useful plasma parameters (such as temperatures and densities) from these techniques have also been described. The unique features of a laser produced plasma formed in a background of liquid have been outlined where strong shockwave emission and the formation of a cavitation bubble are the main observations. The theoretical models describing the evolution of the cavitation bubble and shockwave expansion are also outlined.

References

[1] P. K. Carroll and E. T. Kennedy, "Laser-produced plasmas," *Contemp. Phys.*, vol. 22, no. 1, pp. 61–96, Jan. 1981.

[2] J. A. Bittencourt, *Fundamentals of plasma physics*, 1st ed. Oxford [Oxfordshire]; New York: Pergamon Press, 1986.

[3] S. Amoruso, R. Bruzzese, N. Spinelli, and R. Velotta, "Characterization of laser-ablation plasmas," *J. Phys. B At. Mol. Opt. Phys.*, vol. 32, no. 14, pp. R131–R172, Jul. 1999.

[4] J. F. Ready, *Effects of high-power laser radiation*. Florida: Academic Press, 1971.

[5] A. Dalgarno and N. F. Lane, "Free-Free Transitions of Electrons in Gases," *Astrophys. J.*, vol. 145, p. 623, Aug. 1966.

[6] W. B. Zel'dovich and Raizer, Y.P., *Physics of Shock Waves and High-Temperature Hydrodynamic Phenomena*, Academic Press, New York. 1966.

[7] L. Spitzer, *Physics of Fully Ionized Gases*. New York, Wiley, 1962.

[8] R. K. Singh and J. Narayan, "Pulsed-laser evaporation technique for deposition of thin films: Physics and theoretical model," *Phys. Rev. B*, vol. 41, no. 13, pp. 8843–8859, May 1990.

[9] P. Hough, C. McLoughin, T. J. Kelly, P. Hayden, S. S. Harilal, J. P. Mosnier, and J. T. Costello, "Electron and ion stagnation at the collision front between two laser produced plasmas," *J. Phys. Appl. Phys.*, vol. 42, no. 5, p. 55211, Mar. 2009.

[10] Y. Okano, Y. Hironaka, K. G. Nakamura, and K. Kondo, "Time-resolved electron shadowgraphy for 300 ps laser ablation of a copper film," *Appl. Phys. Lett.*, vol. 83, no. 8, p. 1536, 2003.

[11] C. Ursu, S. Gurlui, C. Focsa, and G. Popa, "Space- and time-resolved optical diagnosis for the study of laser ablation plasma dynamics," *Nucl. Instrum. Methods Phys. Res. Sect. B Beam Interact. Mater. At.*, vol. 267, no. 2, pp. 446–450, Jan. 2009.

[12] D. Salzmann, *Atomic physics in hot plasmas*. New York: Oxford University Press, 1998.

[13] N. Suzuki, S. Kosugi, Y. Ito, N. Inoue, T. Nagoshi, N. Kuze, J. R. Harries, J. P. Sullivan, T. Nagata, E. Sokell, F. Koike, and Y. Azuma, "Probing electron correlation through radiative lifetime measurements upon inner-valence photoionization of Ne and Ar," *J. Phys. B At. Mol. Opt. Phys.*, vol. 49, no. 14, p. 145002, Jul. 2016.

[14] H. Luna, J. Dardis, D. Doria, and J. T. Costello, "Analysis of time-resolved laser plasma ablation using an imaging spectra technique," *Braz. J. Phys.*, vol. 37, no. 4, Dec. 2007.

[15] B. N. Roy, *Fundamentals of classical and statistical thermodynamics*. West Sussex, England New York: John Wiley, 2002.

[16] A. A. Fridman and L. A. Kennedy, *Plasma physics and engineering*. New York: Taylor & Francis, 2004.

[17] M. R. Zaghloul, M. A. Bourham, and J. M. Doster, "A simple formulation and solution strategy of the Saha equation for ideal and nonideal plasmas," *J. Phys. Appl. Phys.*, vol. 33, no. 8, pp. 977–984, Apr. 2000.

[18] A. Anders, *A formulary for plasma physics*. Berlin: Akademie-Verl, 1990.

[19] D. Colombant and G. F. Tonon, "X-ray emission in laser-produced plasmas," *J. Appl. Phys.*, vol. 44, no. 8, p. 3524, 1973.

[20] R. W. P. McWhirter, *Plasma Diagnostic Techniques*. Academic Press Inc., 1965.

[21] N. Konjević, "Plasma broadening and shifting of non-hydrogenic spectral lines: present status and applications," *Phys. Rep.*, vol. 316, no. 6, pp. 339–401, Aug. 1999.

[22] G. Bekefi, Ed., *Principles of laser plasmas*. New York: Wiley, 1976.

[23] G. Abdellatif and H. Imam, "A study of the laser plasma parameters at different laser wavelengths," *Spectrochim. Acta Part B At. Spectrosc.*, vol. 57, no. 7, pp. 1155–1165, Jul. 2002.

[24] H. R. Griem, *Plasma Spectroscopy*. Mc Graw-Hill, 1964.

[25] C. Aragón and J. A. Aguilera, "Characterization of laser induced plasmas by optical emission spectroscopy: A review of experiments and methods," *Spectrochim. Acta Part B At. Spectrosc.*, vol. 63, no. 9, pp. 893–916, Sep. 2008.

[26] J. Cooper, "Plasma spectroscopy," *Rep. Prog. Phys.*, vol. 29, no. 1, pp. 35–130, Jan. 1966.

[27] H. R. Griem, *Principles of Plasma Spectroscopy*. Cambridge University Press, New York, 1997.

[28] R. Noll, *Laser-Induced Breakdown Spectroscopy*. Berlin, Heidelberg: Springer Berlin Heidelberg, 2012.

[29] H. C. Liu, X. L. Mao, J. H. Yoo, and R. E. Russo, "Early phase laser induced plasma diagnostics and mass removal during single-pulse laser ablation of silicon," *Spectrochim. Acta Part B At. Spectrosc.*, vol. 54, no. 11, pp. 1607–1624, Nov. 1999.

[30] A. Herrera-Gómez, A. Hegedus, and P. L. Meissner, "Chemical depth profile of ultrathin nitrided SiO[sub 2] films," *Appl. Phys. Lett.*, vol. 81, no. 6, p. 1014, 2002.

[31] M. Villagran-Muniz, H. Sobral, and E. Camps, "Shadowgraphy and interferometry using a CW laser and a CCD of a laser-induced plasma in atmospheric air," *IEEE Trans. Plasma Sci.*, vol. 29, no. 4, pp. 613–616, Aug. 2001.

[32] I. H. Hutchinson, *Principles of plasma diagnostics*. Cambridge [Cambridgeshire]; New York: Cambridge University Press, 1987.

[33] P. Gregorčič and J. Možina, "High-speed two-frame shadowgraphy for velocity measurements of laser-induced plasma and shock-wave evolution," *Opt. Lett.*, vol. 36, no. 15, p. 2782, Aug. 2011.

[34] F. Amiranoff, R. Fedosejevs, R. F. Schmalz, R. Sigel, and Y. Teng, "Laser-driven shock-wave studies using optical shadowgraphy," *Phys. Rev. A*, vol. 32, no. 6, pp. 3535–3546, Dec. 1985.

[35] P. Hough, C. McLoughlin, T. J. Kelly, S. S. Harilal, J. P. Mosnier, and J. T. Costello, "Time resolved Nomarski interferometery of laser produced plasma plumes," *Appl. Surf. Sci.*, vol. 255, no. 10, pp. 5167–5171, Mar. 2009.

[36] A. Sagisaka, H. Daido, K. Ogura, M. Mori, K. Matsukado, Z. Li, S. Nakamura, K. Takagaki, H. Hazama, M. Suzuki, T. Utsumi, S. V. Bulanov, T. Esirkepov, A. Fukumi, S. Orimo, Y. Hayashi, and M. Nishiuchi, "Characterization of preformed plasmas with an interferometer for ultra-short high-intensity laser-plasma interactions," *Appl. Phys. B Lasers Opt.*, vol. 78, no. 7–8, pp. 919–922, May 2004.

[37] G. Pretzler, "A New Method for Numerical Abel-Inversion," *Z. Für Naturforschung*, vol. 46, no. 7, pp. 639–641, 1991.

[38] J. Ruiz-Camacho, F. N. Beg, and P. Lee, "Comparison of sensitivities of Moiré deflectometry and interferometry to measure electron densities in z -pinch plasmas," *J. Phys. Appl. Phys.*, vol. 40, no. 7, pp. 2026–2032, Apr. 2007.

[39] T. T. P. Nguyen, R. Tanabe, and Y. Ito, "Laser-induced shock process in under-liquid regime studied by time-resolved photoelasticity imaging technique," *Appl. Phys. Lett.*, vol. 102, no. 12, p. 124103, 2013.

[40] Z. Yan and D. B. Chrisey, "Pulsed laser ablation in liquid for micro-/nanostructure generation," *J. Photochem. Photobiol. C Photochem. Rev.*, vol. 13, no. 3, pp. 204–223, Sep. 2012.

[41] R. K. Kushawaha, S. S. Kumar, I. A. Prajapati, K. P. Subramanian, and B. Bapat, "Polarization dependence in non-resonant photo-triple-ionization of CO $_2$," *J. Phys. B At. Mol. Opt. Phys.*, vol. 42, no. 10, p. 105201, May 2009.

[42] D. A. Freiwald and R. A. Axford, "Approximate spherical blast theory including source mass," *J. Appl. Phys.*, vol. 46, no. 3, p. 1171, 1975.

[43] E. de Posada, M. A. Arronte, L. Ponce, E. Rodríguez, T. Flores, and J. G. Lunney, "On the use of shockwave models in laser produced plasma expansion," *J. Phys. Conf. Ser.*, vol. 274, p. 12078, Jan. 2011.

[44] S. S. Harilal, C. V. Bindhu, M. S. Tillack, F. Najmabadi, and A. C. Gaeris, "Internal structure and expansion dynamics of laser ablation plumes into ambient gases," *J. Appl. Phys.*, vol. 93, no. 5, p. 2380, 2003.

[45] T. T. P. Nguyen, R. Tanabe, and Y. Ito, "Effects of an absorptive coating on the dynamics of underwater laser-induced shock process," *Appl. Phys. A*, vol. 116, no. 3, pp. 1109–1117, Sep. 2014.

[46] L. Berthe, R. Fabbro, P. Peyre, L. Tollier, and E. Bartnicki, "Shock waves from a water-confined laser-generated plasma," *J. Appl. Phys.*, vol. 82, no. 6, p. 2826, 1997.

[47] T. Tsuji, Y. Okazaki, Y. Tsuboi, and M. Tsuji, "Nanosecond Time-Resolved Observations of Laser Ablation of Silver in Water," *Jpn. J. Appl. Phys.*, vol. 46, no. 4A, pp. 1533–1535, Apr. 2007.

[48] A. Vogel, "Acoustic transient generation by laser-produced cavitation bubbles near solid boundaries," *J. Acoust. Soc. Am.*, vol. 84, no. 2, p. 719, 1988.

[49] Y. Tomita, M. Tsubota, and N. An-naka, "Energy evaluation of cavitation bubble generation and shock wave emission by laser focusing in liquid nitrogen," *J. Appl. Phys.*, vol. 93, no. 5, p. 3039, 2003.

[50] A. Vogel, "Shock wave emission and cavitation bubble generation by picosecond and nanosecond optical breakdown in water," *J. Acoust. Soc. Am.*, vol. 100, no. 1, p. 148, 1996.

[51] P. Giovanneschi and D. Dufresne, "Experimental study of laser-induced cavitation bubbles," *J. Appl. Phys.*, vol. 58, no. 2, p. 651, 1985.

[52] M. S. Plesset, "The Dynamics of Cavitation Bubbles," *J. Appl. Mech.*, vol. 16, pp. 277–282, 1949.

[53] M. S. Plesset and A. Prosperetti, "Bubble Dynamics and Cavitation," *Annu. Rev. Fluid Mech.*, vol. 9, no. 1, pp. 145–185, Jan. 1977.

[54] Lord Rayleigh, "VIII. *On the pressure developed in a liquid during the collapse of a spherical cavity*," *Philos. Mag. Ser. 6*, vol. 34, no. 200, pp. 94–98, Aug. 1917.

[55] W. Lauterborn, Kurz, T., Metin, R., and Ohl, C. D., "Experimental and theoretical bubble dynamics," *Adv. Chem. Phys.*, vol. 110, pp. 295–380, 1999.

[56] L. Xiu-Mei, H. Jie, L. Jian, and N. Xiao-Wu, "Growth and collapse of laser-induced bubbles in glycerol–water mixtures," *Chin. Phys. B*, vol. 17, no. 7, pp. 2574–2579, Jul. 2008.

Chapter 3

Experimental Systems

During the course of the work presented here a number of different experimental setups were used for the formation, monitoring and probing of laser produced plasmas in air and water. This section will describe the experimental arrangements used during each series of experiments carried out. The basic principles of operation of experimental techniques applied and experimental apparatus used during this work are explained. Information on the calibration procedures carried out on the spectrometer and ICCD cameras used during this work are also detailed.

3.1 Experimental Setup

The study of laser produced plasma emission was carried out using the fundamental wavelength of an Nd:YAG laser (1064 nm) and a simple optical delivery system. A schematic of the experimental setup is shown in figure 3.1.

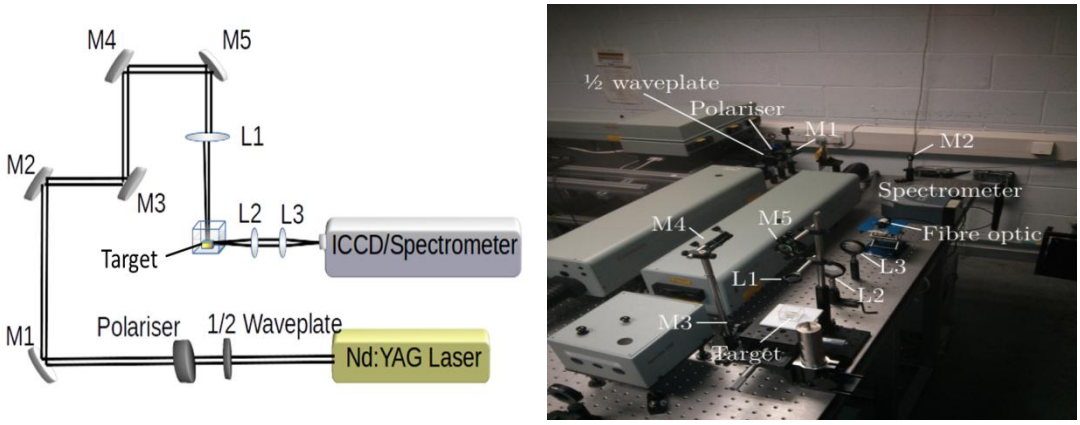

Figure 3.1: Schematic setup for imaging and spectroscopic studies of laser produced plasmas in water and air (left). Photograph of experimental setup in the laboratory (right).

Figure 3.1 demonstrates the experimental setup used during single pulse studies in air and water. The metal target was machined into a rectangle (dimensions of 25 mm width × 15 mm length × 1 mm thickness) held in place by a Teflon mould which was manufactured in-house and positioned inside a square glass cuvette. The Teflon mould also acted as a shock absorber to prevent the physical shock of the laser pulses from cracking the glass cuvette. The cuvettes were purchased from Kromatek [1] with dimensions 20 mm × 20 mm × 25 mm. Aluminium targets of 99.999% purity were used through all experiments and were purchased from Goodfellow [2]. A photograph of the target, mould, cuvette assembly is shown in figure 3.2 below.

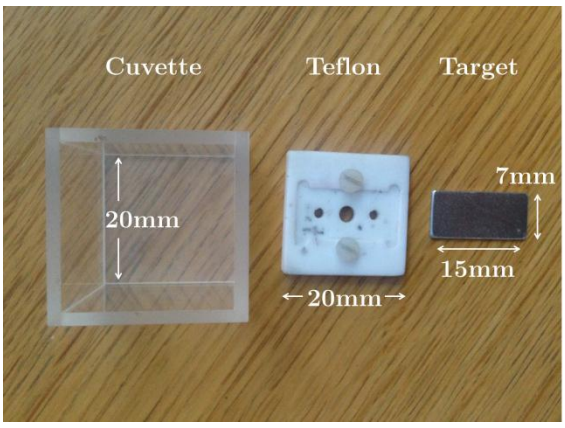

Figure 3.2: Photograph of aluminium target, Teflon mould and glass cuvette used during experiments.

The target and cuvette were fixed to an xyz translation stage. This allowed the laser to ablate a fresh piece of target each shot to avoid cratering effects. Deionised water was used for the experiments in liquid. The volume of water was replaced after every 20 laser shots. This was deemed to be the optimum number of shots which could be fired while avoiding any adverse effects due to physical ablation of nanoparticles into the liquid, further details of which will be included in chapter 7.

The laser delivers pulses with an energy of up to 1 J per pulse at a repetition rate of 10 Hz under normal operation. For the work reported here however, lower energies were required. At 1 J per pulse, ionization of air and water was observed. In order to vary the laser energy a half-wave plate and polariser were inserted into the beamline. The average power was measured as a function of waveplate angle just above the target in the experimental setup in figure 3.1 to account for mirror losses. From figure 3.3 it can be seen that the average power could be varied from approximately 100-500 mW corresponding to 10-50 mJ per pulse for a 10 Hz repetition rate. Due to the strong laser field, full attenuation of the beam could not be achieved.

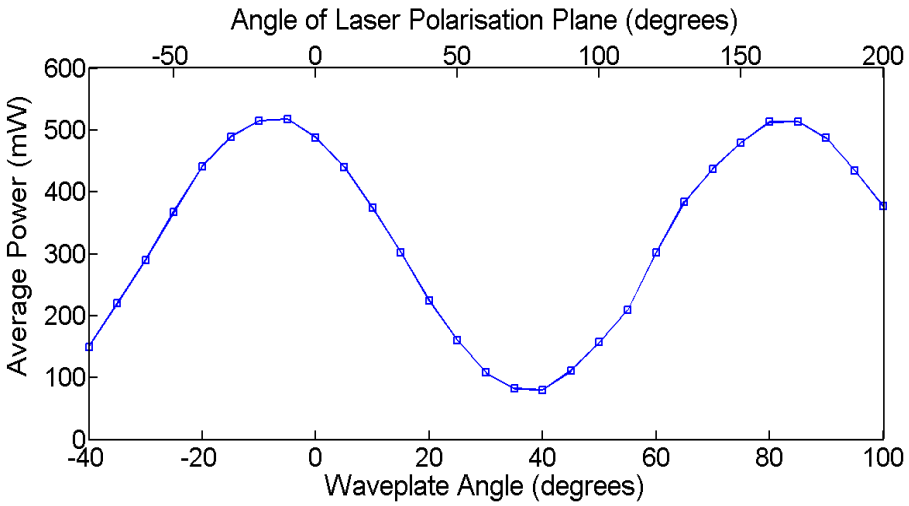

Figure 3.3: Nd:YAG laser (average) power measured as a function of half-wave plate angle.

A plano-convex lens of focal length 150 mm was used to focus the laser onto the target. The light emitted from the target surface was imaged onto an ANDOR intensified CCD camera via two 5 cm diameter bi-convex lenses (L2 and L3 in figure 3.1). The function

of these two lenses was to collect, relay and image, with magnification, light from the plasma onto the 2-dimensional CCD screen.

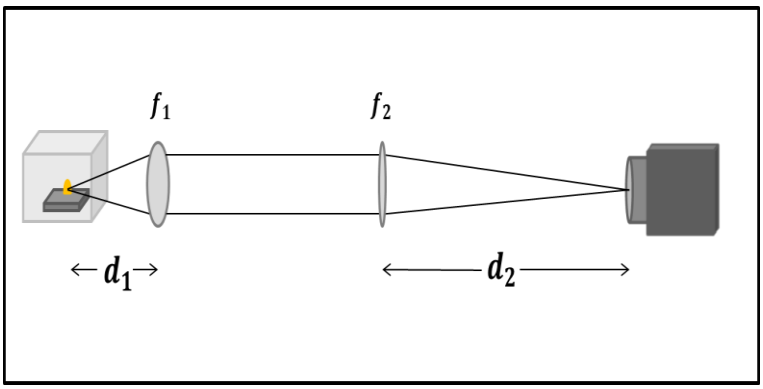

Figure 3.4: Schematic of relay system. Magnification of the object plane onto the image plane of the CCD is achieved by the ratio of f_2/f_1.

The first lens is placed a distance d_1 from the plasma which is equal to the focal length of that lens. The resulting parallel ray is collected by the second lens and focused onto the camera. The second lens is placed at a distance d_2 from the CCD camera equal to the focal length of the second lens. The magnification of the system is varied by changing the ratio of the focal lengths of the two lenses. The focal lengths of L2 and L3 were 90 mm and 330 mm respectively.

During the course of experiments, measurements were made using two different ambient backgrounds; air and water. Due to the change in refractive index at the air-water interface, the effective focal length of the focussing lens will be different due to refraction. The difference in focal length between these two media is given by [3]:

$$\Delta f = l\left(1 - \frac{f}{\sqrt{n^2 f^2 + (n^2 - 1)r^2}}\right) \tag{3.1}$$

where f is the value of the focal length of the lens in air, l is the height of the column of liquid above the target surface, n is the refractive index of the liquid and r is the radius of the unfocused beam.

In the case where $r << f$, this equation simplifies to:

$$\Delta f = l\left(1 - \frac{1}{n}\right) \tag{3.2}$$

This equation was used to find an approximate value for the change in focal length of the laser pulse in water. For fine adjustment a telescope focused at infinity was used. Looking through the focusing lens with the telescope fine adjustment of the laser focusing lens could be achieved by adjusting the lens until a sharp image of the target surface was achieved.

The absorption of light is given by the Beer-Lambert law:

$$I(z) = I_0 e^{-\alpha z} \tag{3.3}$$

Where $I(z)$ is the intensity at a distance z from the surface of the water, I_0 is the intensity at the surface, α is the absorption coefficient which for water at 1064 nm has a value of 0.15 cm^{-1} [4]. The cuvette exhibits a continuous 85% transmission across the visible wavelength range between 340 – 800 nm. A column of 20 mm of deionised water (DIW) was maintained in the cuvette throughout the experiments performed in liquid ambient. This results in a value of 74% of the surface intensity reaching the metal target surface.

Examples of craters formed by the laser pulse on the target surface in air and liquid are shown in figure 3.5 where crater diameters of ~300 µm were measured. The craters were formed using 200 shots of the laser and the target was imaged using a scanning electron microscope (SEM) which is described in section 3.8. The energy at the target surface in both cases is 40 ± 3 mJ per pulse.

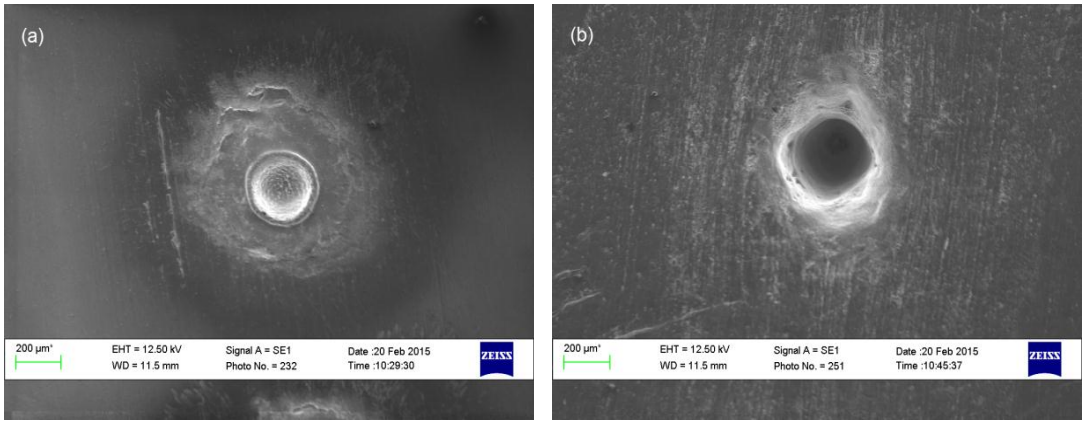

Figure 3.5: SEM images of craters formed using 200 laser shots in (a) air and (b) deionised water. A pulse energy of 40 ± 3 mJ at the target surface was maintained in air and water ambient.

Crater formation was studied in air and liquid as a function of laser pulse energy and will be discussed in chapter 6.

During laser-produced plasma studies in water (chapter 7), a series of double-pulse measurements were carried out which required the use of a slightly different experimental setup. The plasma was created by focussing a 1064 nm pulse onto the target submerged in a background of water. In order to create a second plasma, the second pulse (532 nm) is delivered through the back of mirror M1 (which is transparent to 532 nm radiation) and focussed by the same lens as the first pulse (L1) to the same spot on the target surface. The second pulse is delivered at various time delays (on the order of several microseconds) with respect to the first pulse. Two half-waveplates (WP) and polarisers (P) were used to vary the energy of the two laser pulses. Optical emission is collected via the relay system and focussed onto the ICCD/spectrometer for imaging and spectral analysis. Scattered light from the two laser pulses are blocked from reaching the ICCD by the use of an 800 nm low-pass filter and a notch filter centred at 532 nm. Figure 3.6 shows a side-view of this double-pulse setup.

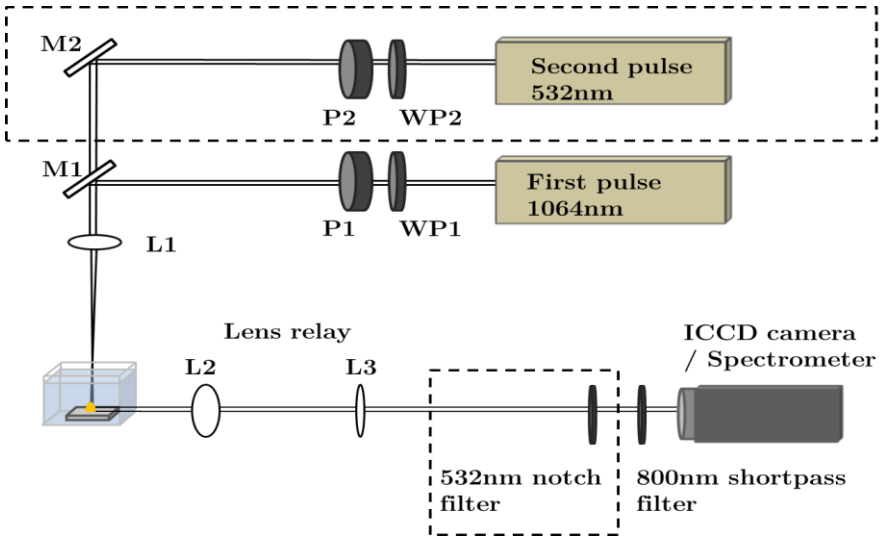

Figure 3.6: Schematic of double-pulse setup used during experiments performed in water. Both laser pulses are focussed through the same lens onto the target surface.

A series of pump-probe experiments were carried out in ambient air using a different experimental configuration to the one described for double-pulse experiments carried out in water. The plasma was created using a 1064 nm pulse which was subsequently probed using a wavelength tuneable second pulse provided by an optical parametric oscillator (OPO). During pump-probe investigations, the OPO pulse is delivered to the expanding plasma orthogonal to the target surface. Figure 3.7 demonstrates the experimental setup used during pump-probe studies (pertaining to results shown in chapter 5).

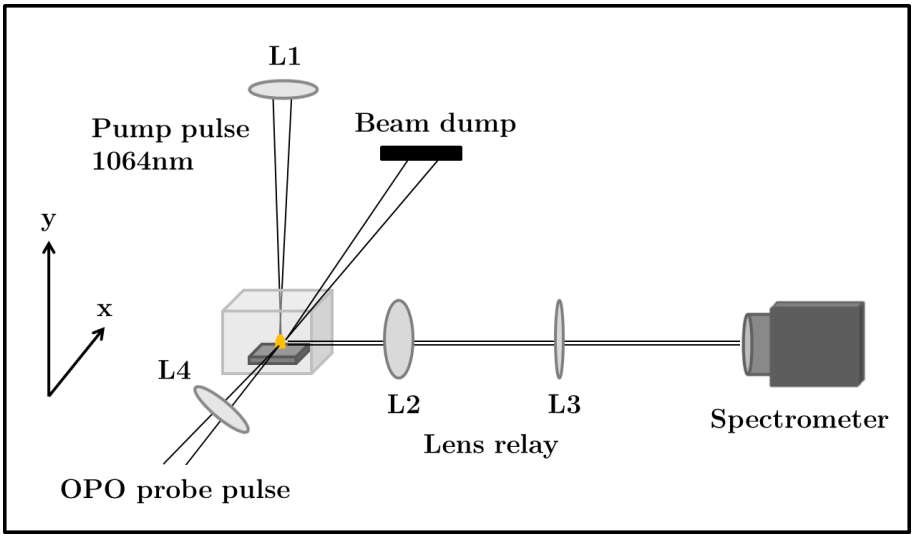

Figure 3.7: Schematic of experimental setup used during pump-probe studies in ambient air. A 1064 nm pulse is used to create the plasma which is subsequently probed using a second pulse delivered orthogonally to the expanding plasma by the OPO.

This slightly different configuration is required to ensure coupling of the radiation provided by the second pulse to the plasma without the creation of a second plasma. The OPO pulse is focussed (L4) through the centre of the expanding plasma plume 2 mm above the target surface. After traversing the plasma plume, the unfocussed probe beam was subsequently blocked by a beam dump.

3.2 Surelite Laser Sytems

The laser systems involved in this work were a Continuum Surelite^{TM} I-10 and Surelite III-10 models. The Surelite models are Q-switched Nd:YAG laser systems with the capacity to deliver intense pulses having temporal duration between 4-6 ns at FWHM and as such these types of lasers are very widely used in laser plasma laboratories. The Surelite III-10 was employed primarily throughout this work for plasma formation operating at the fundamental wavelength of 1064 nm. The Surelite I laser was used at the second harmonic wavelength of 532 nm. Pulses generated by the Surelite systems are linearly polarised and exhibit a Gaussian beam profile. Both lasers were operated in

single shot mode during the course of experiments. A Surelite II-10 was used also as the pump laser to the OPO which will be described in section 3.3. The relevant specifications of the laser systems are shown in table 3.1.

	Surelite I-10	**Surelite II-10**	**Surelite III-10**
Wavelength (nm)	1064, 532, 355, 266	1064, 532, 355, 266	1064, 532, 355, 266
Energy (mJ)	485, 225, 100, 60	600, 300, 160, 80	700, 350, 160, 100
FWHM (ns)	6, 4 (harmonics)	6, 4 (harmonics)	6, 4 (harmonics)
Repetition Rate (Hz)	10 / single shot	10 / single shot	10 / single shot
External Trigger Jitter (ns)	≤ 1	≤ 1	≤ 1

Table 3.1: Characteristic parameters for Surelite Q-switched laser systems [5].

For the present work low energy pulses were required and as such pulse energies in the range of a few to tens of millijoules were typically used for plasma formation. The energy of the Surelite pulses was reduced by means of a polariser and half-waveplate arrangement as outlined in section 3.1.

The principle of Q-switching is to degrade the quality factor (Q-factor) of the resonator (i.e. maintain high losses) during pumping so that the gain can reach a very high value. When population inversion reaches its peak the Q-factor is restored abruptly to a high value. The energy stored by the excited atoms is converted into photons which are now allowed to oscillate within the resonator [6]. Q-switching is realised in either active or passive mode. The former makes use of an electro-optic gate inside the resonator and the latter is achieved by the inclusion of a saturable absorber. The switching of the Q-factor from low to high occurs rapidly which produces intense peak power and relatively short pulse durations [6], [7].

The Surelite laser operates in an active Q-switching operation mode. The combination of a polariser, Pockels cell (PC) and quarter-waveplate within the oscillator is known as the Q-switch. The laser medium is pumped creating a population inversion. The Q-switch prevents optical feedback into the resonator until the gain within the lasing

medium has reached a maximum level. Once gain saturation has occurred in the medium the Q-switch is triggered and oscillation may occur.

The beam propagates within the oscillator cavity making a double-pass though the PC and quarter-waveplate. While the cavity remains closed, the originally horizontally polarised beam is rotated 90° by the double-pass through the PC and is therefore rejected by the polariser. The cavity is opened by applying a high voltage to the birefringent PC which results in a quarter wave rotation for incoming photons. In this case, the polarisation of the beam after traversing the double-pass through the cavity is rotated back to horizontal and is transmitted by the polarizer allowing the pulse to exit via the output coupler. The resonator is housed in a graphite structure which ensures thermal and mechanical stability.

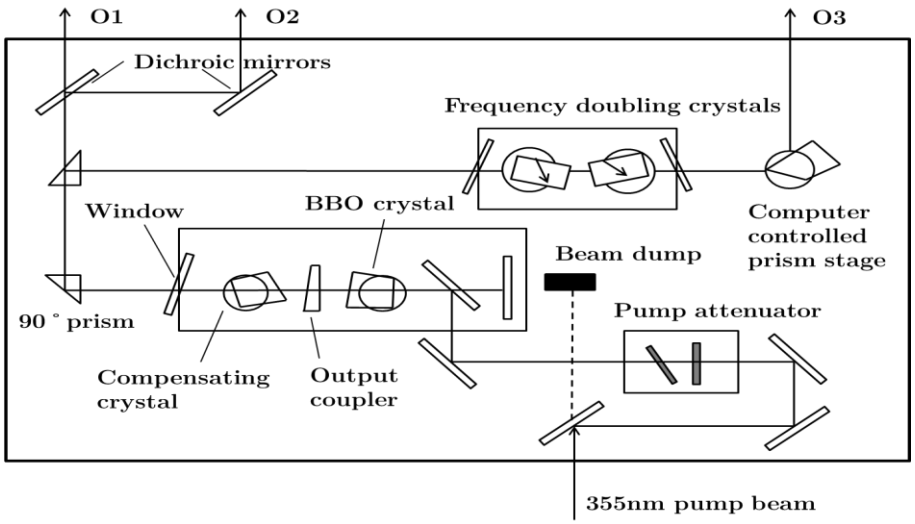

Figure 3.8: Schematic diagram of Surelite laser system. Optional harmonic generation section shown also [5].

Harmonic generation is achieved using a second harmonic generation crystal (potassium dihydrogen phosphate (KDP)). In the frequency doubling process, two 1064nm photons enter the KDP crystal collinearly and with the same circular polarisation. The two photons combine to produce a resulting doubled frequency photon which satisfies energy conservation. This resulting photon will have a horizontal polarisation dictated by the conservation of angular momentum. Linear momentum conservation requires the combined photon to have the same velocity as the incoming photon pair. This second

harmonic generation is achieved within the birefringent material by rotating the crystal to the so-called phase matched angle. The dichoric mirror acts to divert the harmonic beam to the exit port and to send the residual infrared light exiting the SHG crystal to the beam dump.

Higher order harmonics are achievable by the same process of frequency doubling. In this instance the second harmonic beam must be present. To create the third harmonic, one 532 nm photon and one 1064 nm photon combine within a second non-linear crystal to produce a photon of 355 nm. The fourth harmonic is then produced by combining two 532 nm photons in a non-linear crystal.

In standard operating mode, at a pulse repetition rate of 10 Hz, the PC within the cavity will trigger ~180 µs after the flashlamps signal is triggered. This is the optimal delay time for the Q-switch for all Surelite systems used.

3.3 Panther OPO

For experiments where wavelength tunability was required a commercial optical parametric oscillator named the Panther^{TM} OPO was used. The OPO system is a resonator which generates coherent light in the visible and mid-infrared spectral range from a 355 nm Nd:YAG pump laser beam. Continuous tunability from 410 nm to 2550 nm is achievable. The laser system used as the OPO pump laser during the work presented here was a Surelite II-10 which was tripled to the 355 nm wavelength.

The optical parametric process is a three photon interaction in which one photon (the pump photon) is split into a pair of less energetic photons. This process is analogous to a sum frequency generation process in reverse, where two photons combine to form a third more energetic photon. These two photons will not in general have the same energies. The high and low energy photons generated by the process are referred to as the signal and the idler respectively.

The OPO is essentially a resonator with a non-linear gain medium. A generated wave (the signal) is fed back by the resonator to the non-linear crystal causing further generation and thereby amplification occurs.

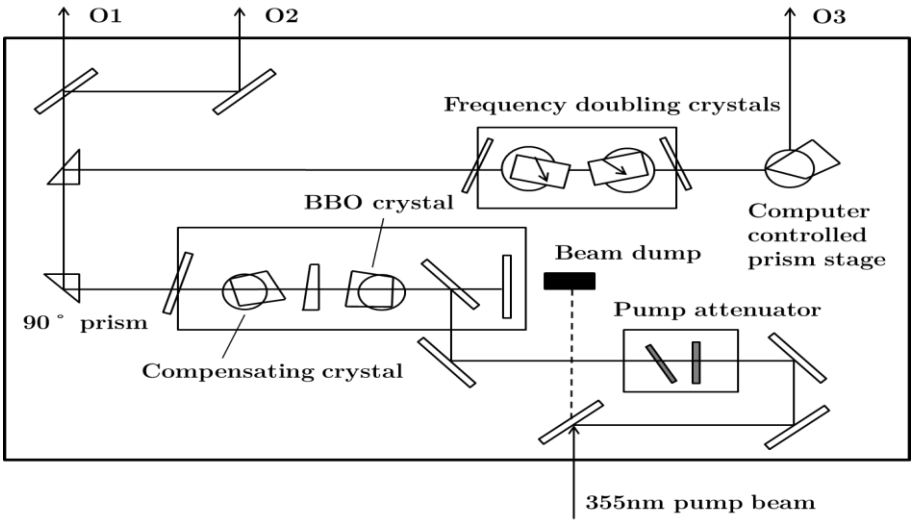

Figure 3.9: Optical layout design of the Panther OPO (O1) is the idler output, (O2) the signal output, and (O3) the doubled output if required. Adapted from [8].

During these interactions energy and momentum are conserved by use of a birefringent non-linear crystal. Inside the Panther OPO a beta-barium borate (BBO) crystal is used as the birefringent material. Such materials exhibit different refractive indices for different polarization states of incoming waves with respect to the crystal optical axis. Energy conservation occurs when the sum of the signal and idler frequencies equals the pump photon frequency. However linear momentum will not in general be conserved due to the two resulting photons having different frequencies to the pump and therefore different velocities. Momentum is conserved within the BBO crystal by tuning the angle that the incoming pump photons make with the crystal's optical axis in a process called phase matching. When the signal and/or pump beams have polarisations orthogonal to the original pump beam there are angles in which the crystal's frequency dependent refractive index will change the signal and idler velocities so as to conserve linear momentum.

Parametric conversion is normally an inefficient process with the majority of the pump beam emerging unchanged from the crystal. By increasing the interaction length in the crystal the efficiency of the process can be improved. This is achieved within the oscillator by reflecting the undepleted pump beam back into the BBO crystal doubling the interaction length between the pump and generated signal and idler waves. A sample spectrum of the Panther OPO output in the optical range from 400 nm to 700 nm is shown in figure 3.10 below.

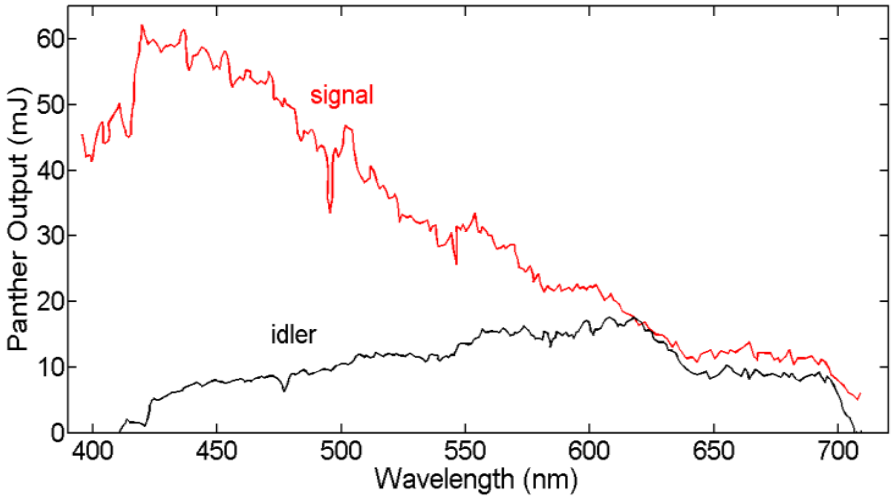

Figure 3.10: OPO power output of signal and idler pulses [8]. The idler output was not used during the course of the work, only the signal output.

Figure 3.10 shows the output of the signal and idler pulses in mJ/pulse over the visible wavelength range. Note that the signal and idler pulses will not in general have the same output wavelength as a function of the phase matching angle in the BBO crystal since the photon energy of the pump photon (355 nm) must equal the sum of the two resulting signal and idler photons.

3.4 ICCD Camera

An ANDOR DV434 model camera with 1024 × 1024 pixels was used for the majority of the work presented here. Each pixel is 13 µm × 13 µm resulting in a total active image

area of 13.3 × 13.3 mm^2 for the (charge coupled device) CCD chip. A transparent ruler with one millimetre spacings was imaged onto the camera to measure the magnification introduced by the lens relay system. Figure 3.11 shows the summed intensity of the image recorded.

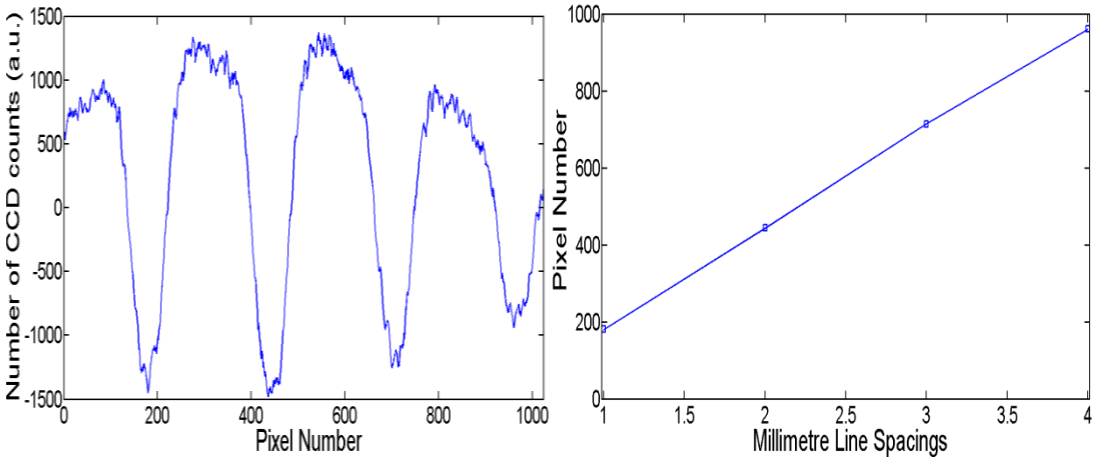

Figure 3.11: Vertically summed image on CCD screen of the one millimetre ruler spacings used to calculate the magnification (left). Calibration graph of the intensity lineout (right).

Each minima in figure 3.11 corresponds to a ruler line. The position of the ruler markings was determined by first applying a smoothing filter to the summed intensity image and then taking the central position of the smoothed plot. The slope of the line (pixels/mm) corresponding to these minima gives a value for the separation between one millimetre spacings on the ruler. For a pixel size of 13 µm, the magnification was measured in this way to be 3.4 ± 0.15 ×.

The intensified CCD camera allows for very fast gate times as low as 3 ns. The ICCD is an evacuated tube which consists of a photocathode, a microchannel plate (MCP) and a phosphor screen [9].

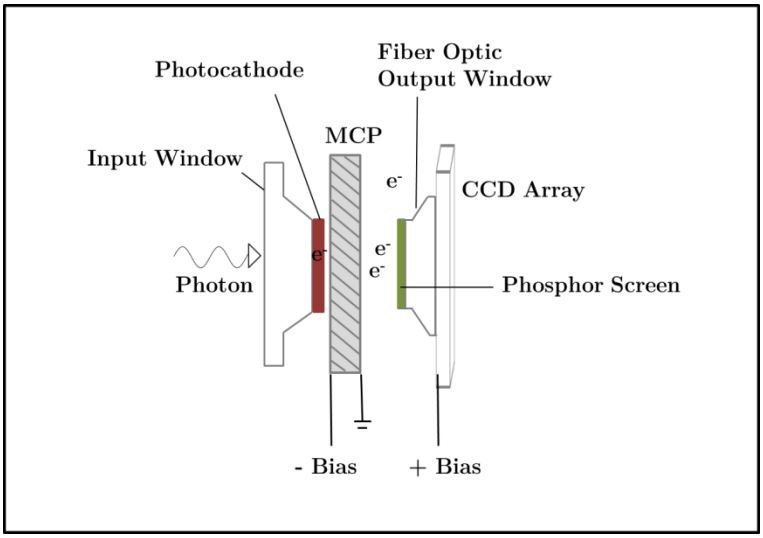

Figure 3.12: Schematic of the Andor ICCD intensifier [10].

When a photon strikes the photocathode a photoelectron is emitted which is accelerated towards the MCP by an applied electric field. A high voltage is applied across the MCP. The inside of each channel (hollow glass capillary) is coated with a secondary electron emitting material much like a dynode in a photomultiplier tube. The primary electron triggers an avalanche of secondary electrons which in turn drives even further electron emission so that a high electron gain is achieved as the electron bunch propagates through the honeycomb glass channel structures of the MCP [9]. By this electron multiplication process the ICCD can produce gains of 10,000× and above which permits low light level detection [10]. Varying the MCP voltage allows for control of the gain. Upon exiting the MCP the electrons are subjected to a high potential difference which keeps the electrons tightly bunched together before striking the phosphor screen where the image is created. The optical output of the image intensifier is coupled to the CCD by either a fibre optic coupler or a lens coupler.

The electron multiplication factor was experimentally measured using a cadmium light source. Emission of Cd(I) 508.58 nm was compared for a range of different software controlled gain settings. Ten individual spectra were recorded and the average obtained at each gain setting. Figure 3.13 shows the resulting exponential gain curve obtained by

the integrated area of the emission line from recorded spectra using a fixed exposure time for the ICCD of 18 ms.

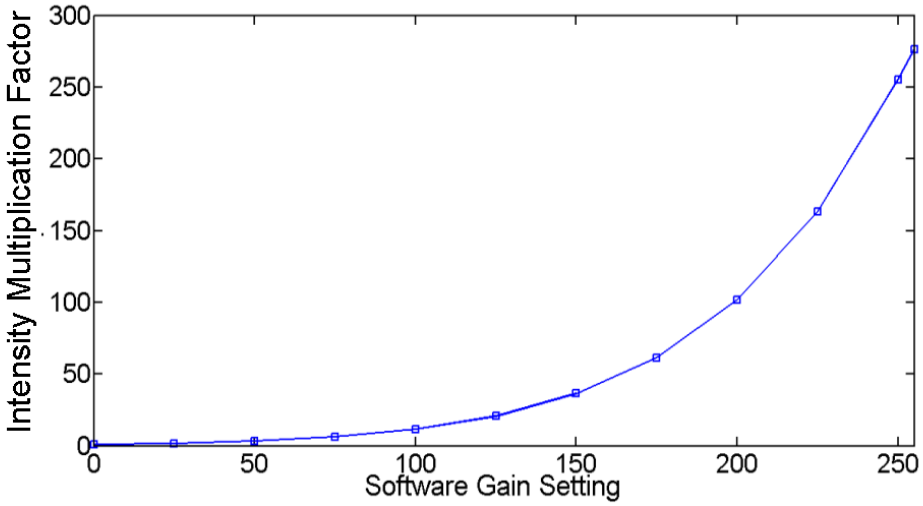

Figure 3.13: Gain calibration curve determined from intensity of recorded Cd(I) emission line at 505.58 nm over a range of software controlled gain settings.

An ANDOR DH5H7 model camera with 512 × 512 pixels was also used during the course of the experimental work. The pixel size for this model is 24 µm with an active area of 12.3 × 12.3 mm^2. Magnification and calibration curves were carried out in the same way as those described for the ANDOR DV434 model.

3.5 Shamrock Spectrometer

An ICCD ANDOR camera mounted to the exit port of a Shamrock SR-163 were used for spectroscopy measurements. The Shamrock spectrometer is based on a Czerny-Turner optical layout [11] having a focal length of 163 mm and a numerical aperture of $f/3.6$. The Shamrock SR-163 is a compact and portable system with many adjustable features. Gratings and slit widths are easily interchangeable which gives flexibility in terms of the desired trade-off between resolution, wavelength range and desired light

levels. For the present work a 1200 lines/mm grating with a 50 µm slit width was used giving an average resolution of 0.46 nm for the system.

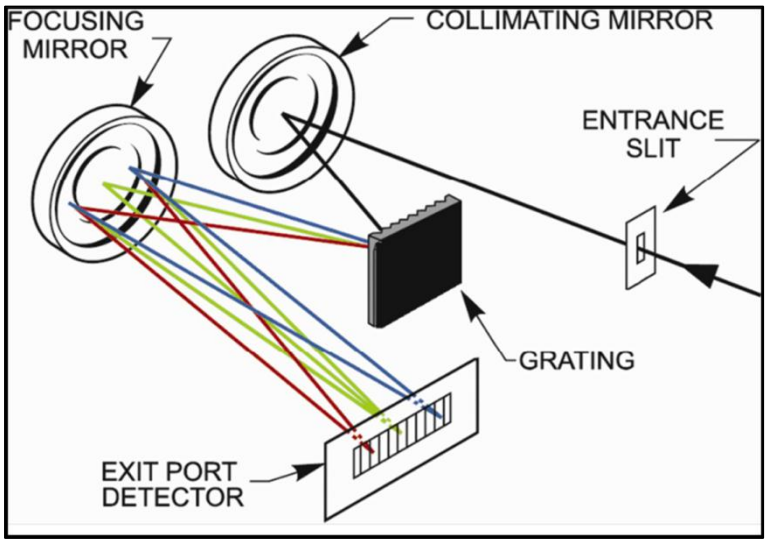

Figure 3.14: Shamrock SR-163 Czerny-Turner spectrometer layout [10].

The wavelength drive is operated via a manual micrometer screw gauge calibrated at 1200 lines/mm to read 1 nm for a translation of 10 µm on the micrometer screw gauge. Light is focussed onto a 200 µm optical fibre (SMA905 0.22 NA single mode) which delivers light into the entrance slit of the spectrometer via an adaptor. Depending on which ANDOR camera was being used to record the spectrogram, a wavelength range of ~60 nm could be captured across the CCD chip for a fixed wavelength/micrometer position.

Wavelength calibration was carried out on the ICCD-Shamrock combination using a Hg-Cd-Zn spectral lamp with known emission lines. An approximate wavelength range can be obtained directly by the Shamrock micrometer screw gauge position and at this fixed position a more accurate calibration is achieved by using the narrow spectral lines of the calibration bulbs. The mixed Hg-Cd-Zn lamp was used to calibrate the spectrometer at each micrometer position of interest which can then be used to translate pixel number to wavelength as shown in figure 3.15.

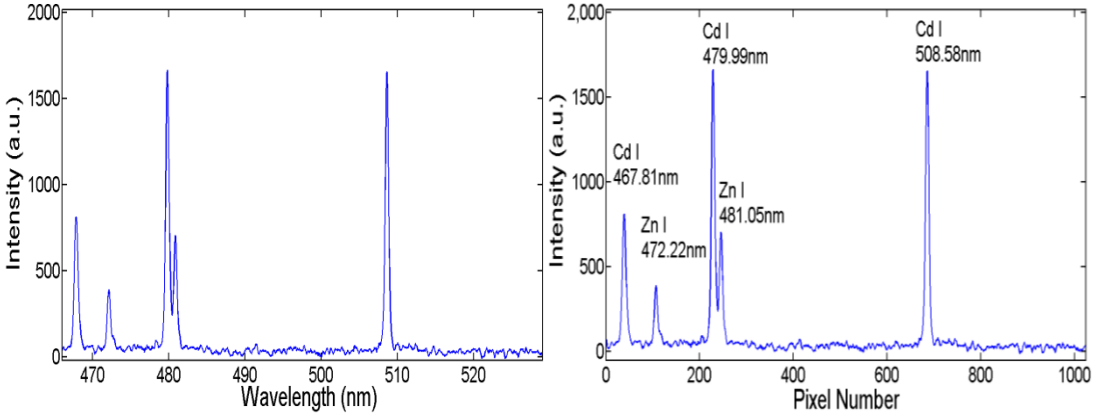

Figure 3.15: Example of wavelength calibration at ~500 nm. Known spectral lines (left) are used to create a calibration curve converting pixel number to wavelength (right).

For intensity calibration a tungsten filament lamp from Oriel (Model 63945) was used. The tungsten lamp is an absolutely calibrated source. The irradiance of the tungsten emission is measured by the National Institute of Standards and Technology (NIST) and a fitting formula is provided in units of mW/m^2/nm [12]:

$$Irradiance = \lambda^{-5}\exp\left(a+\frac{b}{\lambda}\right)\left(c+\frac{d}{\lambda}+\frac{e}{\lambda^2}+\frac{f}{\lambda^3}+\frac{g}{\lambda^4}+\frac{h}{\lambda^5}\right) \tag{3.4}$$

where λ is in nm and the coefficients are given by a = 44.4786393540874, b = -4552.55676009887, c = 0.967336620755997, d = 53.1619077949388, e = -5871.317902886, f = -12482113.1500871, g = 1570247482.57565 and h = 0.

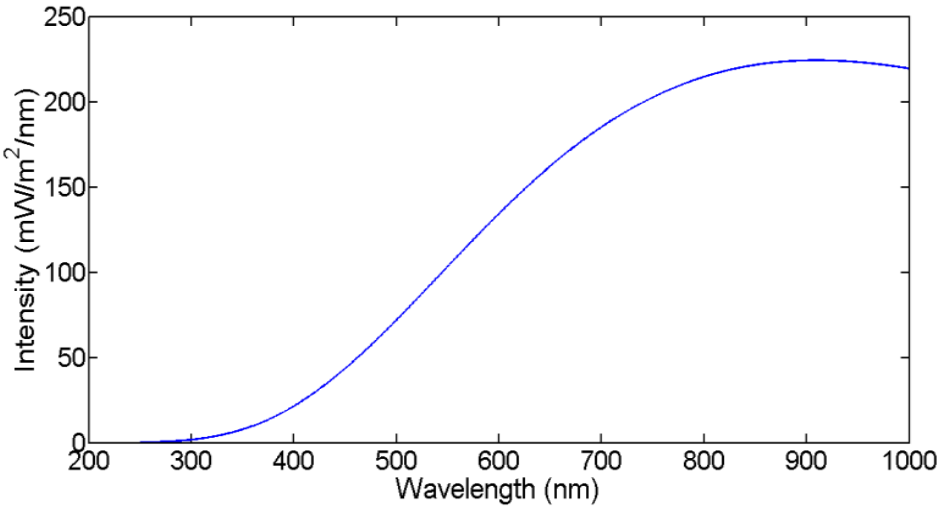

Figure 3.16: Calibration curve fitted by NIST formula.

From this tungsten calibration curve a relative intensity calibration could be obtained by comparing the recorded spectrum with the true spectrum in the region of interest. Figure 3.17 demonstrates the conversion from recorded spectrum to an intensity calibration in (relative) CCD pixel counts at a centre wavelength of 400 nm.

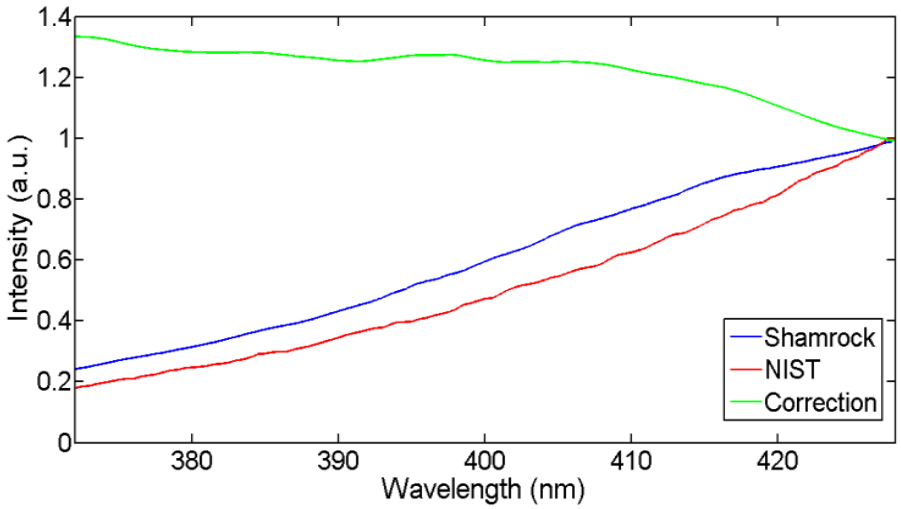

Figure 3.17: Raw data recorded of tungsten spectrum (blue), calibrated spectra by NIST (red) and correction function in the spectral range (green). Data is normalised for ease of visual representation in the figure.

Using the tungsten light source, the correction function α was defined as:

$$\alpha = \frac{measured\ spectrum}{real\ spectrum}$$

for each spectral region of interest. Experimental spectra may then be divided by this correction function to obtain the true spectra, an example of this is shown in figure 3.18 below. The spectra shows the emergence of line emission from the strong continuum emission that is observable at a time delay of 50 ns after plasma ignition.

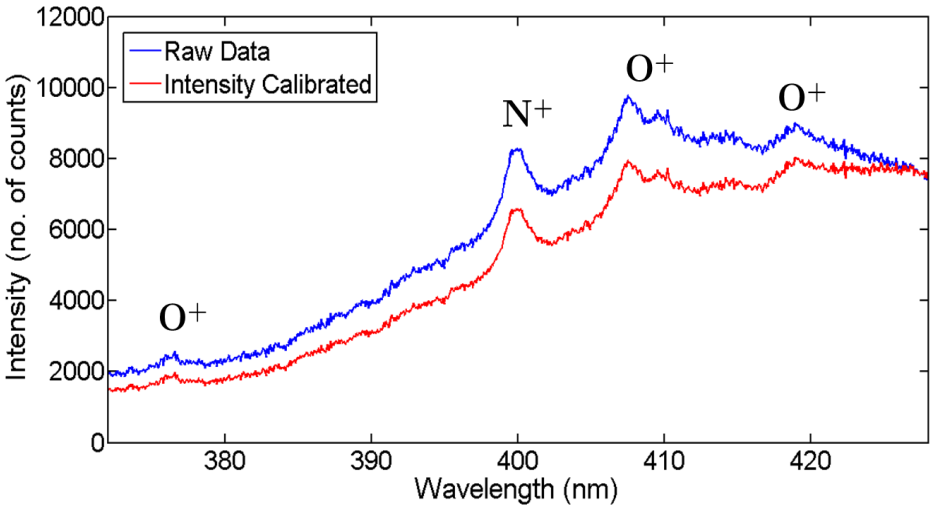

Figure 3.18: Example of aluminium spectra recorded at 50 ns and corresponding intensity calibrated spectra.

In this way intensity calibrations were carried out at each spectral range of interest for both camera-spectrometer combinations since the spectral efficiency of each camera is different. The intensity calibration or "correction factor" for each spectral range of interest (or centre wavelength position) is then used to correct the recorded spectra by taking into account the spectral efficiencies of both the spectrometer and camera.

3.6 Interferometry/Shadowgraphy

Interferometry and shadowgraphy experiments were carried out as plasma diagnostic techniques on laser produced plasmas in air and water. Interferometry is particularly useful as a plasma diagnostics tool at early plasma lifetimes where changes in the electron density are greatest [14]. Electron densities can be extracted from the interferograms which may be difficult to measure accurately by other methods such as spectroscopy due to the strong continuum emission at these very early times. Normaski laser interferometry was chosen as the preferable technique due to its simplicity of design and inherent stability [15]. The experimental design was based on a similar setup

described by Hough *et al.* [16]. The second harmonic of the Surelite II-10 was used in all experiments as the probe beam.

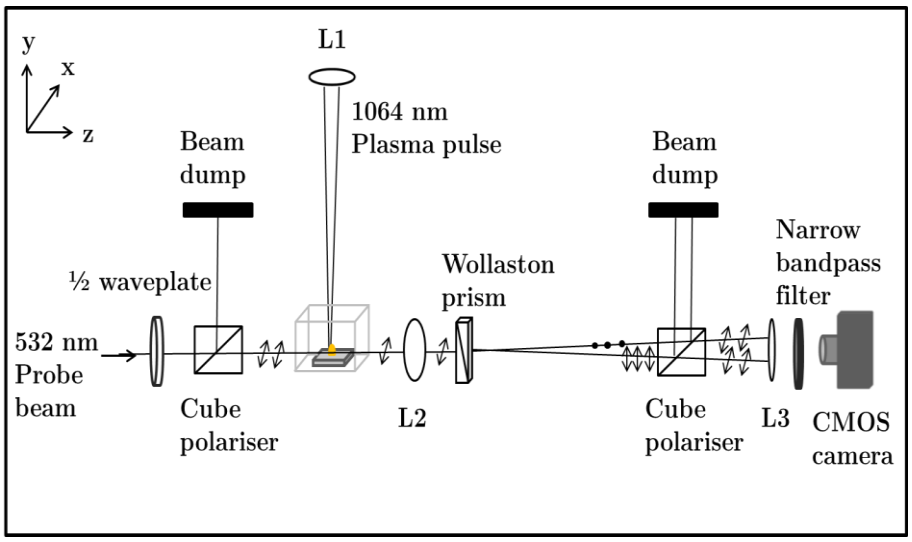

Figure 3.19: Interferometry setup. A 1064 nm pulse is used to form the plasma and a 532 nm pulse is used as the probe beam.

The first beam-splitting cube polariser acts to rotate the polarisation of the probe beam to 45° with respect to the propagation direction (z-direction) so that the beam passing through the plasma contains equal horizontal and vertical polarisation components. In combination with the half-waveplate the probe beam energy is greatly reduced to < 1 mJ. The majority of the probe beam energy is directed towards the beam dump. This is necessary to protect the complementary metal-oxide-semiconductor (CMOS) camera as the laser light is coupled directly onto the imaging chip. After passing through the plasma the beam enters the Wollaston prism whose function is to split the beam into vertical and horizontal polarisation components. The Wollaston prism splits the beams with an angular deviation of 0.6° and introduces an optical path difference between the two orthogonally polarized components. Having orthogonal polarisation with respect to each other, the two beams cannot interfere at this point. A second cube polariser oriented at 45° sets the polarisation of both beams back to 45° once more. The two beams are then spatially overlapped on the CMOS detector plane by a lens (L3) where an interference pattern is produced. The signal recorded will consist of a constant component given by the probe beam intensities, and a sinusoidal component given by

the interference of the two beams [17]. A relay lens system (L2 and L3) acts to magnify the interferogram. Magnifications in the range of 2× to 3× were used during interferometry and shadowgraphy experiments. A narrow band-pass filter centred at 532 nm is positioned in front of the CMOS camera to reject emission from the plasma.

The shadowgraphy setup is identical to the interferometry setup but with the polarising components removed.

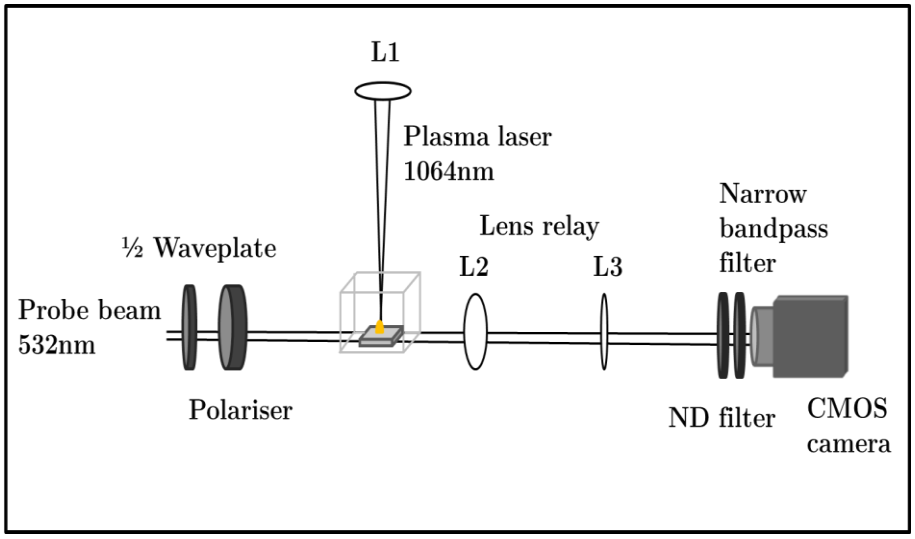

Figure 3.20: Shadowgraphy setup. The lens relay system is used to magnify the image plane onto the CMOS camera.

Where a high density of electrons exists the resulting image will appear darkest as light is deflected away from the electron cloud. The brightest sections of the shadowgram translate to areas of lower electron density where the probe beam passes through undeflected or deflected through some small angle. The recorded signal is proportional to the second derivative of the refractive index of the medium [18] (see section 2.8).

3.7 Synchronisation and Timing

In order to synchronise the arrival time of the laser pulse with the gated camera/spectrometer the laser signal was externally triggered using a Stanford Delay

Generator (model DG535) in combination with an AND gate. A 5V TTL pulse is delivered to initiate the breakdown of the flashlamps followed by a second pulse delayed by 180 µs which is sent to the Q-switch external trigger at a repetition rate of 10 Hz. This signal is then sent to one input of an AND box, the other input comes from the camera trigger. The camera gate can be controlled using a second delay generator triggered by the first and in this way time resolved images and spectra can be obtained.

For the dual laser pulse experiments the timing setup is slightly more complicated. A schematic diagram is shown below for ease of explanation.

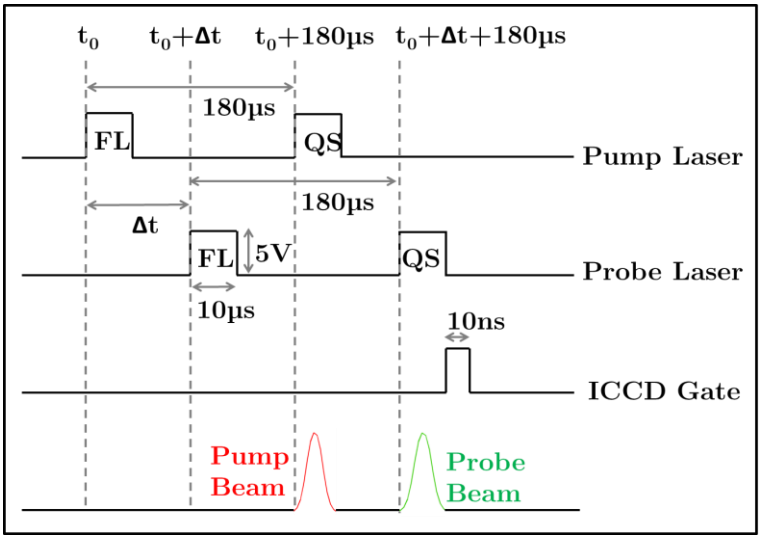

Figure 3.21: Timing diagram adapted from [7]. FL = flashlamps, QS = Q-switch.

The timing sequence of the first delay generator can be considered to be the master timing upon which all others are based. At time t_0 a trigger pulse is generated which is delivered to the flashlamps of the pump laser. Another pulse delayed by 180 µs is sent to the input of an AND gate which is then ANDed with the fire pulse delivered by the computer. These signals are the external triggers for the pump laser. A second pair of identical pulses from a second delay generator are delivered to the probe laser delayed by some offset Δt. The duration of this offset will determine the delay between the two laser pulses. This set of pulses are delivered to the external triggers of the probe laser. This timing sequence is cycled at 10 Hz to ensure thermal stability of the laser rods. The Q-switch signals and the ICCD gate will only fire when the trigger signal from the

computer is fired. This permits single shot measurements while allowing the laser flashlamp trigger repetition rate to remain at 10 Hz. A third delay generator is used to control the intensified CCD gate width and trigger delay. A simplified schematic diagram is shown below in figure 3.22 which demonstrates the concept visually.

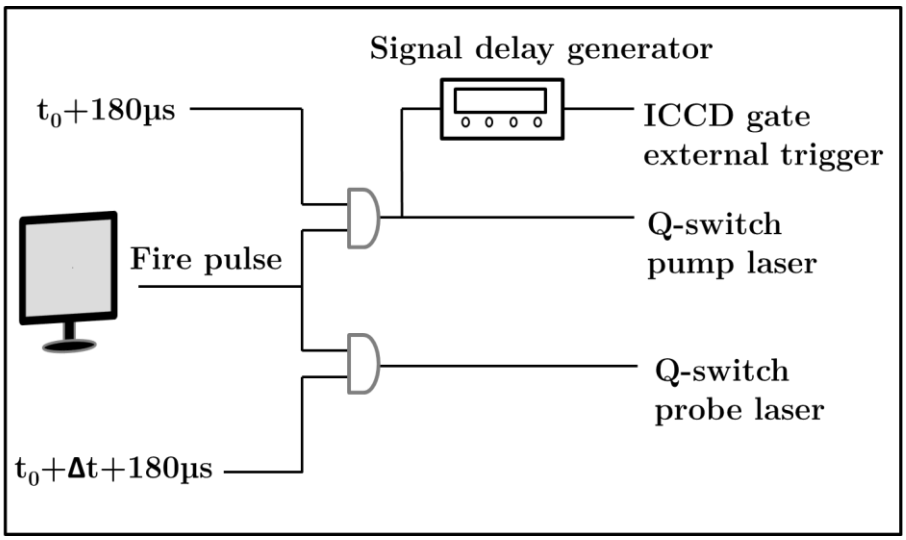

Figure 3.22: Electrical signals circuit diagram. The trigger is generated by the fire pulse from the computer. The time between the pump and probe pulses Δt can be varied by a pulse delay generator (not shown graphically). The ICCD gate width and arrival time are set by another signal delay generator.

3.8 SEM

An EVOLS 15 scanning electron microscope was used to image the craters formed by the laser on the target surface. A SEM uses a beam of focused electrons as the "light source". When this high energy beam of electrons makes contact with the target surface a number of different interactions will occur. Some of the electrons will undergo elastic scattering and others inelastic scattering. The inelastic collisions will result in secondary electrons and radiation being emitted. This secondary electron signal is collected and used to form an image [19]. A schematic diagram demonstrating a typical SEM setup is given in figure 3.23.

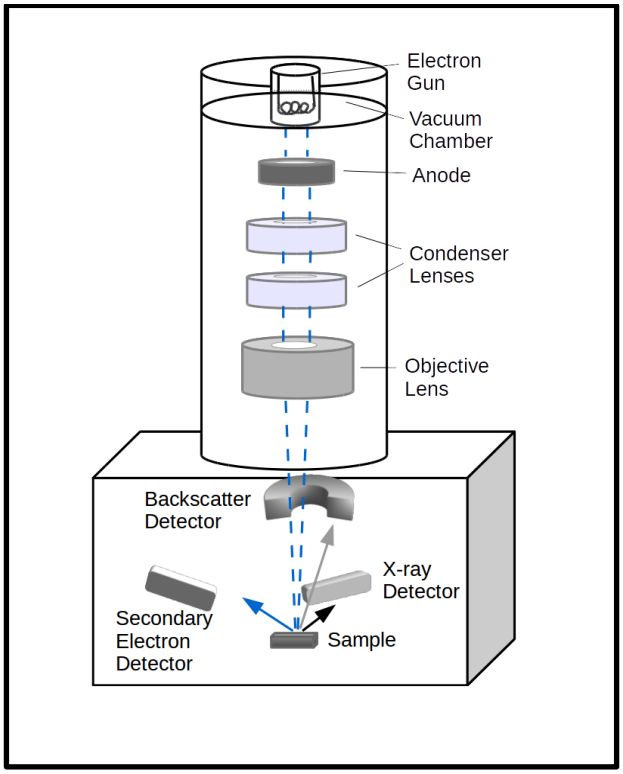

Figure 3.23: Diagram showing the main components of the scanning electron microscope. Adapted from [20].

The top vacuum column in the diagram above houses the electron beam. The electron source may be either a hot cathode thermionic emitter (tungsten filament) or a cold cathode field emission source. The beam of electrons from the filament are then accelerated by the anode and focussed by a series of magnetic lenses towards the sample surface in the target chamber. The electron beam is then raster-scanned across the target surface. The interaction of the electron beam incident on the target produces electrons and photons which may then be measured by a number of detectors located within the target chamber. The type of signal measured depends on the class of interaction taking place between the electron beam and the sample.

Electrons from the electron beam may elastically scatter from the target surface. This type of scattering is highly angle-dependant and the signal detected is due to the backscattered electrons. Interactions of the electron beam with inner-shell electrons will result in vacancies within the atoms of the sample. As outer-shell electrons fill these vacancies, high energy radiation indicative of the sample composition is emitted. This is

known as energy dispersive x-ray spectroscopy (EDX). The inelastic electrons are detected by the secondary-electron detector. This signal comes from the interaction with the electron beam and subsequent electron ejection from the sample surface. As the electron beam traces across the sample surface the number of secondary electrons emitted will vary depending on the topography. These secondary electrons are then accelerated and directed to a scintillator. The light generated by the scintillator is passed to a PMT and an image is formed via conversion of the light signal to a digital form. The beam is raster scanned point by point across the surface and the number of electrons translates to the brightness of the image.

3.9 Summary

An overview of the experimental systems has been presented. The useful information that may be learned about the plasmas formed by implementing these methods has been discussed in chapter 3. The purpose of this chapter was to describe the experimental setups and apparatus used. During the course of this work plasmas were created and studied in different backgrounds and as such the differences in refractive indices had to be considered during experimental design phases. Differences in focussing the plasma beam and energy delivery to the target surface needed to be accounted for. The experimental apparatus used throughout the work has been detailed and the principle of operation of each has been discussed. Optical emission diagnostics were carried out by direct observation of the plasma light emitted in both imaging and spectroscopy modes as a function of time. Plasma probing was achieved using a simple interferometry/shadowgraphy setup. A brief description of the systems used in each particular experiment will be given at the beginning of each results section.

References

[1] Kromatek Ltd., 2015. [Online]. Available: http://www.kromatek.co.uk/.

[2] Goodfellow Cambridge Ltd., 2015. [Online]. Available: http://www.goodfellow.com/.

[3] Z. Yan and D. B. Chrisey, "Pulsed laser ablation in liquid for micro-/nanostructure generation," *J. Photochem. Photobiol. C Photochem. Rev.*, vol. 13, no. 3, pp. 204–223, Sep. 2012.

[4] G. B. Altchuler and I. Yaroslavsky, "Absorption chatacteristics of tissues as a basis for the optimal wavelength choice in photodermatology," *Palomar Med. Technol. Burlingt.*, pp. 1–4, 2004.

[5] Continuum Lasers, *Surelite users manual*. Continuum Inc., 1995.

[6] A. Yariv, *Quantum electronics*, 3rd ed. New York: Wiley, 1989.

[7] B. E. A. Saleh and M. C. Teich, *Fundamentals of photonics*. 2007.

[8] Continuum Lasers, *www.photonicsolutions.co.uk*. Continuum Inc., 2000.

[9] G. C. Holst, *CCD arrays, cameras, and displays*. Winter Park, FL : Bellingham, Wash: JCD Pub. ; SPIE Optical Engineering Press, 1996.

[10] Andor technology plc., *Users manual*. Andor Tecnology, 2000.

[11] W. G. Schrenk, *Analytical Atomic Spectroscopy*. Boston, MA: Springer US, 1975.

[12] Newport Corporation, "www.oriel.com," *Oriel Instrum.*

[13] D. W. Hahn and N. Omenetto, "Laser-Induced Breakdown Spectroscopy (LIBS), Part I: Review of Basic Diagnostics and Plasma–Particle Interactions: Still-Challenging Issues Within the Analytical Plasma Community," *Appl. Spectrosc.*, vol. 64, no. 12, pp. 335–366, Dec. 2010.

[14] A. Sagisaka, H. Daido, K. Ogura, M. Mori, K. Matsukado, Z. Li, S. Nakamura, K. Takagaki, H. Hazama, M. Suzuki, T. Utsumi, S. V. Bulanov, T. Esirkepov, A. Fukumi, S. Orimo, Y. Hayashi, and M. Nishiuchi, "Characterization of preformed plasmas with an interferometer for ultra-short high-intensity laser-plasma interactions," *Appl. Phys. B Lasers Opt.*, vol. 78, no. 7–8, pp. 919–922, May 2004.

[15] R. Benattar, C. Popovics, and R. Sigel, "Polarized light interferometer for laser fusion studies," *Rev. Sci. Instrum.*, vol. 50, no. 12, p. 1583, 1979.

[16] P. Hough, "Laser, Optical and Elctrical Diagnostics of Colliding Laser-Produced Plasmas," Dublin City University, Dublin, 2010.

[17] E. Hecht, *Optics*, 4th ed. Reading, Mass: Addison-Wesley, 2002.

[18] I. H. Hutchinson, *Principles of plasma diagnostics*. Cambridge [Cambridgeshire] ; New York: Cambridge University Press, 1987.

[19] R. F. Egerton, *Physical principles of electron microscopy: an introduction to TEM, SEM, and AEM*. New York, NY: Springer, 2005.

[20] J. Atteberry, "How scanning electron microscopes work." [Online]. Available: http://science.howstuffworks.com/scanning-Electron-Microscope.htm.

Chapter 4

Laser Produced Plasmas in Air

During the course of the work, experiments were carried out in air in order to make comparisons with observations in water. In this chapter the results of experiments performed at atmospheric pressure are presented. Time resolved imaging studies were carried out at the fundamental Nd:YAG wavelength of 1064 nm using pulses with energies of 8 $\pm$ 3 mJ and 52 $\pm$ 3 mJ. Information on the plasma expansion dynamics could be derived from the imaging data. The results of time resolved spectroscopy are also presented which were performed using pulses at wavelengths of both 1064 nm and 532 nm. Some differences in the recorded spectra were observed between the two laser wavelengths, which are discussed. From these time resolved spectroscopic measurements, electron densities and temperatures were obtained and are presented here. The shockwave expansion in air was studied using the well-established shadowgraphy technique. The evolution of the shockwave is recorded as a function of time for a range of laser pulse energies along with corresponding fits to the so-called "point explosion" or "shockwave expansion" model [1].

4.1 Imaging

The dynamic expansion of an aluminium plasma, formed with 1064 nm pulses, into air at atmospheric pressure was studied using gated ICCD imaging. Aluminium was chosen as the target metal as it is a low-Z material and exhibits strong emission lines in the visible region. Unlike the situation that occurs in vacuum where the plasma undergoes an adiabatic expansion at an almost constant velocity, under atmospheric conditions interactions with gas molecules cause a deceleration of the expanding plume. Figure 4.1 shows a series of images demonstrating the plasma expansion occurring in a background of air.

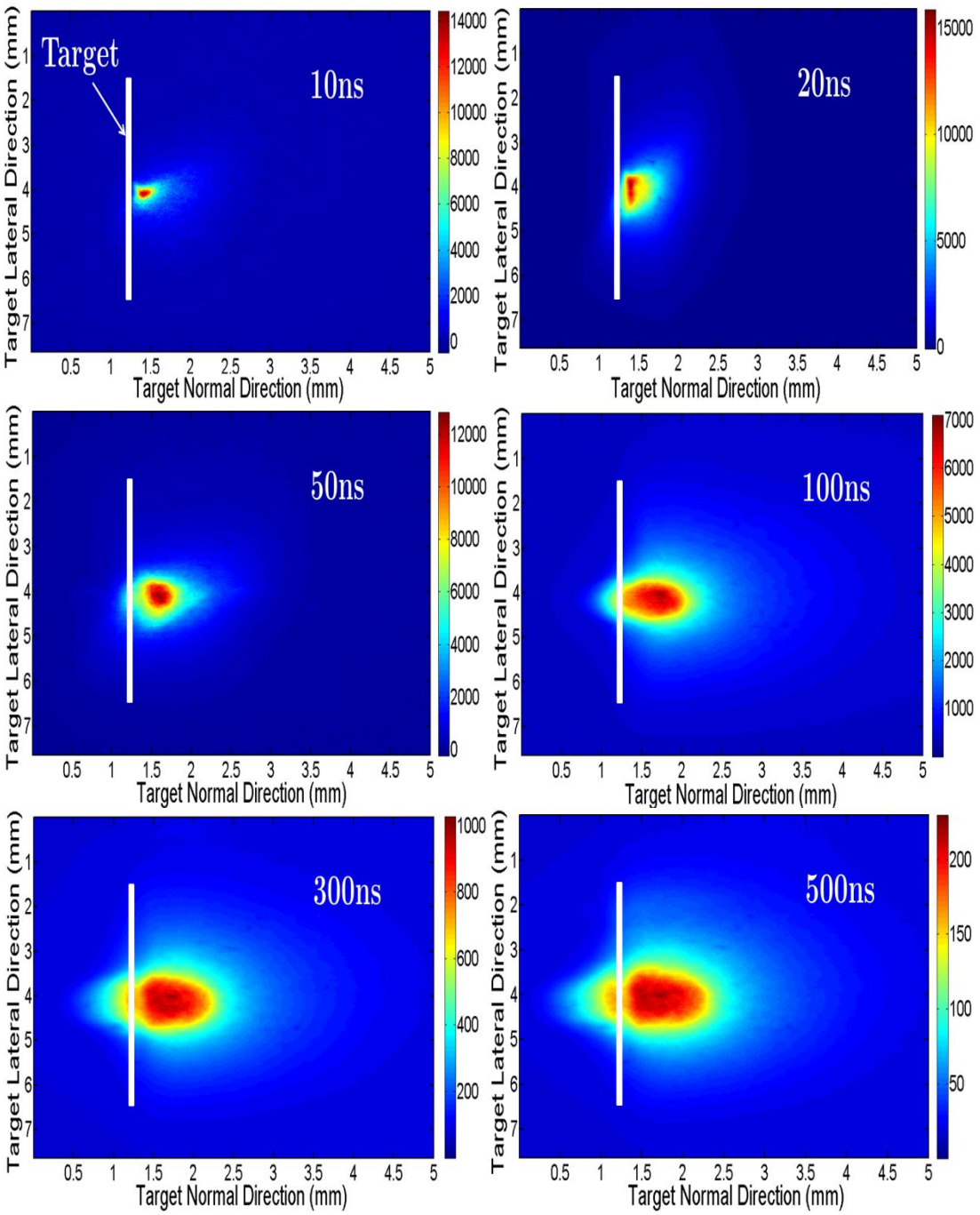

Figure 4.1: Time resolved imaging data recorded single shot using an ICCD gate width of 10 ns. The plasma is formed using 52 mJ, 1064 nm pulses. The intensity (no. of counts) is represented by the colour scale bar shown on the right hand side of each image.

The plasma is seen to expand rapidly away from the target surface at the initial stages, and more gradually at mid to late lifetimes. The visible emission observed behind the target position is due to scattering of plasma radiation from the highly reflective metallic surface. A significant lateral expansion is also observed. Strong emission is

recorded in air at delays out to 500 ns which, as is reported in chapter 7, is not the case for images recorded in water at these plasma lifetimes. The luminous plume front position is extracted from the time resolved imaging data and is shown in figure 4.2 for laser pulse energies of 8 ± 3 mJ and 52 ± 3 mJ. The plume front position was defined as the position at which the ICCD count had dropped to $1/e$ (~0.37) of its maximum value in the expansion direction normal to the target surface (as outlined in section 2.6).

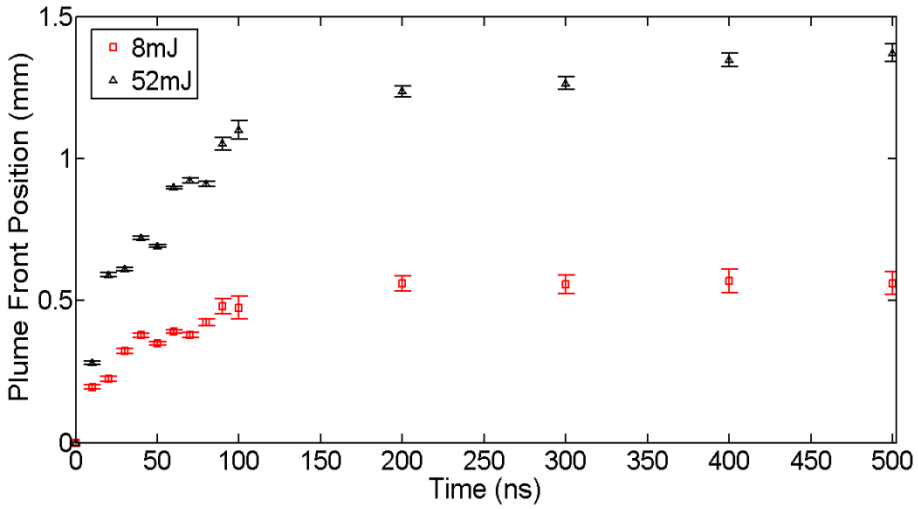

Figure 4.2: Luminous plume front positions measured from imaging data using 1064 nm laser pulses at 8 mJ and 52 mJ.

The expansion of the plasma away from the target surface is shown in figure 4.2 where a greater expansion is observed at higher pulse energy. A similar trend is observed in the plume front position measured using the two laser pulses energies. During the first 50 ns, a very rapid expansion occurs, greater in the case of the 52 mJ pulse where the luminous front has reached *ca.* 0.7 mm compared to 0.4 mm. This is followed by a more gradual expansion until finally a plateau is reached. This plateau is the so-called stopping distance of the plasma and will be discussed in greater detail in chapter 6. The plateau appears to be reached roughly 100 ns after the laser pulse for the 8 mJ case, whereas in the 52 mJ case a very gradual expansion can still be observed until roughly 400 ns where it appears to level off. This trend has been reported in the literature for plume expansion into a background of ambient air where this initial rapid expansion is reported to transition to a much more gradual expansion [2] with greatest expansion

occurring at higher pulse energies [3], [4]. The expansion of the plume is also known to reach this plateau region at earlier delay times as the background pressure increases [5], [6]. During a study on aluminium in air ambient using a 50 mJ, 1064 nm laser pulse, Hussein *et al.* report a stopping distance for the expanding plasma of 1.1 mm occurring approximately 400 ns after the laser pulse which is very similar to findings reported during this work [3]. A deceleration of the plume expansion is occurring due to collisions with air molecules.

4.2 Spectroscopy

The results of spectroscopic studies performed using an aluminium target at atmospheric pressure conditions are presented in this section. A comparison of spectra obtained using different laser wavelengths and different pulse energies is given. A typical time integrated spectrum (using a 1 µs ICCD gate width) of an aluminium plasma, recorded in air at atmospheric pressure, is shown in figure 4.3.

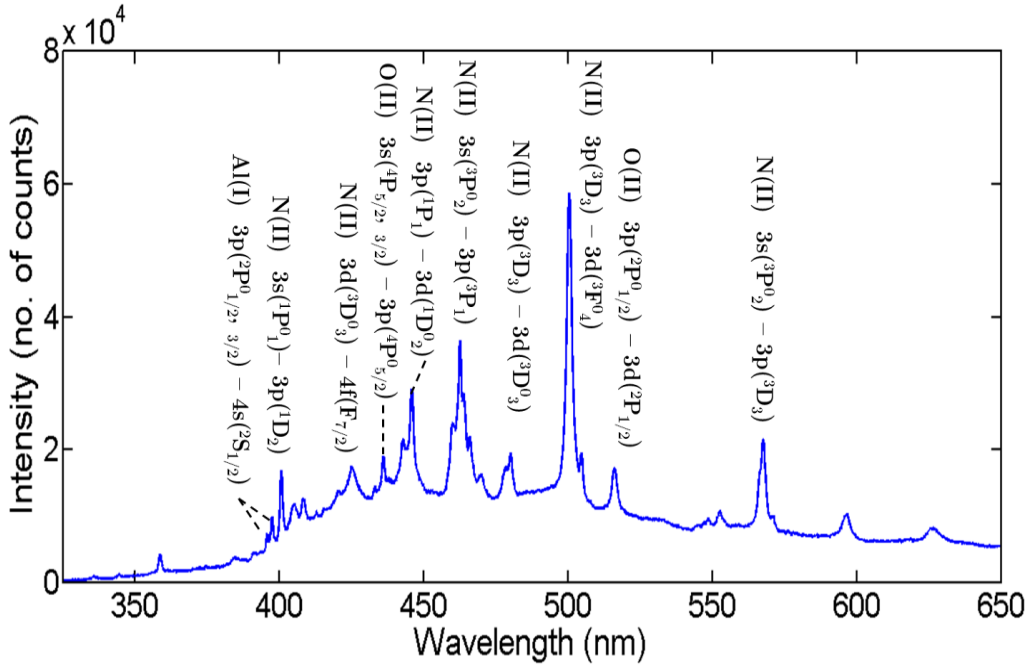

Figure 4.3: Time integrated aluminium emission spectrum recorded using a 52 mJ, 1064 nm laser pulse in air at atmospheric pressure. The main species responsible for the main emission features are identified to be nitrogen and oxygen. An ICCD gate width of 1 µs was used.

From the time integrated spectra, an overview of the main emission lines is revealed. It is apparent that nitrogen emission lines are the most prominent spectral feature present in the spectrum. The identification of atomic emission lines is performed by cross-referencing with the NIST atomic spectra database [7]. The aluminium neutral doublet below 400 nm is discernable from the time integrated spectrum, albeit it appears at relatively low intensity in comparison to the considerable emission strength of the nitrogen and oxygen lines which are readily ionised by the highly excited plasma created in atmospheric air. The analysis of spectra of interest in background gases is complicated by the emission of the ambient gas species which often produce spectra comprising many blended lines, some of which overlap with lines from the target of interest. This problem can be mitigated, at least in part, by gating the CCD camera to obtain time-resolved spectra. Depending on the species, the emission lifetimes of lines of interest from the plasma may be quite different to those of atmospheric species so that they may be separated and distinguished by the use of a suitable delay from the instant of plasma breakdown and gate width of the intensified CCD. In atmospheric air, the emission lifetime of ambient gas species is relatively short compared to aluminium line emission which is measurable out to a time delay of *ca.* 50 µs. By applying an ICCD gate width at the appropriate times corresponding to the observable lifetimes of the ionic species present in the plasma, the spectral features of interest may be observed.

The following results presented in this section are of time resolved spectra performed at two different laser wavelengths (1064 nm and 532 nm) using an ICCD camera operated with a gate width of 10 ns. The particular spectra shown are representative of the different features which occur at each laser wavelength as a function of time. While spectra recorded using both laser wavelengths are comparable, some marked differences are identified between the two. Spectra were also recorded at pulse energies of 8 $\pm$ 3 mJ and 52 $\pm$ 3 mJ in order to investigate the effect of laser pulse energy on temperatures and densities within the plasmas formed in air, these are presented in section 4.4.

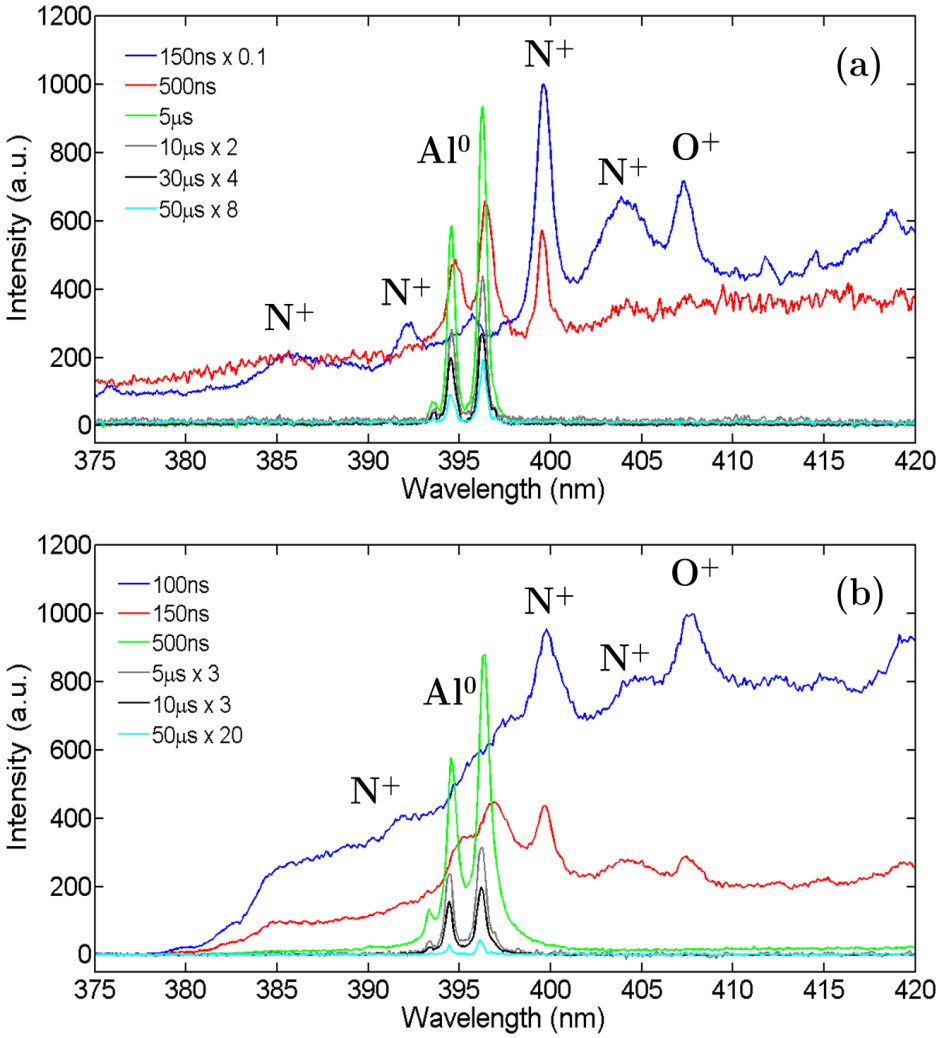

Figure 4.4: Time resolved spectra in the spectral region of the aluminium neutral doublet at 394.4 nm and 396.15 nm recorded using (a) 1064 nm, 52 mJ pulses and (b) 532 nm, 52 mJ pulses.

Similar lifetimes are observed for the aluminium neutral emission recorded at both laser wavelengths with spectra observable in both cases for time delays of up to 50 µs after the laser pulse. The aluminium neutral doublet $3p(^2P^0_{1/2,\ 3/2}) - 4s(^2S_{1/2})$ is seen to emerge from the continuum emission earlier in the case of the 532 nm excitation with the first signs of the neutral doublet appearing after a delay of 150 ns. For plasmas formed with laser pulses at the fundamental infrared wavelength, the aluminium neutral lines begin to be distinctly observable at around 500 ns.

Similar emission lines from background gas species are observed at both laser wavelengths as seen in figure 4.4. The emission of predominantly singly ionised nitrogen and oxygen dominate the spectra for the first few hundreds of nanoseconds before atomic emission from aluminium is detected. These background gas species are seen to emit more strongly in plasma emission spectra recorded using 1064 nm pulses. At these early times, the strongest atomic contribution in this spectral region comes the N(II) line $3s(^1P^0_1) - 3p(^1D_2)$ at 399.5 nm. The spectral feature at a central wavelength of ~404 nm is due to a combination of several singly ionised nitrogen emission lines N(II) $3d(^3F^0_2)$ - $4f(G_{7/2})$, N(II) $3d(^3F^0_4)$ - $4f(G_{9/2})$, and N(II) $3d(^3F^0_3)$ - $4f(G_{7/2})$ at wavelengths of 403.51 nm, 404.13 nm and 404.35 nm respectively. These three N^+ lines have similar emission strength and blend together producing the broad feature observed. A similar feature is observable around 407 nm where atomic oxygen lines are barely resolvable producing what materialises as a single broad spectral line. The oxygen lines contributing to this feature are singly ionised lines O(II) $3p(^4D^0_{7/2})$ - $3d(^4F_{9/2})$, O(II) $3d(^4F_{3/2})$ - $4f(D[2]_{3/2})$ and O(II) $3p(^4D^0_{3/2})$ - $3d(^4F_{3/2})$ at wavelengths of 407.58 nm, 407.7 nm and 407.88 nm respectively.

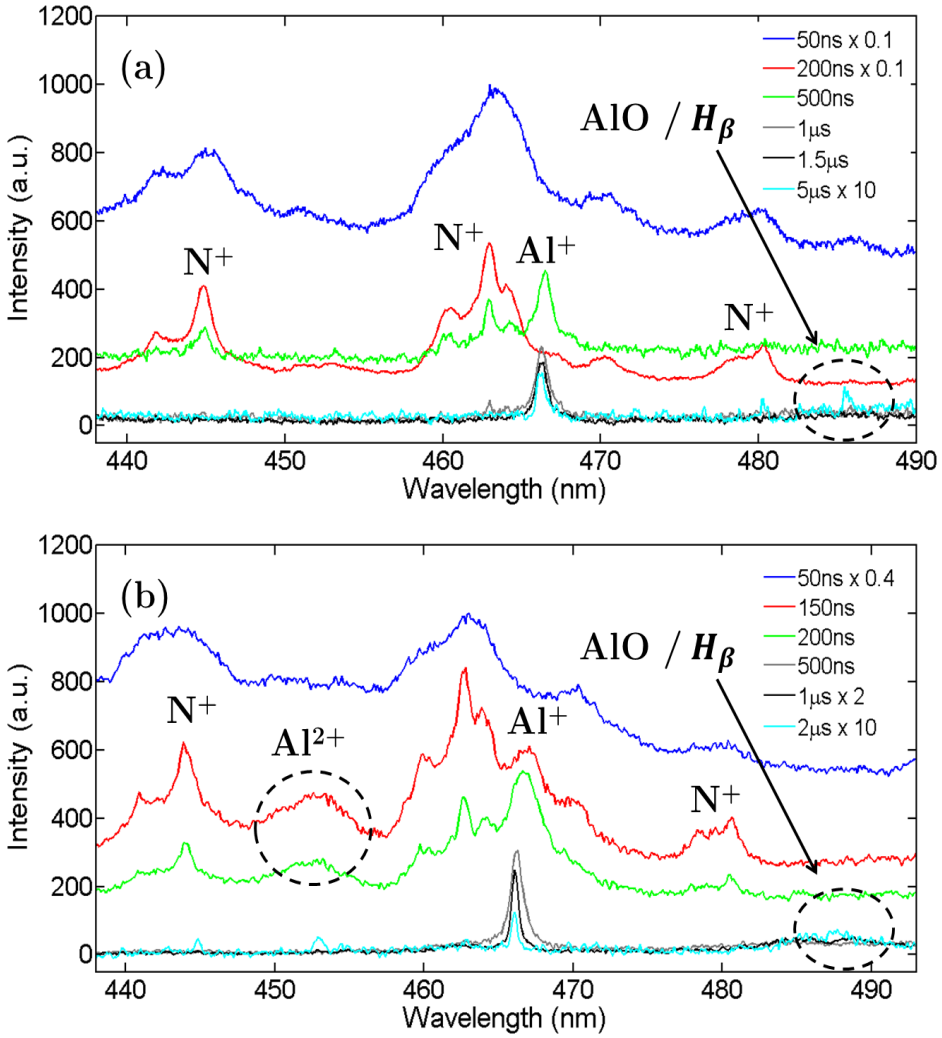

Figure 4.5: Time resolved spectra of an aluminium plasma formed in air in the spectral region of the singly ionised atom at 466.3 nm recorded using (a) 1064 nm, 52 mJ pulses and (b) 532 nm, 52 mJ pulses.

The emergence of the Al(II) line $3p^2(^1D_2) - 4p(^1P^0_1)$ at 466.3 nm occurs at around 500 ns in the 1064 nm plasma and around 200 ns using the 532 nm wavelength. The persistence of the singly ionised atomic line is also prolonged in the 1064 nm case with evidence of emission up to a delay of 5 µs (figure 4.5). Similar to spectra shown in figure 4.4, contributions from ionised atmospheric species dominate the spectra recorded at early plasma lifetimes with significant N^+ emission lines observed around 464 nm which is attributed to strong emission from the N(II) $3s(^3P^0_2) - 3p(^3P_1)$ line at a wavelength of 464.31 nm. Similar atmospheric spectra were observed using 1064 nm and 532 nm

pulses with nitrogen and oxygen again contributing significantly to the observed spectra.

The presence of a weak spectral feature is noted around 485 nm with the first signs of its appearance in figure 4.5 occurring at *ca.* 2 µs. Although weak at these times, this first phase of formation is most apparent for spectra recorded using the 532 nm laser wavelength. This feature may be attributed to the H_β emission profile which appears typically microseconds after plasma ignition due to water vapour in the air at a wavelength of 486.13 nm. Also potentially contributing to this spectral feature is early phase molecular aluminium oxide which exhibits strong band emission around 484 nm. Notable also in the 532 nm spectra is the appearance of a spectral feature around 452 nm. This spectral feature is considered to correspond to a blending of two aluminium doubly ionised emission lines, Al(III) $4p(^2P^0_{1/2})$ - $4d(^2D_{3/2})$ and Al(III) $4p(^2P^0_{3/2})$ - $4d(^2D_{5/2})$ at wavelengths of 451.26 nm and 452.91 nm respectively. This relationship between the H_β /AlO and the appearance of Al^{2+} line emission was studied in greater detail, the results of which will be presented in chapter 5.

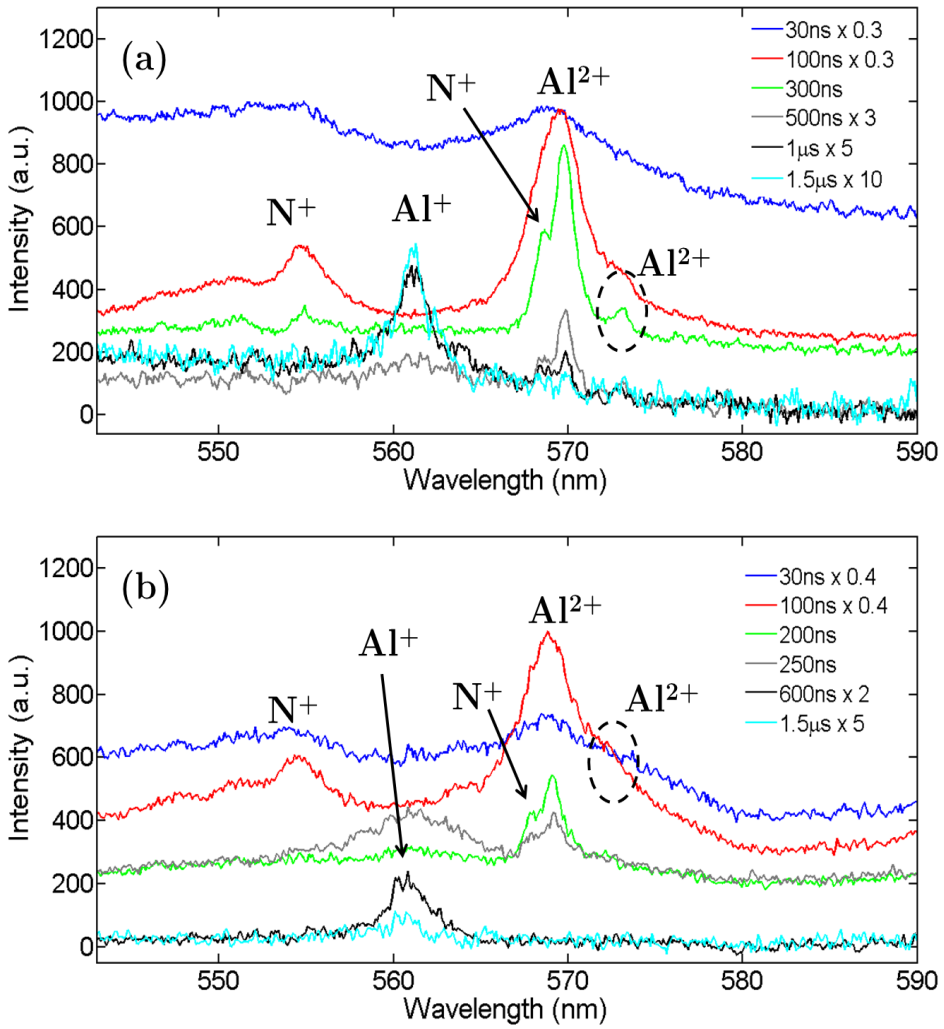

Figure 4.6: Time resolved aluminium spectra recorded using (a) 1064 nm, 52 mJ pulses and (b) 532 nm, 52 mJ pulses showing a doubly ionised aluminium emission feature at 569.66 nm.

Spectra of the Al(III) line $4s(^2S_{1/2})$ – $4p(^2P^0_{3/2})$ at 569.66 nm are more complex than measurements from lower charge states. Here, a nitrogen line at 568.5 nm appears as a shoulder on the main aluminium peak at 569.66 nm. This nitrogen line becomes more distinguishable as a separate peak after 200-300 ns. Present also in this spectral region is the Al(III) line $4p(^2S_{1/2})$ – $4p(^2P^0_{1/2})$ at 572.27 nm appearing as a spectral shoulder which is not well resolved from the main aluminium line of interest. Using the peak fitting software AAnalyzer these unique features may be separated from one another to a degree once the constituent species present are known. However, due to the blending and broad nature of the atomic lines in this spectral region information on the

contributions of each individual line (specifically areas, FWHMs of each feature) may not be reliably known.

Comparing the spectra obtained at each laser wavelength, the emitting lifetime of the Al^{2+} ion appears greatest for plasmas created using 1064 nm pulses. In addition to prolonged emission, the unique spectral features obtained appear better resolved than in the 532 nm case with smoother spectra being obtained. The 572.27 nm line for example is less easily distinguished in spectra obtained using 532 nm laser pulses as the signal to noise ratio is reduced. This may be due to the increase in mass ablation that occurs at shorter laser wavelengths due to stronger laser coupling to the target and higher critical density of the plasma [8], [9].

Contributions from multiple nitrogen emission lines are apparent using both laser wavelengths around 554 nm. The emission line contributing most strongly on the observed spectra is attributed to the N(II) $3s(^5P_3)$ - $3p(^5D^0_4)$ transition at a wavelength of 553.54 nm. Another feature common at both laser wavelengths is the broad feature around 560 nm appearing at roughly 500 ns and 200 ns for the 1064 nm and 532 nm laser wavelengths respectively. This feature is most likely due to contributions of relatively weak Al^+ transitions Al(II) $4p(^1P^0_1)$ - $4d(^1D_2)$ and Al(II) $4d(^1D_2)$ – $7f(^1F^0_3)$ at 559.33 nm and 561.33 nm respectively. The emission lifetime of these Al^+ lines appears similar in both instances with emission up to 1.5 µs being observed. Similar to observations shown in figure 4.5, evidence of these emission lines appears earlier in the case of 532 nm laser pulses presumably due to the higher background continuum associated with 1064 nm plasma emission.

Some evidence of spectral shifting is observed in spectra recorded using both 1064 nm and 532 nm pulses. Voigt profiles were fitted to the recorded spectra in order to quantify the spectral shifts for plasma emission lines from 1064 nm pulses and 532 nm pulses. Figure 4.7 demonstrates the spectral shifts of aluminium neutral lines obtained using 52 mJ pulses at 1064 nm and 532 nm wavelengths.

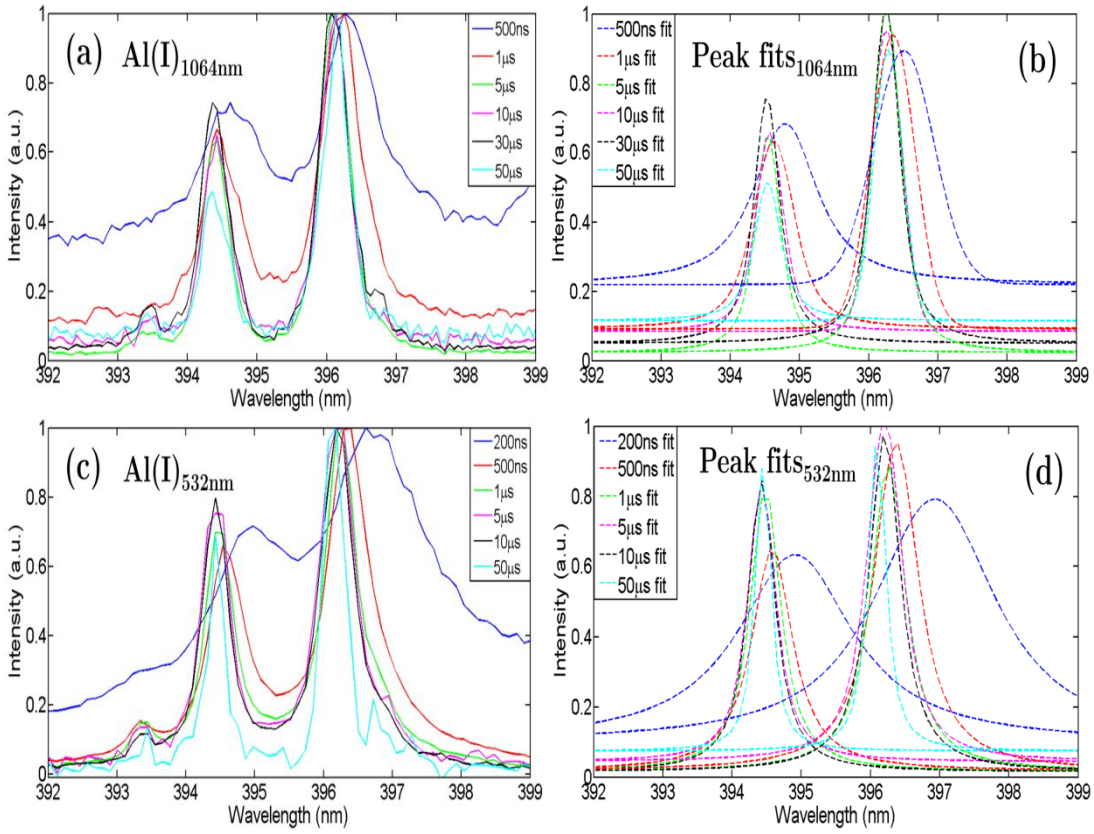

Figure 4.7: Time resolved spectra of aluminium neutral emission lines in air using 52 mJ pulses showing evidence of spectral shifting. Figures correspond to (a) Al(I) spectra at 1064 nm, (b) corresponding peak fit to (a), (c) Al(I) spectra at 532 nm and (d) corresponding peak fit to (c).

Figure 4.7 shows the spectral shifts occurring for both laser wavelengths over the observable lifetimes of the aluminium neutral lines. A larger wavelength shift is apparent in spectra recorded using 532 nm pulses. Spectral shifts were also analysed for the Al(II) emission lines shown in figure 4.8.

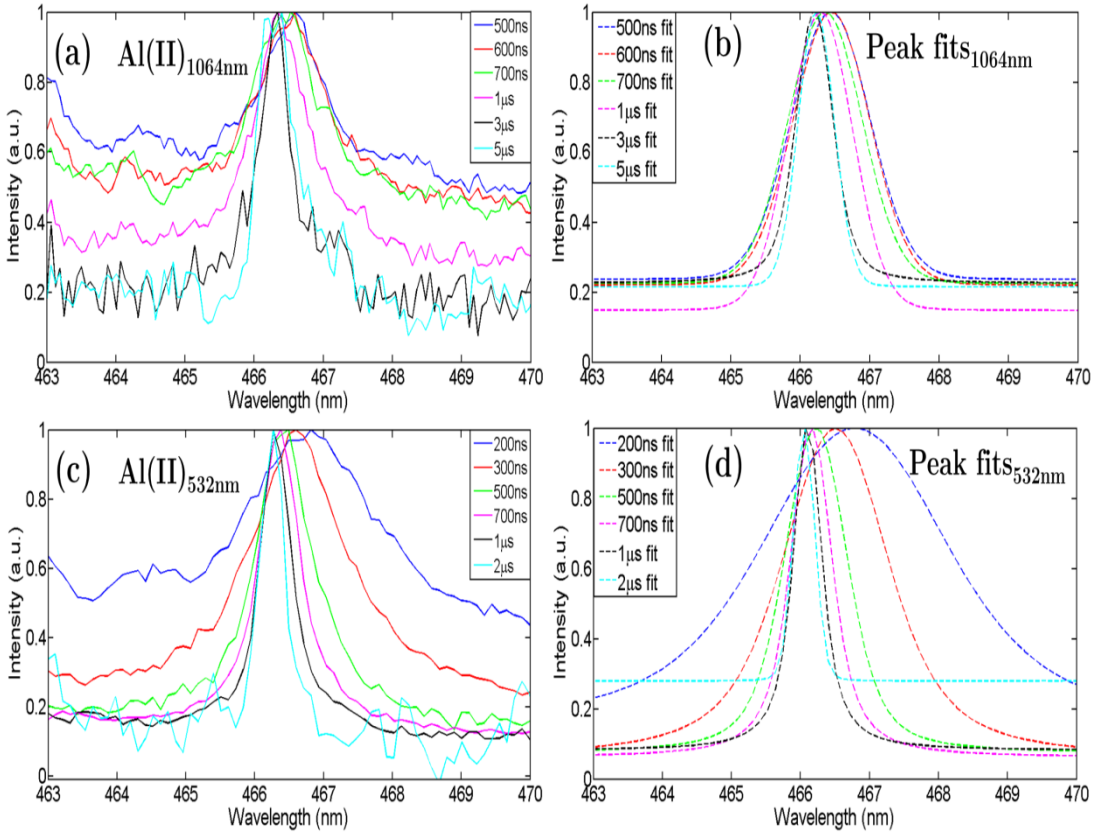

Figure 4.8: Time resolved spectra of aluminium singly ionised emission lines in air using 52 mJ pulses showing evidence of spectral shifting. Figures correspond to (a) Al(II) spectra at 1064 nm, (b) corresponding peak fit to (a), (c) Al(II) spectra at 532 nm and (d) corresponding peak fit to (c).

Shifts of 0.2 ± 0.1 nm and 0.2 ± 0.1 nm respectively for Al(I) and Al(II) spectra at a time delay of 50 µs compared to the earliest time delays were observed for plasmas created with 1064 nm pulses. Using 532 nm pulses the wavelength shifts were 0.5 ± 0.1 nm and 0.7 ± 0.1 nm respectively. No convincing shift could be reliably observed for the Al(III) spectra which are shown in figure 4.9.

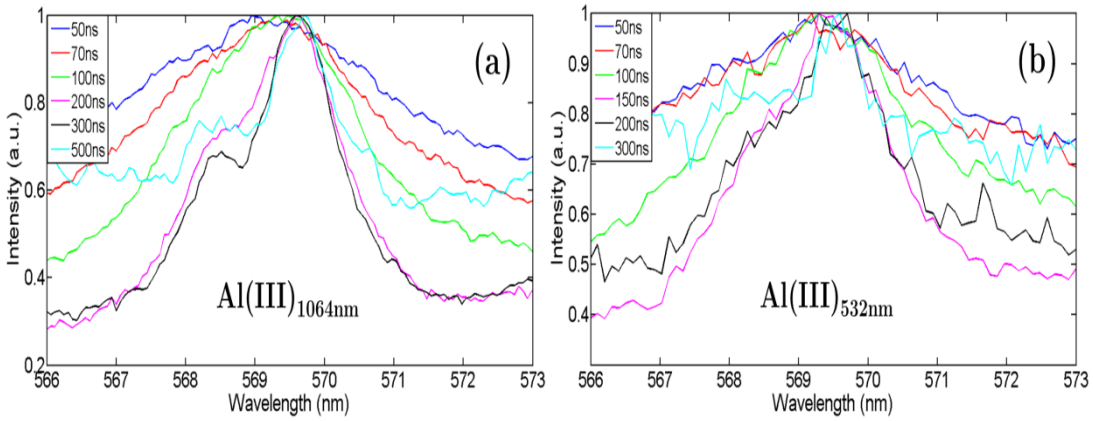

Figure 4.9: Time resolved spectra of aluminium doubly ionised emission lines in air using 52 mJ pulses. Figures correspond to (a) Al(III) spectra at 1064 nm and (b) Al(III) spectra at 532 nm.

Due to the blending of the emission lines in particular at the early delay times the exact wavelength of emitting species may not be reliably stated. These peaks appear better resolved after a delay of *ca.* 200 ns, at which time emission intensities are severely reduced and become adversely affected by noise which is apparent from figure 4.9. As a result, measurable spectral shifts for Al(III) emission lines could not be reliably extracted from peak fitting attempts. The blending of emission lines from N(I) $3d(^3D^0_2)$ – $4p(^2D_2)$ at 558.85 nm, Al(III) $4s(^2S_{1/2})$ – $4p(^2P^0_{3/2})$ at 569.66 nm and Al(III) $4p(^2S_{1/2})$ – $4p(^2P^0_{1/2})$ at 572.27 nm as well as the low emission intensity observed at later delay times makes the quantification of spectral shifts too speculative without additional knowledge such as emission intensities.

The spectral line shifts are due to Stark-shifting of the energy levels. In a high temperature, high density plasma, the electric fields of many surrounding species will perturb the energy levels of the emitting species which causes a wavelength shift of the emitted radiation. Stark-shifting of emission lines in lowly ionised species is dominated by electron collisions. The observance of larger wavelength shifts using 532 nm pulses suggests higher electron densities than those associated with the 1064 nm plasma. Broader emission lines were also observed using the 532 nm pulses. The broadening of the peaks was used to estimate the electron density of the plasmas created using both laser wavelengths, the results of which are presented in section 4.4.

4.3 Shockwave Formation

When a high intensity laser pulse is incident on a target the resulting plasma expansion away from the surface causes a highly energetic shock-front to form. This laser-induced shockwave is formed by a compressive gas front which advances away from the target surface [10]. Using the shadowgraphy setup described in chapter 3, the dynamic evolution of shockwaves formed under atmospheric conditions were studied. The plasma was created using 1064 nm laser pulses at various pulse energies in single shot mode and the subsequent shockwave expansion was measured as a function of time.

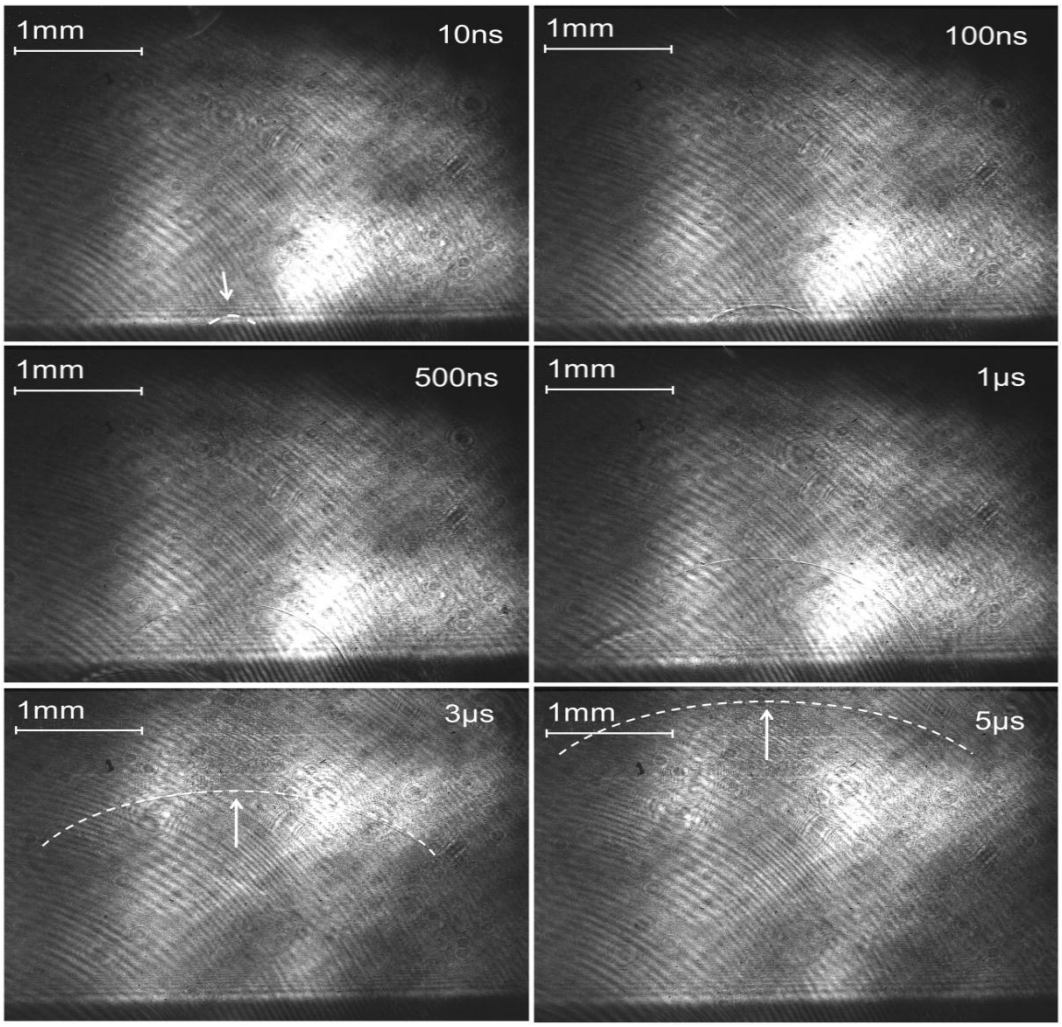

Figure 4.10: Shadowgraphs showing the evolution of the shockwave in air using 8 mJ, 1064 nm laser pulses on an aluminium target. The shock-front becomes more diffuse as time progresses.

The shock-front is observed as early as 10 ns after the laser pulse is fired in air. For an 8 mJ pulse, the shockwave has propagated a distance of approximately 3 mm at a time delay of 5 µs after the laser pulse reached the target. The camera is placed in line with the target-cuvette such that the expansion is observed normal to the target surface. In the initial stages of expansion, i.e., in the first few hundred nanoseconds, the shock-front is easily visible in the recorded shadowgraphs. On microsecond timescales, the shockwave becomes weaker as energy dissipates from the shock-front into the surrounding medium. At 3 µs and 5 µs the shockwave has been highlighted on the shadowgraphs in figure 4.10 for clarity. From these shadowgraphs, the shockwave expansion is extracted as a function of time for laser pulse energies of 8 mJ, 16 mJ, 38 mJ and 52 mJ and shown in figure 4.11. Shown also are fits to the shockwave expansion or point explosion model given by [1]:

$$R = \alpha t^n \tag{4.1}$$

where R represents the plume front position, t is time and α and n are the fitting parameters.

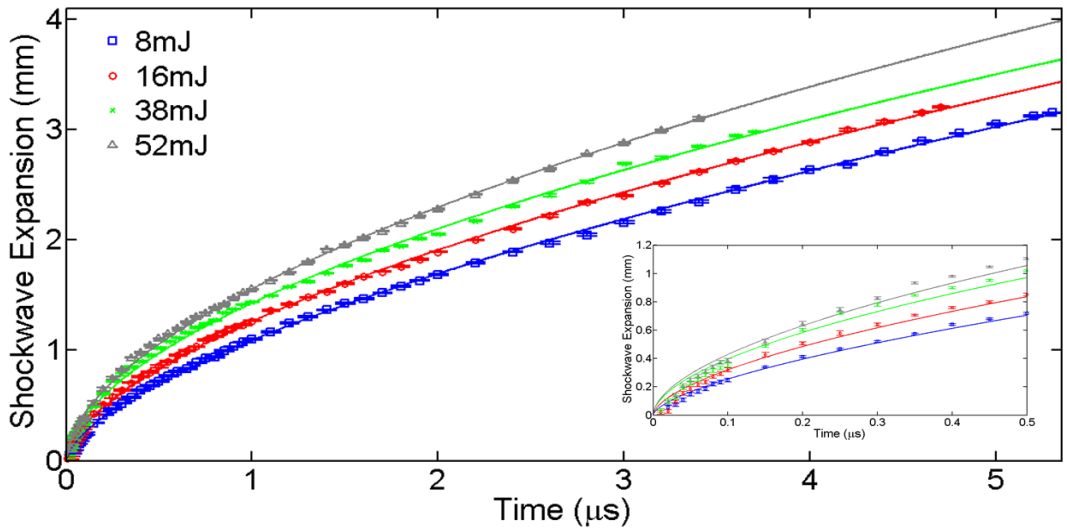

Figure 4.11: Shockwave expansion in air using an aluminium target and 1064 nm laser pulses of energies 8 mJ, 16 mJ, 38 mJ and 52 mJ. $\bar{R}^2$ values obtained by fits to shockwave expansion model were 0.99, 0.99, 0.99 and 0.99 respectively. Inset: Expansion between 0-500 ns.

	α	n	$\bar{R}^2$
8mJ	1.09 ± 0.02	0.63 ± 0.01	0.99
16mJ	1.26 ± 0.02	0.60 ± 0.01	0.99
38mJ	1.43 ± 0.03	0.56 ± 0.02	0.99
52mJ	1.56 ± 0.03	0.56 ± 0.02	0.99

Table 4.1: Fitting parameters obtained by fits to shockwave expansion model [1] (*cf.* corresponding figure 4.11).

In the initial stages, a very high velocity expansion is observed. 50 ns after the laser pulse, instantaneous velocities of 2055 ± 45 ms^{-1}, 2570 ± 32 ms^{-1}, 3059 ± 34 ms^{-1} and 3317 ± 39 ms^{-1} are found for the shockwave velocities at 8 mJ, 16 mJ, 38 mJ and 52 mJ respectively. The values obtained are similar to those reported in the literature in comparable studies where velocities on the order of several kms^{-1} are seen [3], [11], [12]. Velocities are then found to eventually tend towards an approximately linear expansion in the later stages of observable measurements. After 5 µs, an instantaneous velocity of approximately 400 ms^{-1} is found independent of initial laser pulse energy. As the shockwave expands into the surrounding atmosphere it experiences a gradual deceleration with time. This deceleration of the shock-front is caused by collisions with the background gas molecules which act to slow the shock-front as it loses energy through these collisions. The shockwave velocity gradually continues to decrease (at times unavailable for observation using the current setup) until eventually transitioning after a few tens of microseconds into an acoustic wave [13]. The experimental data were fitted to the point-explosion or shockwave expansion model described in detail in section 2.10.2. With increasing pulse energy, the value of $\boldsymbol{a}$ is found to increase. The values obtained for the fitting parameters are shown in tabular form in table 4.1. As $\boldsymbol{a}$ is a value related to the amount of energy delivered to the system for a medium of fixed density [14], this trend is consistent with increasing energy delivered by the laser pulses. The values obtained by the model fits for the parameter $\boldsymbol{n}$ were 0.63 ± 0.1, 0.60 ± 0.1, 0.56 ± 0.2 and 0.56 ± 0.2 for 8 mJ, 16 mJ, 38 mJ and 52 mJ respectively. This trend indicates that the expansion is becoming more spherical with increasing pulse energy. For an 8 mJ pulse, an approximately planar expansion is found from the model fit, meaning that the expansion is occurring preferentially in one dimension. This value of $\boldsymbol{n}$

decreases with increasing energy declining towards a value of approximately 0.5, meaning that the shockwave is tending towards a predominantly two-dimensional expansion with increasing laser pulse energy. These findings suggest that a higher proportion of energy is being delivered into the lateral expansion of the shockwave with increasing laser pulse energy.

The shockwave behaviour was studied using different target materials in a background of air. As before, the shock-front positions were extracted from time resolved shadowgraphy measurements using 8 mJ, 1064 nm laser pulses. The shockwave expansions using aluminium, silver and gold targets are shown in figure 4.12.

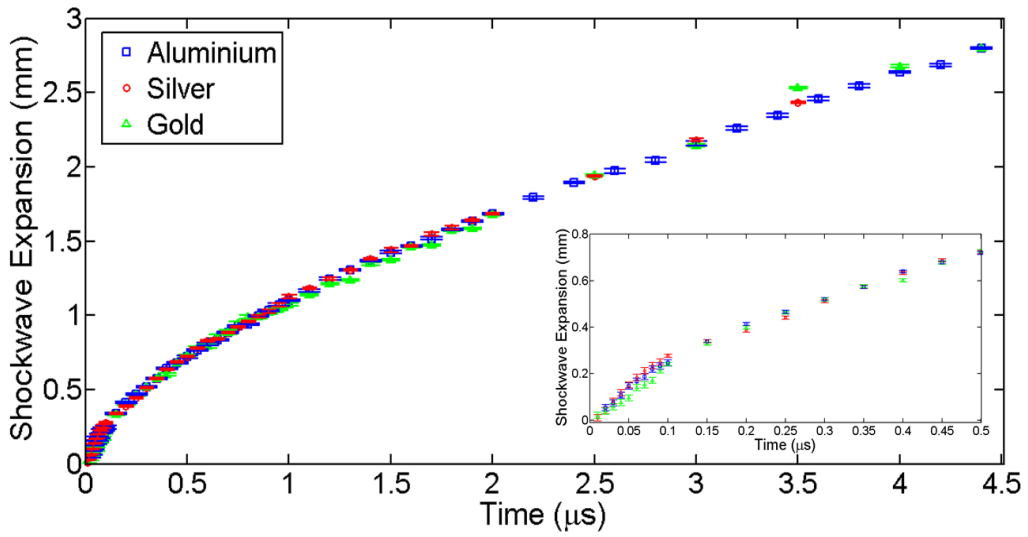

Figure 4.12: Shockwave expansion in air using 1064 nm, 8 mJ pulses measured using aluminium, silver and gold targets. Inset: Expansion between 0-500 ns.

A similar shockwave expansion was found for each of the target materials employed. It would appear from these results that the expansion of the shock-front is not dependent or is at least very weakly dependent on the target material.

4.4 Temperature and Density Calculations in Air

Temperatures and densities were extracted from time resolved aluminium spectroscopy data in air. Measurements relating to the emission spectra such as integrated peak areas and peak widths were calculated using the AAnalyzer peak fitting software. The relevant parameters required for temperature and density calculations were extracted from the literature tables of Konjevic and Wiese [15], [16]. Information related to particular atomic transitions in aluminium were acquired from the NIST atomic database [7]. As a brief reminder, electron densities were calculated using the expression for Stark broadening of a line (see section 2.7.3). The width of the measured line is related to the density of emitting species with a higher density producing a broader peak profile. Measuring the full width at half-maximum of atomic transitions of interest, the electron density may be deduced by the expression:

$$n_e = \left(\frac{\Delta\lambda_{FWHM}}{2w}\right) \times 10^{16} \tag{4.2}$$

where n_e is the electron density, $\Delta\lambda_{FWHM}$ is the full width at half-maximum of the spectral line and w is the electron-impact parameter. The instrument linewidth is deconvolved from the experimentally observed line profile to obtain the "true". For consistency, the Al^+ line at 466.3 nm was used throughout electron density calculations. Electron temperatures were extracted from the ratio of integrated intensities from successive charge states (see equation 2.31). Having calculated electron densities from equation 4.2, the electron temperature was obtained from:

$$\frac{I_1}{I_2} = \frac{f_1 g_1 \lambda_2^3}{f_2 g_2 \lambda_1'^3}\left(4\pi^{\frac{3}{2}} a_0^3 n_e\right)^{-1}\left(\frac{k_B T_e}{E_H}\right)^{\frac{3}{2}} exp\left(\frac{-E_1 + E_2 - E_\infty + \Delta E_\infty}{k_B T_e}\right) \tag{4.3}$$

where I, f, g and λ are the total integrated intensity of the line, the absorption oscillator strength, the statistical weight of the transition and the wavelength respectively. E_1 and E_2 are the excitation energies of the upper and lower energy levels. E_∞ and ΔE_∞ are the ionisation energy of the lower ionic stage and the high density correction factor which accounts for the shift of the ionisation energy due to a strong

electric field. The higher ion stage is denoted by the subscript 1. The ratio of Al^{+} 466.3 nm to Al^{0} 396.15 nm was used to calculate temperatures in aluminium plasmas. Temperatures and densities were obtained for plasmas formed in air using 1064 nm and 532 nm laser wavelengths at pulse energies of 8 mJ and 52 mJ. Fitting parameters extracted are presented in tabular form following model fits to electron densities and temperatures.

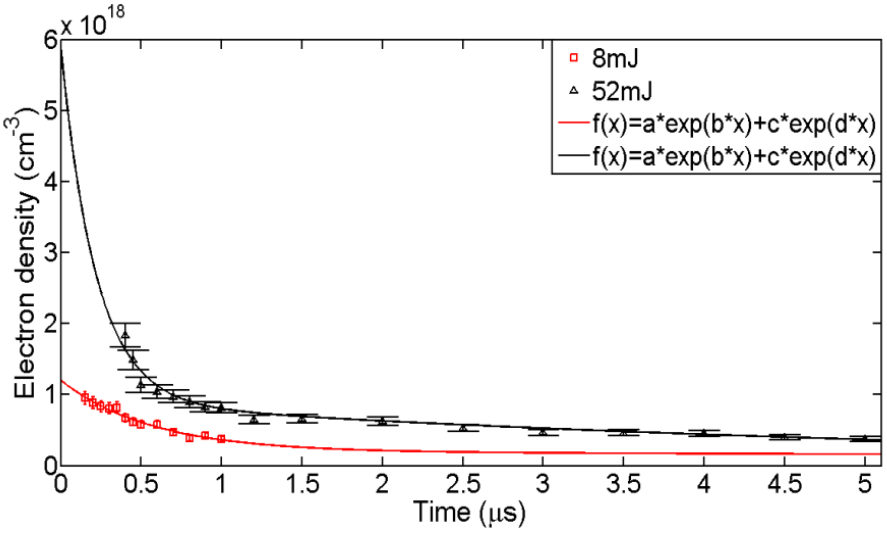

Figure 4.13: Variation in electron density with time delay obtained using 1064 nm laser pulses with energies of 8 mJ and 52 mJ. Shown also are the corresponding double exponential fits with $\bar{R}^2$ values of 0.96 and 0.98 respectively.

	a(cm^{-3})	b(μs^{-1})	c(cm^{-3})	d(μs^{-1})	$\bar{R}^2$
8mJ	$1.17 \pm 0.16 \times 10^{18}$	-1.77 ± 0.37	$2.41 \pm 1.15 \times 10^{17}$	-0.41 ± 0.26	0.96
52mJ	$2.75 \pm 0.22 \times 10^{19}$	-8.39 ± 2.25	$9.12 \pm 0.8 \times 10^{17}$	-0.17 ± 0.03	0.98

Table 4.2: Fitting parameters obtained using double exponential fit to electron density values obtained for plasmas formed by 1064 nm pulses (*cf.* corresponding figure 4.13).

A higher electron density was found using 52 mJ pulses with an average density approximately 2× that observed using 8 mJ pulses for measurements recorded over the same time delay range (roughly 500-1000 ns). Electron densities of $1.84 \pm 0.17 \times 10^{18}\,cm^{-3}$ and $0.95 \pm 0.09 \times 10^{18}\,cm^{-3}$ were obtained using 8 mJ, 1064 nm and 52 mJ, 1064 nm laser pulses respectively in ambient air. The values were obtained at the earliest

measurements at delay times of 0.15 µs and 0.4 µs respectively. The density is seen to initially decrease very rapidly before tailing off slowly after approximately 1 µs. The experimental data was best fit to a double exponential decay at both laser pulse energies. The goodness of fits using a single exponential fit were 0.96 and 0.78 for 8 mJ and 52 mJ pulses respectively. This would appear to indicate that for times up to ~1 µs, the trend follows a single exponential decay while at later times, a more gradual decay occurs. In the case of 52 mJ pulses, the electron density is best fit to a sum of two exponential terms, one for the early phase rapid decay, and another for the more gradual subsequent decay. The addition of a third exponential term does not seem to improve the goodness of the fit. $\bar{R}^2$ values obtained by a triple exponential fit to the experimental data presented in figure 4.13 were 0.95 and 0.97 for 8 mJ and 52 mJ respectively. The origin of a double exponential decay is postulated to come about by confinement of the plasma [17]. These fast and slow components are similar to observations reported during studies of plasma expansion into a gas background where slower decay rates were observed as the pressure of the background gas was increased [18]. With additional background pressure, an increase in collision frequency occurs for electrons and ions resulting in an increase in ionisation, recombination and plasma emission [19], [20], [21]. As the plasma evolves under atmospheric pressure conditions, a fast and a slow component are observed in the electron density decay rate in air.

A rapid reduction in electron density is observed at early times ($<$ 500 ns) which is reflected in the differences in the decay terms "b" obtained from the double exponential fits (table 4.2). Values of -1.77 $\pm$ 0.37 μs^{-1} and -8.39 $\pm$ 2.25 μs^{-1} are extracted from fits for the fast decay term "b" using 8 mJ and 52 mJ pulses respectively. The physical consequence of higher values for the decay terms is a more rapid decline in electron density occurring for higher pulse energy. Values of -0.41 $\pm$ 0.26 μs^{-1} and 0.17 $\pm$ 0.03 μs^{-1} are obtained for decay terms "d" for 8 mJ and 52 mJ pulses respectively, which corresponds to the gradual decay observed in electron densities at later time delays. The contrast between fast and slow components (decay terms "b" and "d") being greatest in

the case of 52 mJ pulses provides further evidence that a much more rapid decay is occurring at higher pulse energy.

The corresponding results for electron temperatures are shown in figure 4.14 below where values of 1.10 ± 0.05 eV and 1.40 ± 0.07 eV are obtained at the earliest recorded measurements at 150 ns and 400 ns for pulse energies of 8 mJ and 52 mJ respectively.

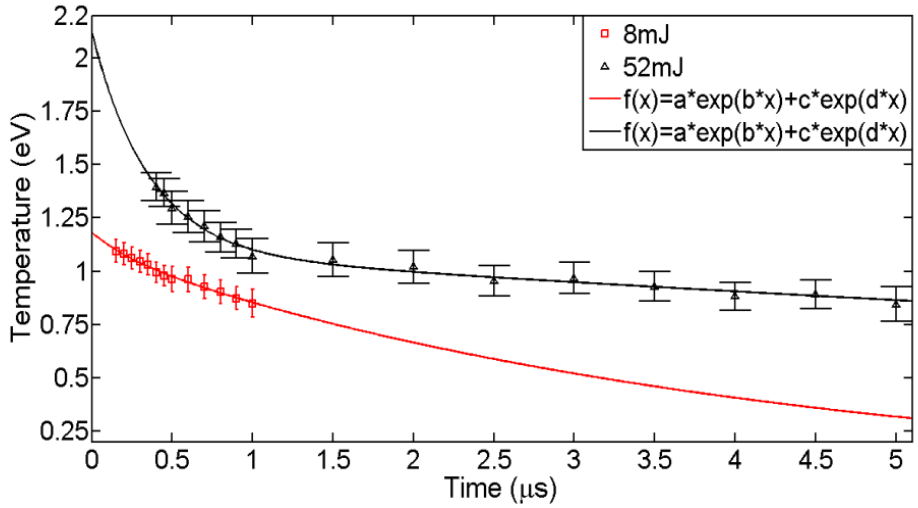

Figure 4.14: Electron temperatures for plasmas created with 1064 nm laser pulses with energies of 8 mJ and 52 mJ, obtained using a line ratio method. Shown also are the corresponding double exponential fits with $\bar{R}^2$ values of 0.99 and 0.99 respectively.

	a(eV)	b(μs^{-1})	c(eV)	d(μs^{-1})	$\bar{R}^2$
8mJ	0.09 ± 0.05	-4.08 ± 2.04	1.09 ± 0.13	-0.25 ± 0.11	0.98
52mJ	1.03 ± 0.24	-2.84 ± 0.57	1.09 ± 0.02	-0.05 ± 0.01	0.99

Table 4.3: Fitting parameters obtained using double exponential fit to electron temperature values obtained for plasmas formed by 1064 nm pulses (*cf.* corresponding figure 4.14).

Similar to the electron density trend with time delay, the temperature shows a more rapid decline in the 52 mJ case. Here a rapid reduction in the temperature is observed in the early phase (< 1 μs) with a reduced cooling rate occurring in the later stages. In the case of the 8 mJ pulses, the temperature decay appears almost like a single exponential. From the parameters obtained by double exponential fits (table 4.3) a much greater variation appears from the decay terms "b" and "d" for 52 mJ pulses. It

would appear that a more rapid rate de-excitation is occurring in the higher temperature plasma.

The results of electron densities and temperatures obtained for aluminium plasmas formed using 532 nm laser pulses are presented next. As in the case of the 1064 nm pulses, spectra were recorded at pulse energies of 8 mJ and 52 mJ. Double exponential fits were one again chosen as best fits to the data (in particular for data at times > 1 µs).

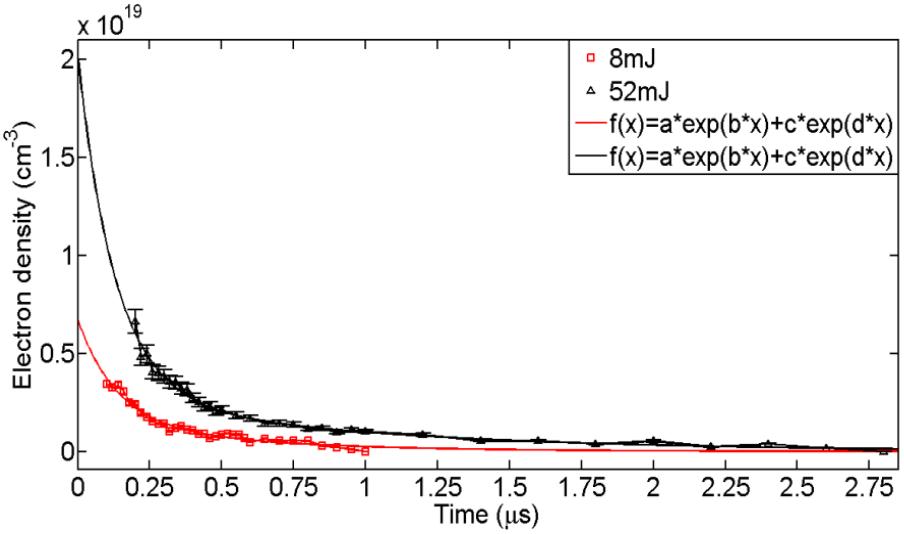

Figure 4.15: Electron densities obtained for plasmas formed using 532 nm laser pulses with energies of 8 mJ and 52 mJ. Shown also are the corresponding double exponential fits with $\bar{R}^2$values of 0.97 and 0.98 respectively.

	a(cm^{-3})	b(μs^{-1})	c(cm^{-3})	d(μs^{-1})	$\bar{R}^2$
8mJ	$5.03 \pm 0.13 \times 10^{18}$	-7.72 ± 4.24	$1.70 \pm 0.95 \times 10^{18}$	-1.92 ± 0.71	0.97
52mJ	$1.73 \pm 0.16 \times 10^{19}$	-7.74 ± 2.43	$2.91 \pm 0.51 \times 10^{18}$	-1.09 ± 0.34	0.98

Table 4.4: Fitting parameters obtained using double exponential fit to electron density values obtained for plasmas formed by 532 nm pulses (*cf.* corresponding figure 4.15).

Similar to observations using the 1064 nm laser, a sharp reduction in electron densities is seen in the earliest observable stages of line emission. Comparing the results of both laser wavelengths, (figure 4.13 and 4.15) although a similar rate of decay is observed in both, with comparable decay rates being obtained, a higher electron density is seen

using 532 nm pulses. At a delay of 0.5 µs, electron densities of 1.13 ± 0.1 $\times 10^{18}$ cm^{-3} and 2.13 ± 0.19 $\times 10^{18}$ cm^{-3} are obtained using 1064 nm, 52 mJ pulses and 532 nm, 52 mJ pulses respectively. A notable distinction between the two laser wavelengths is also apparent in the temperature measurements, with lower temperatures found using the 532 nm laser as shown in figure 4.16.

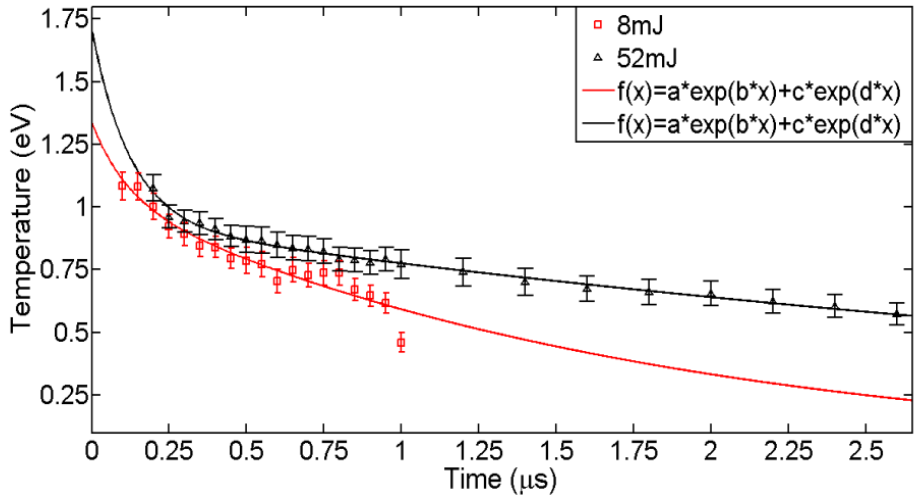

Figure 4.16: Temperatures obtained using 532 nm laser pulses with energies of 8 mJ and 52 mJ. Shown also are the corresponding double exponential fits with $\bar{R}^2$ values of 0.99 and 0.99 respectively.

	a(eV)	b(µs^{-1})	c(eV)	d(µs^{-1})	$\bar{R}^2$
8mJ	0.29 ± 0.16	-9.16 ± 4.29	1.05 ± 0.24	-0.58 ± 0.29	0.91
52mJ	0.77 ± 0.46	-8.07 ± 1.71	0.94 ± 0.02	-0.19 ± 0.02	0.99

Table 4.5: Fitting parameters obtained using double exponential fit to electron temperature values obtained for plasmas formed by 532 nm pulses (*cf.* corresponding figure 4.16).

Very little initial differences are found in the electron temperature using 8 mJ and 52 mJ pulses at early times. The earliest observable measurement yields a temperature of 1.08 ± 0.06 eV for both 532 nm pulses at time delays of 100 ns and 200 ns respectively. The departure between the two temperature decay curves varies more significantly as time progresses with values of 0.59 ± 0.04 eV and 0.77 ± 0.06 eV at a time delay of 1 µs post plasma ignition with the 8 mJ and 52 mJ laser pulses respectively. A comparison of

the "fast" decay term "b" for the two pulse energies indicates a similar decay rate at early times for temperatures greater than ~1 eV. At later times, a faster rate of cooling is observed for the 8 mJ plasma with "slow" decay term values of -0.58 ± 0.29 μs^{-1} and -0.19 ± 0.02 μs^{-1} being obtained for 8 mJ and 52 mJ pulses respectively. This apparent rapid decay at late delay times for the 8 mJ case may however be caused by the relative "poorness" of the fit to the experimental data with an $\overline{R}^2$ value of 0.91 being obtained.

For a laser produced plasma of intermediate electron density (around 10^{21} cm^{-3}) the ionisation balance of the plasma can be calculated using the collisional radiative equilibrium (CRE) model developed by Colombant and Tonan [22]:

$$f_z = \frac{n_{z+1}}{n_z} = \frac{S(z)}{\alpha_r(z+1) + n_e \alpha_{3b}(z+1)} \tag{4.4}$$

where f_z is the ratio of ion densities from one ion stage to the next, $S(z)$ is the collisional ionisation coefficient, $\alpha_r(z+1)$ is the radiative recombination coefficient and $\alpha_{3b}(z+1)$ is the three-body recombination coefficient. The ionisation balance describes the degree of ionisation present in the plasma as a function of temperature.

For a given electron density the solution to the model may be used to calculate the expected ion fractions of a laser produced plasma as a function of temperature. Using a fixed electron density of 10^{18} cm^{-3} (the approximate electron density found from present measurements) the ion fractions for an aluminium plasma were calculated using equation 4.4, the results of which are shown in figure 4.17.

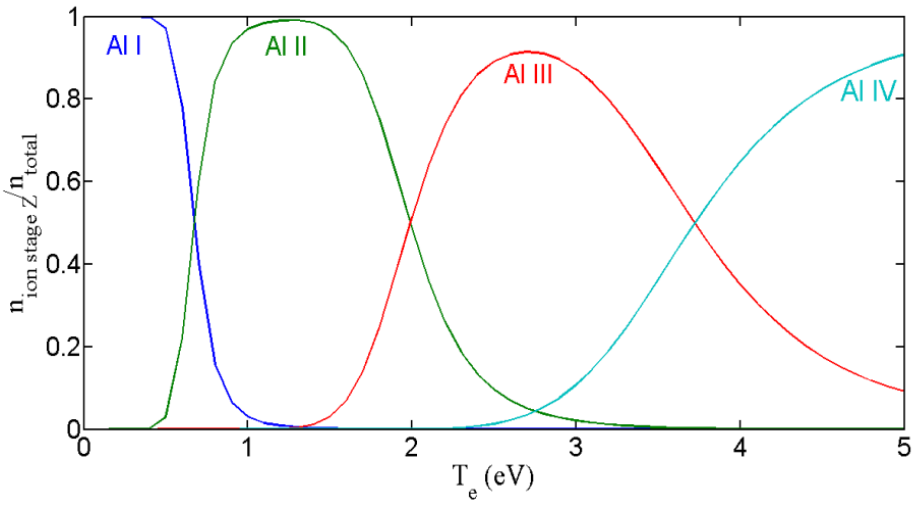

Figure 4.17: Ion fraction as a function of electron temperature (T_e) in an aluminium plasma calculated using the Colombant and Tonan CRE model [22].

For low temperatures, the ionisation balance is largely dominated by neutral species. As the temperature increases, the number of ions present in the plasma increases with higher charge states appearing. An estimate of the electron temperature of the plasma can be obtained by comparing spectra obtained in present measurements with figure 4.17. Al(III) emission was the highest ion stage observed in laser produced plasmas recorded in ambient air which places an upper limit of ~2.2 eV for the electron temperature. This is in line with experimentally determined temperature measurements (figure 4.14 and 4.16) which do not exceed 2.2 eV. By looking at the general trends observed in time resolved spectra recorded using 1064 nm and 532 nm pulses, a qualitative comparison can be made with the trends expected by the CRE model. In plasma emission spectra recorded using 1064 nm pulses (figure 4.4 (a), 4.5 (a) and 4.6 (a)) the dominant emission of each species appears at different delay times with respect to the laser pulse. For 1064 nm, 52 mJ pulses, the peak emission of A(III), Al(II) and Al(I) species occurs at time delays of 100 ns, 500 ns and 5 µs respectively. This result agrees with the behaviour predicted by the CRE model where higher charge states exist at higher electron temperatures. From figure 4.17, for a fixed electron density of 10^{18} cm^{-3}, a maximum in the fraction of Al(II) present in the plasma occurs at a temperature just above 1 eV. This is in general agreement with the trends observed from

experimentally determined temperatures of *ca.* 2 eV, 1.25 eV and 1 eV are observed at delay times of 100 ns, 500 ns and 1 µs respectively, corresponding to maximum emission intensities of Al(I), Al(II) and Al(III) species. For the case of aluminium plasma created using 532 nm pulses, slightly higher electron densities and lower electron temperatures were observed. The strongest recorded emission intensities of plasma species present occurred at earlier delay times than those spectra recorded using 1064 nm pulses with maximum emission observed at delays of 100 ns, 200 ns and 500 ns for Al(III), Al(II) and Al(I) respectively (figure 4.4 (b), 4.5 (b) and 4.6 (b)). Equation 4.4 predicts a large contribution from 3-body recombination as the electron density increases. This results in a lower fractional contribution from higher charge states at a given temperature. This may explain the ionic emission occurrence at shorter delay times post plasma ignition and the slightly shorter emission lifetimes observed for all species using 532 nm pulses.

4.5 Summary

Results from time resolved imaging experiments show rapid plume expansion in the initial phases, followed by a plateau region reached at later times. This plateau appears to be reached at earlier times using low laser pulse energy values (few mJ). The laser-induced compressive shock-front was studied as a function of laser pulse energy using shadowgraphy. Similar to the results of imaging of the plasma plume, a rapid expansion of the shock-front is seen at the earliest observable times. With increasing laser pulse energy, a more rapid expansion is found for the shockwave evolution. As time progresses (to *ca.* 1 µs) the shock-front appears more diffuse as it loses energy through collisions with the surrounding gas molecules. As the energy of the shockwave dissipates with time, the evolution begins to approximate a linear expansion, at approximately several microseconds after plasma breakdown at the laser focus. The shockwave expansion shows good agreement with the point-explosion or shockwave expansion model. By applying the shockwave expansion model to the experimental data, a planar expansion is revealed for shockwaves at low laser pulse energy. The behaviour of the shockwave is

found to transition to an approximately cylindrical expansion at higher laser pulse energies. The physical implication of this finding is that as the pulse energy increases, the lateral contribution to the overall shockwave expansion becomes greater. The shock-front expansion appears to be independent of the target material.

Spectroscopic measurements of aluminium in air reveals significant emission contributions from atmospheric species, namely from singly ionised nitrogen and oxygen. A comparison of spectra recorded using 1064 nm and 532 nm laser pulses was carried out which revealed subtle difference in time resolved spectra. For atomic aluminium emission, very similar spectra are obtained at both laser wavelengths with neutral emission persisting in both cases for approximately 50 µs. For aluminium ions however, optical emission is observed to persist longer in plasmas created with 1064 nm laser pulses compared to those formed with the second harmonic of the Nd:YAG laser used. This is considered to be an effect related to the strength of the continuum emission in spectra recorded from plasmas produced using the 1064 nm laser. Firstly, due to the higher plasma temperature, early phase continuum emission is observed to persist longer in the case of plasmas formed using 1064 nm pulses so that the emergence of discrete line emission, observable above the background continuum, is delayed compared to the 532 nm case. As a consequence, the ionic species appear at earlier times in the 532 nm spectra. However, with an initially lower temperature, emission from ions in plasmas created with 532 nm pulses dies away sooner than for plasmas formed with 1064 nm pulses since the rate of electron excitation depends on plasma temperature. Relatedly it should also be noted that the average ionization stage will be higher for plasmas created with 1064 nm pulses. Hence, at later stages of plasma expansion, when recombination is an important process, these plasmas will have higher ion stages for longer as a consequence and hence line emission from lowly charged ions should persist for longer times than for plasmas formed by 532 nm pulses. Evidence of Stark-shifting of emission lines is observed for plasmas created using both laser wavelengths. Larger Stark-shifts are observed using 532 nm pulses indicating higher electron densities arising within the plasma. This result is further supported by electron

densities determinations from Stark-broadened linewidth measurements on emission line profiles for plasmas formed using both laser wavelengths.

Early phase molecular H_β emission at 486.13 nm is apparent several microseconds after the plasma breakdown for plasmas generated by laser pulses at both wavelengths. The appearance of a broad spectral feature occurring at a wavelength of *ca.* 452 nm can be seen in emission spectra recorded using 532 nm pulses. This feature is attributed to the contributions of several Al(III) lines which appear blended resulting in the appearance of a broad spectral feature. Emission of these Al(III) lines appears relatively briefly, at time delays of roughly 100-200 ns after plasma formation and are not apparent in spectra recorded using 1064 nm pulses. These spectral features were also apparent during pump-probe experiments using the OPO laser and are discussed in further detail in chapter 5.

Average electron densities of approximately $1\times10^{18}\,cm^{-3}$ and $2\times10^{18}\,cm^{-3}$ are obtained using 1064 nm and 532 nm pulses respectively. In both cases, higher electron densities are found using higher energy pulses. Evidence of a rapid initial decay followed by a more gradual decay at late delay times was observed at both laser wavelengths. This behaviour was attributed to a "fast" and "slow" component in the evolution of the electron density due to the relatively high pressure experienced by the plasma in atmospheric conditions. A more rapid rate of decay was observed using higher pulse energies suggesting a greater decay rate of excited species occurring for plasmas formed using 52 mJ pulses.

The electron density will depend strongly on the coupling of the laser radiation with the target. The reflectivity of radiation from the metallic surface plays a significant role in this coupling. Reflectivity depends on thermal conductivity, roughness and laser wavelength. For the case of aluminium, the reflectivity at 1064 nm and 532 nm is ~0.95 and 0.92 respectively [25], [27]. After the initial formation of the plasma, more radiation is then reflected from the target surface for pulses of longer wavelength and available for absorption by the plasma. The decay of electron density occurs largely through recombination interactions between electrons and ions. Electron generation can occur by

competing processes of electron impact ionization and photoionisation. If the recombination time constant is comparable to the laser pulse duration, an electron generated by ionization can effectively contribute to the IB absorption [25]. In aluminium an approximate value of < 1 ns can be obtained for the electron impact ionization time constant in aluminium [25], [28], [29]. A pulse duration of ~5 ns was used during this work, which is sufficiently large for an increased rate of ionisation during the laser pulse due to electron-ion collisions. Having a higher photon energy (2.31 eV compared to 1.17 eV), the rate of photoionisation will be greatest for 532 nm laser pulses and hence a greater electron density is apparent from the calculations.

Electron temperatures are found to increase as a function of increasing laser pulse energy as expected. Higher pulse energies are also associated with increased mass ablations rates [23] which produces a greater intensity in line emission strength and therefore an increase in plasma temperatures. A slightly higher rate of cooling was observed from temperature measurements obtained using 532 nm pulses, while the 1064 nm pulses appear to produce a higher temperature plasma. This difference in observed temperature is related to the plasma shielding that occurs at each laser wavelength and has been reported in aluminium for the same laser wavelengths used during this work [24], [25]. As the laser pulse impinges on the target surface, seed electrons are produced via photoionisation and multi-photon ionisation. Continued absorption of the trailing edge of the laser pulse results in the formation of more highly ionised species through collisions with ground state and excited atoms. Absorption of the laser pulse occurs through the inverse Bremsstrahlung process. IB absorption can be estimated by the following expression

$$\alpha_{IB}(cm^{-1}) \approx 1.37 \times 10^{-35} \lambda^3 n_e^2 T_e^{-\frac{1}{2}} \tag{4.5}$$

Where λ (µm) is the laser wavelength, T_e (K) is the electron temperature and n_e (cm^{-3}) is the electron density [26]. Due to the λ^3 dependence, a much greater absorption of 1064 nm pulses occurs. The temperature begins to drop with time as the plasma expands with thermal energy being converted to kinetic energy of plasma species. This

temperature dependence of the plasma as a function of wavelength explains the stronger continuum emission observed using 1064 nm pulses due to both free-free and free-bound processes.

References

[1] D. A. Freiwald and R. A. Axford, "Approximate spherical blast theory including source mass," *J. Appl. Phys.*, vol. 46, no. 3, p. 1171, 1975.

[2] B. Kumar and R. K. Thareja, "Synthesis of nanoparticles in laser ablation of aluminum in liquid," *J. Appl. Phys.*, vol. 108, no. 6, p. 64906, 2010.

[3] A. E. Hussein, P. K. Diwakar, S. S. Harilal, and A. Hassanein, "The role of laser wavelength on plasma generation and expansion of ablation plumes in air," *J. Appl. Phys.*, vol. 113, no. 14, p. 143305, 2013.

[4] Tanski M., Barbucha R., Kocik M., Garasz K., and Mizeraczyk J., "Diagnostics of UV Laser Generated Plasma Plume Dynamics in Ambient Air Using Time-Resolved Imaging," *Przegląd Elektrotechniczny*, vol. 88, no. 8, 2012.

[5] S. S. Harilal, C. V. Bindhu, M. S. Tillack, F. Najmabadi, and A. C. Gaeris, "Plume splitting and sharpening in laser-produced aluminium plasma," *J. Phys. Appl. Phys.*, vol. 35, no. 22, pp. 2935–2938, Nov. 2002.

[6] S. S. Harilal, C. V. Bindhu, M. S. Tillack, F. Najmabadi, and A. C. Gaeris, "Internal structure and expansion dynamics of laser ablation plumes into ambient gases," *J. Appl. Phys.*, vol. 93, no. 5, p. 2380, 2003.

[7] "NIST Atomic Spectra Database," *http://physics.nist.gov/asd.* .

[8] R. Fabbro, E. Fabre, F. Amiranoff, C. Garban-Labaune, J. Virmont, M. Weinfeld, and C. E. Max, "Laser-wavelength dependence of mass-ablation rate and heat-flux inhibition in laser-produced plasmas," *Phys. Rev. A*, vol. 26, no. 4, pp. 2289–2292, Oct. 1982.

[9] F. Dahmani, "Experimental scaling laws for mass-ablation rate, ablation pressure in planar laser-produced plasmas with laser intensity, laser wavelength, and target atomic number," *J. Appl. Phys.*, vol. 74, no. 1, p. 622, 1993.

[10] Wang F., Chen L., and Wu J.Y., "Characteristics of Plasma and Detonation Waves Induced on an Aluminium Target by Nanosecond Laser Ablation," *Lasers Eng.*, vol. 29, pp. 133–154, 2014.

[11] M. Hauer, D. J. Funk, T. Lippert, and A. Wokaun, "Time resolved study of the laser ablation induced shockwave," *Thin Solid Films*, vol. 453–454, pp. 584–588, Apr. 2004.

[12] C. Porneala and D. A. Willis, "Time-resolved dynamics of nanosecond laser-induced phase explosion," *J. Phys. Appl. Phys.*, vol. 42, no. 15, p. 155503, Aug. 2009.

[13] P. Gregorčič, J. Diaci, and J. Možina, "Two-dimensional measurements of laser-induced breakdown in air by high-speed two-frame shadowgraphy," *Appl. Phys. A*, vol. 112, no. 1, pp. 49–55, Jul. 2013.

[14] S. H. Jeong, R. Greif, and R. E. Russo, "Propagation of the shock wave generated from excimer laser heating of aluminum targets in comparison with ideal blast wave theory," *Appl. Surf. Sci.*, vol. 127–129, pp. 1029–1034, May 1998.

[15] N. Konjevic and W. L. Wiese, "Experimental Stark widths and shifts for non-hydrogenic spectral lines of ionized atoms," *J. Phys. Chem. Ref. Data*, vol. 5, no. 2, p. 259, 1976.

[16] N. Konjević, M. S. Dimitrijević, and W. L. Wiese, "Experimental Stark Widths and Shifts for Spectral Lines of Neutral Atoms (A Critical Review of Selected Data for the Period 1976 to 1982)," *J. Phys. Chem. Ref. Data*, vol. 13, no. 3, p. 619, 1984.

[17] P. Hough, C. McLoughlin, T. J. Kelly, S. S. Harilal, J. P. Mosnier, and J. T. Costello, "Time resolved Nomarski interferometery of laser produced plasma plumes," *Appl. Surf. Sci.*, vol. 255, no. 10, pp. 5167–5171, Mar. 2009.

[18] C. Colón, G. Hatem, E. Verdugo, P. Ruiz, and J. Campos, "Measurement of the Stark broadening and shift parameters for several ultraviolet lines of singly ionized aluminum," *J. Appl. Phys.*, vol. 73, no. 10, p. 4752, 1993.

[19] S. Amoruso, J. Schou, and J. G. Lunney, "Multiple-scattering effects in laser ablation plume propagation in gases," *Europhys. Lett. EPL*, vol. 76, no. 3, pp. 436–442, Nov. 2006.

[20] J. Gonzalo, F. Vega, and C. N. Afonso, "Plasma expansion dynamics in reactive and inert atmospheres during laser ablation of Bi(2)Sr(2)Ca(1)Cu(2)O(7−y)," *J. Appl. Phys.*, vol. 77, no. 12, p. 6588, 1995.

[21] R. K. Singh, A. Kumar, B. G. Patel, and K. P. Subramanian, "Role of ambient gas and laser fluence in governing the dynamics of the plasma plumes produced by laser blow off of LiF–C thin film," *J. Appl. Phys.*, vol. 101, no. 10, p. 103301, 2007.

[22] D. Colombant and G. F. Tonon, "X-ray emission in laser-produced plasmas," *J. Appl. Phys.*, vol. 44, no. 8, p. 3524, 1973.

[23] R. E. Russo, X. L. Mao, H. C. Liu, J. H. Yoo, and S. S. Mao, "Time-resolved plasma diagnostics and mass removal during single-pulse laser ablation," *Appl. Phys. Mater. Sci. Process.*, vol. 69, no. 7, pp. S887–S894, Dec. 1999.

[24] H. Hegazy, E. AlAshkar, H. H. Abou-Gabal, M. N. Aly, and N. Hamed, "Spectroscopic Evolution of Plasma Produced by Nd-YAG Laser," *IEEE Trans. Plasma Sci.*, vol. 42, no. 6, pp. 1674–1684, Jun. 2014.

[25] N. M. Shaikh, S. Hafeez, B. Rashid, and M. A. Baig, "Spectroscopic studies of laser induced aluminum plasma using fundamental, second and third harmonics of a Nd:YAG laser," *Eur. Phys. J. D*, vol. 44, no. 2, pp. 371–379, Aug. 2007.

[26] J. J. Chang and B. E. Warner, "Laser-plasma interaction during visible-laser ablation of methods," *Appl. Phys. Lett.*, vol. 69, no. 4, p. 473, 1996.

[27] Chemical Rubber Company and D. R. Lide, Eds., *CRC handbook of chemistry and physics: a ready-reference book of chemical and physical data*, 84th ed. Boca Raton: CRC Press, 2003.

[28] S. Amoruso, M. Armenante, V. Berardi, R. Bruzzese, and N. Spinelli, "Absorption and saturation mechanisms in aluminium laser ablated plasmas," *Appl. Phys. Mater. Sci. Process.*, vol. 65, no. 3, pp. 265–271, Sep. 1997.

[29] W. B. Zel'dovich and Raizer, Y.P., *Physics of Shock Waves and High-Temperature Hydrodynamic Phenomena*, Academic Press, New York. 1966.

Chapter 5

Optical Emission Spectroscopy of AlO in Air

In the previous chapter the characteristic emission of aluminium plasmas was studied during the different phases of the plasma lifetime in ambient air; from plasma ignition and prompt continuum emission to the later line emission phases. The focus of this chapter is the study of the very late stages of the plasma lifetime in air, beyond the relatively early atomic and ionic line emission phase, using optical emission spectroscopy at delay times of tens of microseconds. During this condensation phase, the appearance of molecular aluminium monoxide (AlO) emission was observed and subsequently investigated. The origin of molecular species during laser ablation may be brought about by recombination of atomic species present in the plasma, and also by removal of molecules excited by the laser matter interaction [1]. Using 1064 nm wavelength pulses, the observation of AlO becomes apparent several hundred microseconds after the aluminium plasma formation in air. AlO exhibits strong vibrational excitations in the blue-green visible region between 440-550 nm. This band is referred to as the B-X system of AlO [2]. Time resolved optical emission spectroscopy was used to study the vibrational AlO emission structure. Using a freely available diatomic molecular computation model, temperatures were extracted from vibrational emission spectra of the $X^2\Sigma^+$ - $B^2\Sigma^+$ states of the AlO molecule over the observable emission lifetime. The

study of molecular spectra are of particular interest in LIBS experiments where measurements are in general limited to the relatively short lifetimes of emission lines [3]. The determination of temperatures by molecular emission spectroscopy provides a means in which to study plasma parameters when line emission is no longer available.

A series of experiments were carried out using a wavelength tuneable optical parametric oscillator (OPO) to deliver a second laser pulse to the plasma during the condensation phase. Using a 1064 nm pre-pulse for plasma formation and the OPO pulse as a time synchronised re-heating pulse, a series of experiments were carried out to probe (i) early phase ionic species and (ii) late phase molecular aluminium oxide. During the early phase studies, the re-heating OPO pulse was set at wavelengths of 430 nm, 466 nm and 484 nm to study the effect of tuning the re-heating pulse to wavelengths corresponding to an ionic emission lines (at 466.3 nm) in the early stages of the plasma lifetime and subsequently tune to the central emission band of the later phase AlO molecules (at 484 nm). The OPO pulse was delivered to the plasma at a fixed time delay of 500 ns for these early phase measurements. For the later phase studies, the time between the pre-pulse and re-heating pulse was varied and the wavelength of the OPO output was fixed at 484 nm corresponding to the central vibrational AlO bandhead of the B-X system ($\Delta v = 0$). A series of measurements were then carried out to probe the AlO during different phases of the visible emission lifetime. By varying the time between the first and second pulses (termed the inter-pulse delay time), a series of spectroscopy measurements were carried out to investigate the effect of the re-heating pulse during different phases of the AlO lifetime.

5.1 Molecular Emission

Using optical emission spectroscopy, vibrational excitations in diatomic AlO were studied using a 30 mJ, 1064 nm pulse and a 500 ns ICCD gate width. Chapter 4 presented measurements of atomic emission spectra using an aluminium target under

atmospheric conditions. For ionic species, this emission occurred over lifetimes of several hundred nanoseconds. The emission from diatomic vibrational transitions occurs over a comparatively longer duration on the order of tens of microseconds for the experimental conditions described here. Similar to previous measurements, the spectra were recorded in single shot mode refreshing the target position with each laser pulse to avoid cratering effects. The first several hundred nanoseconds following breakdown in the spectral region of interest is dominated by the hydrogen Balmer beta (H_β) line emission profile at 486.13 nm. The appearance of atomic hydrogen emission is associated with plasma formation in atmosphere due to the presence of water vapour. The precise time at which the AlO emission may be observed is complicated by the superposition of the H_β emission as spectra recorded are spatially integrated due to optical collection via fibre optic. Figure 5.1 demonstrates the observed emission in the first 6 µs after the laser pulse is fired.

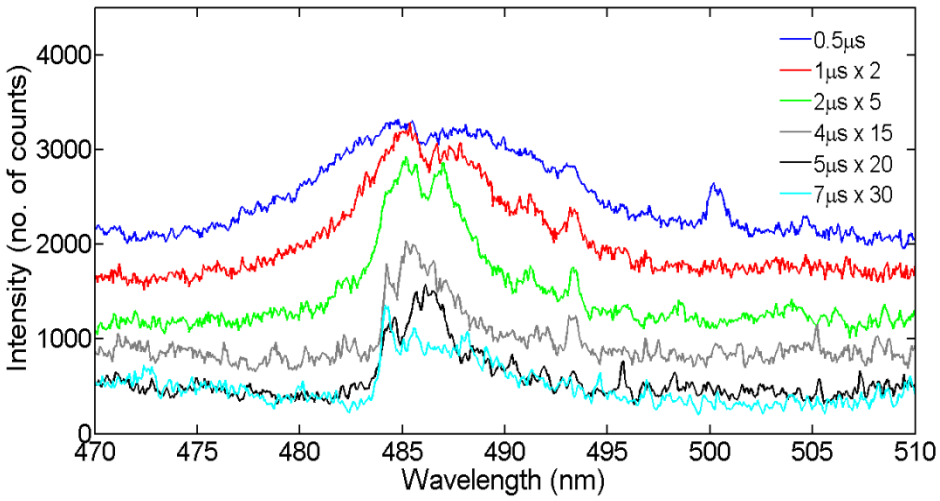

Figure 5.1: Time resolved emission spectra of H_β in air using a 500 ns ICCD gate width and 30 mJ, 1064 nm pulses. Early phase plasma emission in this spectral region is dominated by the H_β emission.

The H_β emission appears as two broad spectral peaks in the recorded spectra with a peak separation of roughly 0.5 nm as seen in figure 5.1. This asymmetry in profile can also be used in the determination of the electron density [4], [5], [6]. This study of optical breakdown of gaseous H_2 using laser pulses has been investigated since the mid-

sixties [7] and has been well documented in many studies since then [8], [9], [10]. H_β emission spectra are used during this work to estimate electron densities the results of which are shown in section 5.2. At 7 µs the AlO emission begins to dominate recorded spectra. The characteristic edges of the $\Delta\nu = -1, 0, 1$ band heads are clearly observed at 7 µs. These are ground state transitions within the AlO molecule occurring at wavelengths of 464.82 nm, 484.21 nm and 507.93 nm respectively [11].

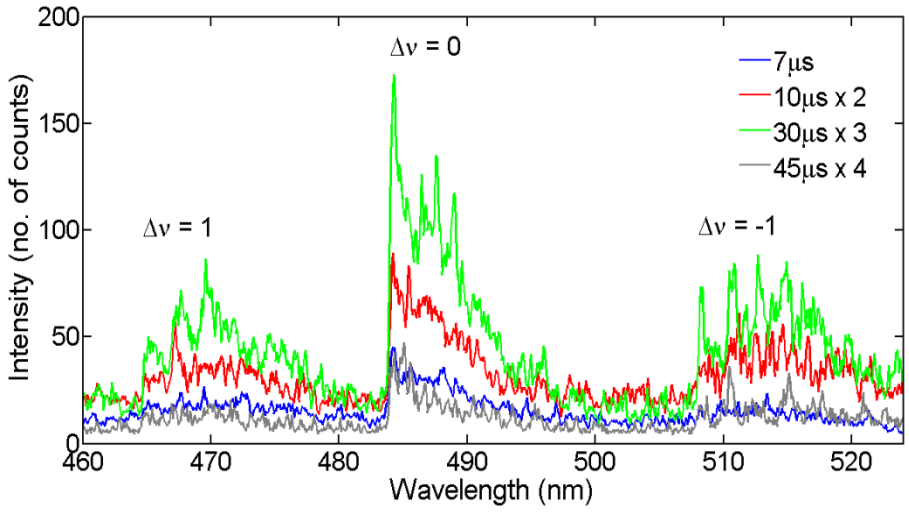

Figure 5.2: Time resolved spectra recorded using 30 mJ, 1064 nm pulses and an ICCD gate width of 500 ns. Spectra demonstrate the vibrational bandhead emission in the blue-green wavelength region indicating the presence of monatomic aluminium oxide over the observable emission lifetime.

Molecular emission was observed up to a delay time of 45 µs using a 30 mJ, 1064 nm pulse. Emission from the $\Delta\nu = -1, 0, 1$ vibrational bands is clearly discernable after a delay of 10 µs. While the sharp edge of the $\Delta\nu = 0$ band is clearly visible in the early phases of molecular emission, the structure of the individual transitions within the vibrational bands appears washed away due to high density broadening effects.

The study of the AlO band emission using a single 30 mJ, 1064 nm pulse revealed different phases of molecular emission over the observable emission lifetime. Diagnosing the characteristic behaviour of the AlO molecule from the single pulse case revealed information on the conditions of the plasma during the times i.e., between delay times of 7-45 µs post plasma ignition. This information was used to inform the timing of

subsequent re-heating experiments. From time resolved emission spectra estimates on the electron densities could be determined in the early stages of the plasma lifetime. Estimations of molecular temperatures could also be inferred from the recorded spectra, the results of which are presented in the following section.

5.2 Temperature and Density Calculations

The emission spectra from the H_β line can be used to infer electron densities in the first several microseconds of early observable emission. The determination of electron densities from the hydrogen Balmer lines and H_β line (486.13 nm) emission in particular is a well-established technique of estimating electron densities [12], [13], [14]. Due to the broad emission profile, electron density calculations using the Stark broadened H_β line is considered the more accurate choice of hydrogen line in the Balmer series for electron density determination [5], [15], [16]. However due to the superposition of the H_β with the AlO emission, densities were deemed unreliable at time delays beyond 6.5 µs. Using the Stark halfwidth of the H_β line, an approximate formula is used to deduce the electron density (cm^{-3}) given by [17], [18]:

$$n_e = 10^{16}\left(\frac{w_s}{0.94666}\right)^{1.49} \tag{5.1}$$

where w_s is the FWHM (nm) of the Stark contribution (Lorentzian component) to the experimental profile. Figure 5.3 shows an example of the experimentally obtained H_β spectra recorded at 2 µs and the corresponding fit of the asymmetric peak profile.

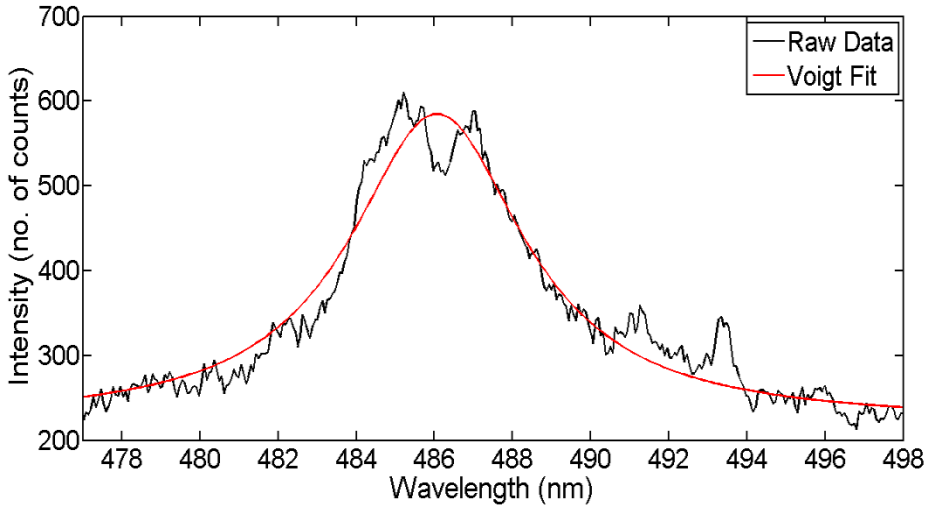

Figure 5.3: An example of the peak fitting procedure applied to the H_β profile using the AAnalyzer software. Figure shows a single Voigt profile fit to experimental data used to estimate the electron density.

Figure 5.4 shows the evolution of the electron density measured from the H_β profile where a rapid decrease in electron density is apparent at early delay times followed by a more gradual decay at later times.

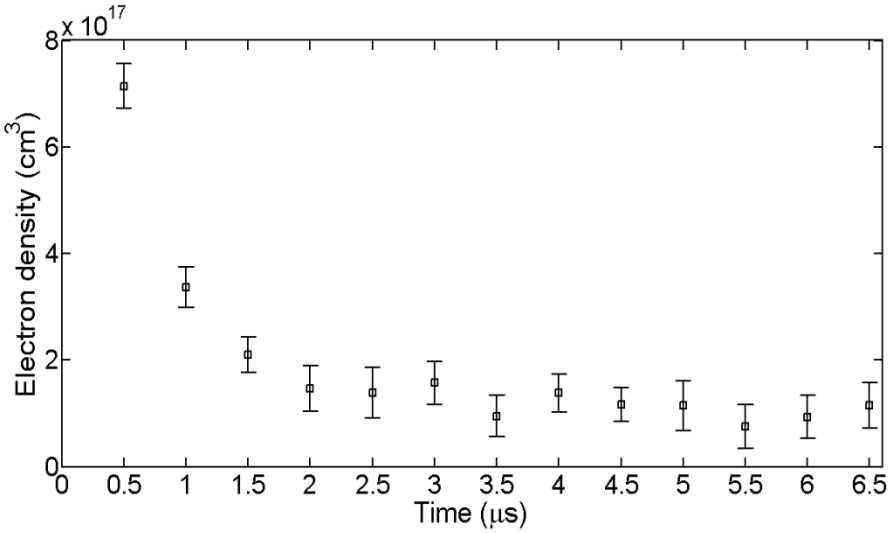

Figure 5.4: Electron densities calculated using the H_β emission Stark widths from time resolved spectra recorded using 30 mJ, 1064 nm pulses and an ICCD gate width of 500 ns.

The instant at which the AlO emission begins to dominate recorded spectra occurs at a delay time of *ca.* 7 µs. This was defined as the time at which the H_β emission is

sufficiently supressed such that AlO emission becomes the dominant spectral feature. This was further evidenced by the computational model fits. The AlO emission spectra were fit to a computational model to extract temperatures. At times earlier than 7 µs, the goodness of the fit was severely affected by the presence of the H_β line resulting in large residuals and unrealistic temperature estimates.

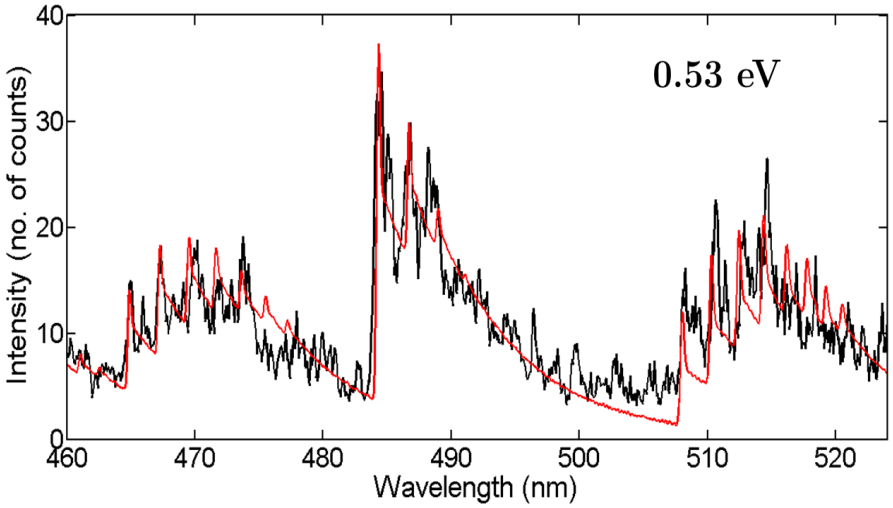

Figure 5.5: Demonstrates the experimental spectrum of AlO emission at a time delay of 10 µs and corresponding computational fit used to estimate the temperature.

The temperatures of the most intense vibrational AlO transitions ($\Delta v = -1, 0$ and 1) were estimated using a program described by Paringger *et al.* [1]. The model computes temperatures using a list of known diatomic line strengths and compares them to experimental data. The tables of known line strengths are used to generate spectra as a function of temperature and spectral resolution. An algorithm is then employed to determine the temperature by minimising the discrepancy between the computed and experimentally recorded emission spectrum using a least squares method. For a pulse duration $\leq$ 10 ns, temperatures within the molecular ensemble tend to equilibrate meaning that the vibrational temperature T_v = rotational temperature T_r = gas temperature T [1]. An example of the computational model in operation is shown in figure 5.5 where the molecular spectrum obtained at a delay of 10 µs post plasma ignition is shown. Good agreement is found between the theoretical and experimental spectra where a temperature of 0.53 $\pm$ 0.04 eV is obtained from the model fit. The

goodness of the experimental fit to the theoretical fit can be estimated from the difference spectrum. Temperatures were extracted from the model fits over the observable emission lifetime of the AlO molecule (at delay times of 7-45 µs) the results of which are shown in figure 5.6.

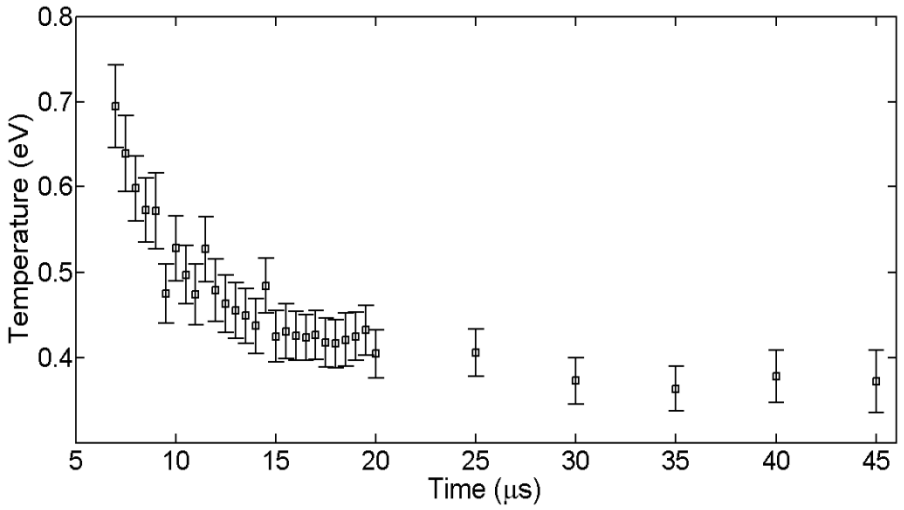

Figure 5.6: Gas temperatures extracted from fits to experimentally obtained AlO spectra using 30 mJ, 1064 nm pulses.

In the first few microseconds post formation, the gas ensemble experiences a rapid decrease in temperature until a plateau is reached approximately 15 µs after the laser pulse arrival at the target. Vibrational temperatures of 0.69-0.53 eV were extracted at time delays of 7-10 µs respectively. After this point a very slow decrease in temperature takes place for the remainder of the vibrational emission lifetime. At delay times > 10 µs this behaviour transitions to a lower rate of cooling with temperatures reaching *ca.* 0.4 eV in this late phase.

The system was analysed from a thermodynamic perspective in an attempt to understand the different phases of AlO emission. The two main pathways of AlO formation are given by: [3], [19]

$$Al + O_2 \rightleftharpoons AlO + O \tag{5.2}$$

$$Al + O \rightleftharpoons AlO \tag{5.3}$$

which compete with molecular oxygen formation via recombination of atomic oxygen, i.e.

$$O + O \rightleftharpoons O_2 \tag{5.4}$$

The dominant direction of these reversible reactions is determined by the Gibbs free energies of the reactions which are temperature dependant. The change in the Gibbs free energy of a reaction, ΔG, is given by:

$$\Delta G = \sum \Delta G_{products} - \sum \Delta G_{reactants} \tag{5.5}$$

The sign of ΔG indicates the energetically favoured direction of these reversible reactions, i.e. whether the reaction taking place is endothermic or exothermic in nature. Using ideal gas thermochemical tables [20] the Gibbs free energy, G, of the above reactions can be evaluated for a temperature range between 0-0.52 eV. The Gibbs free energies of the above equations (5.2, 5.3 and 5.4) were calculated as a function of temperature for the forward (molecular formation) and reverse (molecular dissociation) directions and are shown in figure 5.7.

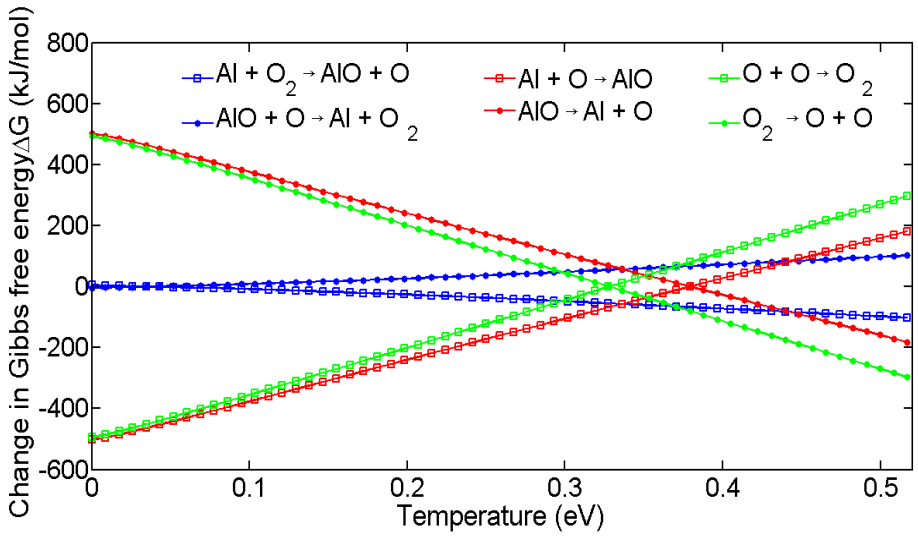

Figure 5.7: Calculations of the change in the Gibbs free energy of the AlO formation/dissociation and related O_2 formation/dissociation reactions as a function of temperature.

At high temperatures > 0.5 eV, the forward direction of AlO is proceeds via equation 5.2 where a value of *ca.* -100 kJ/mol is obtained for the Gibbs free energy of the AlO formation reaction. At the same temperature, the opposite trend is found for equations 5.3 and 5.4 in the forward directions where positive values are retrieved for the Gibbs free energies of the reactions meaning energy is required for the reaction to take place. As the gas cools, the energetically favourable direction of reaction 5.2 and 5.3 reverses, according to figure 5.7 at temperatures of 0.38 eV and 0.30 eV respectively. Now the formation of AlO takes place via equation 5.2 and equation 5.3 with the formation of molecular oxygen also being favoured at these temperatures. The forming of AlO by equation 5.2 is termed formation "channel 1" and formation via equation 5.3 is termed "channel 2" for ease of reference henceforth.

The delay in the onset of dominant AlO emission observable during laser plasma emission is related to the reactions described by equations 5.2 and 5.3 [3]. The formation of AlO occurs initially via channel 1 at early times in the plasma lifetime where temperatures exceeding 1 eV are typical. At these temperatures, strong dissociation occurs via channel 2 meaning two competing reactions are taking place at high temperature. The delay in significant AlO emission is thought to be related to these competing processes with dissociation of the AlO via equation 5.3 occurring at a greater rate than the formation channel via equation 5.2. As the plasma cools to temperatures <0.44 eV, the rate of AlO formation via channel 1 becomes greater than the rate of dissociation via channel 2. This may be considered a critical temperature in the scheme of competing reactions which are taking place. An increase in the number of AlO species present in the gaseous ensemble should then be expected below this temperature as a result. Below the equilibrium temperature of equation 5.3 at 0.38 eV, the reaction reverses direction and AlO formation is expected to occur via both channels. From the temperatures estimates extracted from fits to the computational model (figure 5.6), the temperature approaches 0.4 eV at delay times > 15 µs. This coincides with the observation of strong emission and fine structure of the individual transitions in the AlO band emission profile apparent from recorded spectra (figure 5.2).

The integrated intensity over the entire observable AlO band emission (460-524 nm) is shown in figure 5.8.

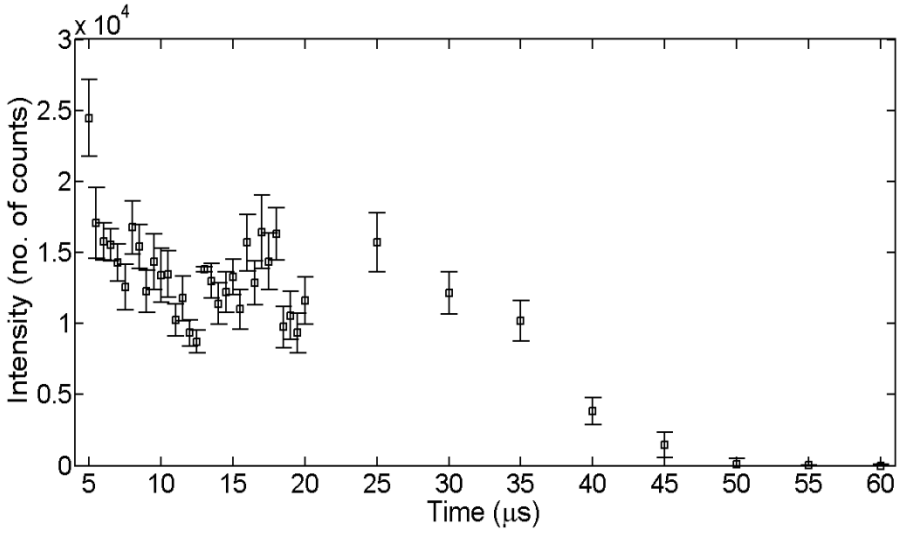

Figure 5.8: Integrated intensity of time resolved AlO spectra (from figure 5.2) recorded using 30 mJ, 1064 nm pulses and an ICCD gate width of 500 ns.

While the temperature is seen to continually decrease as a function of delay time from figure 5.6 (most significantly for time delays < 10 µs), no decrease is observed in the emission strength of the AlO (figure 5.8) which appears to fluctuate at certain periods over the observable emission lifetime. The trend appears to undergo a series of oscillations at delay times *ca.* 12 µs and 20 µs. This repeated recovery of the emission intensity may be explained by the temperature dependent trends (or dominant reaction direction) described by equation 5.3. The first elevation (12 µs) in emission intensity may occur by a reduction in the rate of AlO dissociation which is expected to occur at a temperature of *ca.* 0.44 eV from calculations of the Gibbs free energy. As the temperature of the ensemble cools even further, a second broad peak in the emission intensity is observed (centred at *ca.* 20 µs) which may be attributed to the AlO formation channel described by equation 5.3, predicted to occur at temperatures below 0.38 eV. These trends appear to confirm the behaviour expected by the Gibbs free energy calculations.

According to estimates from computational model fits (figure 5.6), the time at which the temperature of the gas falls below the critical value of 0.44 eV should occur at a time delay of *ca.* 15 µs. Values of 0.47 ± 0.04 eV and 0.40 ± 0.03 eV are found from temperature estimates at delay times of 12 µs and 20 µs respectively. These estimates largely correspond to the trends expected from the Gibbs free energy calculations where strong AlO formation via the two possible reaction pathways is expected at a delay time of *ca.* 20 µs. While a good level of agreement is found, the temperatures estimated by the computational model appear to be slightly overestimated in comparison to the trends expected by the Gibbs free energy calculations. From the increase in emission intensity the enhancement in AlO emission is expected from the experimental data to occur at a time delay of *ca.* 10-12 µs.

From the recorded emission spectra and corresponding temperature measurements it is evident that the AlO reaction pathways are changing as a function of temperature with AlO formation becoming more energetically favourable as the temperature of the gas cools. By examining the different reactions taking place it is clear that routes to AlO production in a laser produced plasma are complicated by competing processes which delay the onset of dominant AlO formation and change the contribution of AlO species to the overall ensemble as a function of the gas temperature.

5.3 Re-heating of Early Phase Plasma Species

By delivery of a second laser pulse to the plasma during the late condensation phase, a series of so-called "re-heating" measurements were carried out. A series of experiments were carried out in ambient air using the OPO as the second laser pulse to study the effect of re-heating during the early phase of the plasma lifetime. The plasma is formed using a 30 mJ, 1064 nm pre-pulse and a second pulse from the OPO is fired at a fixed inter-pulse delay time of 500 ns with respect to the first pulse. As detailed in chapter 3, the OPO pulse is delivered orthogonally to the first pulse. In this way the OPO pulse is

coupled to the plasma created by the first pulse preventing the formation of a secondary plasma. The second re-heating pulse is delivered by the OPO at three different wavelengths; 484 nm, 466 nm and 430 nm with approximately 15mJ per pulse (14 mJ, 16 mJ and 19 mJ respectively). A wavelength of 484 nm was chosen to probe the central emission band of the vibrational AlO B-X emission system. The objective was to investigate potential re-heating effects (fragmentation, excitation etc.) on AlO molecules present in the plasma at early time delays (500 ns). The OPO pulse was then tuned to a wavelength of 466 nm (16 mJ) in an attempt to excite the Al(II) $3p^2(^1D_2)$ – $4p(^1P^0_1)$ transition (466.3 nm). The OPO was then tuned to 430 nm (19 mJ) as a control to observe the re-heating effects of a second laser pulse. As the energy of the OPO pulse decreases slightly with increasing wavelength, 430 nm was chosen as a comparison in order to rule out any effects related purely to the additional energy delivery of a second laser pulse to the ensemble.

Figure 5.9 below serves to demonstrate the measurement process and the effect of the second pulse provided by the OPO. Using an ICCD gate width of 20 ns, spectra were recorded for three separate experimental conditions; (i) the 1064 nm pulse only ("No OPO"), (ii) the initial 1064 nm pulse followed by the OPO pulse at an inter-pulse delay of 500 ns ("OPO") and (iii) the OPO pulse in the absence of the plasma ("OPO only"). All three spectra are recorded at the same "absolute" time which, for the example shown below in figure 5.9, is 520 ns after plasma formation.

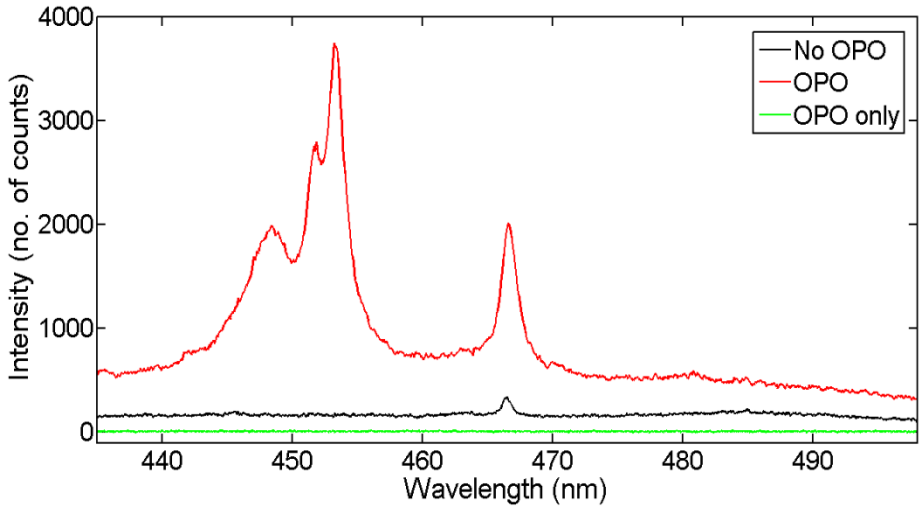

Figure 5.9: Spectra obtained using the (i) 30 mJ, 1064 nm pre-pulse only ("No OPO"), (ii) both pre-pulse and re-heating 466 nm pulse ("OPO") and (iii) the 466 nm pulse only ("OPO only"). All spectra are recorded at a delay time of 520 ns with respect to the pre-pulse using an ICCD gate width of 20 ns.

The OPO pulse is delivered orthogonally to the plasma expansion direction to ensure coupling of the OPO radiation to the plasma without the creation of a second plasma. This is evident from figure 5.9 where no plasma emission is observed in the "OPO only" spectrum. The effect of the OPO pulse in the presence of the plasma is also apparent. From time resolved aluminium spectra in air reported previously in chapter 4, for pulse energies of 8 mJ and 52 mJ, emission of the Al^{+} line at 466.3 nm is typically still observable at a delay time of 500 ns after the 1064 nm pulse has arrived at the target (see figure 4.5) and hence the observation of this line is expected here for a 30 mJ pulse. This is evident in present results shown in figure 5.9 where the emission of the A^{1+} line can be seen in the spectrum obtained using the single 30 mJ, 1064 nm pulse termed the "No OPO" spectrum. With the addition of the OPO pulse however, the appearance of three distinct spectral lines is noted around 450 nm in addition to a significant enhancement in the Al^{+} emission strength. These lines were attributed to three Al(III) emission lines (which are discussed alongside the more detailed results shown presently) and were not observable using a single laser pulse. Spectra recorded using the OPO only are not shown in the data presented in the following sections for the purpose of clarity although the data was recorded to ensure that any perceived effects were correctly

attributable to the OPO pulse coupling with the plasma and not merely a double-pulse effect due to any potential secondary plasma formation.

Figure 5.10 shows a series of spectra recorded at different time delays with respect to the initial 30 mJ, 1064 nm pre-pulse using an OPO wavelength of 430 nm.

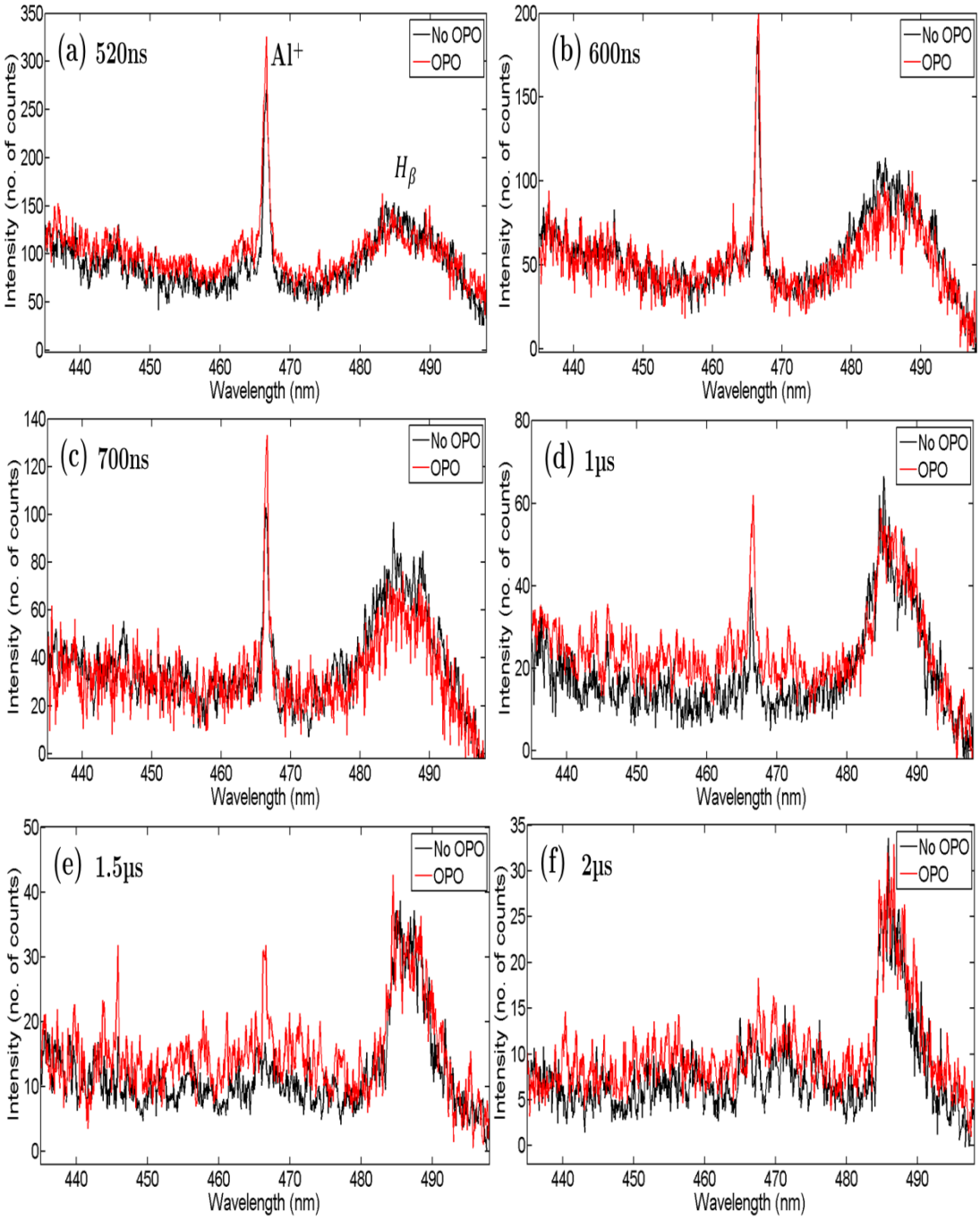

Figure 5.10: Time resolved spectra obtained using a 30 mJ, 1064 nm pre-pulse ("No OPO") and a 19 mJ, 430 nm re-heating pulse ("OPO") using an ICCD gate width of 20 ns. Spectra recorded at time delays of (a) 520 ns (b) 600 ns (c) 700 ns (d) 1 µs (e) 1.5 µs and (f) 2.5 µs with respect to the pre-pulse using a 500 ns inter-pulse delay.

Spectra obtained using the 1064 nm pulse only ("No OPO") show weak emission of the Al^+ line which decays *ca.* 1.5 µs after plasma ignition. H_β emission is observed as in previous spectra (figure 5.1) at a time delay of *ca.* 500 ns. No significant differences are

observed with the addition of the OPO pulse at a wavelength of 430 nm. The emission spectra appear similar to the single 1064 nm pulse case where, at the delay times shown, Al^{+} emission is weakly observed followed at later times by AlO emission. No Al^{2+} emission lines are observed in this spectral region identical to single pulse spectra.

The wavelength of the OPO was then tuned to 484 nm and the measurements were repeated under the same experimental conditions. The recorded emission spectra are shown in figure 5.11.

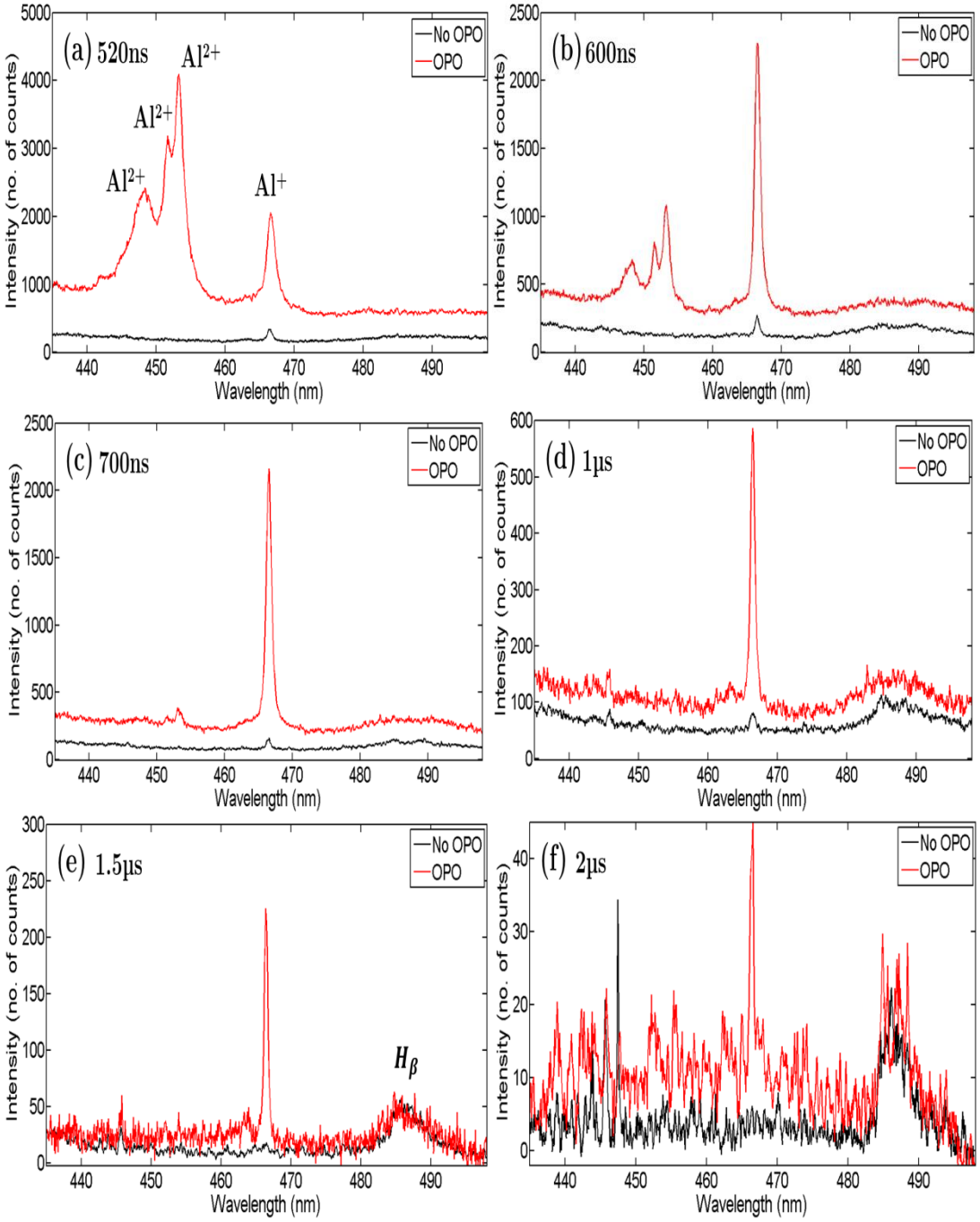

Figure 5.11: Time resolved spectra obtained using a 30 mJ, 1064 nm pre-pulse ("No OPO") and a 19 mJ, 484 nm re-heating pulse ("OPO") using an ICCD gate width of 20 ns. Spectra recorded at time delays of (a) 520 ns (b) 600 ns (c) 700 ns (d) 1 µs (e) 1.5 µs and (f) 2.5 µs with respect to the pre-pulse using a 500 ns inter-pulse delay.

With the delivery of the OPO pulse at a wavelength of 484 nm additional emission lines are observed around 450 nm. These spectral lines are attributed to doubly ionised aluminium transitions Al(III) 447.98 nm $4f(^2F^0_{5/2})$ - $5g(^2G_{7/2})$, Al(III) 451.26 nm

$4p(^2P^0_{1/2})$ - $4d(^2D_{3/2})$ and Al(III) 452.91 nm $4p(^2P^0_{3/2})$ - $4d(^2D_{5/2})$. These particular transitions do not appear in the single pulse studies carried out during this work and are uniquely observed here by the addition of the OPO pulse. The lifetime of the Al^{2+} lines is relatively short with emission observed for less than 100 ns after the arrival of the OPO pulse. These lines have been reported is other works however, using higher pulse energies (800 mJ) [21]. The strength of the Al^+ emission line at 466.3 nm increases significantly also with the addition of the OPO pulse. No apparent change is observed in the AlO emission profile. This may indicate that conditions are too hot at a time delay of 500 ns for condensation of plasma species into the molecular phase.

The OPO wavelength was then changed to 466 nm and spectra were again recorded with and without the addition of the OPO pulse (delivered at a time delay of 500 ns with respect to the initial pre-pulse). Figure 5.12 shows a number of time resolved spectra obtained under these conditions.

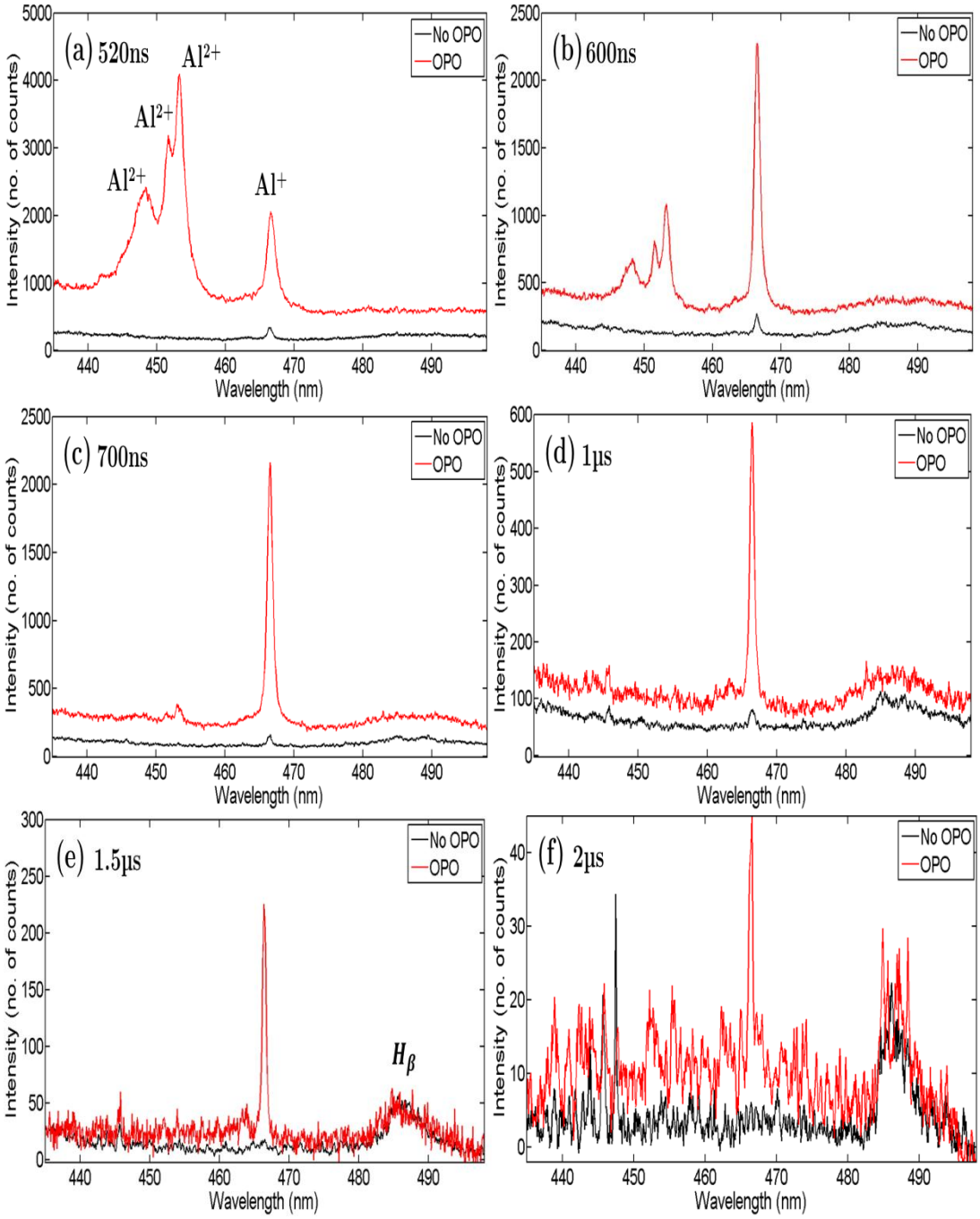

Figure 5.12: Time resolved spectra obtained using a 30 mJ, 1064 nm pre-pulse ("No OPO") and a 15 mJ, 466 nm re-heating pulse ("OPO") using an ICCD gate width of 20 ns. Spectra recorded at time delays of (a) 520 ns (b) 600 ns (c) 700 ns (d) 1 µs (e) 1.5 µs and (f) 2.5 µs with respect to the pre-pulse using a 500 ns inter-pulse delay.

The addition of the OPO pulse at 466 nm produces a very distinct increase in both the Al^{2+} and Al^{+} line emission strength. The Al^{2+} lines at 450 nm are visible in emission spectra up to a time delay of 200 ns after the delivery of the OPO pulse (i.e. at a time delay of 700 ns) as seen in figure 5.12 (c). A strong enhancement in the intensity and

observable lifetime of the Al^{+} emission line at 466.3 nm is also evident with the addition of the OPO pulse at 466 nm.

In summary, while the Al^{2+} emission lines are observable using an OPO wavelength of 484 nm, the intensity and persistence of the lines was much greater using an OPO wavelength of 466 nm. A similar enhancement was found in the Al^{+} emission. No significant change was observed in the strength of the emission lines in this spectral region (435-495 nm) using an OPO wavelength of 430 nm. The explanation for these results is thought to relate to the differences in the plasma temperature as a function of laser pulse wavelength. As previously mentioned (chapter 4) the dominant plasma heating mechanism is inverse Bremsstrahlung (IB) absorption via free electrons given by [22]:

$$\alpha_{IB} = 1.37x10^{-35}\lambda^{3}n_e^{2}T_e^{\frac{1}{2}} \tag{5.6}$$

where λ is the laser wavelength in µm, T_e is the electron temperature in K, n_e is the electron density per cm^3. Due to the λ^3 dependence for the IB absorption a higher plasma temperature is expected by re-heating the plasma with longer wavelength pulses. As the temperature of the plasma is indicative of the ion stages present, a higher population of Al^{2+} ions is expected using the 484 nm (2.56 eV) pulses. This Al^{2+} population density may then produce the transitions at 448nm, 452 nm and 453 nm observed in emission spectra via collisional excitation processes. Using the 430 nm (2.88 eV) re-heating pulse, less radiation is coupled to the plasma via IB absorption and hence a lower temperature plasma is expected. It is proposed that for 19 mJ pulses at this laser wavelength the plasma temperature is too low for a significant population density of Al^{2+} ions to be formed. At a photon energy of 2.88 eV, no direct route to Al^{2+} is possible and hence we see no evidence of the Al^{2+} emission lines observed using the 484 nm re-heating pulse.

The strong emission strength of the Al^{2+} and Al^{+} emission lines observed at an OPO wavelength of 466 nm is believed to be caused by a resonant effect. By the previous reasoning, re-heating using 466 nm (2.66 eV) pulses should results in a plasma

temperature lower than that achieved using the 484 nm re-heating pulse, yet much stronger emission is observed in both the Al^{2+} and Al^{+} emission lines. This enhancement is believed to taking place via resonant multi-photon absorption of the 466 nm photons. Due to the high probability of absorption at this particular wavelength, a three-photon absorption process may occur via:

$$Al^{+} + 3h\nu \rightarrow Al^{2+} + e^{-} + E_k \tag{5.7}$$

The energy level diagram of the transitions of interest is shown in figure 5.13.

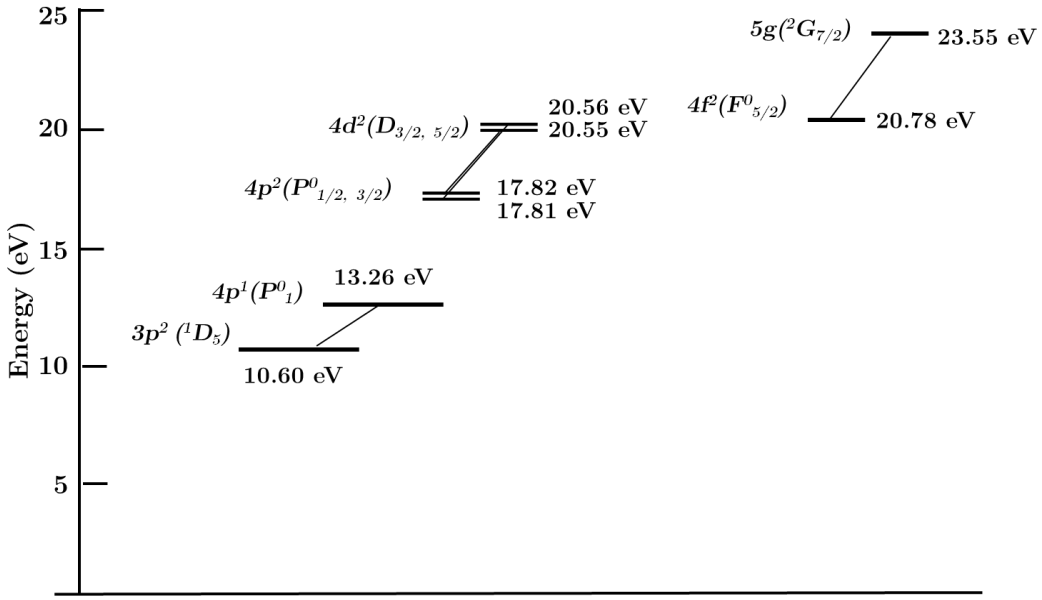

Figure 5.13: Energy level diagram showing the energy levels of transitions of interest.

From the excited upper level of the singly charged ion (13.26 eV), three photon absorption is required to reach the second ionisation potential of aluminium (18.83 eV). It is postulated that this resonance-enhanced multiphoton ionisation (REMPI) is the main route to Al^{2+} in this case and would explain the strong enhancement in ionic emission observed at this particular laser pulse wavelength.

5.4 Re-heating of Molecular AlO

The following series of experiments were carried out to investigate the effect of re-heating during the late phases of emission where molecular AlO species are forming in the plasma. A wavelength of 484 nm was chosen to probe the central emission band of the vibrational AlO B-X emission system. Fixing the OPO wavelength at 484 nm a series of experiments were carried out under ambient atmospheric conditions using six inter-pulse delay times. 0.5 µs, 1 µs, 2 µs, 5 µs and 10 µs delays, with respect to the initial 1064 nm pre-pulse, were chosen in order to probe the AlO molecule at various stages in its lifetime. The ICCD gate width was increased to 100 ns and the spectral range of the spectrometer centred on the AlO vibrational band emission. The pulse energies remained the same as in previous experiments with a 30 mJ, 1064 nm pre-pulse used for plasma formation and a 15 mJ, 484 nm re-heating pulse delivered by the OPO.

By probing the AlO molecule at different delay times some interesting differences in the spectra were observed. The resulting behaviour was separated into two regimes depending on the inter-pulse delay (time delay between the first and second pulse). The "early phase" behaviour observed using short inter-pulse delays $\leq$ 2 µs is presented first followed by observations using "late phase" inter-pulse delays $\geq$ 5 µs.

5.4.1 Short Inter-Pulse Delay

Spectra obtained using short inter-pulse delay times were studied for time delays up to 15 µs after the delivery of the OPO pulse (15 mJ, 484 nm). Figure 5.14 below shows spectra obtained using the 1064 nm pre-pulse only. Figure 5.15 shows spectra obtained at corresponding delay times using the OPO pulse at inter-pulse delays of 0.5 µs, 1 µs and 2 µs. Recorded spectra are shown at various time delays with respect to the delivery of the initial 1064 nm pre-pulse (30 mJ, 1064 nm).

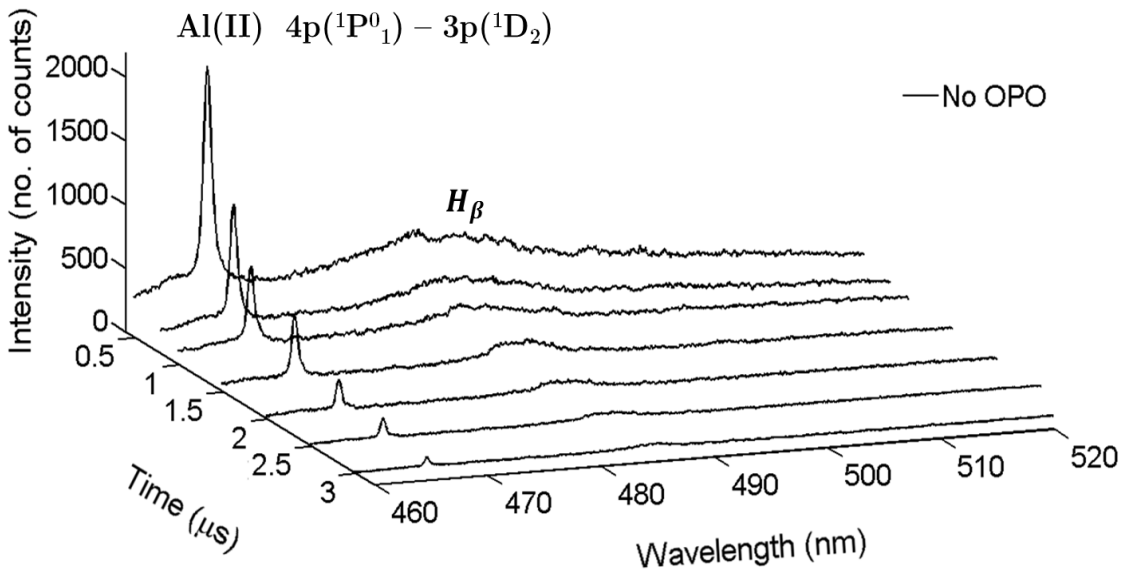

Figure 5.14: Time resolved spectra obtained using the 30 mJ, 1064 nm pre-pulse only. Spectra are shown at delay times of 0.51 µs, 0.8 µs, 1 µs, 1.5 µs, 2 µs, 2.5 µs and 3 µs. An ICCD gate width of 100 ns was used.

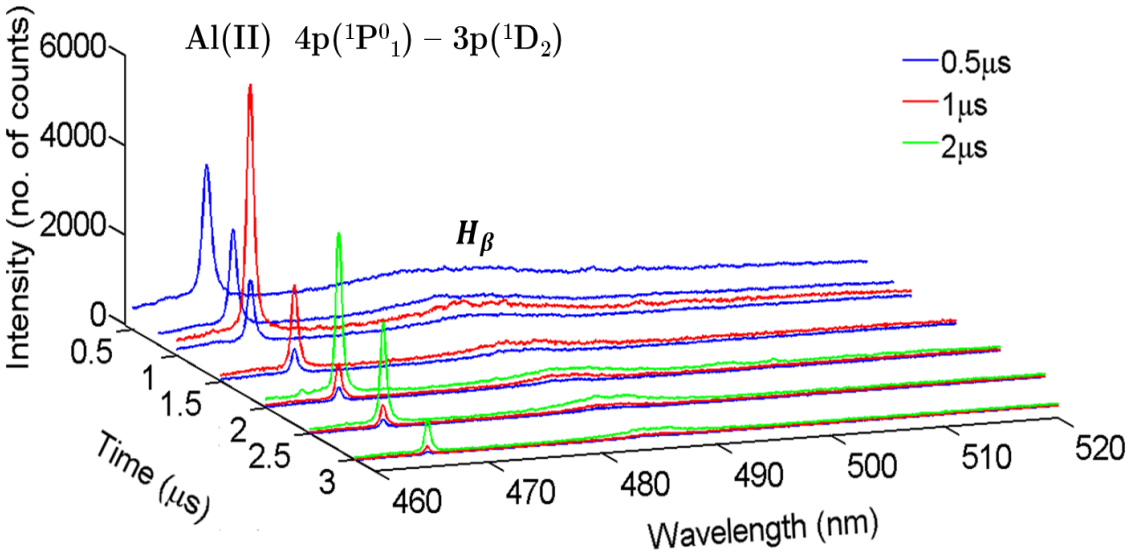

Figure 5.15: Time resolved spectra obtained using a 30 mJ, 1064 nm pre-pulse and a 15 mJ, 484 nm re-heating pulse using inter-pulse delays of 0.5 µs, 1 µs and 2 µs. Spectra are shown at delay times of 0.51 µs, 0.8 µs, 1 µs, 1.5 µs, 2 µs, 2.5 µs and 3 µs with respect to the initial pre-pulse. An ICCD gate width of 100 ns was used.

The introduction of the OPO pulse at these early inter-pulse delay times has the effect of strongly enhancing the Al^+ emission line at 466.3 nm. By comparing figure 5.14 and

figure 5.15, the maximum enhancement in Al^+ emission strength occurs using an inter-pulse delay of 1 µs where an increase of approximately 3× the emission intensity is observed. This may indicate that the enhancement observed in the Al^+ emission is caused by re-excitation of ions from the plasma undergoing the processes of cooling which remain close to the aluminium target where the incoming OPO pulse passes parallel to the surface. If re-excitation is the cause of the enhanced Al^+ emission strength, then it follows from the data that the optimum time for this re-excitation occurs at a time delay of 1 µs. This coincides with the time delay at which Al^{2+} emission has almost fully disappeared. For the pulse energies used throughout this work, the maximum ion stage observed was Al^{2+}. Subsequent to the strong initial Al^{2+} emission, the Al^+ species begin to dominate the emission spectra of the cooling plasma which occurs at time delays *ca.* 1 µs post plasma ignition (observed in chapter 4). At this delay time, the introduction of the OPO pulse to the cooling plasma appears to produce the strongest enhancement of the re-excited Al^+ emission.

Spectra obtained at late time delays are shown in figure 5.16 where the presence of AlO is observed. Emission recorded using the single pre-pulse ("No OPO") are shown as well as spectra recorded using the re-heating OPO pulse at inter-pulse delays of 0.5 µs, 1 µs and 2 µs.

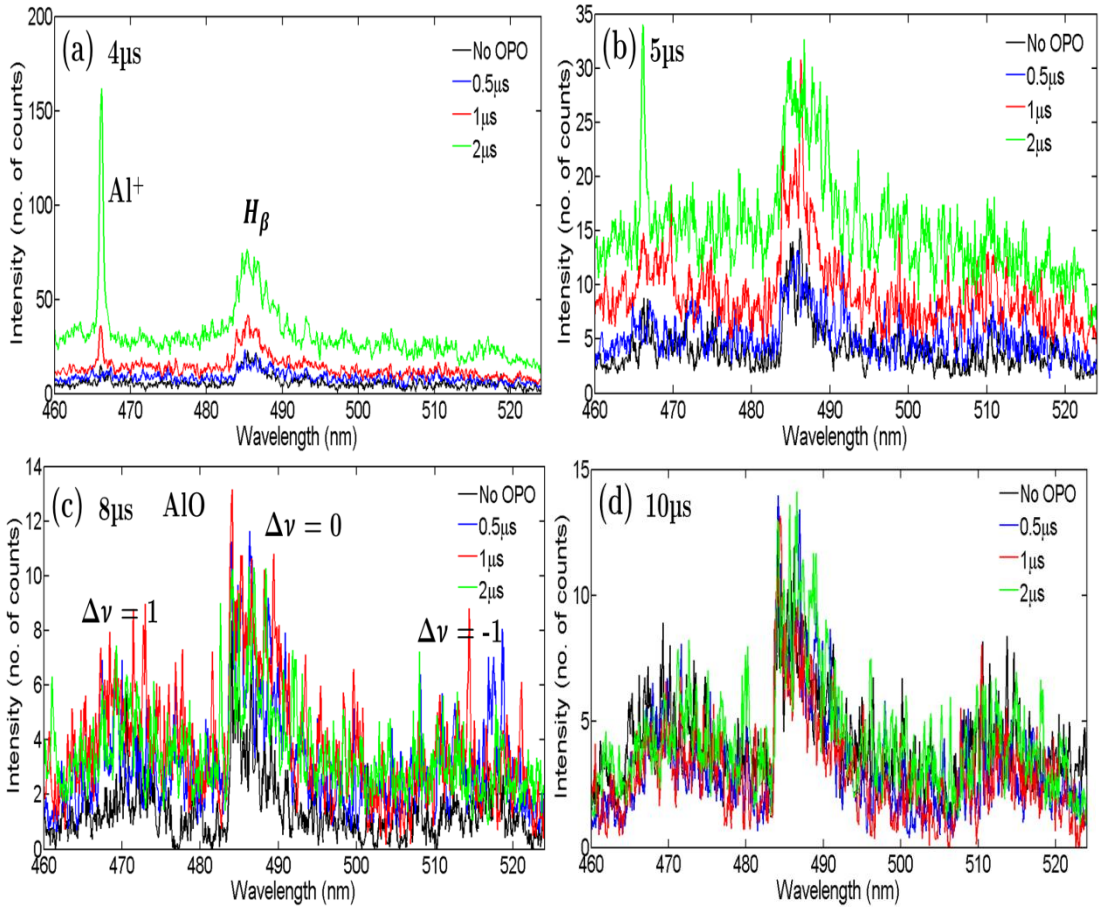

Figure 5.16: Time resolved spectra obtained using a 30 mJ, 1064 nm pre-pulse and a 15 mJ, 484 nm re-heating pulse. Recorded spectra show AlO emission using the pre-pulse only ("No OPO") compared to those spectra obtained with the addition of the re-heating pulse at short inter-pulse delays (0.5 µs, 1 µs and 2 µs). Spectra shown correspond to delay times of (a) 4 µs (b) 5 µs (c) 8 µs and (d) 10 µs with respect to the initial pre-pulse. An ICCD gate width of 100 ns was used.

At a time delay of 4 µs (with respect to the initial plasma ignition) the emission of Al^+ from the initial pre-pulse ("No OPO") has decayed to zero and the emission of AlO begins to appear in the recorded spectra (figure 5.16 (a)). The introduction of the OPO pulse at early inter-pulse delay times ≥ 1 µs appears to bring about a negligible effect on the AlO emission spectra. As previously shown, the sharp $\Delta v = -1, 0, 1$ vibrational bands appear in the emission spectra at time delays > 5 µs (figure 5.16 (c) and (d)).

5.4.2 Long Inter-Pulse Delay

Using the pre-pulse only (30 mJ, 1064nm) the Al^+ 466.3 nm line is observable up to *ca.* 3 µs after the pulse has fired (figure 5.14). By the time the OPO pulse arrives at the long inter-pulse delays, i.e., at 5 µs and 10 µs the Al^+ emission due to the initial pre-pulse has decayed entirely. The addition of the OPO re-heating pulse at long inter-pulse delay times sees re-excitation of the Al^+ emission as seen in figure 5.17.

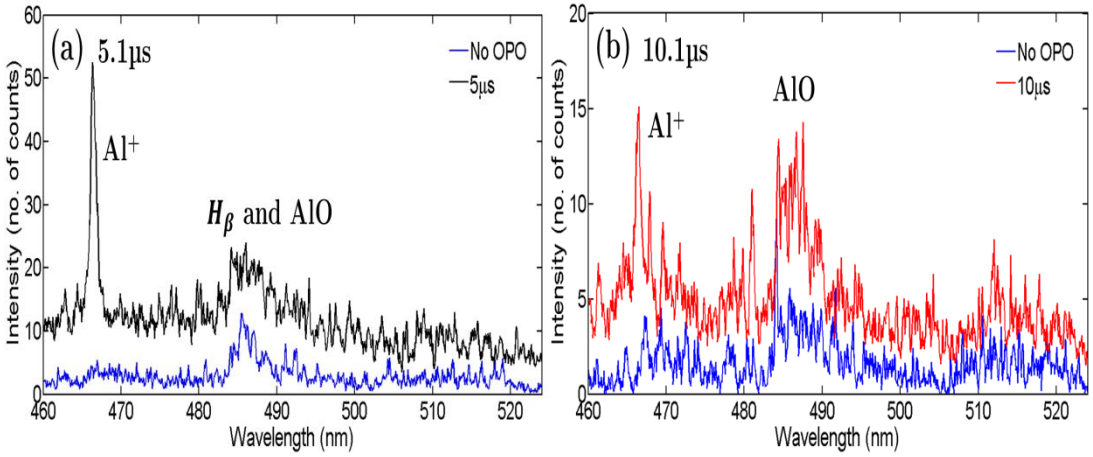

Figure 5.17: Time resolved spectra obtained using a 30 mJ, 1064 nm pre-pulse and a 15 mJ, 484 nm re-heating pulse. Recorded spectra show AlO emission using the pre-pulse only ("No OPO") compared to those spectra obtained with the addition of the re-heating pulse at long inter-pulse delays (5 µs and 10 µs). Spectra shown correspond to delay times of (a) 5.1 µs and (b) 10.1 µs with respect to the pre-pulse. An ICCD gate width of 100 ns was used.

However, the most notable effect of the OPO pulse at these long inter-pulse delays is observed in the AlO emission spectra. Here a slight increase in the emission intensity was clearly evidenced. Figure 5.17 shows spectra recorded at various time delays with respect to the pre-pulse using inter-pulse delays of 5 µs and 10 µs. For comparative purposes the emission of the pre-pulse only (30 mJ, 1064 nm) at each respective time delay is also shown in figure 5.17 (termed "No OPO").

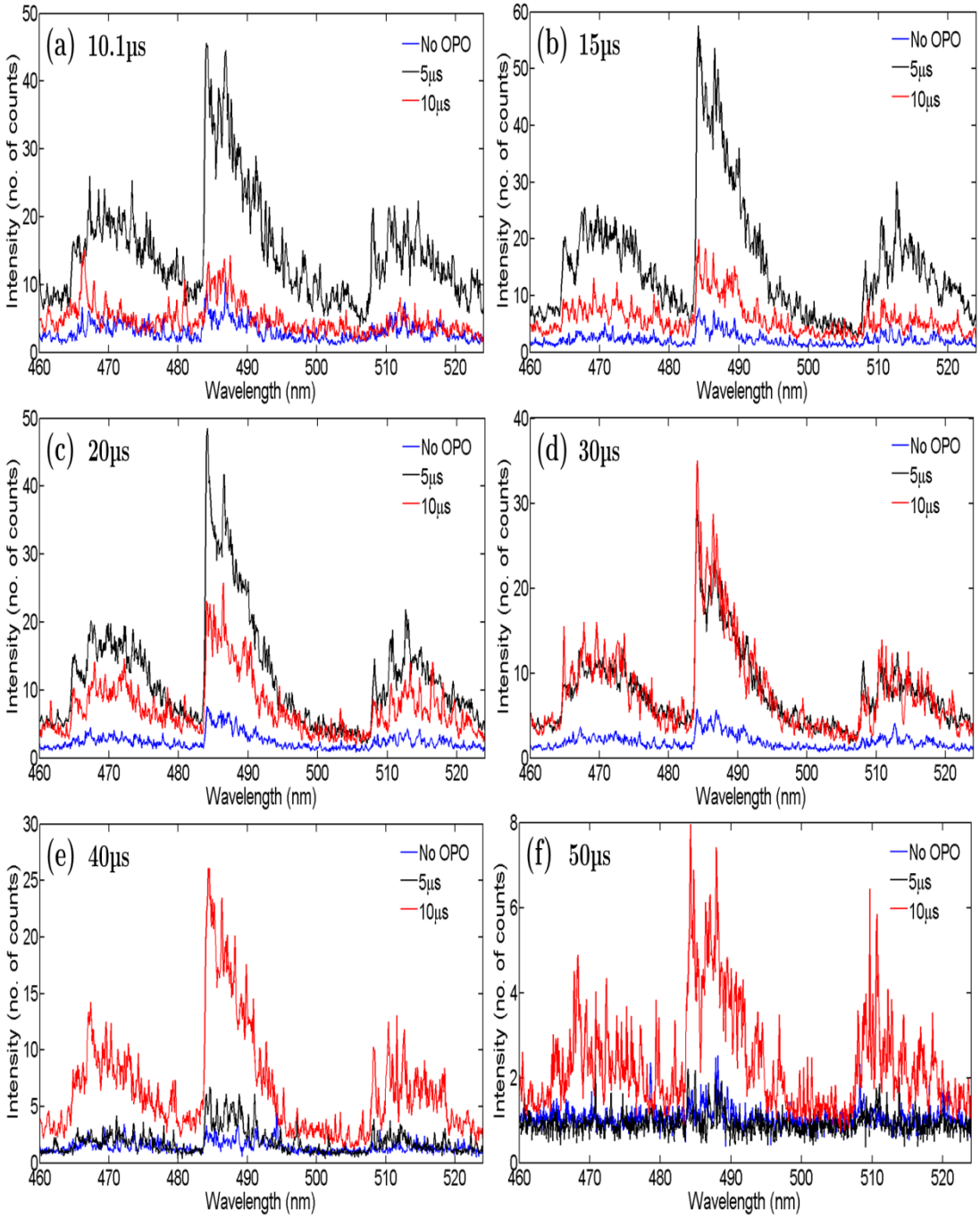

Figure 5.18: Time resolved spectra obtained using a 30 mJ, 1064 nm pre-pulse and a 15 mJ, 484 nm re-heating pulse. Recorded spectra show AlO emission using the pre-pulse only ("No OPO") compared to those spectra obtained with the addition of the re-heating pulse at long inter-pulse delays (5 µs and 10 µs). Spectra shown correspond to delay times of (a) 10.1 µs (b) 15 µs (c) 20 µs (d) 30 µs (e) 40 µs and (f) 50 µs with respect to the initial pre-pulse. An ICCD gate width of 100 ns was used.

The strongest enhancement in the AlO emission is observed using an inter-pulse delay of 5 µs. The maximum emission strength appears from the recorded spectra to occur at

different delay times with respect to the delivery of the OPO pulse. Figure 5.19 shows the integrated intensity as a function of time delay with respect to the initial pre-pulse.

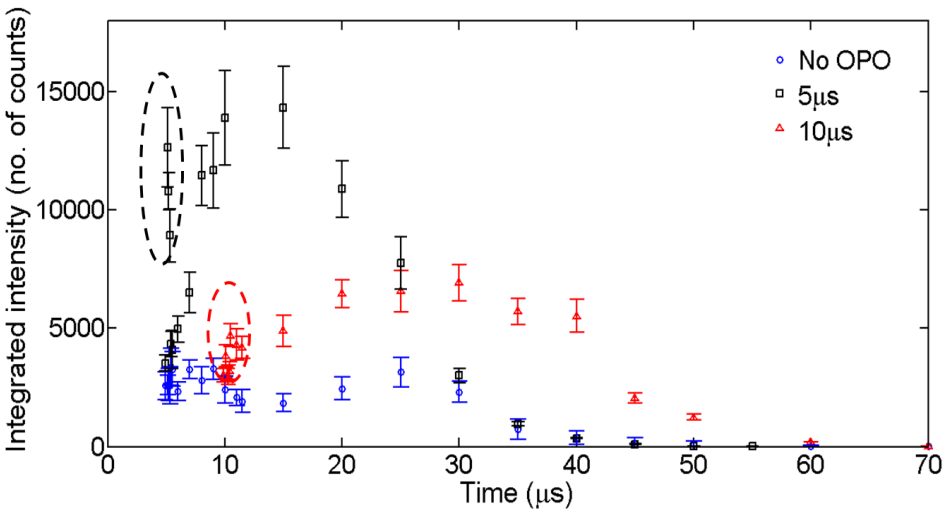

Figure 5.19: Integrated intensity of AlO emission obtained using a 30 mJ, 1064 nm pre-pulse and a 15 mJ, 484 nm re-heating pulse. Integrated intensity of AlO emission using the pre-pulse only ("No OPO") is compared to emission obtained with the addition of the re-heating pulse at long inter-pulse delays (5 µs and 10 µs). Data shown correspond to delay times with respect to the initial pre-pulse. An ICCD gate width of 100 ns was used.

An initial increase in intensity is observed just after the delivery of the OPO pulse using both 5 µs and 10 µs inter-pulse delays. This initial increase after the delivery of the OPO pulses is due to the contribution from the Al^+ emission line at 466.3 nm as indicated in figure 5.19 by the circles with broken lines. A delay is then observed in the onset of peak AlO emission intensity in both cases. A maximum in the molecular emission strength is observed at time delays of *ca.* 10-15 µs and *ca.* 20-30 µs respectively for the 5 µs and 10 µs inter-pulse delays. The emission due to the single pre-pulse case is also shown ("No OPO"). By comparison to the single pre-pulse emission, a significant enhancement in the recorded AlO emission strength is obtained by using a long inter-pulse delay for the incoming OPO pulse.

From the temperature estimates using the single 30 mJ, 1064 nm pulse presented in figure 5.6 a relatively higher temperature is expected at the onset of AlO formation at *ca.* 5 µs compared to the temperature of the gas after a 10 µs delay. From a

thermodynamic perspective, a lower gas temperature should favour a higher rate of AlO formation, in contrast to the behaviour observed here. This means that the delivery of the re-heating OPO pulse at long inter-pulse delay times has affected the major route to AlO formation which must be taking place through some other channel.

One simple explanation may be related to the amount of AlO molecules present in the plasma at the time of the incoming OPO pulse. Energy delivered by the OPO pulse may be absorbed by the molecular AlO species and slowly re-emitted over a period of tens of microseconds as the molecules vibrate. Supposing that a greater quantity of AlO exists in the plasma at a delay time of 5 µs compared to the later 10 µs delay would explain the increase in AlO emission observed. However, from the intensity of recorded emission spectra, the density of AlO species appears roughly constant.

A theory is proposed which considers the dominant species present during the different phases of the plasma lifetime. From measurements using the single 30 mJ, 1064 nm pulse (figure 5.6), the temperature of the gas at time delays ≤ 10 µs is expected to be too high (0.5 eV) for AlO formation via channel 2. This means that any AlO formation at these early delay times must occur via channel 1 (repeated here for ease of explanation):

$$Al + O_2 \rightarrow AlO + O \qquad (5.2a)$$

Since O_2 is readily available from the atmosphere, this implies that atomic aluminium is the limiting species which determines the amount of AlO which subsequently forms. In the high temperature regime we also expect the related reactions to proceed in following way:

$$AlO \rightarrow Al + O \qquad (5.3a)$$

$$O_2 \rightarrow O + O \qquad (5.4a)$$

We consider now the different temperature regimes of the gas as a function of delay time which are present in the cooling plasma shown in figure 5.20.

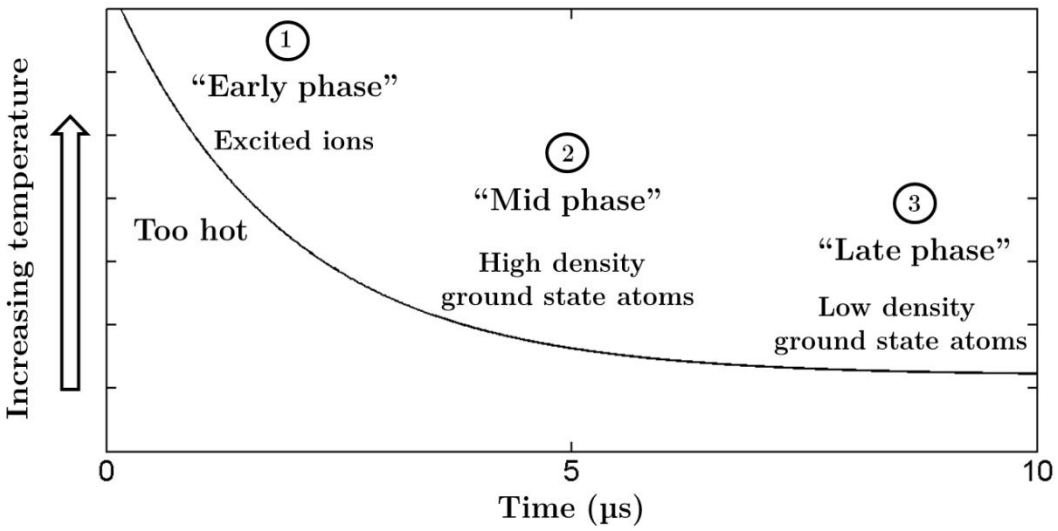

Figure 5.20: Schematic of the three distinct temperature epochs post plasma ignition. The three temperature regimes, "early phase", "mid phase" and "late phase" correspond to inter-pulse delays of ≤ 2 µs, 5 µs and 10 µs respectively.

In the "early phase" of the plasma lifetime (i.e. ≤ 2 µs) the temperature (which is expected to be ≈ 1 eV) is too high for significant AlO formation. While formation via channel 1 is favoured at these high temperatures, the competing dissociation channel is more readily occurring. This is evidenced in the emission spectra where AlO is not observed until delay times of *ca.* 5 µs. The observation of AlO at these time delays must require that the rate of molecular formation occurs at a higher rate than dissociation. As the temperature decreases ("mid phase"), the rate of dissociation via equation 5.3a begins to decrease also. As a consequence, less Al is expected at 10 µs ("late phase") due to the decrease in the temperature of the ensemble at that delay time. In addition, the de-excitation of aluminium ions present in the plasma to their ground state configuration is also taking place at *ca.* 4-5 µs (figure 5.16 (a) and (b)). This will also result in less available ground state aluminium atoms at a delay time of 10 µs. Hence, a higher population of aluminium atoms is expected at a delay time of 5 µs, resulting in more reactant species available for AlO formation via the dominant reaction mechanism in this high temperature regime described by equation 5.2a.

It is postulated that once the temperature of the plasma has dropped to a level conducive to AlO formation (at a delay time ≥ 5 µs), a greater presence of aluminium

atoms is expected at 5 µs and consequently a greater number of AlO species is subsequently formed accounting for the significant increase in emission observed. The delivery of the OPO pulse results in additional heating of the plasma species. Since condensation occurs after a period of plasma cooling, the AlO molecules form and re-emit radiation some microseconds later. Since a higher density of plasma species is expected at the earlier delay time of 5 µs, a higher rate of collisional cooling is expected. This explains the faster rate of de-excitation of AlO species using a 5 µs inter-pulse delay as seen in figure 5.19.

A final explanation for the observed behaviour may be related to a possible third formation channel given by:

$$Al^+ + O^- \rightarrow AlO \tag{5.8}$$

Using the early inter-pulse delay times, addition of the OPO pulse leads to a large population density of excited ions (as seen previously in figure 5.15). Significant AlO formation via equation 5.2 is countered by strong dissociation via equation 5.3 at these early delay times. During the époch of the "mid phase" (figure 5.20), formation of AlO overcomes dissociation as seen in recorded visible emission spectra (figures 5.1 and 5.2). Delivery of the OPO pulse at this time delay (5 µs) results in ionisation of the aluminium atoms producing a greater population of Al^+ ions in comparison to the amount observed using the 10 µs inter-pulse delay (figure 5.17). If the AlO formation is taking place by this third channel, this may account for the strong enhancement in the recorded AlO emission strength observed using the 5 µs inter-pulse delay.

5.5 Conclusions

This chapter details the optical emission studies carried out in ambient air at long time delays (≥ 50 µs) after plasma ignition. During this époch where line emission is weak or even absent, the formation of molecular species is detected from the vibrational band emission spectra. Plasma parameters such as electron densities and temperatures may

be ascertained from the molecular emission spectra available at these late delay times after the delivery of the laser pulse. The availability of a plasma diagnostic at such late plasma lifetimes alleviates the pressing requirement of fast gating systems and has particular relevance for LIBS measurements. By studying the temperature dependent thermodynamic reactions taking place, different rates of formation and dissociation were identified which were related to the experimental AlO emission spectra observed.

A series of re-heating experiments were carried out using a second laser pulse delivered by the OPO at a delay time of 500 ns to probe the early phase plasma species. Using an OPO wavelength of 430 nm, no significant differences were observed in the recorded emission spectra over the spectral range in question. At 484 nm, the emergence of several Al^{2+} emission lines was observed in addition to an increase in the emission strength of the Al^{+} 466.3 nm line. As the Al^{2+} emission lines were not observed using an OPO wavelength of 430 nm, the effect was concluded to depend on the plasma temperature and hence, the number density of excited Al^{2+} ions. Through collisional processes these Al^{2+} ions may then emit particular Al^{2+} and Al^{+} lines observed en route to the ground state. By tuning the OPO pulse to a wavelength of 466 nm, strong Al^{2+} and Al^{+} lines were observed. Due to the greater emission strength observed here compared to the 484 nm case (where a higher plasma temperature is expected), a resonant process was concluded to be taking place. As the photon frequency is resonant with the Al^{+} 466.3 nm transition, a higher probability of absorption is expected and multi-photon ionisation more readily occurs. REMPI was thought to be the explanation for the enhanced ionic emission strength observed using the 466 nm OPO re-heating pulse.

The wavelength of the OPO was tuned to 484 nm to probe the AlO species present in the plasma during different phases of the gaseous lifetime. By varying the inter-pulse delay time, the OPO pulse was delivered to the plasma at a number of "short" ($\leq$ 2µs) and "long" delay times (5 µs and 10 µs). Re-heating at early delay times sees re-excitation of aluminium ions present in the plasma formed by the first pulse. Re-heating during the late phase of plasma emission sees enhancement in the AlO emission

intensity. A delay in the onset of maximum emission intensity was also observed using the long inter-pulse delays. After delivery of the OPO pulse, the intensity of AlO emission was seen to increase as a function of delay time with a maximum occurring 10 µs and 20 µs after the delivery of the second pulse for inter-pulse delays of 5 µs and 10 µs respectively. A number of arguments were tabled to account for the increase in emission and the delay in maximum emission intensity observed.

Due to the high temperatures associated with laser produced plasmas, collisional cooling is a necessary step in the promotion of cluster growth [23] and likewise for molecular formation. Since a higher density of plasma species is expected at the earlier time delay of 5 µs, a greater number of collisions is expected which explains the faster rate of de-excitation observed from figure 5.19. The first proposal proffered to explain the enhancement in the emission strength simply relates to the amount of AlO present in the plasma at the different delay times. The energy delivered by the OPO is absorbed and slowly re-emitted by the molecules via vibrational transitions as the ensemble cools. If a higher density of AlO exists in the plasma at 5 µs compared to 10 µs, then this energy may be re-emitted tens of microseconds later resulting in a higher observed emission intensity. From the recorded emission spectra no clear evidence for a higher AlO density is found at 5 µs. Since AlO is present in emission spectra at time delays $\geq$ 5 µs, it follows that the rate of formation begins to overcome the rate of dissociation.

In the higher temperature regime expected by the earlier temperature measurements, the major route available for AlO formation occurs via channel 1. The second theory proposed to explain the increase in AlO emission relates to the amount of ground state aluminium present in the ensemble. At delay times $\leq$ 2 µs, a high density of excited ions is present in the plasma. At 5 µs, the amount of atomic aluminium is expected to be greater than at 10 µs meaning the main formation pathway (channel 1) may take place more readily. Additionally, dissociation is favoured by equation 5.3 at higher temperatures meaning a higher rate of Al gas.

A final argument is put forward which involves the idea of a third formation channel by the bonding of Al^+ and O^- (equation 5.8). This theory is supported by the increase in Al^+ emission strength observed in the recorded spectra at the earlier time delay of 5 µs.

References

[1] C. G. Parigger, A. C. Woods, D. M. Surmick, G. Gautam, M. J. Witte, and J. O. Hornkohl, "Computation of diatomic molecular spectra for selected transitions of aluminum monoxide, cyanide, diatomic carbon, and titanium monoxide," *Spectrochim. Acta Part B At. Spectrosc.*, vol. 107, pp. 132–138, May 2015.

[2] C. G. Parigger and J. O. Hornkohl, "Computation of AlO B2Σ+→X2Σ+ emission spectra," *Spectrochim. Acta. A. Mol. Biomol. Spectrosc.*, vol. 81, no. 1, pp. 404–411, Oct. 2011.

[3] X. Bai, V. Motto-Ros, W. Lei, L. Zheng, and J. Yu, "Experimental determination of the temperature range of AlO molecular emission in laser-induced aluminum plasma in air," *Spectrochim. Acta Part B At. Spectrosc.*, vol. 99, pp. 193–200, Sep. 2014.

[4] N. K. Podder, E. J. Clothiaux, and E. Oks, "A method for density measurements employing an asymmetry of lineshapes in dense plasmas and its implementation in a vacuum spark discharge," *J. Quant. Spectrosc. Radiat. Transf.*, vol. 65, no. 1–3, pp. 441–453, Apr. 2000.

[5] C. G. Parigger, L. D. Swafford, A. C. Woods, D. M. Surmick, and M. J. Witte, "Asymmetric hydrogen beta electron density diagnostics of laser-induced plasma," *Spectrochim. Acta Part B At. Spectrosc.*, vol. 99, pp. 28–33, Sep. 2014.

[6] C. G. Parigger, D. H. Plemmons, and E. Oks, "Balmer series Hβ measurements in a laser-induced hydrogen plasma," *Appl. Opt.*, vol. 42, no. 30, p. 5992, Oct. 2003.

[7] M. M. Litvak, "Electron Recombination in Laser-Produced Hydrogen Plasma," *J. Appl. Phys.*, vol. 37, no. 12, p. 4462, 1966.

[8] L. L. Wiese and J. A. Augis, "Time- and space-resolved spectroscopic studies of electrical breakdowns in an argon-hydrogen mixture," *J. Appl. Phys.*, vol. 48, no. 11, p. 4528, 1977.

[9] J. H. Eickmans, W.-F. Hsieh, and R. K. Chang, "Plasma spectroscopy of H, Li, and Na in plumes resulting from laser-induced droplet explosion," *Appl. Opt.*, vol. 26, no. 17, p. 3721, Sep. 1987.

[10] J. Ashkenazy, R. Kipper, and M. Caner, "Spectroscopic measurements of electron density of capillary plasma based on Stark broadening of hydrogen lines," *Phys. Rev. A*, vol. 43, no. 10, pp. 5568–5574, May 1991.

[11] K. Yahiaoui, S. Abdelli-Messaci, S. Messaoud-Aberkane, T. Kerdja, and H. Kellou, "Emission study of alumina plasma produced by a KrF laser," *Spectrochim. Acta Part B At. Spectrosc.*, vol. 93, pp. 20–27, Mar. 2014.

[12] H. R. Griem, *Plasma Spectroscopy*. Mc Graw-Hill, 1964.

[13] R. Žikić, M. A. Gigosos, M. Ivković, M. á. González, and N. Konjević, "A program for the evaluation of electron number density from experimental hydrogen balmer beta line profiles," *Spectrochim. Acta Part B At. Spectrosc.*, vol. 57, no. 5, pp. 987–998, May 2002.

[14] S. Jovićević, M. Ivković, Z. Pavlović, and N. Konjević, "Parametric study of an atmospheric pressure microwave-induced plasma of the mini MIP torch — I. Two-

dimensional spatially resolved electron-number density measurements," *Spectrochim. Acta Part B At. Spectrosc.*, vol. 55, no. 12, pp. 1879–1893, Dec. 2000.

[15] C. G. Parigger and E. Oaks, "Hydrogen Balmer series spectroscopy in laser-induced breakdown plasmas," *Int Rev At. Mol Phys*, vol. 1, pp. 13–23, 2010.

[16] M. Ivković, N. Konjević, and Z. Pavlović, "Hydrogen Balmer beta: The separation between line peaks for plasma electron density diagnostics and self-absorption test," *J. Quant. Spectrosc. Radiat. Transf.*, vol. 154, pp. 1–8, Mar. 2015.

[17] N. Konjević, M. Ivković, and N. Sakan, "Hydrogen Balmer lines for low electron number density plasma diagnostics," *Spectrochim. Acta Part B At. Spectrosc.*, vol. 76, pp. 16–26, Oct. 2012.

[18] W. L. Wiese, D. E. Kelleher, and D. R. Paquette, "Detailed Study of the Stark Broadening of Balmer Lines in a High-Density Plasma," *Phys. Rev. A*, vol. 6, no. 3, pp. 1132–1153, Sep. 1972.

[19] S. Yuasa, "Ignition and combustion of aluminum in oxygen/nitrogen mixture streams," *Combust. Flame*, vol. 108, no. 4, pp. 387–390, Mar. 1997.

[20] *JANAF, Thermochemical Tables*, 2nd ed. Michigan: The Dow Chemical Company, 1974.

[21] P. Yeates, "A Spectroscopic and Diagnostic Study of Laser Plasma Generation and Evolution under Multi-variable Target Conditioning," Dublin City University, Dublin, 2004.

[22] W. B. Zel'dovich and Raizer, Y.P., *Physics of Shock Waves and High-Temperature Hydrodynamic Phenomena*, Academic Press, New York. 1966.

[23] M. A. Duncan, "Invited Review Article: Laser vaporization cluster sources," *Rev. Sci. Instrum.*, vol. 83, no. 4, p. 41101, 2012.

Chapter 6

Comparison of Single Pulse Studies in Air and Liquid Ambient

In vacuum, a laser ablated plume will freely expand in the absence of collisions, with a constant velocity equal to the initial velocity v_0 [1]. In higher pressure environments, the plume dynamics proceed very differently with background molecules acting to slow the expanding plume. In this chapter, a comparison of laser produced plasmas in water and air is presented. The motivation of the work presented in this section is to provide an overview of the plasma behaviour in both environments and also to study the differences between them. The plume expansion dynamics are compared using time resolved imaging and the plume behaviour is found to evolve very differently in both cases. The data are compared to two expansion models and the applicability of each is assessed in both environments. The unique physical properties of the plasmas that are formed in these two distinct environments are further evidenced in the quite different craters profiles that form during the laser interaction with the target in air and water. Crater formation was studied for a range of laser pulse energies in air and water using a SEM. When the laser pulse impinges on the target surface and creates a plasma, the rapid expansion of the plume creates a compressive shock-front which is radially emitted from the point of impact. A comparison of the different shockwave behaviours was carried out using shadowgraphy to probe the shock-front dynamically. Interferometry

was also carried out in both environments to estimate the electron density at early plasma lifetimes.

6.1 Imaging in Air and Water

6.1.1 Imaging at a Fixed Laser Pulse Energy

A comparison of plasma expansion in liquid and air was carried out using aluminium as the target metal and deionised water as the liquid. The data was taken at low laser pulse energy 6 $\pm$ 3 mJ as a preliminary investigation into the differences that may occur between the different ambient media. Using single-shot time resolved imaging, the evolution of the plasma was recorded in 50 ns increments for the first 500 ns of the plasma lifetime with the aid of an intensified CCD camera or ICCD. Broadband imaging was employed over the wavelength range 300-800 nm. The optical gate width for each image was 50 ns.

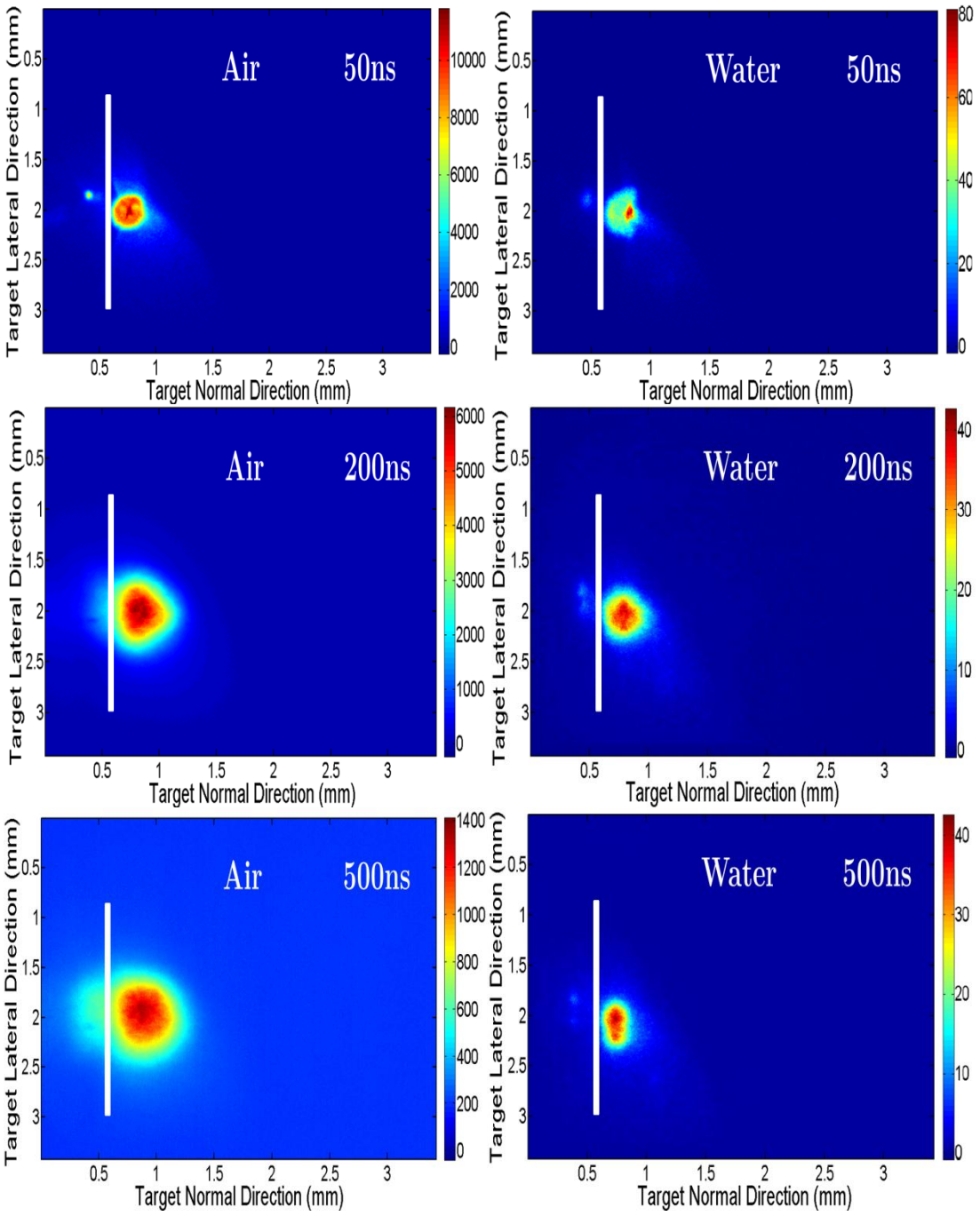

Figure 6.1: False-colour images of the expansion of an aluminium plasma in air and water ambient at various plasma lifetimes. The plumes were formed using a 6 mJ, 1064 nm laser pulse. The intensity (no. of counts) is represented by the colour scale bar shown on the right hand side of each image.

The visible emission observed behind the target position is due to scattering of plasma radiation from the highly reflective metallic surface. Due to the higher pressure experienced by the plasma plume that forms in liquid, a greater confinement of the

plasma expansion is expected in water compared to air [2] and indeed that is what is observed here. While the plasma in ambient air is free to expand to some appreciable distance away from the target surface, the plasma formed in water is highly confined. The air plasma appears to expand rapidly at the initial stages of formation and evolution before reaching a plateau. From the images recorded in water, a similar evolution is observed for early plasma lifetimes followed by a visible "contraction" at times $>$ 300 ns. The emission strength was much weaker in the case of water due to rapid de-excitation of the plasma in the high density background. A high ICCD gain was required in order to detect emission up until 500 ns. This issue was not encountered for the emission recorded in air where visible emission was easily observable over the same time range.

6.1.2 Plume Front Comparison

Using these data the luminous plume front positions were then plotted as a function of time for air and water, the results of which are shown in figure 6.2. The plume front position was defined as the position at which the ICCD count had dropped to $1/e$ (~0.37) of its maximum value in the expansion direction normal to the target surface. The error associated with each measurement of the plume front position was defined as the point at which the ICCD counts were $\pm$ 2% of the plume front position. The objective was to investigate the broad overall behaviour of the plume front expansion for both air and water ambient. Shown are the fits for air and water to the Taylor-Sedov [3] shockwave expansion model $R = \alpha t^n$ with α and n as the fitting parameters.

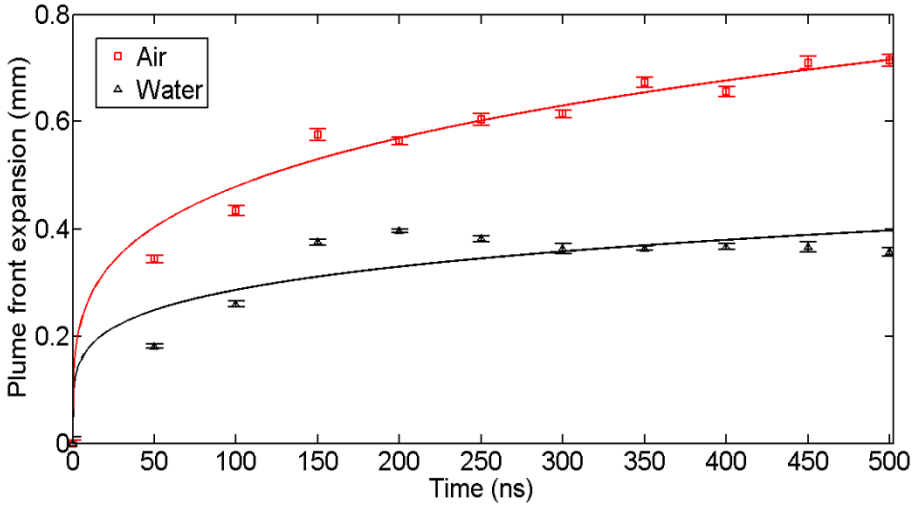

Figure 6.2: Plume front positions for aluminium plasma expansion in air and water using 6 mJ, 1064 nm pulses. Shockwave expansion models are fitted to the data in both environments and are represented by the solid lines ($\overline{R^2}$ = 0.97 and 0.89 for air and water respectively).

	α	n	$\overline{R^2}$
Air	0.12 ± 0.06	0.38 ± 0.10	0.97
Water	0.10 ± 0.06	0.34 ± 0.15	0.89

Table 6.1: Fitting parameters obtained by fits to shockwave expansion model in air and water at 6 mJ corresponding to figure 6.2.

The air and water plume expansion data shown in figure 6.2 at low laser pulse energy can be said to show reasonable agreement with the model fits for longer time delays, > 300 ns. For an ideal spherical expansion, the shockwave expansion model predicts a $t^{0.4}$ dependence. The values corresponding to the fits obtained in figure 6.2 were 0.38 and 0.34 for air and water respectively.

The plume expansion appears to reach a plateau at an earlier time delay in water than in air. In similar studies comparing plasma expansion in air and water ambient it has been reported that the expansion rate is comparable only at early plasma lifetimes [4]. The authors of that paper have reported that the plume expansion reaches a plateau region in water much earlier than in air at the same laser energy with saturation occurring at ~300 ns and 800 ns respectively. From figure 6.2 the plume front expansion appears to level off in water at a time delay of roughly 200 ns whereas in air this

plateau appears from the data to occur at a later stage, around 400 ns. The ratio of α values for air and water ambient is 1.2 which demonstrates the magnitude of pressure experienced by the higher density environment in water [4], [5]. Figure 6.3 shows the plume front positions in air and water and the corresponding fits to the drag force model $R = R_0(1 - e^{-\beta t})$.

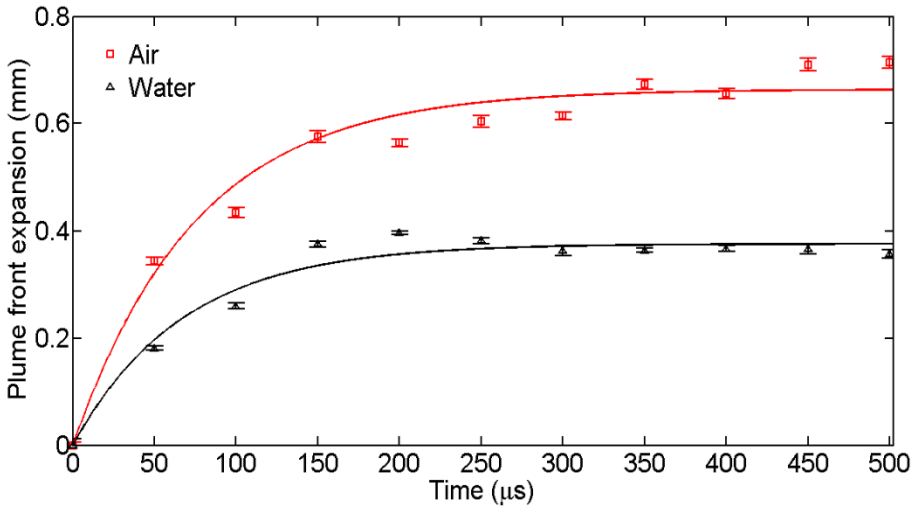

Figure 6.3: Plume front positions measured for plasma expansion in air and water ambient. Shown also are the fits to the drag force model ($\overline{R^2}$= 0.96 and 0.91 for air and water respectively).

	$\beta(ns^{-1})$	$R_0\ (mm)$	$\overline{R^2}$
Air	0.011 ± 0.005	0.66 ± 0.04	0.96
Water	0.014 ± 0.007	0.37 ± 0.06	0.91

Table 6.2: Fitting parameters obtained by fits to drag force expansion model in air and water at 6 mJ corresponding to figure 6.3.

The drag force model predicts that the plume will finally come to a rest due to resistance from collisions with the background gas [6]. The ejected species experience a viscous force proportional to their velocity through the background gas [1], [7]. Stopping distances of 0.66 mm and 0.37 mm (represented by the R_0 parameter in the drag force expansion model [7], [8] were extracted from the model fits in air and water respectively. These values indicate the final distance reached by the expanding plume represented by the plateau regions of figure 6.3. Hence, for the same laser pulse energy, the final

stopping distance measured in air is approximately twice that of water demonstrating the strong confinement that occurs in a liquid environment.

In addition, looking at the adjusted R^2 values for each model, better agreement with the experimental data is found in air using both the drag force and the Taylor-Sedov models. More suitable descriptions of the plasma formation and dynamics in water could be provided by direct simulations such as those carried out by Noack and Vogel [9].

6.2 Comparison as a Function of Laser Energy

An investigation of the plume dynamics in air and water was carried out as a function of laser pulse energy using 1064 nm laser pulses. The focusing lens for the laser pulse was adjusted in each case to compensate for refractive index changes and the pulse energy adjusted to compensate for energy attenuation in the water (see details in chapter 3). A series of time resolved images were acquired using a 50 ns gate width in air and water for a range of laser pulse energies of 8 $\pm$ 3 mJ, 16 $\pm$ 3 mJ, 38 $\pm$ 3 mJ and 52 $\pm$ 3 mJ. The plume front positions were extracted from these images. Once again these data were fitted to the two analytical shockwave models for both air and water ambient for each laser pulse energy used.

6.2.1 Air

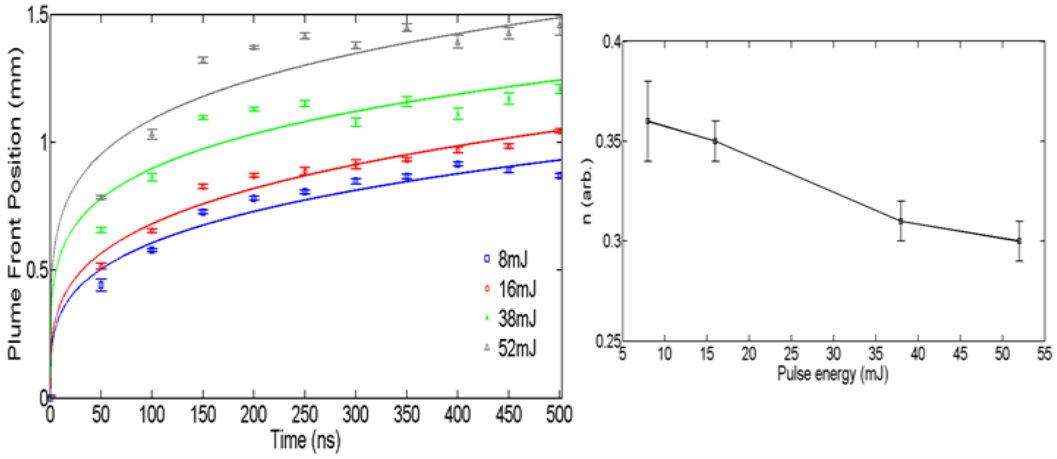

Figure 6.4: Plume front positions in air at 8 mJ, 16 mJ, 38 mJ and 52 mJ. Raw data is shown as well as shockwave expansion fits to the data ($\overline{R^2}$ = 0.96, 0.97, 0.94 and 0.92 respectively).

	α	n	$\overline{R^2}$
8mJ	0.11 ± 0.04	0.36 ± 0.02	0.96
16mJ	0.12 ± 0.04	0.35 ± 0.01	0.97
38mJ	0.19 ± 0.08	0.31 ± 0.01	0.94
52mJ	0.24 ± 0.09	0.30 ± 0.01	0.92

Table 6.3: Fitting parameters obtained by fits to shockwave expansion model in air at 8 mJ, 16 mJ, 38 mJ and 52 mJ corresponding to figure 6.4.

The plume front expansion is seen to increase as the laser pulse energy increases, similar to findings reported in other works [5]. A rapid expansion is observed at early lifetimes with a more gradual expansion occurring subsequently at approximately 200 ns. The expansion then appears to saturate at later times around 300-400 ns. The shockwave expansion model fits show best agreement at low pulse energy. As the pulse energy is increased, the agreement begins to deviate. The values obtained for the fitting parameter n are seen in decrease with increasing laser pulse energy. As previously mentioned, the ideal value for n is 0.4 for a spherical expansion [10]. From this it can be concluded that the shockwave expansion model becomes a less appropriate choice of model with increasing pulse energy. The drag force model was also applied to the plasma expansion in air, the results of which are presented in figure 6.5.

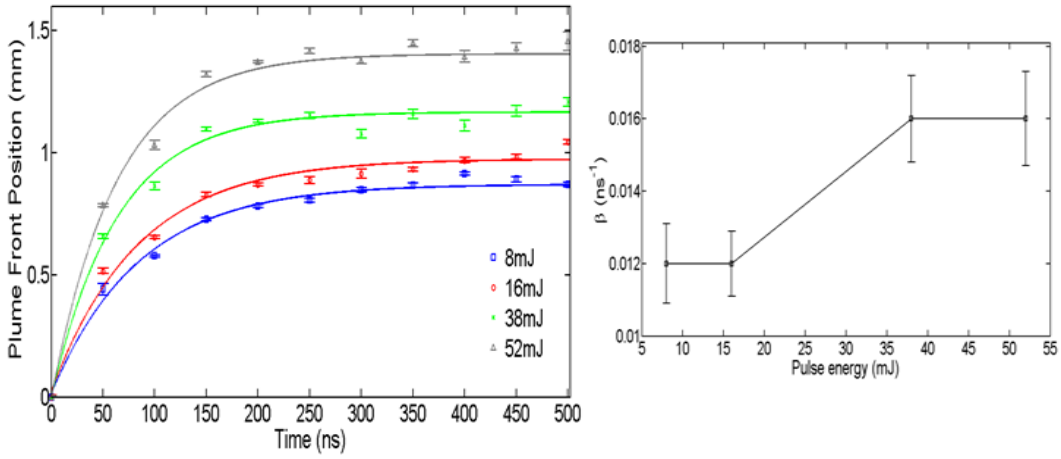

Figure 6.5: Plume front positions in air at 8 mJ, 16 mJ, 38 mJ and 52 mJ. Raw data is shown as well as drag force model fits to the data ($\overline{R^2}$ = 0.99, 0.99, 0.98 and 0.98 respectively).

	$\beta\ (ns^{-1})$	$R_0\ (mm)$	$\overline{R^2}$
8mJ	0.012 ± 0.0011	0.87 ± 0.03	0.99
16mJ	0.012 ± 0.0009	0.97 ± 0.04	0.98
38mJ	0.016 ± 0.0012	1.17 ± 0.04	0.98
52mJ	0.016 ± 0.0013	1.41 ± 0.04	0.97

Table 6.4: Fitting parameters obtained by fits to drag force expansion model in air at 8 mJ, 16 mJ, 38 mJ and 52 mJ corresponding to figure 6.5.

From the slowing parameter β using the drag force model fits, some evidence of a higher rate of slowing is observed for higher laser pulse energies. The physical meaning of this is that the energy of the plume front is further dampened as the pulse energy increases.

From figures 6.4 and 6.5 good agreement is observed using both models with the drag force model demonstrating somewhat better representation of the data judging by the goodness of the fits. Both expansion models are shown together for ease of comparison in figure 6.6.

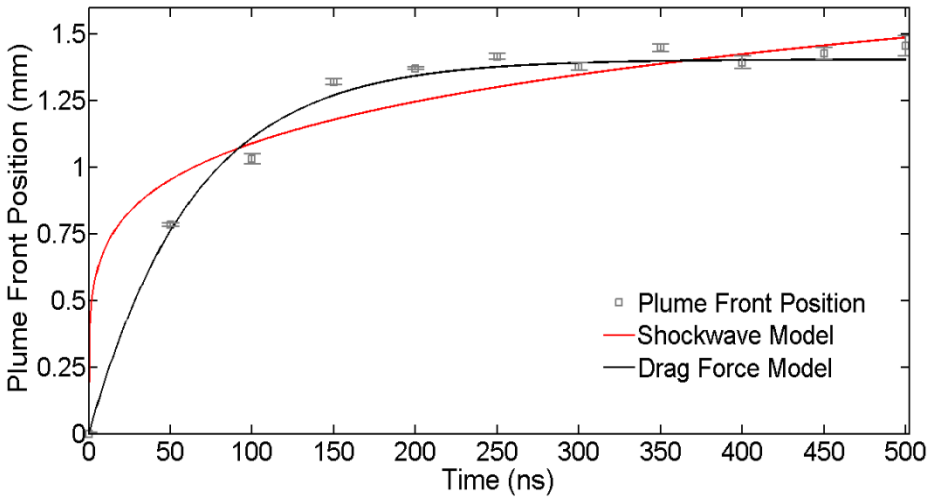

Figure 6.6: Plume front expansion and corresponding fits to shockwave model and drag force model ($\overline{R^2}$= 0.96 and 0.99 respectively). Measurements were taken using an 8 mJ, 1064 nm pulse.

The shockwave expansion model predicts that the plume front should expand continuously as a function of time. While this can be considered a good approximation at early times, it does not describe the behaviour of the plumes at times $>$ 200 ns. Pressure is exerted on the plume front by the surrounding medium which causes a deceleration of the expanding plume front which is not accounted for in the shockwave model. In this regime expansion is seen to taper off. This deceleration is taken into consideration by the drag force model and hence is deemed to be the more realistic model to best represent the observed behaviour.

6.2.2 Water

Figure 6.7 shows the plume front positions extracted from the imaging data measured in deionised water at a range of laser pulse energies.

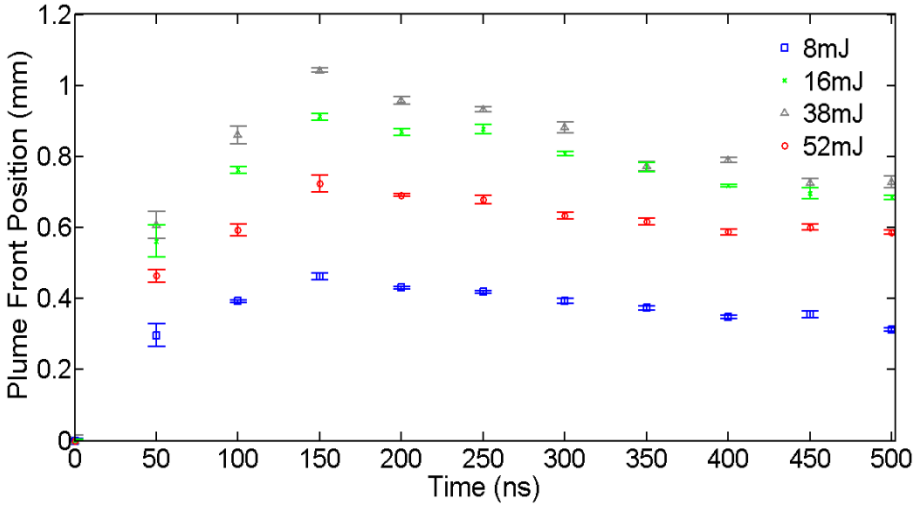

Figure 6.7: Plume front positions measured in deionised water using 1064 nm pulses having energies of 8 mJ, 16 mJ, 38 mJ and 52 mJ.

An expansion phase is initially observed in the first 150 ns after plasma initiation. As the pulse energy increases, a greater expansion occurs. As time proceeds, this expansion is followed by an apparent contraction phase at time delays > 150 ns. This trend is in contrast to the case in air where expansion was seen to reach a saturation level at approximately this time. In order to explain this phenomenon the data was divided into two regimes. Different models were applied to the data in each regime; the shockwave expansion model at early times (i.e. < 150 ns) and exponential cooling for later times.

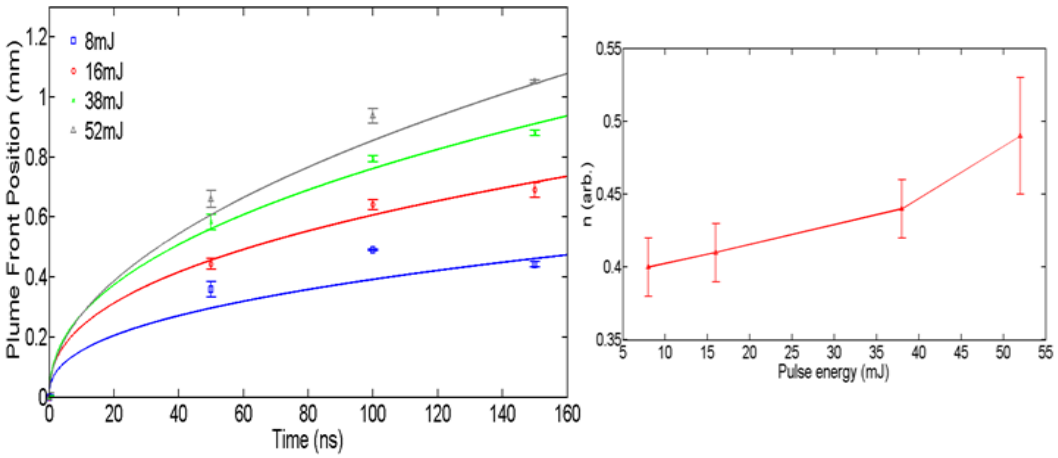

Figure 6.8: Plume front expansion in water up to 150 ns using laser pulse energies of 8 mJ, 16 mJ, 36 mJ and 52 mJ. Corresponding fits to the shockwave expansion model are also shown the $\overline{R^2}$ values retrieved were 0.95, 0.97, 0.97 and 0.96 respectively.

	α	n	$\overline{R^2}$
8mJ	0.06 ± 0.03	0.40 ± 0.02	0.95
16mJ	0.08 ± 0.02	0.41 ± 0.02	0.97
38mJ	0.09 ± 0.03	0.44 ± 0.02	0.97
52mJ	0.10 ± 0.03	0.49 ± 0.04	0.96

Table 6.5: Fitting parameters obtained by fits to shockwave expansion model in water at 8 mJ, 16 mJ, 38 mJ and 52 mJ corresponding to figure 6.8.

The fits show similar agreement for each laser pulse energy. With increasing laser pulse energy, the values obtained for the fitting parameter α become larger. As α is related to the amount of energy released in the explosion, for a fixed background density this result is in agreement with the trend predicted by the shockwave expansion model [3], [11], [12]. The values obtained for the fitting parameter n are found to increase with laser pulse energy. For an 8 mJ pulse a $t^{0.4}$ dependence is revealed. The value of the exponent increases with increasing pulse energy reaching an approximately $t^{0.5}$ dependence for a 52 mJ pulse. As previously stated in section 2.10.2, the parameter n will take a value of 0.6, 0.5 and 0.4 for one, two and three-dimensional expansion respectively. This suggests that with increasing pulse energy, the behaviour of the plume front is transitioning from a predominantly spherical expansion to a more cylindrical expansion. The data were also fitted to the drag force model with comparable agreement being observed.

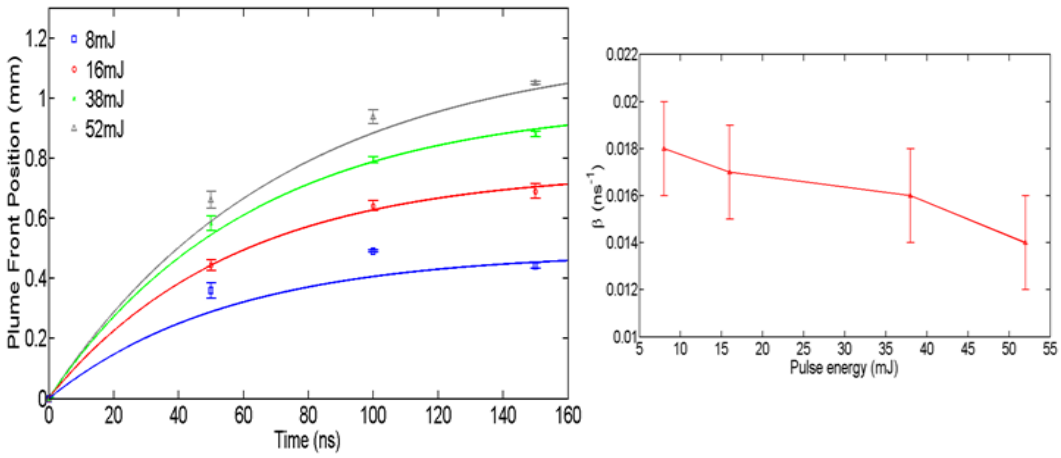

Figure 6.9: Plume front expansion in water up to 150 ns using laser pulse energies of 8 mJ, 16 mJ, 36 mJ and 52 mJ. Corresponding fits to the drag force model are also shown the $\overline{R^2}$ values retrieved were 0.96, 0.99, 0.99 and 0.96 respectively.

	$\beta\ (ns^{-1})$	$R_0\ (mm)$	$\overline{R^2}$
8mJ	0.018 ± 0.0022	0.49 ± 0.18	0.96
16mJ	0.017 ± 0.0016	0.76 ± 0.18	0.99
38mJ	0.016 ± 0.0017	0.98 ± 0.21	0.99
52mJ	0.014 ± 0.0020	1.17 ± 0.26	0.96

Table 6.6: Fitting parameters obtained by fits to drag force expansion model in water at 8 mJ, 16 mJ, 38 mJ and 52 mJ corresponding to figure 6.9.

Similar to the case in air, the stopping distances calculated were found to increase as a function of laser pulse energy. The slowing parameter β was found to decrease with increasing pulse energy, in contrast to the trend observed in air. This result implies that the plume front experiences less drag as the laser pulse energy is increased in water.

For times > 150 ns an exponential decay (Ae^{-kt}) was used to fit to the data, the results of which are shown in figure 6.10.

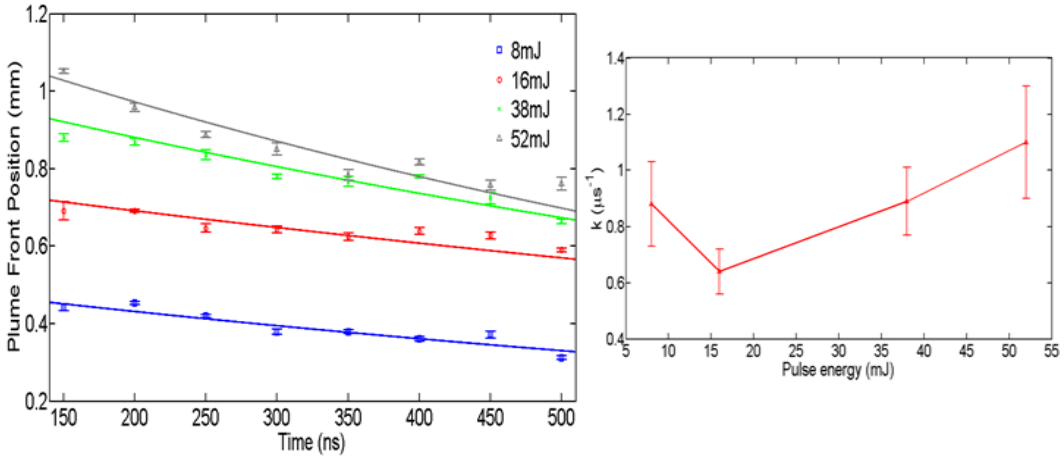

Figure 6.10: Plume front positions data in water and exponential decay fits for 8 mJ, 16 mJ, 38 mJ and 52 mJ pulse energies ($\overline{R^2}$= 0.97, 0.91, 0.96 and 0.95 respectively).

	A	$k\ (ns^{-1})$	$\overline{R^2}$
8mJ	0.52 ± 0.08	0.00088 ± 0.00015	0.97
16mJ	0.79 ± 0.07	0.00064 ± 0.00008	0.91
38mJ	1.05 ± 0.08	0.00089 ± 0.00012	0.96
52mJ	1.21 ± 0.09	0.00110 ± 0.00020	0.95

Table 6.7: Fitting parameters obtained by fits to cooling model in water at 8 mJ, 16 mJ, 38 mJ and 52 mJ corresponding to figure 6.10.

The contraction of the plume was found to decrease with increasing pulse energy. As can be observed from figure 6.7 and 6.10 a slightly more rapid rate of cooling is observed using the 52 mJ pulse. However, from the experimental error bars associated with the cooling rate k, no definitive conclusion can be draw.

The expansion in air and water was found to behave similarly for early plasma lifetimes where both models show good visual agreement with the plume front expansion. In the case of air the expansion is found to saturate at ~200 ns. This plateau of the plume front is observed up to a delay of 500 ns indicating that the luminous plume front remains effectively stationary during this period. This deceleration of the plume front is attributed to the pressure provided by the background gas as the plasma expands. Although both the shockwave and drag force models are observed to fit well to the data, the drag force model better describes the behaviour of the plume expansion over the entire duration of the plasma lifetimes measured. A comparison of the plume front expansion in air and water at 52 mJ is shown in figure 6.10 demonstrating the behaviour in both environments up to 500 ns.

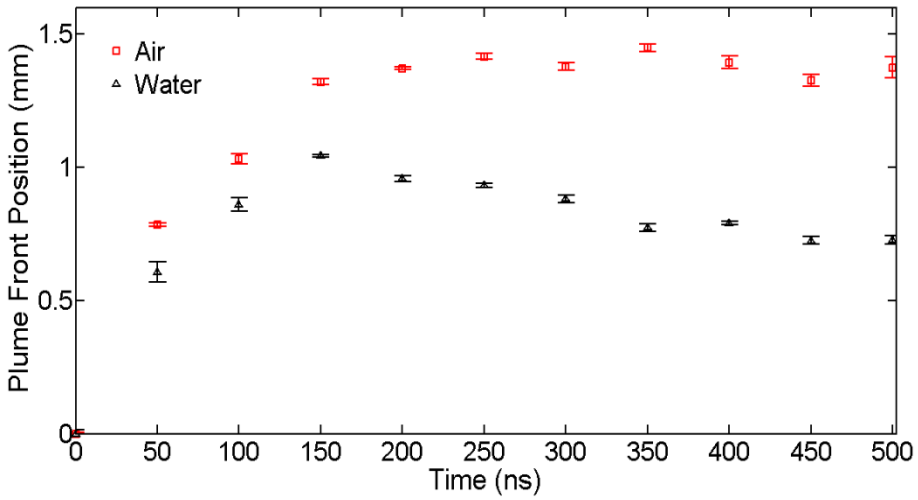

Figure 6.11: Plume front expansion in air and water at 52 mJ. An expansion is observed for both backgrounds for the first 150 ns with the plume front reaching 1.4 mm in air compared to *ca.* 1.0 mm in water ambient. Beyond this the plume front reaches a plateau region in air while a contraction occurs in water ambient.

In a background of air the initial expansion rate was found to be greater than in water. The saturation of the plasma expansion in water is observed at ~150 ns. At later times however, a different behaviour is observed to that of air whereby the plasma undergoes a contraction phase, from ~150 ns onwards. For the range of energies employed during experiments, a more rapid cooling of the plasma was apparent at higher laser pulse energies. Two possible hypothesis were envisioned to explain this phenomenon. The first possible explanation is a physical cooling of the plasma. The pressure of the plasma formed by the laser pulse is initially much greater than the pressure of the surrounding liquid and expansion occurs. At some later stage the pressures equalise and no further expansion takes place. From the results presented here, this appears to occur at a plasma lifetime of ~150 ns. Heat is conducted from the plasma to the surrounding liquid and a cooling of the plasma follows which obeys Newton's law of cooling. Following plume stagnation, in water the pressure exerted by the surrounding water on the plume eventually becomes so great that a contraction occurs.

6.3 Crater Formation in Air and Water

The craters formed by the laser pulse on the target surface were studied for ablation in air and water backgrounds. Using 200 laser pulses at various energies on an aluminium target, the craters were examined using a SEM. The craters formed in both environments showed very distinct profiles.

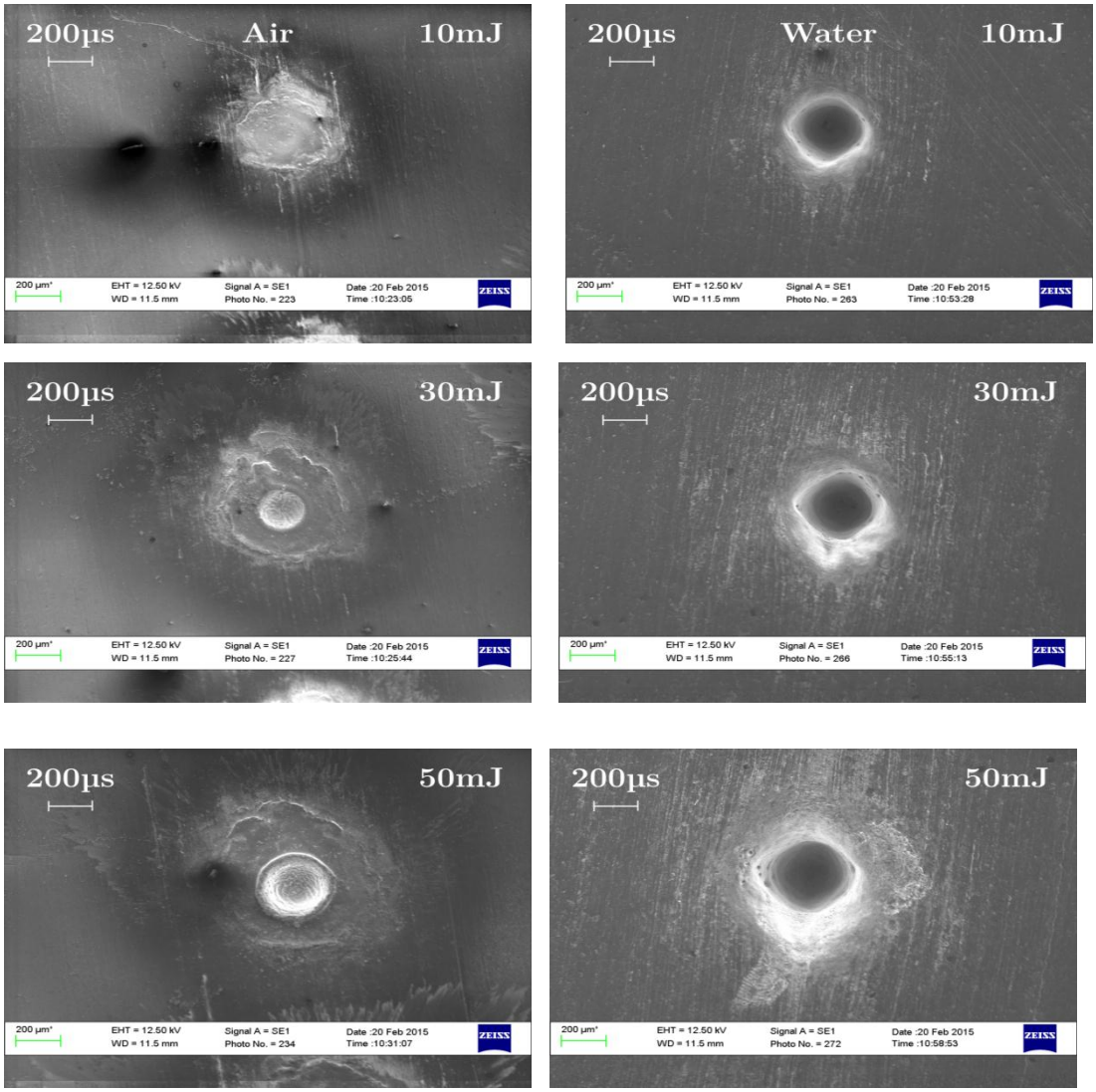

Figure 6.12: Craters formed in air (left hand column) and water (right hand column) at 10 mJ, 30 mJ and 50 mJ after 200 laser shots using an aluminium target and 1064 nm laser pulses.

Craters formed at a selection of laser pulse energies are shown in figure 6.12. At low pulse energy in air, not much material removal is observed from the SEM image. Limited removal of the target material is apparent with only a small indentation appearing on the target surface.

Ejected target material is located in the surrounding area of impact creating an appreciable outer crater of ejected mass. As the pulse energy is increased a shallow crater is formed which is also surrounded by an area of ejected material.

Craters formed in water appear to exhibit a much sharper profile with very little ejected material surrounding the crater site. Similar findings have been reported by Patel *et al.* [13] where the lack of target material is attributed to the vaporisation of the surrounding environment. Their hypothesis is outlined as follows. The incident laser beam acts to vaporise the water molecules surrounding the point of laser impact creating an instantaneous new phase of water molecules at the target surface. The pressure exerted by this instantaneously generated phase of water molecules prevents the re-deposition of evaporated metal particles.

Due to the pressure of the surrounding liquid, much more energy is transferred into the bulk material as compared to the case in air. This results in well-defined, deep craters being formed in the liquid environment which are clearly observed in the SEM images. Patel *et al.* accredit the considerable depth of the crater formed in water to a self-focussing of the laser beam onto the target surface [13]. They postulate that the curvature of the vaporised liquid layer above the target surface created by the laser pulse acts as a lens causing further focussing of the laser beam.

As the laser pulse energy increases, some evidence of an increase in crater diameter is observable in figure 6.12 around the periphery of the crater edges. The appearance of ejected target material becomes evident at higher pulse energies although to a lesser extent than that observed in air. Measurement of the diameter of craters formed in air and water was challenging in particular for the case in air where the crater edges are not easily defined. In this case, the crater diameter was defined as the diameter of material removed in the inner circular region not inclusive of the surrounding outer ring of ejected material. Assuming a Gaussian laser beam profile, the radial size of the ablated crater is related to the threshold fluence F_{thres} by:

$$F_{thres} = F\exp\left(-r_d^2/2r_f^2\right) \tag{6.1}$$

From which:

$$r_d^2 = 2r_f^2[\ln(F) - \ln(F_{thres})] \tag{6.2}$$

Which can be rewritten as:

$$D_d = \sqrt{2} D_f \left[ln\left(\frac{F}{F_{thres}}\right)\right]^{\frac{1}{2}} \tag{6.3}$$

Where r_d and D_d are the radius and diameter of the crater, F is the applied fluence, and r_f and D_f are the radius and diameter of the focussed beam [14], [15]. This equation is fitted to the experimental data in figure 6.13.

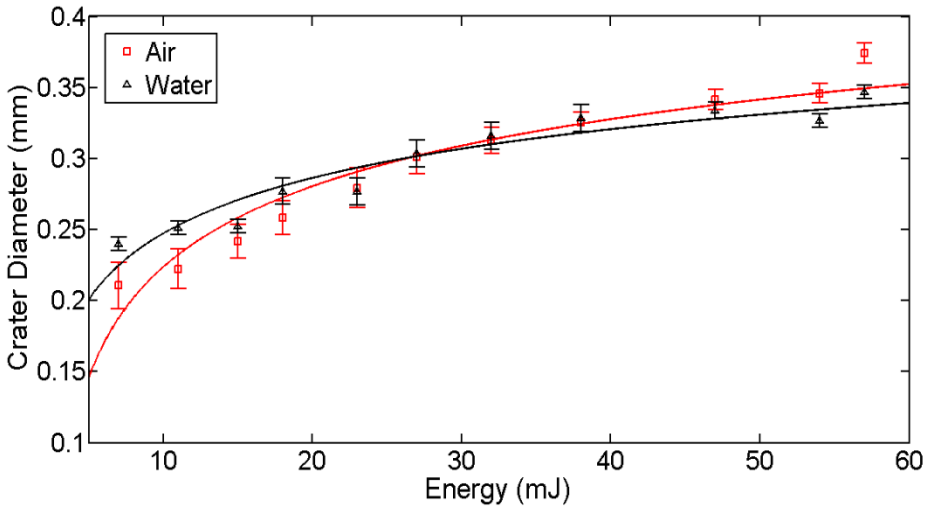

Figure 6.13: Crater diameters measured from SEM images in air and water for a range of laser pulse energies between 7-57 mJ. Shown also are fits to equation 6.3 ($\overline{R^2}$ = 0.93 and 0.90 for air and water respectively).

	D_f (mm)	F (Jcm^{-2})	$\overline{R^2}$
Air	0.20 ± 0.01	2.98 ± 0.25	0.93
Water	0.17 ± 0.02	1.30 ± 0.01	0.90

Table 6.8: Fitting parameters obtained by fits to ablated crater equation in air and water as a function of laser pulse energy corresponding to figure 6.13.

In both cases the crater diameter appears to increase with increasing laser pulse energy. The crater diameter measured in water exhibits a slightly weaker dependence on pulse energy than in air. The ablation threshold for aluminium calculated by the fitting of equation 6.3 to the data was 2.98 ± 0.25 Jcm^{-2} and 1.3 ± 0.01 Jcm^{-2} for air and water respectively. These values show similar agreement with threshold fluences of aluminium reported in the literature of 4 Jcm^{-2} in atmospheric air [16] and 1.4 Jcm^{-2} in water [13].

The higher ablation threshold observed in air may be due to the additional focusing of the laser beam in water ambient leading to a higher power density for the same laser fluence.

6.4 Shadowgraphy in Air and Water

A series of shadowgraphy measurements were carried out as a function of laser pulse energy in air and water the results of which are presented in chapter 4 and chapter 7 respectively. Here the shockwave behaviour is compared in air and water at a single laser pulse energy to highlight the salient features observed in each environment.

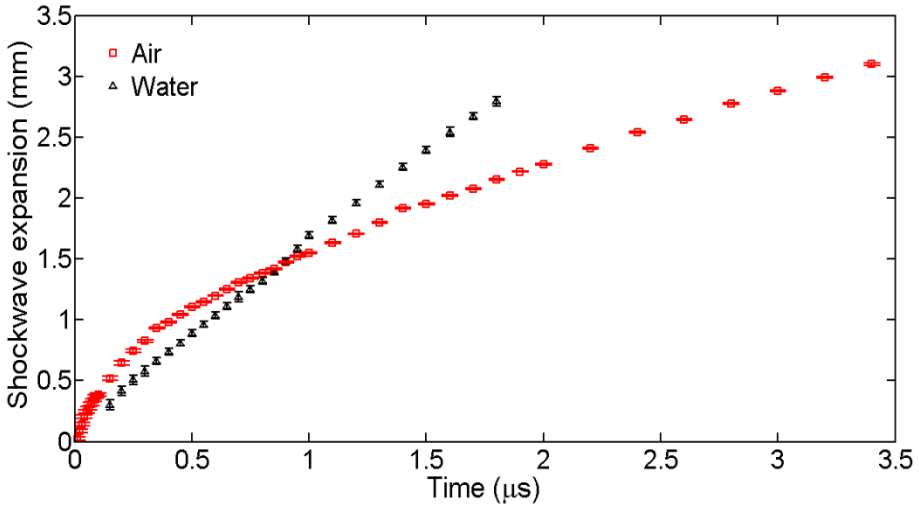

Figure 6.14: Shockwave expansion measured in air and water using 1064 nm, 52 mJ pulses.

Figure 6.14 shows two very different trends for the shockwave expansion in air and water. The first notable observation is the high velocity expansion occurring in the water. The shockwave disappears from the camera field of view (~3 mm from the target surface) before 2 µs whereas in air the shockwave is still observable until ~3.5 µs.

At early times a very rapid expansion is observable in both cases. In air, an instantaneous velocity of 3575 ± 57 ms^{-1} is reached for a pulse energy of 52 mJ. After

the first few hundred nanoseconds, the shockwave expansion velocity begins to drop, eventually tending towards a linear expansion (i.e., constant velocity) after ~2 µs where an average velocity of 584 ± 6 ms^{-1} is observed.

For the case of plume expansion in water the velocity of the shock-front is approximately constant. Some evidence of a high velocity component is observable at time delays < 400 ns. In this regime, an average velocity of 1965 ± 113 ms^{-1} is found for the shockwave expansion in water for a 52 mJ pulse. The transition to linear expansion occurs roughly 300-400 ns after plasma ignition. In this later regime, values of 1508 ± 25 ms^{-1} are measured for the shockwave expansion velocity in water.

The shockwave appears to travel at a velocity close to the speed of sound in that liquid which for the case of water is 1485 ms^{-1}. The shockwave velocity observed in air however far exceeds that of the speed of sound in air and was found to be a similar order of magnitude compared to previous studies [17], [18].

6.5 Interferometry in Air and Water

Normarski interferometry studies were carried out in air and water ambient at a range of laser pulse energies on an aluminium target. Interferometry is a useful methos for extracting plasma densities at times close to plasma ignition when optical spectra tend to be dominated by continuum emission and techniques such as Stark analysis of line profiles are not possible. The intention was to compare the electron densities in both environments as an additional method to calculations extracted from time resolved spectroscopy data. Interferograms were recorded in 10 ns intervals between 0-400 ns. The Normaski interferometry setup was used as described previously in chapter 3.

Interferometry was carried out in a background of air using 1064 nm laser pulses for the formation of the plasma. Interferograms were recorded using laser pulse energies of 8

mJ, 16 mJ, 38 mJ and 52 mJ. Figure 6.15 shows the interferograms recorded for the range of pulse energies used.

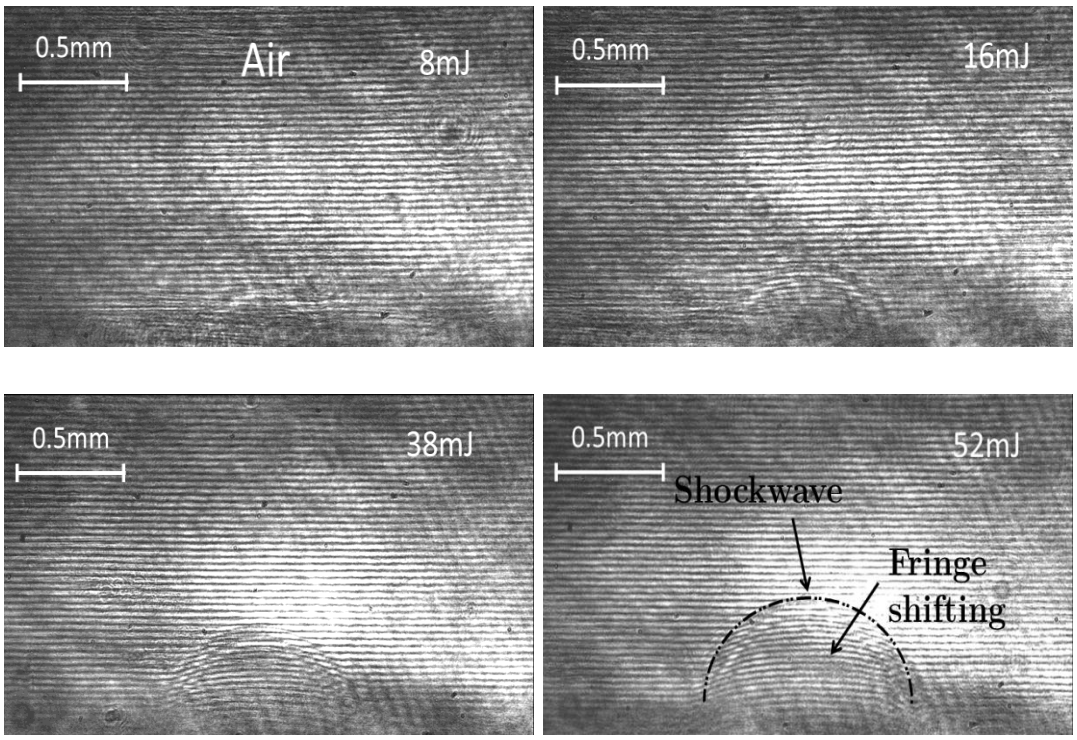

Figure 6.15: Interferograms recorded in air 50 ns after the laser pulse is fired using 8 mJ, 16 mJ, 38 mJ and 52 mJ pulses.

The greatest fringe shifts were recorded at high laser pulse energy. This demonstrates that the electron density within the plasma depends on the energy of the laser pulse used in its creation. For pulse energies of 8 mJ and 16 mJ, no discernable shifting of fringes were observed while for 38 mJ and 52 mJ pules, clear fringe shifts can be seen. As mentioned previously, a shock-front is created by compression of the gas due to the explosive delivery of energy to the target by the laser pulse. As such this compression creates a shock-front which is also observable from the interferograms. Interferograms were recorded up to 400 ns after the laser pulse is fired. Figure 6.16 demonstrates the dynamic evolution of the interferograms recorded in air using 52 mJ pulses.

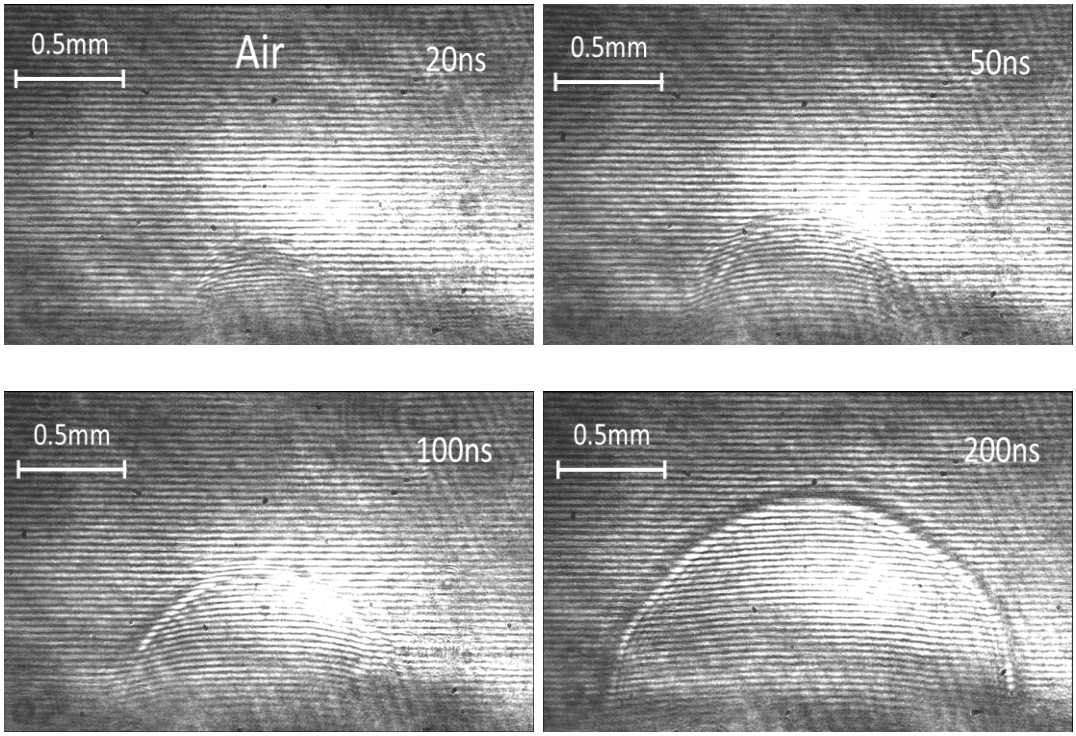

Figure 6.16: Interferograms recorded in air at 20 ns, 50 ns, 100 ns and 200 ns using a 52 mJ pulse.

The observed fringe shifts (with respect to the background interferogram in the absence of the plasma) are greatest within the first 100 ns of the laser pulse arriving at the target as is seen in figure 6.16. At times $>$ 100 ns minor fringe shift patterns are recorded up to roughly 200 ns for a 52 mJ laser pulse. This indicates that a rapid change in the electron density is occurring in the first 100 ns after the laser pulse. This is attributed to the high density of free electrons present in the early lifetime of the plasma due to high collision rates.

In the case of water for the range of laser pulse energies attempted, no clear interference fringes were observable. Figure 6.17 shows the interferograms recorded at a plasma lifetime of 50 ns at four different laser pulse energies.

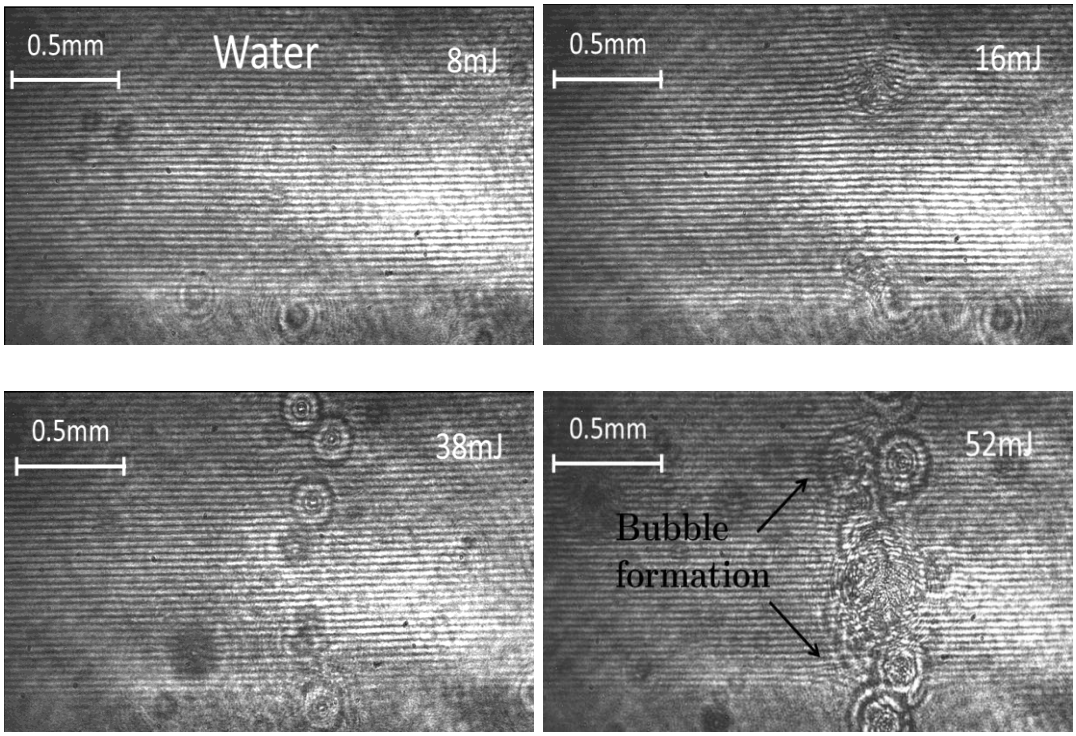

Figure 6.17: Interferograms recorded in water at 50 ns using pulse energies of 8 mJ, 16 mJ, 38 mJ and 52 mJ.

Bubble formation obscures the images in the first ~100 ns as is apparent from the interferograms in figure 6.17. The origin of the bubbles is due to localised vapourisation of the water. As the energy of the laser pulse increases, the production of bubbles increases, making the probing of the plasma electron density more challenging. The positions of the bubbles that are produced in the water vary in an apparently random fashion from shot to shot. For the range of laser pulse energies attempted, no evidence of interference fringes could be detected from the interferograms in water. Figure 6.18 shows a series of interferograms recorded using 8 mJ pulses, where the obscurity of images due to bubble production is minimised.

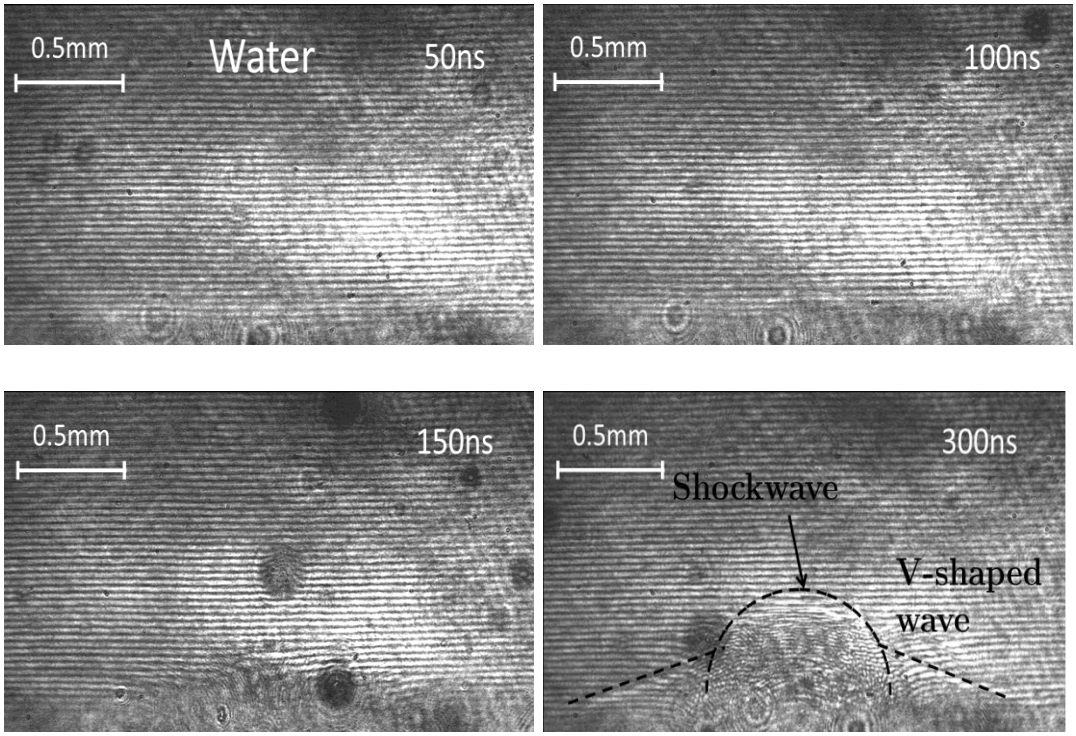

Figure 6.18: Interferograms recorded in water using an 8 mJ laser pulse at 50 ns, 100 ns, 150 ns and 300 ns.

Using 8 mJ pulses, no discernable fringe shifts are observed in water. Despite the absence of clear discernible and measureable fringe shifts, the appearance of the shockwave and V-shaped waves are observable in the interferograms after ~200 ns (figure 6.18) where a strong turbulent shock-front is observed similar to observations from shadowgraphy which are presented in chapter 7. Using higher pulse energies, the images are obscured by the strong presence of vapour bubbles. As a consequence interferometry was abandoned as a diagnostic for plasmas formed in water. In conclusion on this point, the objective of studying interferograms in water was to extract electron densities (via equation 2.41) present in the plasma at early delay times where continuum emission dominates spectroscopic data, especially in liquids. However, what can be deduced from the interferograms is that at times $>$ 200 ns only minor shifting of the interference fringes are observed in comparison to the case in air. This would indicate that the electron density for plasmas formed in liquids is relatively low for time delays in excess of 100 ns which is consistent with the paucity of emission for the plasma at these times.

6.6 Summary

From the results presented here it would appear that the expansion dynamics of a laser produced plasma are very different depending on the media in which they are formed. In the present work a study of the expansion of an aluminium plasma in air and water was investigated and different mechanisms were found to occur in each. At early plasma lifetimes the expansion of the plume in air could be concluded to follow either the shockwave or drag force models for the range of laser pulse energies used with a similar departure from the experimental data occurring using both models. These findings were in agreement with similar works [4]. Also, for plume expansion in water, a similar rapid expansion occurs at early times ($<$ 150 ns). Since the shockwave model predicts an infinite expansion as time increases, this was concluded to be a valid assumption only at early times where rapid expansion occurs. As time proceeds, a deceleration of the plume is observed due to resistance from collisions with the background gas. One important condition of the shockwave expansion model is that the ablated mass is small compared to the mass of background gas which is set in motion [19], [20]. This assumption is valid then for a plume expanding in an environment of low ambient pressure. As a result, the drag force model is concluded to be the more appropriate of the two expansion models in describing the plasma expansion in both air and water.

In the case of water, the expansion models could not be used to describe the behaviour at delay times greater than 150 ns. Here Newton's law of cooling was used to model the apparent contraction phase of the plasma observed in water. This effect was attributed to a rapid cooling of the interaction region between the plasma and the surrounding liquid. The effect was found to increase with laser pulse energy. Two explanations were proposed to account for the effects observed in water. The first explanation offered was an earlier extinction of emitting species as they de-excite and exchange excess energy more rapidly with the surrounding environment. This early extinction may be caused by an increased number of collisions provided by the high pressure background. The second possibility is that the pressure of the liquid medium at later times becomes comparable

and even greater than that of the expanding plume and a physical contraction of the plasma occurs. These two hypotheses were put forward in an effort to explain the contraction of the plasma observed in water ambient at times > 150 ns.

From shadowgraphy measurements, two very unique behaviours were discovered for the evolution of the shockwave in both environments. In air, a rapid expansion was observed initially in the first few hundred nanoseconds which then gradually transitioned to a linear behaviour after roughly 2 µs. In the case of water, an approximately linear behaviour was observed for the entirety of the observable expansion. Some evidence of a non-linear velocity expansion is apparent at very early times (< 400 ns). The velocity of the shockwave expansion in water was found to be several times greater than in air.

From interferometric studies in air, the electron density was found to be greatest at early plasma lifetimes using high energy laser pulses where strong fringe shifts were observed until a delay times of roughly 200 ns for a 52 mJ pulse. For 8 mJ and 16 mJ pulses, no significant shifting of fringes were observed. The results obtained for plasmas created in water however were deemed inconclusive. Using 8 mJ laser pulses, no clear shifting of fringes was observed similar to the case of air. For higher laser pulse energies, the recorded images were distorted by the strong presence of vapour bubbles. In studies comparing plasmas formed in air and water ambient in the literature, a higher electron density is reported by roughly an order of magnitude in a background of water [4], [21], [22]. As a consequence it is unlikely that a lower electron density exists for plasmas formed in the higher density water ambient as the findings of interferometric studies might suggest. It is therefore expected that for present measurements the images obtained in air and water are not easily comparable due to the substantial increase in the rate of bubble formation found in water as the laser pulse energy increases.

Craters formed in air and water were also studied as a function of laser pulse energy. The SEM images showed very unique features for both environments. After 200 laser shots in air, a limited amount of the material removal was noted by the presence of shallow craters. Surrounding the craters, rings of ejected target material were formed. As the laser pulse energy increased, the diameter of the craters formed increased also

indicating a greater amount of ablated material. The craters formed in water were considerably different. Here a very distinctive crater profile was observed with greater depth and sharper edges than those produced in a background of air. Some evidence of an increased diameter was observed with increasing pulse energy however the profile of the craters formed in water showed relatively little variation with pulse energy. The differences in the appearance of the craters formed in air and water demonstrate visually the strong role of confinement effects experienced by a plasma formed in a liquid environment.

References

[1] S. Lafane, T. Kerdja, S. Abdelli-Messaci, S. Malek, and M. Maaza, "Plasma dynamics study by fast imaging and Sm1−xNdxNiO3 thin film deposition," *Appl. Surf. Sci.*, vol. 256, no. 5, pp. 1377–1381, Dec. 2009.

[2] G. Yang, "Laser ablation in liquids: Applications in the synthesis of nanocrystals," *Prog. Mater. Sci.*, vol. 52, no. 4, pp. 648–698, May 2007.

[3] D. A. Freiwald and R. A. Axford, "Approximate spherical blast theory including source mass," *J. Appl. Phys.*, vol. 46, no. 3, p. 1171, 1975.

[4] B. Kumar and R. K. Thareja, "Synthesis of nanoparticles in laser ablation of aluminum in liquid," *J. Appl. Phys.*, vol. 108, no. 6, p. 64906, 2010.

[5] C. Porneala and D. A. Willis, "Time-resolved dynamics of nanosecond laser-induced phase explosion," *J. Phys. Appl. Phys.*, vol. 42, no. 15, p. 155503, Aug. 2009.

[6] S. S. Harilal, C. V. Bindhu, M. S. Tillack, F. Najmabadi, and A. C. Gaeris, "Internal structure and expansion dynamics of laser ablation plumes into ambient gases," *J. Appl. Phys.*, vol. 93, no. 5, p. 2380, 2003.

[7] D. B. Geohegan, "Fast intensified-CCD photography of YBa2Cu3O7−x laser ablation in vacuum and ambient oxygen," *Appl. Phys. Lett.*, vol. 60, no. 22, p. 2732, 1992.

[8] S. S. Harilal, C. V. Bindhu, M. S. Tillack, F. Najmabadi, and A. C. Gaeris, "Plume splitting and sharpening in laser-produced aluminium plasma," *J. Phys. Appl. Phys.*, vol. 35, no. 22, pp. 2935–2938, Nov. 2002.

[9] J. Noack and A. Vogel, "Laser-induced plasma formation in water at nanosecond to femtosecond time scales: calculation of thresholds, absorption coefficients, and energy density," *IEEE J. Quantum Electron.*, vol. 35, no. 8, pp. 1156–1167, Aug. 1999.

[10] R. K. Kushawaha, S. S. Kumar, I. A. Prajapati, K. P. Subramanian, and B. Bapat, "Polarization dependence in non-resonant photo-triple-ionization of CO $_2$," *J. Phys. B At. Mol. Opt. Phys.*, vol. 42, no. 10, p. 105201, May 2009.

[11] S. H. Jeong, R. Greif, and R. E. Russo, "Shock wave and material vapour plume propagation during excimer laser ablation of aluminium samples," *J. Phys. Appl. Phys.*, vol. 32, no. 19, pp. 2578–2585, Oct. 1999.

[12] E. de Posada, M. A. Arronte, L. Ponce, E. Rodríguez, T. Flores, and J. G. Lunney, "On the use of shockwave models in laser produced plasma expansion," *J. Phys. Conf. Ser.*, vol. 274, p. 12078, Jan. 2011.

[13] D. N. Patel, R. P. Singh, and R. K. Thareja, "Craters and nanostructures with laser ablation of metal/metal alloy in air and liquid," *Appl. Surf. Sci.*, vol. 288, pp. 550–557, Jan. 2014.

[14] J. Jandeleit, G. Urbasch, H. D. Hoffmann, H.-G. Treusch, and E. W. Kreutz, "Picosecond laser ablation of thin copper films," *Appl. Phys. Mater. Sci. Process.*, vol. 63, no. 2, pp. 117–121, Aug. 1996.

[15] D. Batani, "Short-pulse laser ablation of materials at high intensities: Influence of plasma effects," *Laser Part. Beams*, vol. 28, no. 2, pp. 235–244, Jun. 2010.

[16] I. Vladoiu, Stafe, M., Negutu, C., and Popescu I. M., "The dependence of the ablation rate of metals on nanosecond laser fluence and wavelength," *J. Optoelectron. Adv. Mater.*, vol. 10, no. 12, pp. 3177–3181, 2008.

[17] P. Hough, T. J. Kelly, C. Fallon, C. McLoughlin, P. Hayden, E. T. Kennedy, J. P. Mosnier, S. S. Harilal, and J. T. Costello, "Enhanced shock wave detection sensitivity for laser-produced plasmas in low pressure ambient gases using interferometry," *Meas. Sci. Technol.*, vol. 23, no. 12, p. 125204, Dec. 2012.

[18] S. S. Harilal, G. V. Miloshevsky, P. K. Diwakar, N. L. LaHaye, and A. Hassanein, "Experimental and computational study of complex shockwave dynamics in laser ablation plumes in argon atmosphere," *Phys. Plasmas*, vol. 19, no. 8, p. 83504, 2012.

[19] T. Kerdja, S. Abdelli, D. Ghobrini, and S. Malek, "Dynamics of laser-produced carbon plasma in an inert atmosphere," *J. Appl. Phys.*, vol. 80, no. 9, p. 5365, 1996.

[20] A. Kumar, R. K. Singh, K. P. Subramanian, B. G. Patel, S. Sunil, and I. A. Prajapati, "Effects of ambient pressure and laser fluence on the temporal evolution of 426.7 nm CII line in laser-blow-off of multilayered LiF-C thin film," *J. Phys. Appl. Phys.*, vol. 39, no. 22, pp. 4860–4866, Nov. 2006.

[21] B. Kumar and R. K. Thareja, "Growth of titanium nanoparticles in confined plasma," *Phys. Plasmas*, vol. 19, no. 3, p. 33516, 2012.

[22] B. Kumar and R. K. Thareja, "Laser ablated copper plasmas in liquid and gas ambient," *Phys. Plasmas*, vol. 20, no. 5, p. 53503, 2013.

Chapter 7

Laser Produced Plasmas in Liquid Environments

This chapter will present the main results on experiments carried out on laser produced plasmas created in a liquid background. Initial experiments were performed using a single Nd:YAG laser at the both the fundamental wavelength of 1064 nm and also at the second harmonic wavelength of 532 nm. The objective of these initial experiments was to observe the dynamic behaviour of a laser produced plasma in a liquid medium using imaging and spectroscopy and compare the results to those reported in the literature.

Shadowgraphy experiments were also performed to investigate the shockwave formed during intense laser-matter interactions in a liquid environment. The shock-front formed in water was studied as a function of laser pulse energy. During the investigation of the shockwave, the appearance of a bubble was discovered some microseconds after the plasma was formed. The behaviour of this bubble was measured as a function of time and at different laser pulse energies. Shockwave dynamics were also studied for a range of different liquids and metals.

The final experiments performed were double-pulse imaging and spectroscopic studies in water. The first pulse (1064 nm) was focussed onto the submerged target for plasma generation. The second pulse (532 nm) is delivered through the same focussing lens as

the first pulse and a second plasma is formed. Temperatures and densities were calculated from the spectroscopic data obtained from these single and double-pulse experiments.

Through the use of the techniques described, a rigorous study of laser produced plasmas in liquids could be achieved. Double pulse experiments performed in water reveal novel information on the cavitation bubble environment. The results of imaging measurements of the plasma formed within the cavitation bubble show for the first time the dynamic evolution of the plasma created in this environment. High order ionic emission is apparent from spectra obtained within the cavitation bubble. Self-absorption of aluminium neutral emission lines is observed at times corresponding to bubble formation and collapsing phases suggesting evidence of compression at these times. From the techniques applied and by comparison to observations in ambient air, strong evidence of a low pressure gaseous environment is revealed within the cavitation bubble.

7.1 Single Pulse Studies in Water

Ablation of a solid target submerged in liquid will result in the release of material. Continual firing of the laser will result in the formation of a colloidal suspension of nanoparticles. This suspension of nanoparticles will act as scattering centres effectively reducing the amount of light reaching the detector. To avoid these effects the volume of water was replaced after every 20 shots fired and the time resolved data was recorded in a non-chronological order (i.e. in a semi-random manner with respect to time delay). The fluctuations in the recorded signal after 20 laser shots fired were deemed to be no greater than the natural fluctuation of a laser produced plasma i.e. $\pm$ 10%. The data were obtained by summing all pixel intensity values for successive images and normalising to unity. Emission was recorded for the first 10ns of the plasma lifetime. The integrated intensity was found to decrease by approximately 20%, 40%, 50% and 60% after 50, 100, 150 and 200 shots fired respectively. Visual discoloration of the

solution can be observed when an appreciable amount of debris is present in solution, typically after ~500 laser shots have been fired.

7.1.1 Imaging

The dynamics of a laser produced plasma formed in deionised water using a 1064 nm Nd:YAG laser were studied using time resolved imaging. Single shot images were recorded with an ICCD operated with a gate width of 10 ns. An 800 nm short-pass filter was placed in front of the CCD sensor to block scattered light from the laser itself.

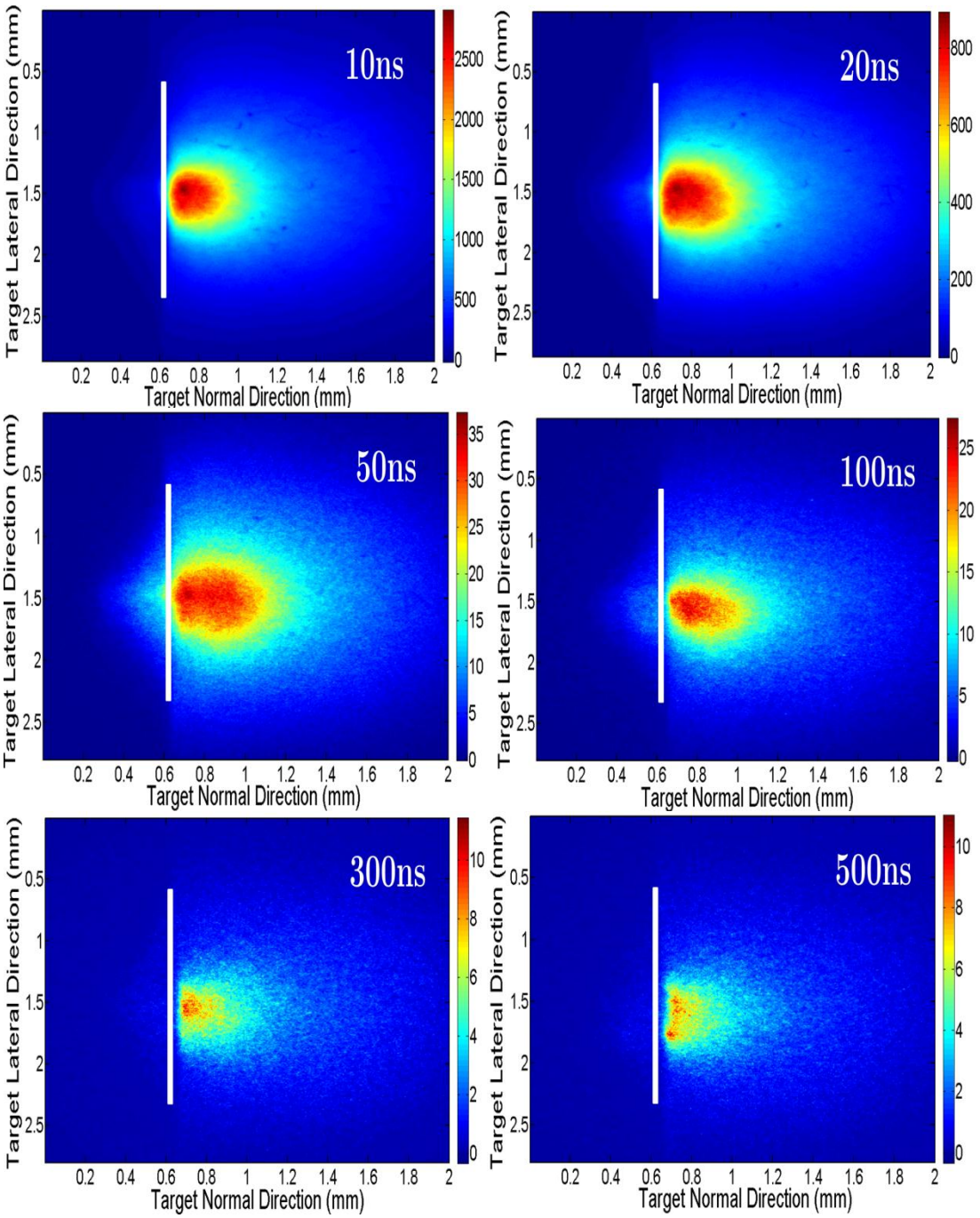

Figure 7.1: Time resolved images of aluminium plasma emission in deionised water created using 1064 nm, 52 mJ pulses for time delays of 10, 20, 50, 100, 300 and 500 ns. The ICCD gate width used was 10 ns. The intensity (no. of counts) is represented by the colour scale bar shown on the right hand side of each image.

Time resolved images of emission from aluminium plasmas at short and long time delays are shown in figure 7.1. The visible emission observed behind the target surface position is due to scattering of the plasma radiation from the highly reflective metallic surface. From visual inspection of the images it can be noted that the plasma emission

is strongest at early times and is seen to weaken considerably from 100 ns onwards. The plasma appears to expand initially and then appears to contract after ~100 ns. At long delays (i.e. > 300 ns) it is clear that the plasma emission has faded significantly. The evolution of the luminous plume front was extracted from image lineouts as a function of time (as described in section 2.6). The plume front was defined as the position at which the count intensity was $1/e$ (~0.37) of its maximum value in the expansion direction normal to the target surface. The plume front position is then the distance of the plume front from the target position.

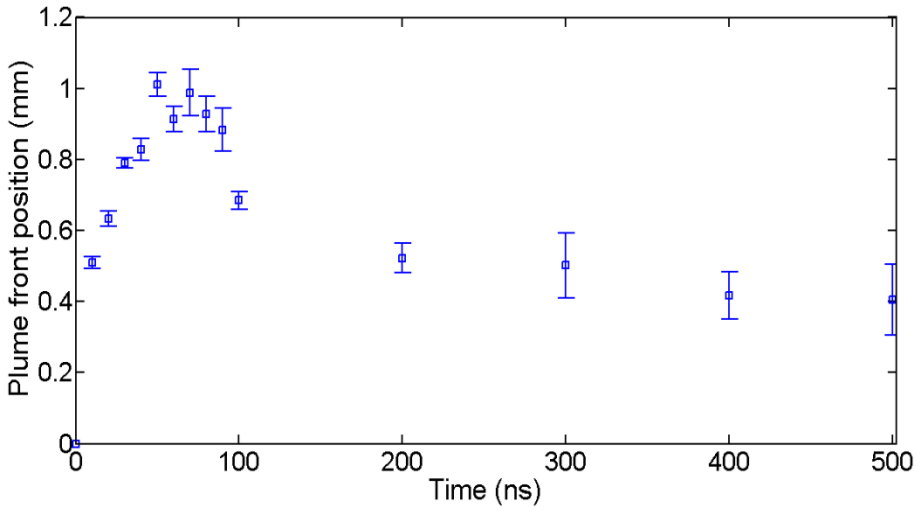

Figure 7.2: Plume front position of an aluminium plasma in deionised water using 1064 nm, 52 mJ pulses extracted from imaging data, some of which are shown in figure 7.1.

Figure 7.2 shows the luminous plume front expansion, measured as a function of time. A rapid expansion of the plasma is observed reaching a distance of *ca.* 1 mm followed by an apparent "contraction". This contraction occurs between 80 to 100 ns and is followed by a much more gradual receding of the plume front up to a delay of 500 ns. This observation may be attributed to one of two processes. Either the expanding plume is being physically forced back by the pressure of the surrounding liquid or the plume is expanding non-adiabatically into the liquid environment and thus heat is being conducted from the plasma to the liquid. A similar behaviour has been previously reported for plasmas formed in water on metallic wire [1], [2] where the apparent

contraction of the plume was attributed to a fast cooling of ablated material in the outer plasma regions due to the interaction of the plasma with the surrounding liquid.

Single pulse imaging studies were also carried out using the 532 nm output of the Surelite Nd:YAG laser. A notch filter centred at 532 nm was place in front of the ICCD camera to reject scattered light from the laser pulse. A contrasting behaviour was observed compared to the case of the 1064 nm laser with visible plasma emission exhibiting longer persistence times. The strength of plasma emission in terms of ICCD counts was also much greater using the 532 nm pulses. A series of images for time delays from 25 ns to 2 µs is shown in figure 7.3.

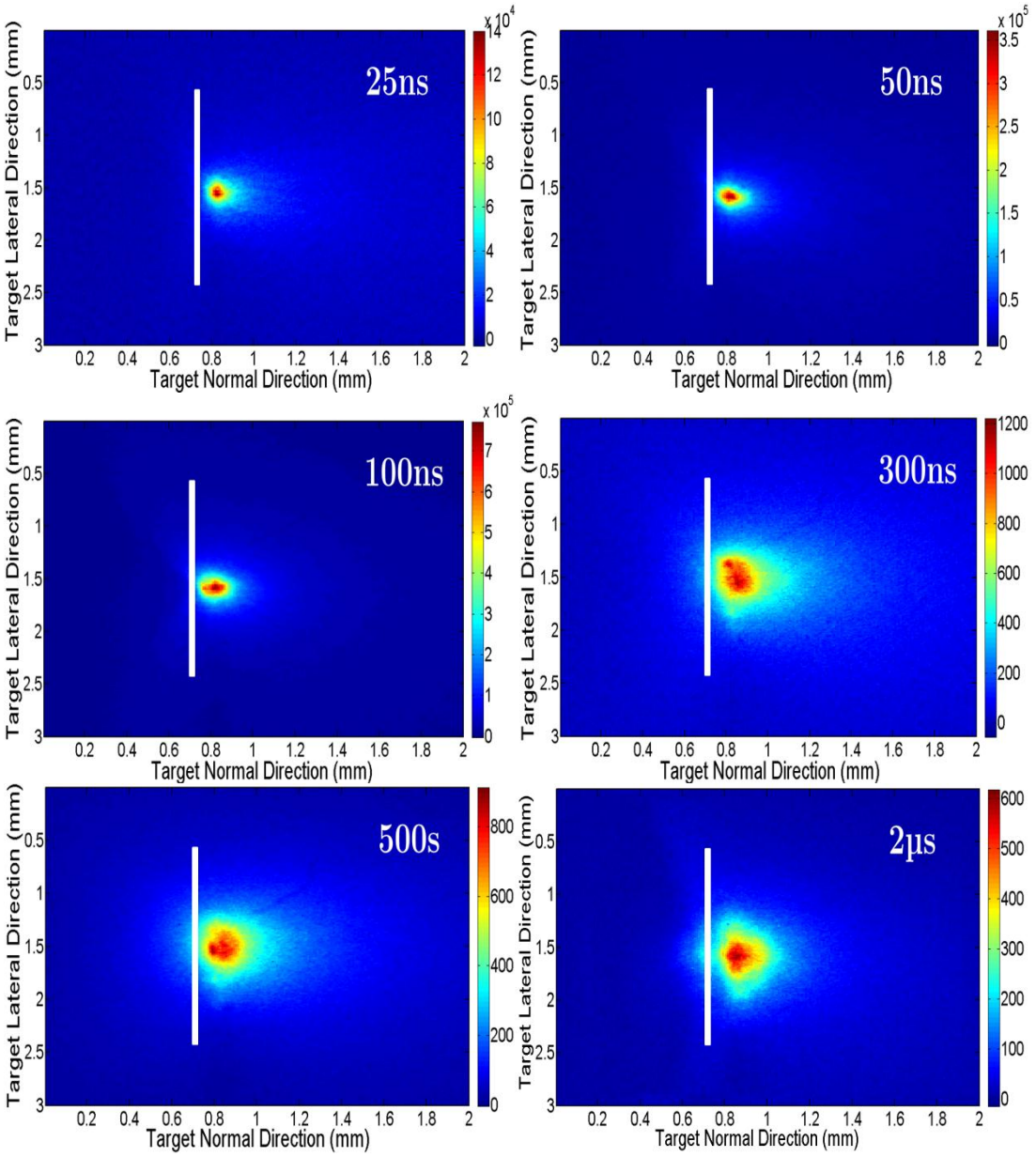

Figure 7.3: Time resolved images of aluminium plasma emission in deionised water using 532 nm, 52 mJ pulses and a 25 ns ICCD gate width. The intensity (no. of counts) is represented by the colour scale bar shown on the right hand side of each image.

Measurable plasma emission continued to be observed until ~10 µs after the 532 nm pulse was incident on the target. This is a significantly longer duration of plasma emission in comparison to the emission observed using the 1064 nm laser. The luminous plume front expansion was extracted from the imaging data using the procedure described previously and the results are shown in figure 7.4. A distinctly different behaviour is observed compared to the 1064 nm case shown in figure 7.2. An initial

expansion of the plume is observed at early times ~400 ns. As time increases a plateau is reached whereby the plasma plume appears to remain stationary in space and is not seen to contract as was the case with the 1064 nm laser. This plateau, observed for the plume front expansion in water has been reported in a similar study [3], and is comparable to the dynamic behaviour observed for a plasma expanding into a background of air.

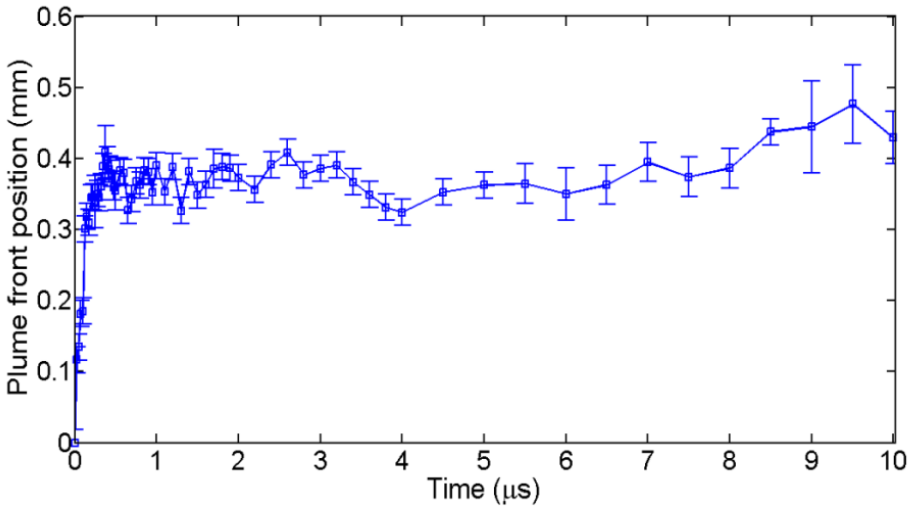

Figure 7.4: Plume front position of an aluminium plasma in deionised water using 532 nm, 52 mJ laser pulses.

For the plasma formed using the 1064 nm laser the luminous plume front reaches a distance of ~1 mm very rapidly and then is seen to contract. This is in contrast to the 532 nm case where the plume front expansion occurs gradually and a more confined plume is observed reaching a maximum size of ~0.4 mm.

The differences in the dynamic behaviour were thought to be due to the differences in the plasma temperatures. As the temperature of a laser produced plasma in collisional-radiative equilibrium scales as $(I\lambda^2)^{0.6}$ [4], the temperature of the plasma created by the 1064 nm laser will be something of the order of 2.3 times greater than that of the 532 nm case. It is conceivable then that the hotter plasma will lose its energy more quickly due to an increased number of collisions occurring between the highly energetic ions and electrons with the surrounding high pressure liquid and so it radiates more brightly but

for a shorter time period than in the case of the cooler but more slowly expanding 532 nm plasma.

7.1.2 Spectroscopy

Time integrated spectroscopy was carried out using single laser pulses at wavelengths of 1064 nm and 532 nm on aluminium targets in deionised water. Although broadband emission was the main observation, some slight evidence of neutral line emission was observed using 532 nm laser pulses. Typical emission spectra recorded using 52 mJ pulses are shown in figure 7.5.

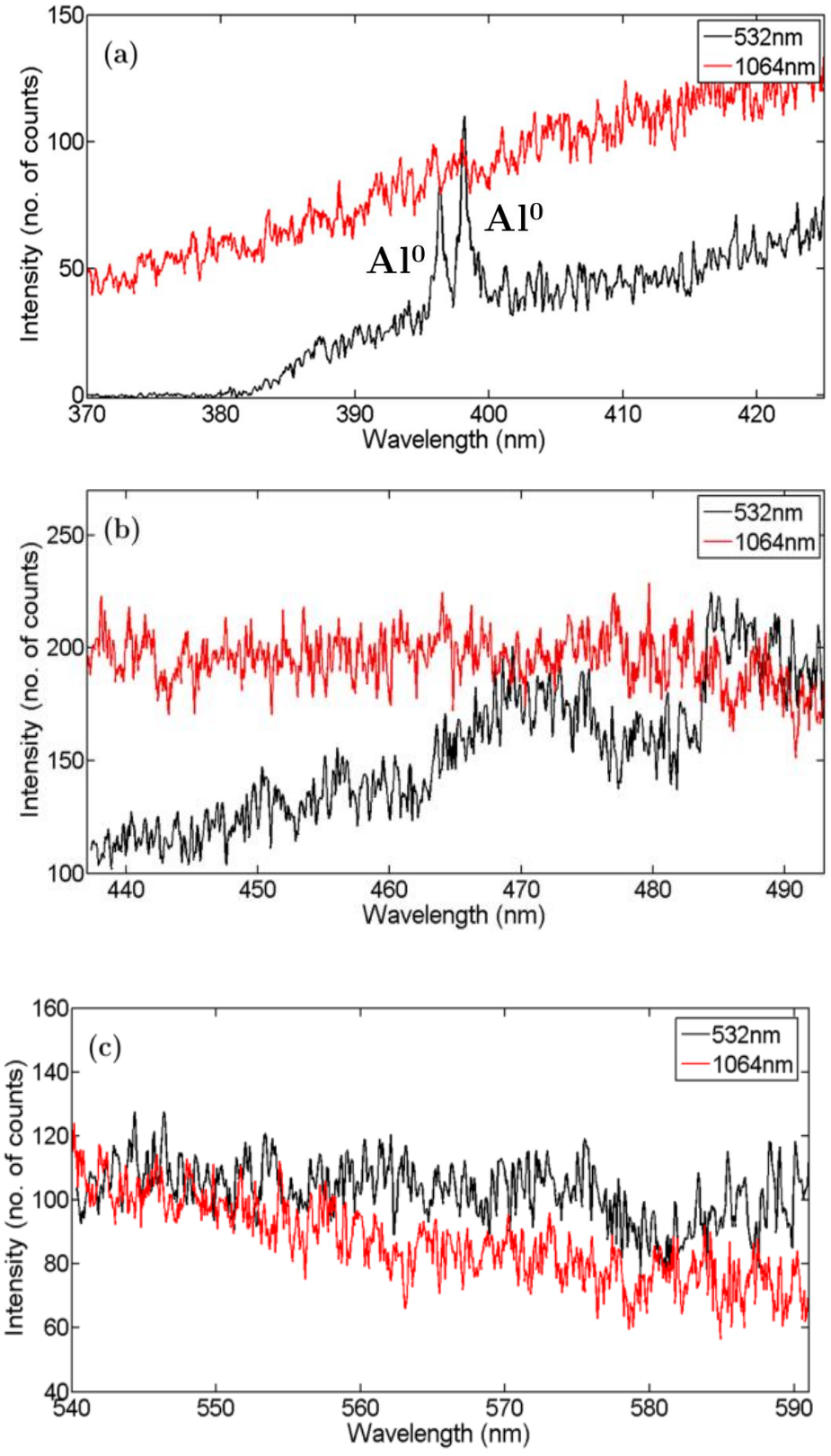

Figure 7.5: Time integrated spectra recorded in deionised water for a single 532 nm and 1064 nm pulses at 52 mJ per pulse in spectral regions of interest; (a) aluminium neutral region, (b) aluminium singly ionised region, and (c) aluminium doubly ionised region.

Some evidence of atomic line emission can be noted from the time integrated spectrum of the aluminium neutral doublet $3p(^2P^0_{1/2,\ 3/2}) - 4s(^2S_{1/2})$ using the 532 nm laser (figure 7.5 (a)). Aside from this, the spectra show little or no evidence of ionic emission in water at both laser wavelengths with broadband continuum emission dominating the recorded spectra. In the case of 1064 nm laser pulses, continuum emission was rapidly quenched in the order of several hundreds of nanoseconds (laser pulse energy dependant) suggesting rapid cooling of the plasma and fast electron-ion recombination. Due to the high thermal capacity of the surrounding water molecules a rapid exchange of energy causes fast quenching of the plasma [1]. The plasma created in water is hot and dense and the majority of energy delivered to the system has dissipated on a short a time scale. Electron temperatures of several thousand Kelvin have been typically reported for laser produced plasmas in liquids with rapid extinction also being observed [2], [5]. Radiative-recombination processes are thought to account for the continuum emission observed in laser plasma formed in water. The absence of line emission in the present studies is believed to be related to the rapid condensation of the plasma into nanoparticles. Nanoparticle formation in less dense media such as air will occur several microseconds post plasma ignition during the plasma cooling phase. In a liquid environment, the plasma cooling phase occurs on a timescale of a few hundred nanoseconds and as a result nanoparticle formation occurs on a much faster timescale. It is proposed that the absence of line emission may be due to the rapid quenching of the plasma which occurs as a result of the nanoparticle formation.

7.2 Shadowgraphy

7.2.1 Shockwave Formation

When a laser pulse is focussed onto a solid target *in vacuo,* it is well known that a shock-front propagates back into the target as the plasma plume expands away from it

[6]. In a high pressure environment such as a gaseous or liquid ambient, the plasma launches a strong shockwave as it expands into its confining environment with a velocity which depends on quantities such as the energy deposited by the plasma as well as the ambient density and specific heat [7]. Shadowgraphy studies were carried out in order to investigate the laser-induced shockwave dynamics associated with a plasma expanding into a liquid environment. The 1064 nm laser was used to form the plasma and single shot shadowgrams were recorded for a range of laser pulses energies (8 $\pm$ 3 mJ, 16 $\pm$ 3 mJ, 32 $\pm$ 3 mJ and 52 $\pm$ 3 mJ). Figure 7.6 shows some examples of shadowgrams recorded at different times after plasma breakdown for a laser pulse energy of 8 mJ.

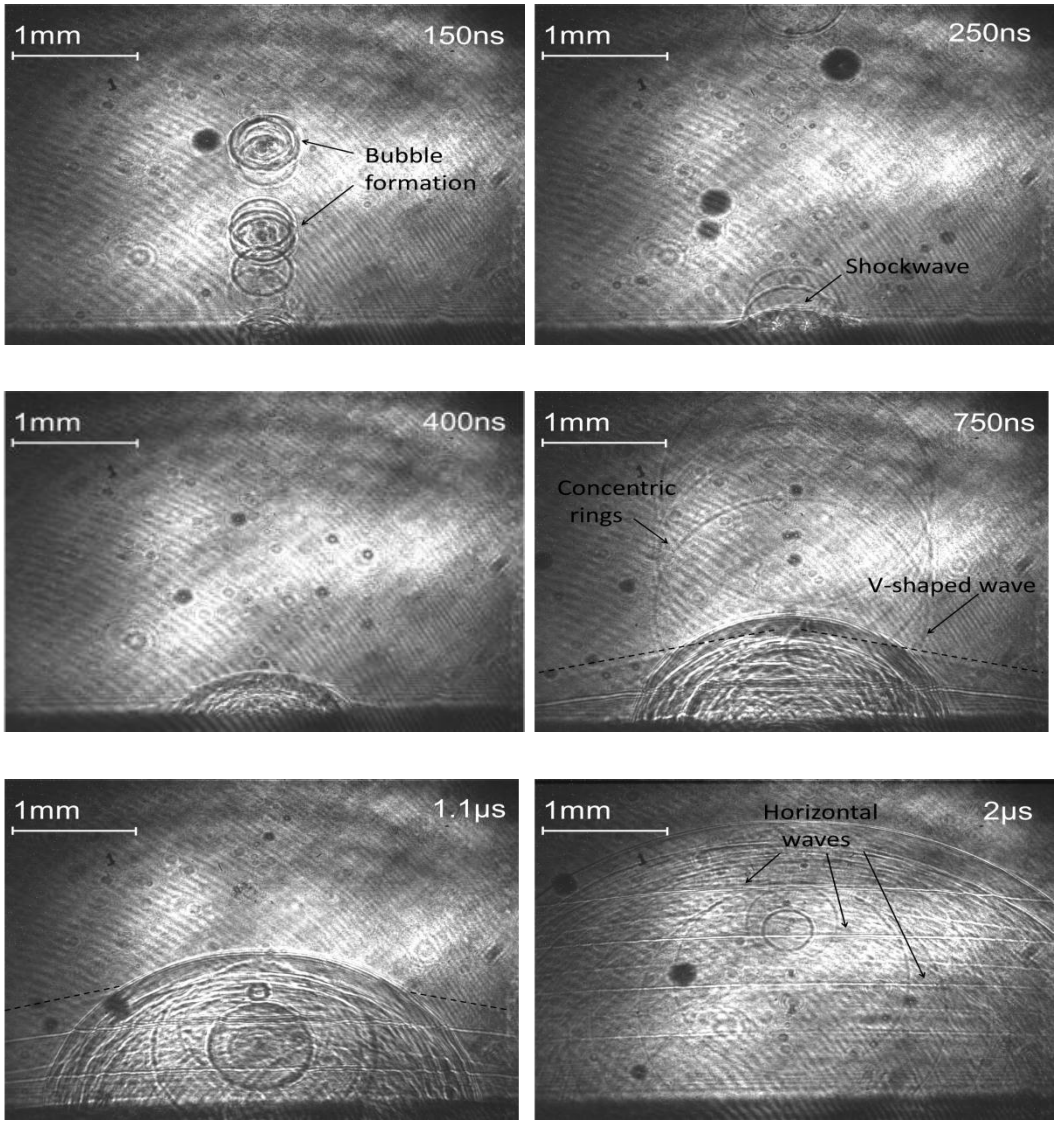

Figure 7.6: Shadowgrams of shockwave emitted from a laser produced aluminium plasma in water ambient using 8 mJ laser pulses at different time delays.

The shockwave first appears in the shadowgrams ~200 ns after the laser-target interaction has taken place. Images in this first 200 ns show production of bubbles similar to that seen in figure 7.6 at 150 ns. These tiny air bubbles may form due to impurities in the water. The shockwave may be masked at these early times by the presence of the bubbles. The first visual evidence of the shockwave appears around ~250 ns. A turbulent shock-front is apparent in the initial stages of the shock-front formation in water. The shockwave then begins to expand radially from the deflagration zone. Another interesting feature observed in the shadowgrams was the appearance of

concentric rings, an example of which can be seen in figure 7.6 at a delay time of 750 ns after the delivery of the laser pulse. These rings were observed to increase in diameter as a function of delay time and are believed to be caused by shockwaves emanating radially outward from impurity sites in the water. An inverted V-shaped wave appears around 400 ns which is indicated with a white arrow in figure 7.6 at 750 ns. The presence of this type of wave has also been noted in similar works [8], [9]. During a study of the underwater laser-induced shock process Nguyen *et al.* [9] made observations of this inverted V-shaped wave using a custom-designed photoelasticity imaging technique. When a laser-induced shock wave forms at the target surface, a mechanical impulse is also generated within the solid [10]. The photoelasticity method allows the stress waves produced within the bulk target to be imaged. A longitudinal, compressive wave front is created in the bulk (termed a P-wave). When this stress wave induced in the solid phase exceeded the distance travelled by the shockwave front in the water, a V-shape wave was detected. The origin of the V-shaped wave is postulated to be a shockwave travelling horizontally along the target interface at an acoustic velocity [9]. This V-shaped wave is observable in the shadowgrams until roughly 1.5 µs at which point the energy of the wave has dissipated making the wave indistinguishable in the shadowgram. Horizontal waves are then detected around 750 ns. These horizontal waves are seen to be evenly spaced in the shadowgrams indicating a constant velocity through the water. The spacing between the vertical waves is 0.48 ± 0.4 mm. The appearance of these waves has been reported in a recent paper on bubble dynamics where they attribute the phenomenon to sound waves generated by shockwave reflections from the surface of the target [11]. Taking the velocity of sound in water to be 1480 ms^{-1} yields a value of 6172.8 ± 258.79 ms^{-1} for the acoustic velocity of aluminium which is consistent with the literature value of 6135 ms^{-1} and strongly suggests the origin of the horizontal waves to be sound waves.

The shock-front position was retrieved from the shadowgrams as a function of time for a range of laser pulses energies.

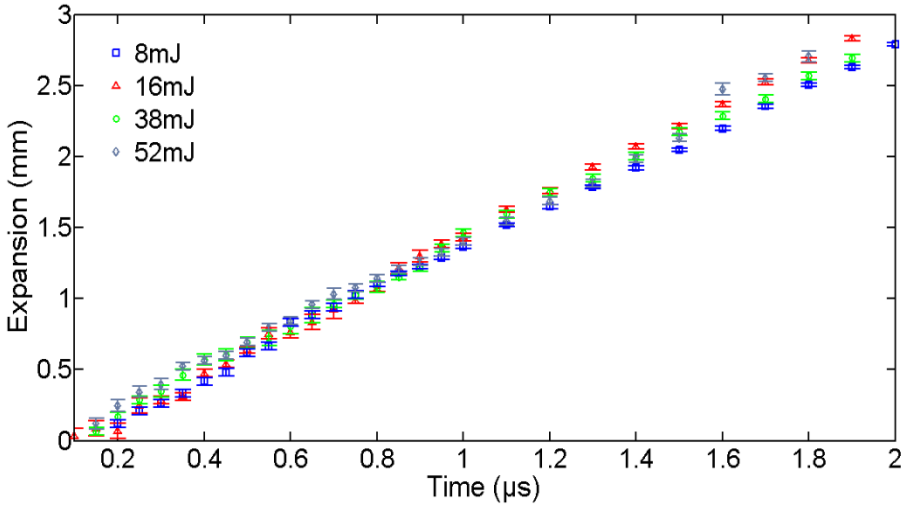

Figure 7.7: Shockwave expansion launched by a laser produced aluminium plasma plume in water for a range of laser pulse energies (8 mJ, 16 mJ, 38 mJ and 52 mJ).

From figure 7.7 the expansion of the shockwave appears to be roughly constant and independent of laser pulse energy. However at early times < 450 ns there is some evidence of a non-linear expansion occurring. These two different expansion regimes have been reported in the literature where a transition from rapid expansion to a linear behaviour is observed [12], [13]. In these works the authors report supersonic velocities of *ca.* 2600 ms^{-1} in the initial stages of the shockwave expansion at times < 200 ns. In the shadowgrams recorded in the present work, the location of the shock-front was not easily discernable from the images at early times due to the presence of bubbles as previously mentioned.

The expansion of the plasma plume was fit to a linear regression model shown in figure 7.8.

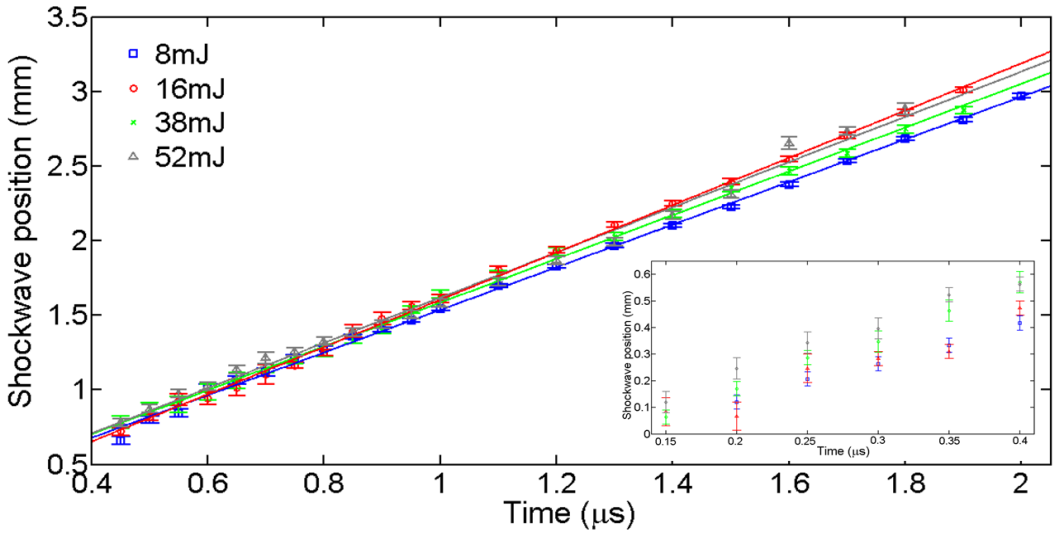

Figure 7.8: Linear fits to the shockwave data obtained using 1064 nm laser pulses of various energies of 8 mJ, 16 mJ, 32 mJ and 52 mJ ($\overline{R^2}$= 0.99, 0.99, 0.99 and 0.99 respectively). Inset shows evidence of a non-linear behaviour in the shockwave expansion for delay times < 450 ns.

	$m(ms^{-1})$	$\overline{R^2}$
8mJ	1430 ± 9.5	0.99
16mJ	1456 ± 15	0.99
38mJ	1469 ± 13	0.99
52mJ	1508 ± 4.5	0.99

Table 7.1: Fitting parameters obtained by linear regression fits to shockwave expansion in water using 8 mJ, 16 mJ, 38 mJ and 52 mJ pulses corresponding to figure 7.8.

The expansion of the plasma plume was fit to a linear regression model. The shockwave expands to approximately 2.5 mm in 1.6 μs. Assuming the shock-front expansion is independent of laser pulse energy, an average value of 1464 ± 14 ms^{-1} is obtained in the late regime at times > 400 ns. In the assumption of an entirely linear behaviour in both early and late regimes, an average velocity of 1489 ± 7 ms^{-1} is retrieved. This indicates that two velocity components exist during the shockwave expansion, an initial high velocity component which transitions to a lower velocity expansion several hundred nanoseconds after the delivery of the laser pulse.

The expansion of the shockwave in the early regime exhibits some evidence of non-linearity, i.e. the plasma exhibits a high initial expansion velocity but starts to

decelerate and continues to do so until *ca.* 400 ns at which point a constant velocity is reached. It is expected that the non-linearity of the expansion (deceleration of the shock-front) would be more evident at times earlier than 150 ns. Events occurring at these earlier times however were not observable in the measurements here due to the bubble formation.

The shockwave was also studied for a range of different liquids at a fixed laser energy of 8 mJ shown in figure 7.9.

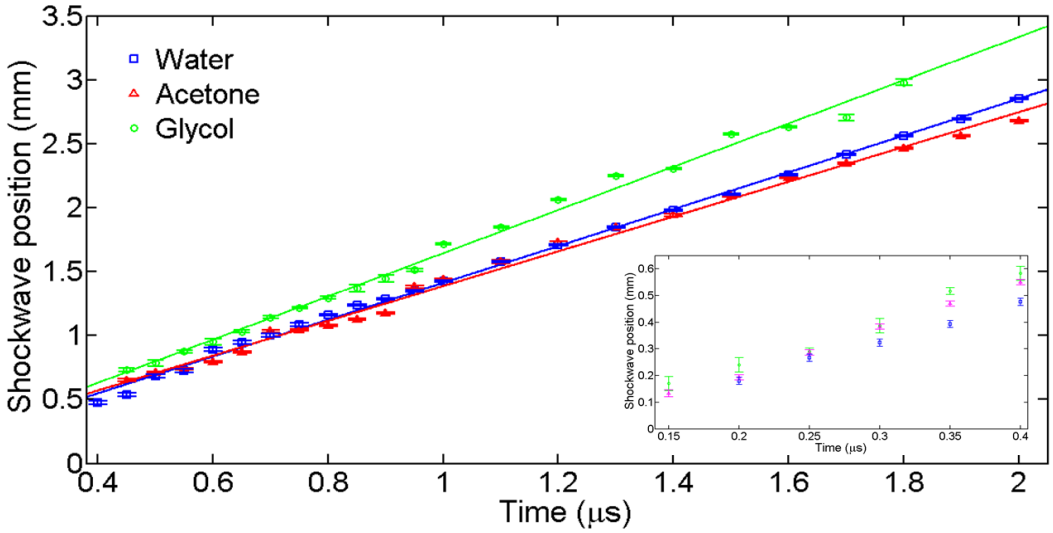

Figure 7.9: Shockwave expansion in water, acetone and ethylene glycol using 1064 nm, 8 mJ pulses. The data were fit to a linear trend with $\overline{R^2}$ values = 0.99, 0.99 and 0.99 obtained for water, acetone and ethylene glycol respectively. Inset shows evidence of a non-linear behaviour in the shockwave expansion for delay times < 450 ns.

	$m(ms^{-1})$	$\overline{R^2}$
Water	1360 ± 5	0.99
Acetone	1440 ± 5	0.99
Glycol	1690 ± 10	0.99

Table 7.2: Fitting parameters obtained by linear regression fits to shockwave expansion in water, acetone and glycol using a fixed laser pulse energy of 8 mJ corresponding to figure 7.9.

The shockwave velocity appears approximately constant in the three liquid environments. Under the assumption of a linear expansion at late time (i.e., 0.4 μs to 2 μs), shock-front velocities of 1360 ± 5 ms^{-1} and 1440 ± 5 ms^{-1} were measured in acetone

and water respectively using a laser pulse energy of 8 mJ. On the other hand the velocity observed in glycol was higher with the linear fit returning a value of 1690 ± 10 ms^{-1}. This trend is likely due to the differences in acoustic velocity of the respective liquids which are reported to be 1144 ms^{-1}, 1496 ms^{-1} and 1660 ms^{-1} at a temperature of 25 °C for acetone, water and ethylene glycol respectively. Looking at the data for all times between 0.4 µs and 2 µs the shock-front expansion obtained for plasma formed on aluminium targets using 8 mJ pulses for all three liquid environments seen in figure 7.9 is linear to a reasonable approximation. Some slight evidence of a non-linear behaviour was again observed at early delay times < 450 ns. Under the assumption of an exclusively linear behaviour for the shockwave expansion (i.e., 0.15 µs to 2 µs), velocities of 1409 ± 2 ms^{-1}, 1480 ± 5 ms^{-1} and 1733 ± 6.5 ms^{-1} are obtained for acetone, water and ethylene glycol respectively which are quite close to the values obtained for the exclusively linear late time regime.

Shock-fronts were also measured for different metals in water at a fixed pulse energy of 8 mJ. The shock-front expansions for each metal do not follow a monotonic trend with atomic mass.

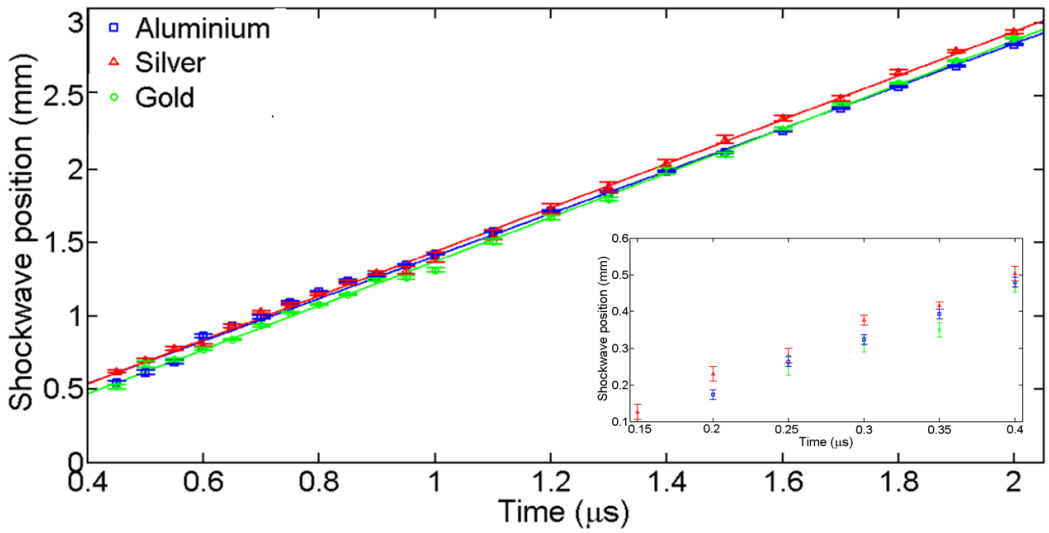

Figure 7.10: Shockwave expansion extracted from time resolved shadowgraphy data for plasmas formed on aluminium, silver and gold targets submerged in water at a fixed laser energy of 8 mJ. Linear fits to the data resulted in residual $\overline{R^2}$ values of 0.99, 0.99 and 0.99 for aluminium, silver and gold.

	$m(ms^{-1})$	$\overline{R^2}$
Aluminium	1454 ± 5	0.99
Silver	1503 ± 6	0.99
Gold	1508 ± 1	0.99

Table 7.3: Fitting parameters obtained by linear regression fits to shockwave expansion using aluminium, silver and gold targets at a fixed laser pulse energy of 8 mJ corresponding to figure 7.10.

Looking to figure 7.10 and time delays in excess of 400 ns, predominantly linear shock-front expansion trends were observed for the different metals studied. The velocities extracted appear to be independent of the target material. Values of 1454 ± 5 ms^{-1}, 1503 ± 6 ms^{-1} and 1508 ± 1 ms^{-1} were determined for shock-front velocities in the linear regime for aluminium, silver and gold respectively. Similar to the observations in different liquids, a small non-linear velocity component was present in the early regime at times < 400 ns. Assuming a linear relationship for the entire observable lifetime of the shockwave results in velocities of 1481 ± 5.5 ms^{-1}, 1515 ± 3.5 ms^{-1} and 1511 ± 4.5 ms^{-1} using aluminium, silver and gold targets, As before, this suggests a high velocity expansion in the initial stages of the shock-front expansion which sees deceleration out to *ca.* 400 ns followed by a largely constant expansion velocity out to several microseconds after plasma breakdown in liquid ambient.

When the shockwave has expanded far from the target surface the appearance of horizontal, evenly spaced waves are observed. The spacing of these horizontal waves are clearly very different depending on the target material. Figure 7.11 below shows shadowgram images obtained in water at a fixed time delay of 2 μs after the plasma pulse (8 mJ, 1064 nm) using aluminium, silver and gold targets of 1 mm thickness each.

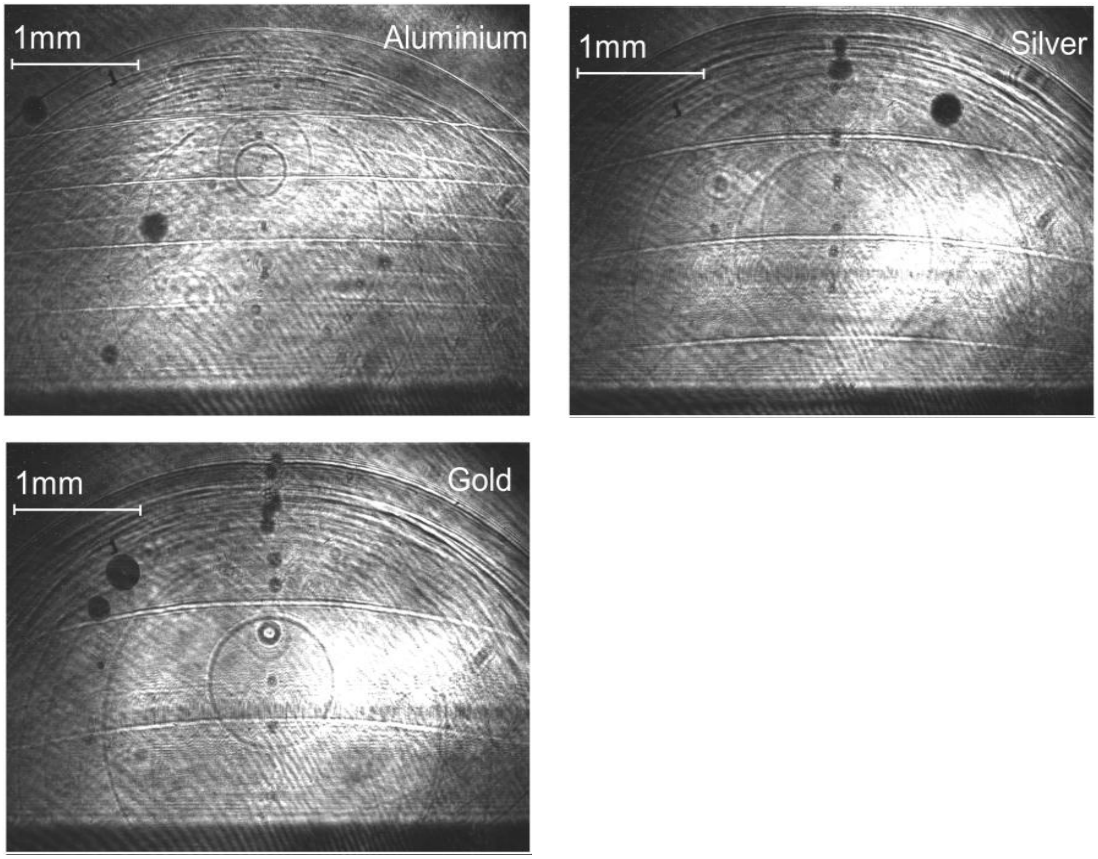

Figure 7.11: Shadowgrams of shockwave emitted from a laser produced plasma in water ambient using 8 mJ laser pulses in aluminium, silver and gold at a fixed time delay of 2 µs.

The spacing of the waves is closest for the aluminium target with the most distant spacing occurring for the gold target. Following the method described by Tanabe *et al.* [11], the spacing between the horizontal waves may be related to the acoustic velocity of the target material. Taking the acoustic velocity of aluminium, silver and gold to be 6135 ms^{-1}, 3650 ms^{-1} and 3240 ms^{-1} respectively, and the velocity of sound in water to be 1480 ms^{-1}, the origin of these waves seems likely due to acoustic waves reflections from the target surface. The measured distances between waves from figure 7.11 are calculated to be 482.9 ± 4 µm, 779.2 ± 11 µm and 899.1 ± 16 µm for aluminium, silver and gold respectively. Comparison to the theoretical values of 482.5 µm, 811.0 µm and 913.2 µm shows good agreement and further evidence that sound waves reflections account for the presence of these horizontal waves.

After the disappearance of the shockwave came the appearance of another feature namely a bubble, or "cavitation bubble" as it is referred to in the literature, is formed by vapour released from the plasma [18], [19].

7.2.2 Cavitation Bubble

The delivery of a high intensity laser pulse to a liquid will result in the formation of a cavitation bubble. This process, termed "optical cavitation" is the sudden breaking of liquid molecules bonds by particles, or photons [20]. After plasma creation, a bubble of gas is generated having internal pressure and temperature very much greater than that of the surrounding medium [21]. As energy is transferred from the expanding plasma to the surrounding liquid, local heating results in the production of a layer of water vapour at the boundary of the plasma volume. As the plasma cools this layer of water vapour grows into a cavitation bubble [5]. The presence of the cavitation bubble can be seen in the shadowgrams of figure 7.12 where a dark hemispherical shape is observed due to the deflection of the probe beam. The cavitation bubble of figure 7.12 was formed using an 8 mJ, 1064 nm laser pulse.

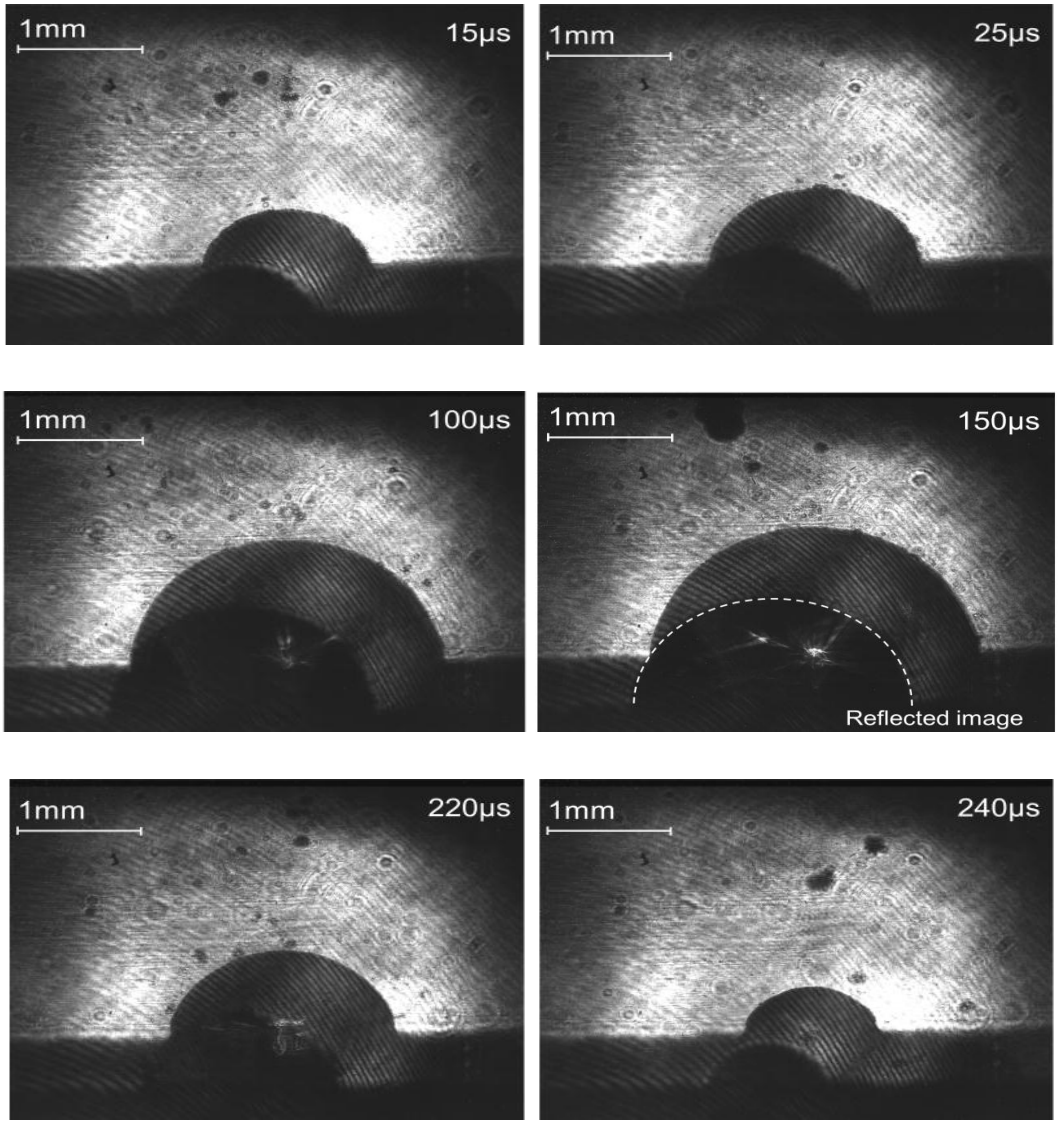

Figure 7.12: Shadowgrams of the cavitation bubble that appears some microseconds after the 8 mJ, 1064 nm laser pulse has fired. Images show the growth and collapse of the bubble.

The appearance of the hemispherical bubble is first observed ~1 µs after the laser pulse arrival at the target surface. The bubble then increases in size until a maximum value, which is dependent on the laser pulse energy, is reached. When the bubble has reached its maximum size the temperature of the bubble interior is equal to the temperature of the surrounding liquid [22]. Subsequently the bubble begins to collapse due to compression from the surrounding liquid, reducing in size before disappearing entirely. A "double-image" is seen in the images of figure 7.12. This is not two bubbles growing simultaneously, merely a reflection from the cubic cuvette. The bubble radius was

measured as a function of time for laser energies of 8 mJ and 52 mJ and is shown in figure 7.13.

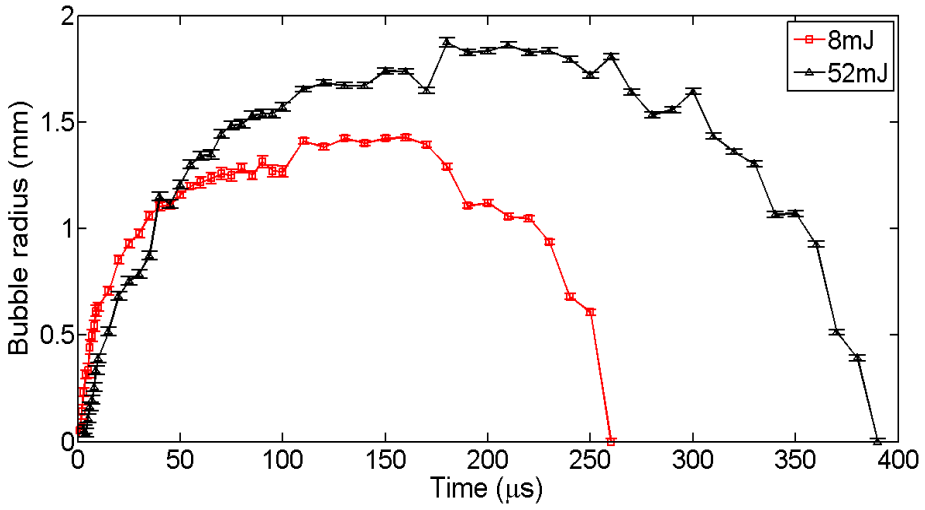

Figure 7.13: Bubble radius expansion as a function of time for 8 mJ and 52 mJ pulses.

After the collapse of the bubble, a series of growth and decay cycles of smaller bubbles is seen which occurs for several hundreds of microseconds after the disappearance of the initial bubble. This phenomenon is more easily observed at higher laser pulse energies. The secondary bubbles that form have a smaller radius and exhibit an irregular profile as seen in figure 7.14.

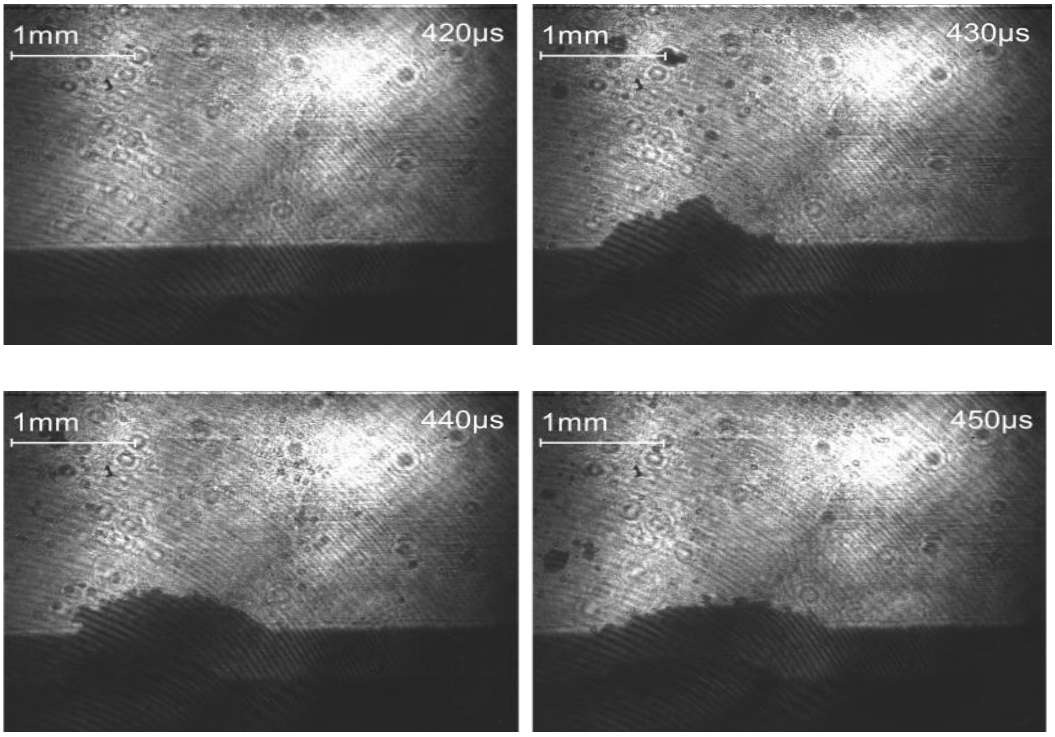

Figure 7.14: Shadowgrams of an unstable tertiary cavitation bubble observed ~0.5 ms after the initial 52 mJ, 1064 nm laser pulse was fired onto an aluminium target submerged in water.

Figure 7.14 shows the full evolution of the expansion of the initial cavitation bubble that forms and the subsequent secondary, tertiary and quaternary bubbles formed at a laser pulse energy of 52 mJ.

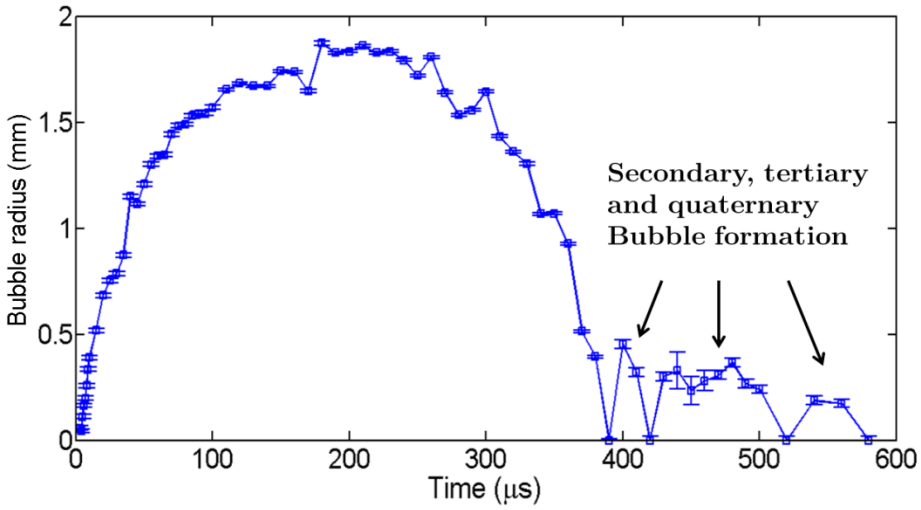

Figure 7.15: Cavitation bubble radius expansion as a function of time extracted from shadowgrams using 52 mJ, 1064 nm laser pulses. The formation of secondary and tertiary bubbles occurs at times > 400 μs.

From the images, the time at which the cavitation bubble reaches a maximum expansion occurs around 200 μs after the initial laser pulse has fired. The cavitation bubble is initially formed with a temperature and internal pressure much greater than the surrounding liquid and so expansion occurs [21]. As the bubble expands the pressure drops until such time as it collapses from the force of the surrounding liquid. If the bubble contains sufficient energy upon collapse, this energy may be expended in the formation of successive smaller bubbles (observable in figure 7.14). The measured radius of the bubble is used to infer the internal pressure $P(t)$ and temperature $T(t)$ from the following equations [23], [24]

$$P(t) = \left(P_\infty + \frac{2\sigma}{R}\right)\left(\frac{R_\infty^3 - h^3}{R(t)^3 - h^3}\right)^\gamma \tag{7.1}$$

$$T(t) = T_\infty \left(\frac{R_\infty^3 - h^3}{R^3 - h^3}\right)^{\gamma - 1} \tag{7.2}$$

where P_∞ and T_∞ are the pressure and temperature of the liquid, σ is the surface tension of the liquid, R is the experimentally determined bubble radius, R_∞ is the ambient radius of the bubble, (the radius at which the pressure inside the bubble corresponds to the liquid pressure) h is the van der Waals hard-core radius determined by the excluded

volume of the water molecules and γ is the ratio of specific heats. The calculated internal pressure and temperature are shown in figure 7.16.

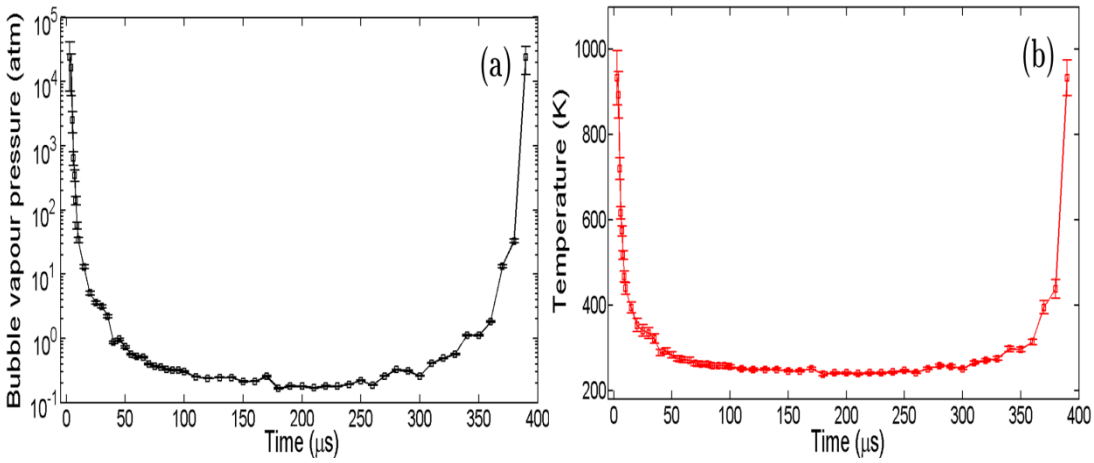

Figure 7.16: Cavitation bubble internal (a) vapour pressure and (b) temperature as a function of time calculated from data shown in figure 7.15 using 1064 nm, 52 mJ pulses.

The calculated internal pressure and temperature show the theoretical trends observed within the cavitation bubble during the growth and collapse phases. The bubble initially exists in a high temperature, high pressure environment and expansion occurs. As the bubble expands, the internal pressure begins to decrease due to the increased volume of the bubble. This expansion reaches a plateau region around 100-250 µs where the internal vapour pressure drops below the pressure of the surrounding liquid. The bubble then undergoes a collapse phase where the internal pressure and temperature increase due to the decrease in cavitation bubble volume. These trends have been reported in previous works [2], [25] and are shown here to highlight the main features typically found within the cavitation bubble during its life-cycle.

The symmetry of the cavitation bubble, i.e. its vertical and lateral expansion dimensions, was also investigated. For the low laser pulse energy case (8 mJ), a symmetrical expansion was observed which is demonstrated in figure 7.17. However in the high energy case a discrepancy was observed between the vertical and lateral expansion as shown in figure 7.18. The expansion could only be tracked up to 110 µs,

after which time the bubble diameter had expanded beyond the dimensions observable by the CMOS camera used to capture these images.

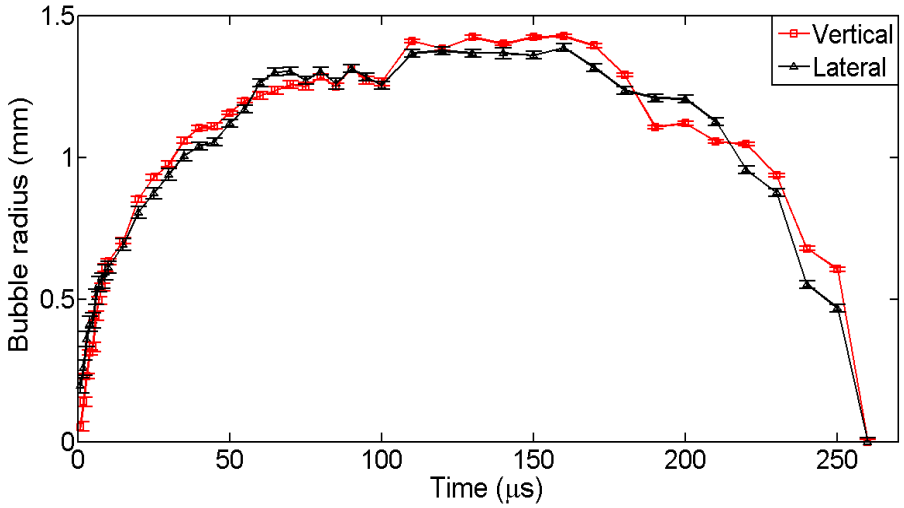

Figure 7.17: The vertical and lateral expansion of the cavitation bubble compared for an 8 mJ pulse.

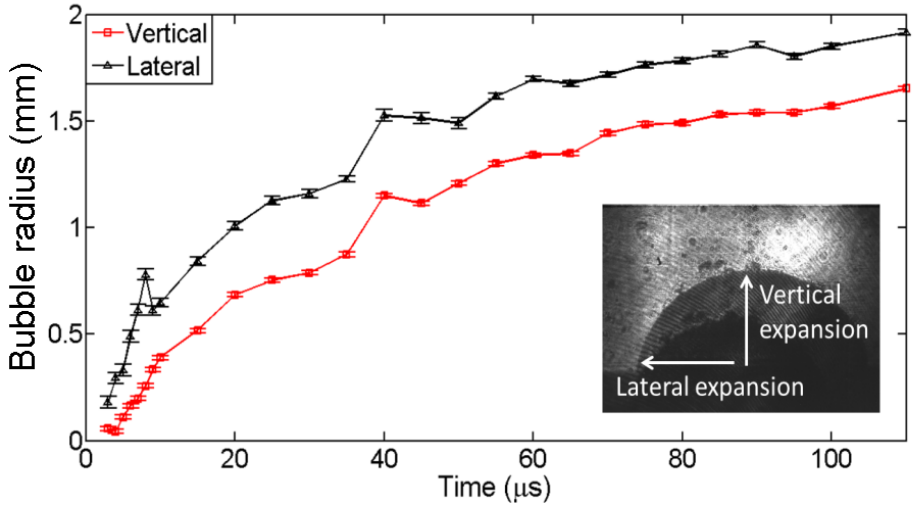

Figure 7.18: The vertical and lateral expansion of the cavitation bubble compared for a 52 mJ pulse. The bubble diameter could only be observed up to 110 µs after which time the bubble had expanded beyond the view of the CMOS camera. Inset demonstrates the defined vertical (normal) and lateral (parallel) expansion directions.

The cause of the discrepancy in the high and low pulse energy cases is unclear. Potential explanations may be related to focussing or irregularities in the profile of the laser pulse causing elevated lateral expansion of the cavitation bubble at high pulse energies.

7.3 Double Pulse Studies in Water

7.3.1 Imaging

After observation of the cavitation bubble from the shadowgraphy experiments the next phase of experimentation was to probe the bubble using imaging and spectroscopy techniques. To investigate the dynamics of the laser produced plasma formed within the cavitation bubble, a double-pulse method was used [5], [28]. In this instance, the first laser pulse is used to create the cavitation bubble and a second laser pulse is delivered colinear to the first, forming a plasma inside the cavitation bubble. Both laser pulses are focussed through the same lens as described in the experimental setup (figure 3.6). A second laser pulse of wavelength 532 nm, with an energy of 52 $\pm$ 3 mJ was delivered 200 µs after the initial ablation pulse (corresponding to the maximum radius of the bubble as observed from the shadowgraphy data) and focused through the same lens as the first pulse onto the target-bubble interface. An 800 nm short pass filter and a 532 nm band stop filter were inserted into the experimental setup to block scattered light from the two laser pulses. As noted earlier, optical emission from the initial plasma formed by the 1064 nm laser is long extinguished at the time of the incoming second laser and so any emission observed is due to excitation by the 532 nm pulse.

Time resolved imaging data were recorded with an ICCD camera operated with a 25 ns gate width to study the evolution of the plasma emission from within the bubble following irradiation with the delayed 532 nm pulse. A 1064 nm, 52 $\pm$ 3 mJ pulse was used for the formation of the initial plasma. A second pulse is delivered 200 µs later corresponding to the maximum radius of the bubble as observed from the shadowgraphy data (figure 7.15). The images obtained were very different from those shown in figure 7.1 and figure 7.3 where a single laser pulse was used.

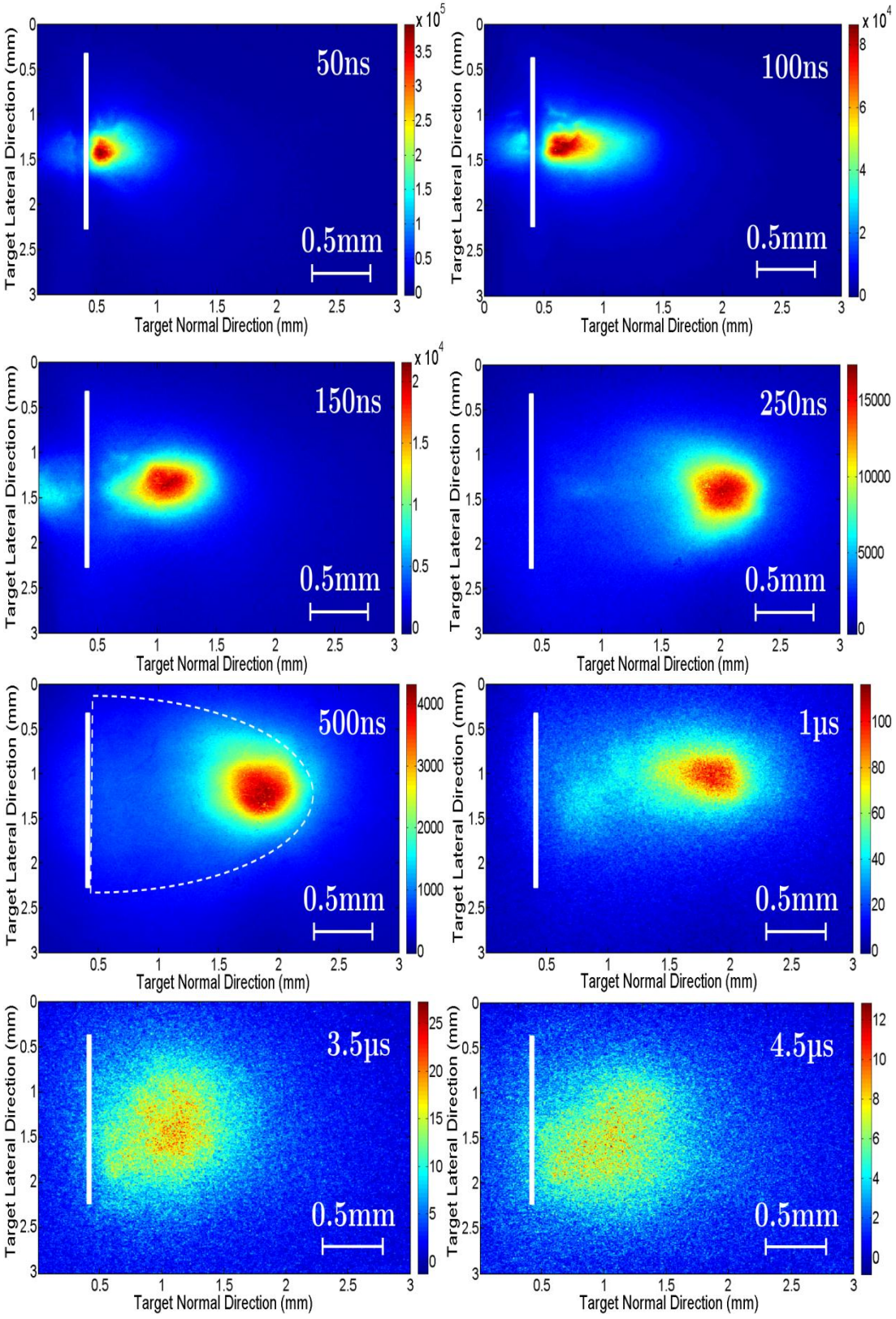

Figure 7.19: Images taken in double pulse experiments on an aluminium target submerged in deionised water. The second pulse is fired 200 µs after the first where the bubble expansion is a maximum. The times on each image refer to the delay between the arrival of the second laser pulse and the triggering of the ICCD. The ICCD gate width was 25 ns. The intensity (no. of counts) is represented by the colour scale bar shown on the right hand side of each image.

It is clear from figure 7.19 that delivery of the second pulse to the cavitation bubble leads to a very bright localised emission region which not only expands but also appears to move away from the target surface. A distinctly different behaviour is observed in the dynamic evolution of the plasma formed within the cavitation bubble compared with the observations of single pulse imaging in water (figure 7.1 and figure 7.3) where a highly confined plasma was observed. This displacement of the plasma plume away from the target surface is distinct also from the free expansion observed in gas or vacuum environments. The luminous plume front, which is a visual representation of the density and temperature, traditionally displays an exponential decay as a function of distance away from the target position if formed *in vacuo*. The peak intensity of the plume emission for a plasma created in vacuum remains at a fixed position close to the target surface until the plasma emission is extinguished. However, in the cavitation bubble, the plasma drifts as a self-contained entity to a well-defined distance from the target surface. As the plasma plume drifts normal to the target, the emitted intensity profile is no longer highest close to the target surface. Somewhat similar behaviour has been observed during the expansion of an aluminium plume into low pressure ambient gases [29], [30]. The explanation during this study was due to the luminous excitation of the background gas by the plasma resulting in an apparent plume splitting. In our case, spectroscopy confirms little to no evidence of excitation of the background environment.

In the first 100 ns, the plume front expands away from the target surface as expected from a typical plasma expansion. After *ca.* 100ns, the entire plasma plume appears to drift away from the surface of the target. A maximum displacement of the brightly emitting plume occurs at *ca.* 250 ns. Here a distance of ~1.8 mm is reached by the expanding plume which appears from shadowgraphs measurements to coincide with the physical extent of the cavitation bubble. After this time the plasma appears to remain stationary, at the outer edge of the bubble, until ~1 µs. During this period where the luminous plume front position appears to remain approximately stationary a significant reduction in the mission intensity is observed. The plasma is then seen to move back towards the target surface. At this point the plasma emission appears diffuse in contrast

to the tightly confined, bright emission plume observed as it moves away from the target to the bubble periphery. Emission from the plasma plume formed within the bubble is detectable up to 10 µs after the second pulse is fired. Figure 7.20 shows the position of the plume front as a function of time extracted from the imaging data.

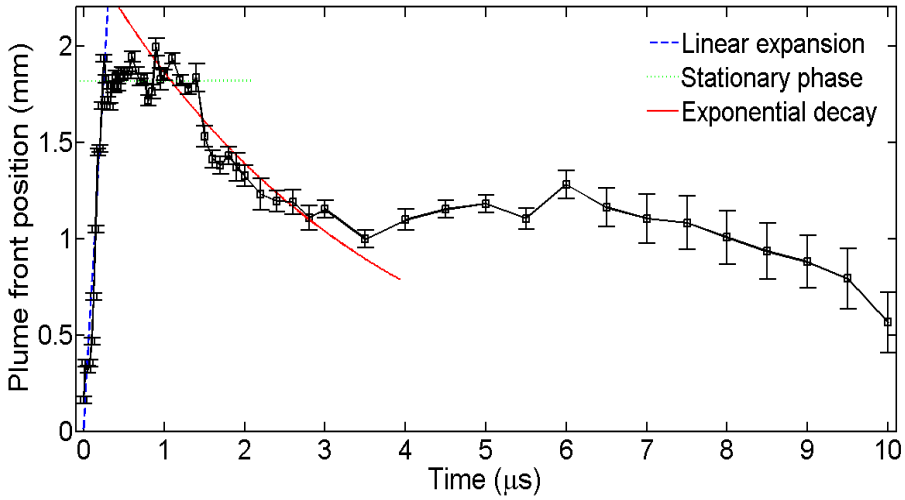

Figure 7.20: Plume front position extracted from time resolved double pulse imaging data within cavitation bubble. Time zero corresponds to the maximum bubble size occurring at an inter-pulse delay of 200 µs.

Three identifiable regions exist. The first, from 0-250 ns, shows a rapid linear expansion of the plume front (v = 7 mm/µs) followed by an almost static plume front position from 250 ns to 1.5 µs. From 1.5 µs onwards, the plume front position reverts approximately exponentially in line with radiative cooling (k = 0.30 µs^{-1}). The distance between the target surface and the outer region of the bright emission plume is *ca.* 1.8 mm which is in good agreement with the dimensions of the bubble periphery extracted from figure 7.15.

A similar investigation was carried out at times corresponding to the formation and collapse phases during the cavitation bubble life-cycle. These times were deduced from shadowgraphy (figure 7.15) to be 30 µs and 330 µs respectively which were then set as the arrival times for the second (532 nm) laser pulse. From figure 7.15 it is clear that at inter-pulse delays of 30 µs and 330 µs, the rate of change of the bubble radius is much greater than at 200 µs. With a much higher rate of change of bubble radius, one might

expect that a plume produced in these environments will have a much higher centre of mass velocity, a similar expansion velocity and a smaller stopping distance given the smaller dimensions of the cavitation bubble 30 µs and 330 µs after formation.

Figure 7.21 shows time resolved images of a plasma formed in the cavitation bubble at an inter-pulse delay of 30 µs.

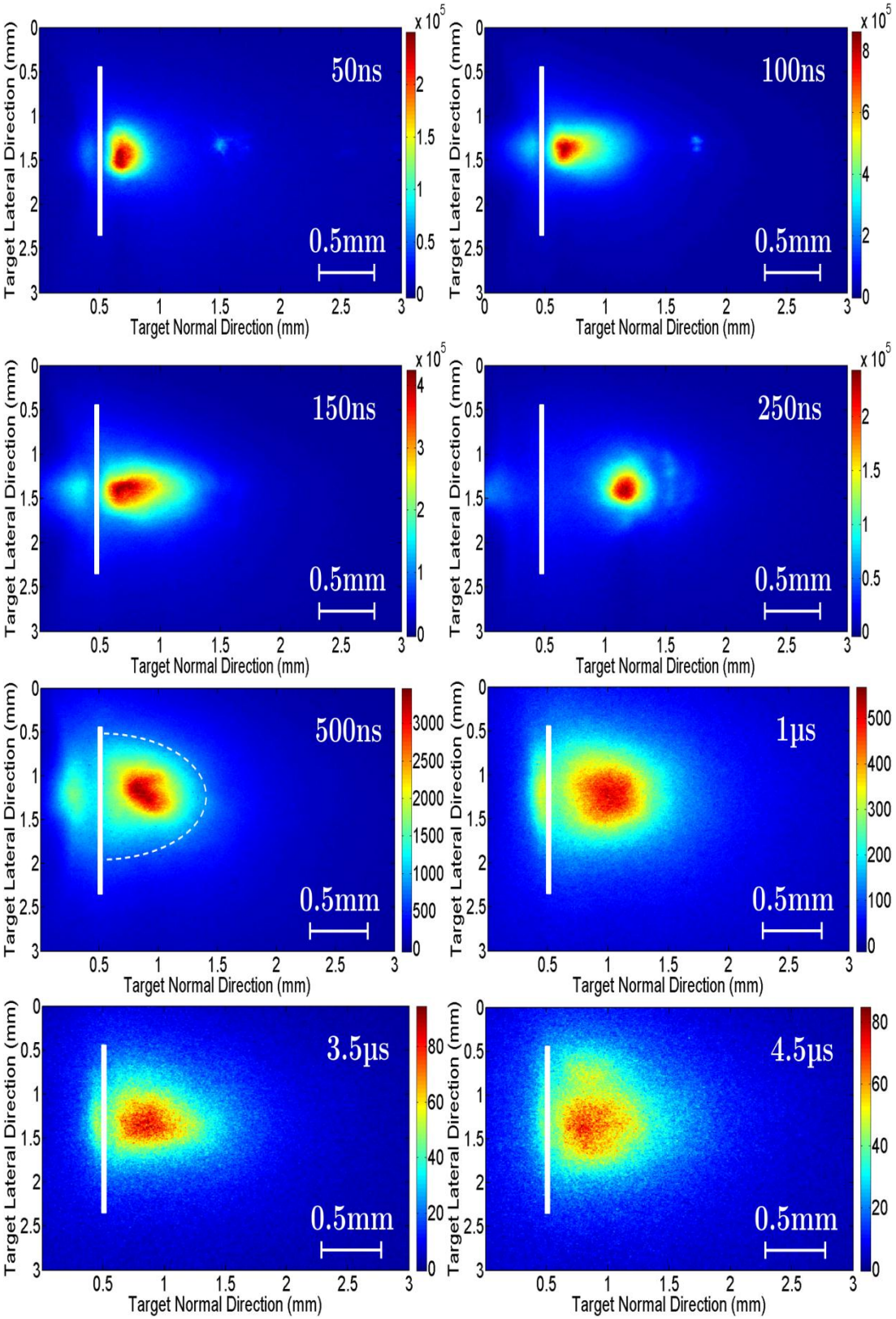

Figure 7.21: Images taken for double pulse irradiation of an aluminium slab target submerged in deionised water. A plasma was formed initially with a 1064 nm, 52 mJ pulse. The second pulse (532 nm, 52 mJ) was fired 30 µs later corresponding to the époch of initial bubble formation region. The times on each image refer to the delay between the arrival of the second laser pulse and the triggering of the ICCD. The ICCD gate width was 25 ns.

Figure 7.21 shows the same general trends in behaviour as were observed in figure 7.19. The plasma is seen to drift away from the target surface to a fixed stopping distance which subsequently expands forming a diffuse emission profile apparently contained within the physical dimensions of the cavitation bubble. In figure 7.22 the luminous plume front position is plotted as a function of time.

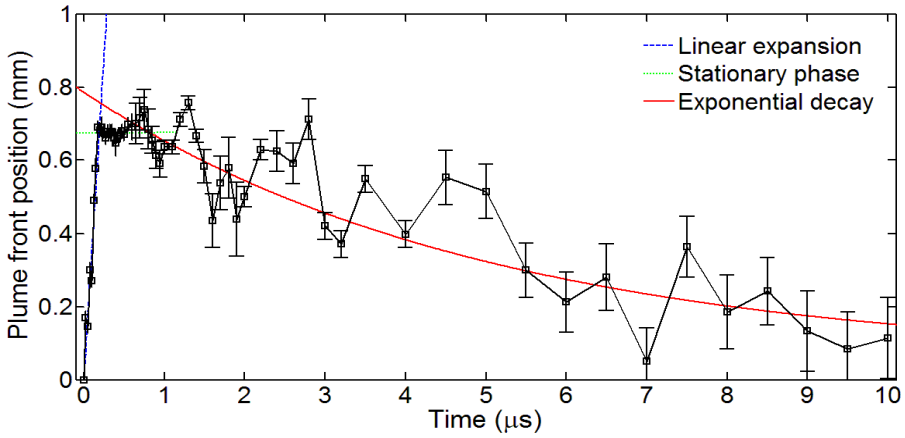

Figure 7.22: Plume front position extracted from time resolved double pulse imaging data within cavitation bubble. Time zero corresponds to the époch of bubble formation occurring at an inter-pulse delay of 30 μs.

The trend in the plume front behaviour is similar to that observed in figure 7.20, however notable differences are also evident. The luminous plume front exhibits an initial expansion phase (v = 4 mm/μs) with a velocity less than that observed in figure 7.20 due to the higher pressure environment found within the cavitation bubble at this inter-pulse delay time. The ultimate stopping distance of the plume front is smaller due to the smaller bubble size. The subsequent decay appears to be much more gradual and chaotic than in the 200 μs case where k = 0.30 μs^{-1} compared to k = 0.16 μs^{-1} here. One plausible explanation is the fact that the bubble is smaller, meaning that the plasma is denser when it expands to fill the water vapour bubble. This causes more collisional excitation which sustains a higher temperature for longer. This would explain the longer decay time and less monotonic decay.

Figure 7.23 shows time resolved images of a plasma formed in the cavitation bubble at an inter-pulse delay of 330 μs.

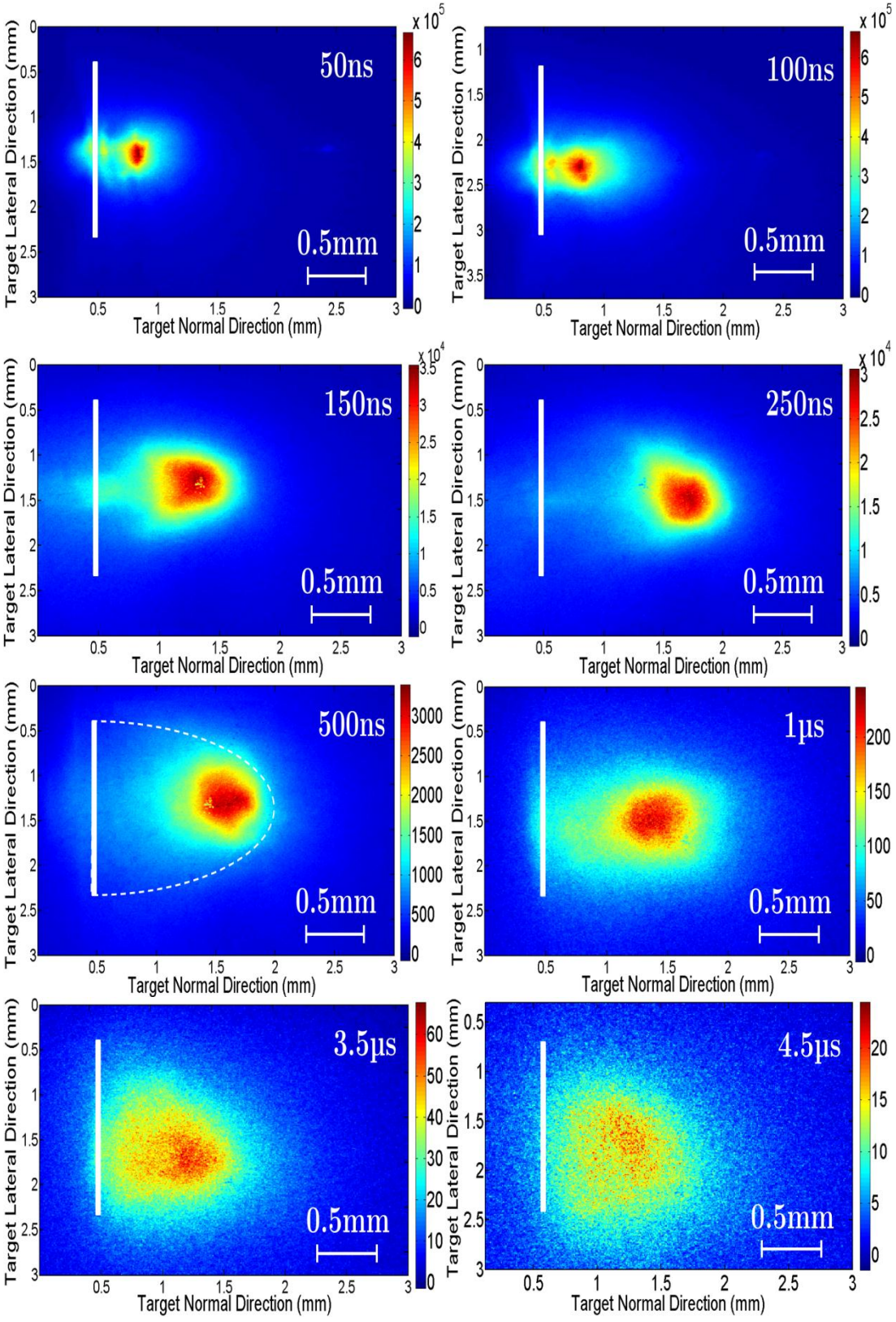

Figure 7.23: Images taken for double pulse irradiation of an aluminium slab target submerged in deionised water. A plasma was formed initially with a 1064 nm, 52 mJ pulse. The second pulse (532 nm, 52 mJ) was fired 330 µs later corresponding to the époch of the bubble collapse region. The times on each image refer to the delay between the arrival of the second laser pulse and triggering of the ICCD. An ICCD gate width of 25 ns was used.

The same general behaviour is observed during the époch of bubble collapse with physical displacement of the plasma plume occurring *ca.* 150 ns after plasma formation. The plume drifts to a distance of approximately 1.3 mm normal to the target surface in line with the dimensions expected from shadowgraphy images of the cavitation bubble radius at a delay of 330 µs (figure 7.15). The plume front positions were measured from the imaging data during the collapsing phase and are shown in figure 7.24. A similar trend is observed compared to imaging experiments carried out using 30 µs and 330 µs inter-pulse delay times.

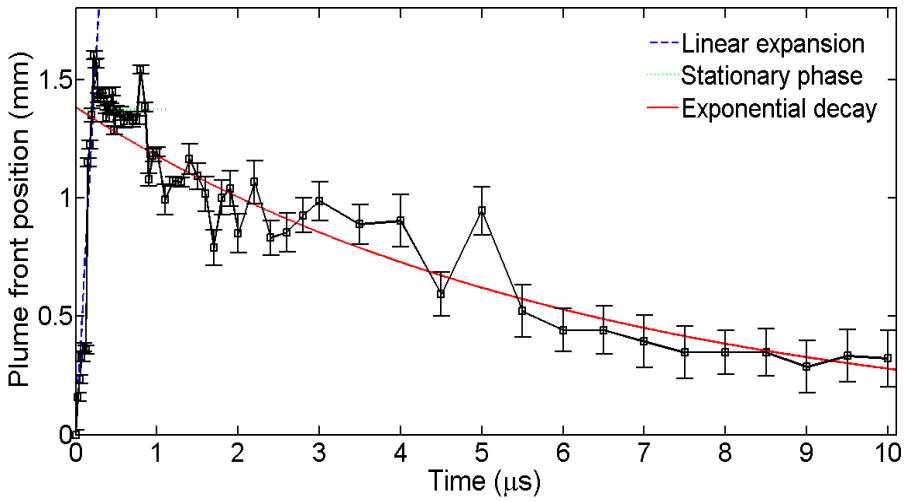

Figure 7.24: Plume front position extracted from time resolved double pulse imaging data within cavitation bubble. Time zero corresponds to the époch of bubble formation occurring at an inter-pulse delay of 330 µs.

An initial expansion velocity v = 6 mm/µs is observed for the luminous plume front at a 330 µs inter-pulse delay. Bubble radius values of 0.78 mm, 1.83 mm and 1.30 mm were extracted from shadowgraphy measurements at time delays of 30 µs, 200 µs and 330 µs respectively. Hence, the trend in plume expansion velocities measured in the early expansion phase (at time delays ≤ 250 ns) follows the different pressure regimes present within the cavitation bubble at these times. A decay rate of k = 0.16 µs^{-1} is observed from figure 7.24 which is the same as the decay rate observed using a 30 µs inter-pulse delay and lower than that observed at a 200 µs inter-pulse delay. Again, this is likely due to the smaller volume of the cavitation bubble during the periods of formation and

collapse. An increase in collisional events is expected in this reduced volume leading to additional excitation and longer decay times.

Interpretation

In an attempt to explain the observed dynamics of the plasma plume formed inside the cavitation bubble, a qualitative interpretation is proposed. A traditional laser plasma, one created in vacuum or ambient gas, will have an associated expansion velocity and an associated "centre of mass velocity". The first of these is the velocity at which the plume is expanding along the directions of the pressure gradients in the surrounding environment and the second is the speed at which the entire plume is moving away from the target surface. In air or vacuum plasma expansion, the expansion velocity is much greater than the centre of mass velocity. However, when the plasma is created inside the cavitation bubble, the bubble itself is expanding. This interior of the bubble is a low pressure water vapour environment. The expansion of the bubble causes mass diffusion of plasma species to the outer regions. Thus, the plasma is not formed in a static velocity field but in an outwardly flowing one. This increases the centre of mass velocity causing the whole plume to move away from the target more quickly than it expands. Figure 7.25 shows the centre of mass velocity (v_{CM}) and expansion velocity (v_{EX}) components extracted from the imaging data in the two extremes of high pressure (30 µs) and low pressure bubble environments (200 µs). The velocities were extracted by first taking intensity lineouts through the centre of the plasma plume images in a direction normal to the target surface (as outlined in section 2.6). From these one-dimensional lineouts, v_{CM} was defined as the velocity of the peak emission intensity of the plasma plume and v_{EX} was defined as the FWHM of the plume.

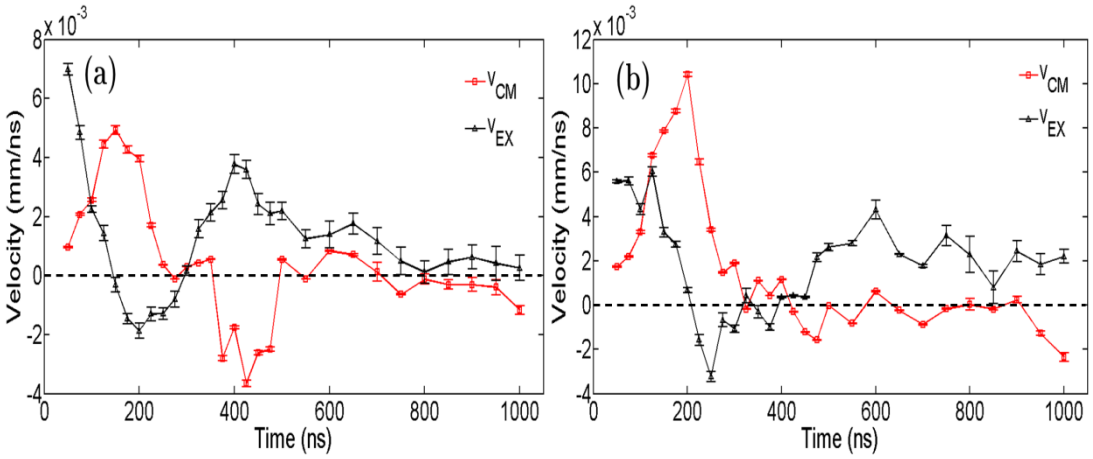

Figure 7.25: Centre of mass velocity (v_{CM}) and plume expansion velocity (v_{EX}) extracted from imaging data using an inter-pulse delay of (a) 30 µs and (b) 200 µs.

Similar trends are observed in the velocity components of the plumes created during the formation and collapse phases of the cavitation bubble life-cycle. v_{CM} is seen to increase until *ca.* 200 ns, corresponding to the time at which the plume has travelled to the periphery of the cavitation bubble, after which point a decrease in velocity occurs until *ca.* 300 ns where the velocity approaches zero. A negative velocity is subsequently observed (*ca.* 450 ns) due to the recoil initiated by the plume collision at the bubble boundary which is most apparent in the 30 µs case. Finally, a stationary period is encountered until a delay of 1 µs where the plume position remains relatively fixed. While similar in both environments, v_{EX} follows a different trend to v_{CM}. In the first initial phase, before plume collision with the bubble wall, an approximately constant decrease is observed for v_{EX}. This is in contrast to the increasing centre of mass velocity observed, supporting the idea of mass diffusion into the low pressure environment of the cavitation bubble. The v_{EX} becomes negative at the point of plume collision with the bubble wall (~200 ns) due to compression of the entire plasma plume as evidenced from the imaging data (figures 7.19 and 7.21). The expansion velocity subsequently increases and remains positive until a delay of ≈ 1 µs due to the diffusion of the plasma plume into the surrounding bubble environment.

A dimensionless "dispersion parameter" can be used to relate the ratio of the centre of mass position (p_{CM}) to the plume expansion (p_{EX}). From the one-dimensional lineouts

extracted from the images, p_{CM} was defined as the position of peak emission intensity and p_{EX} was defined as the position at which the ICCD count had dropped to $1/e$ (~0.37) of its maximum value in the expansion direction normal to the target surface. Figure 7.26 shows the "dispersion parameter" during several phases of the plume expansion for inter-pulse delays of 30 µs and 200 µs respectively.

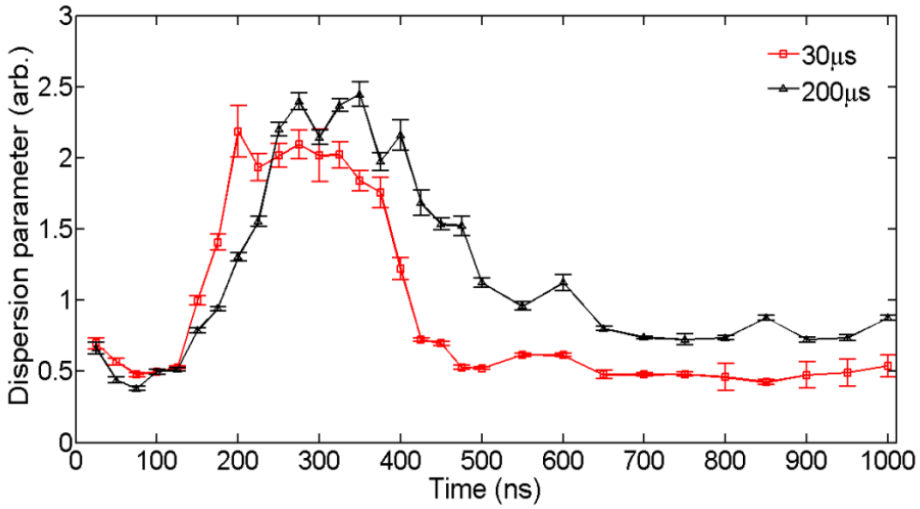

Figure 7.26: Dispersion parameter (p_{CM}/p_{EX}) extracted from imaging data using an inter-pulse delay of 30 µs and 200 µs corresponding to phases of high changing pressure and low changing pressure respectively.

In the initial 100 ns, a similar trend is observed in both bubble environments. The expansion velocity dominates at early times which results in a value for the dispersion parameter of < 1. Between 150-200 ns, a value > 1 is obtained as the centre of mass position begins to drift from the target surface. During this time period a much greater value is obtained for the dispersion parameter using the 30 µs inter-pulse delay. This indicates that, for a 30 µs inter-pulse delay, the plasma is drifting much faster than it is expanding. This result is in line with the trend expected by the qualitative hypothesis. An approximately static period is subsequently obtained for the dispersion parameter, coinciding with the time at which the plume front encounters the periphery of the cavitation bubble wall (*ca.* 200 ns and 250 ns for inter-pulse delays of 30 µs and 200 µs respectively). In the final phase, i.e., after plume expansion in the direction normal to the target surface is prohibited by the boundary of the cavitation bubble, the dispersion

parameter decreases in both cases as diffusion occurs while the centre of mass velocity remains essentially constant.

In summary the displacement of the plasma plume is as follows. The plume is created in the flowing velocity field of the expanding bubble and drifts away from the target until such a time as the front of the plume encounters the wall of the bubble. The trailing edge of the plume is still travelling in the velocity field and thus the plasma is compressed. Behind the plume there exists a low pressure vapour environment into which the plume can expand and fill the volume of the bubble. The plume then exists in a state of hydrodynamic equilibrium and radiates energy eventually cooling and losing visibility.

7.3.2 Spectroscopy

Time resolved spectroscopy experiments were carried out within the bubble. As before for the imaging data, the second pulse (532 nm, 52 mJ) was delivered several microseconds after the initial plasma is formed (via the 1064 nm, 52 mJ pre-pulse). The results of spectroscopy data on the related cavitation bubble will be presented in this section.

At times corresponding to the initiation and growth of the cavitation bubble, line emission was observed. This line emission was not observable before bubble generation or after the time of collapse. For these times, only broadband continuum was observed, similar to the single pulse spectroscopic data (figure 7.5). Time resolved spectroscopy data was measured once again with the second pulse delivered at an incoming time of 200 µs with respect to the first using an ICCD gate width of 25 ns. This was considered to be the time at which the greatest stability of the bubble should be expected and hence the least fluctuations in the recorded spectra.

With the intention of calculating electron temperatures and densities within the bubble, time resolved spectra of aluminium neutrals, singly charged ions and doubly charged

ions were measured. Figure 7.27 shows several of the spectra recorded for each of the species of interest.

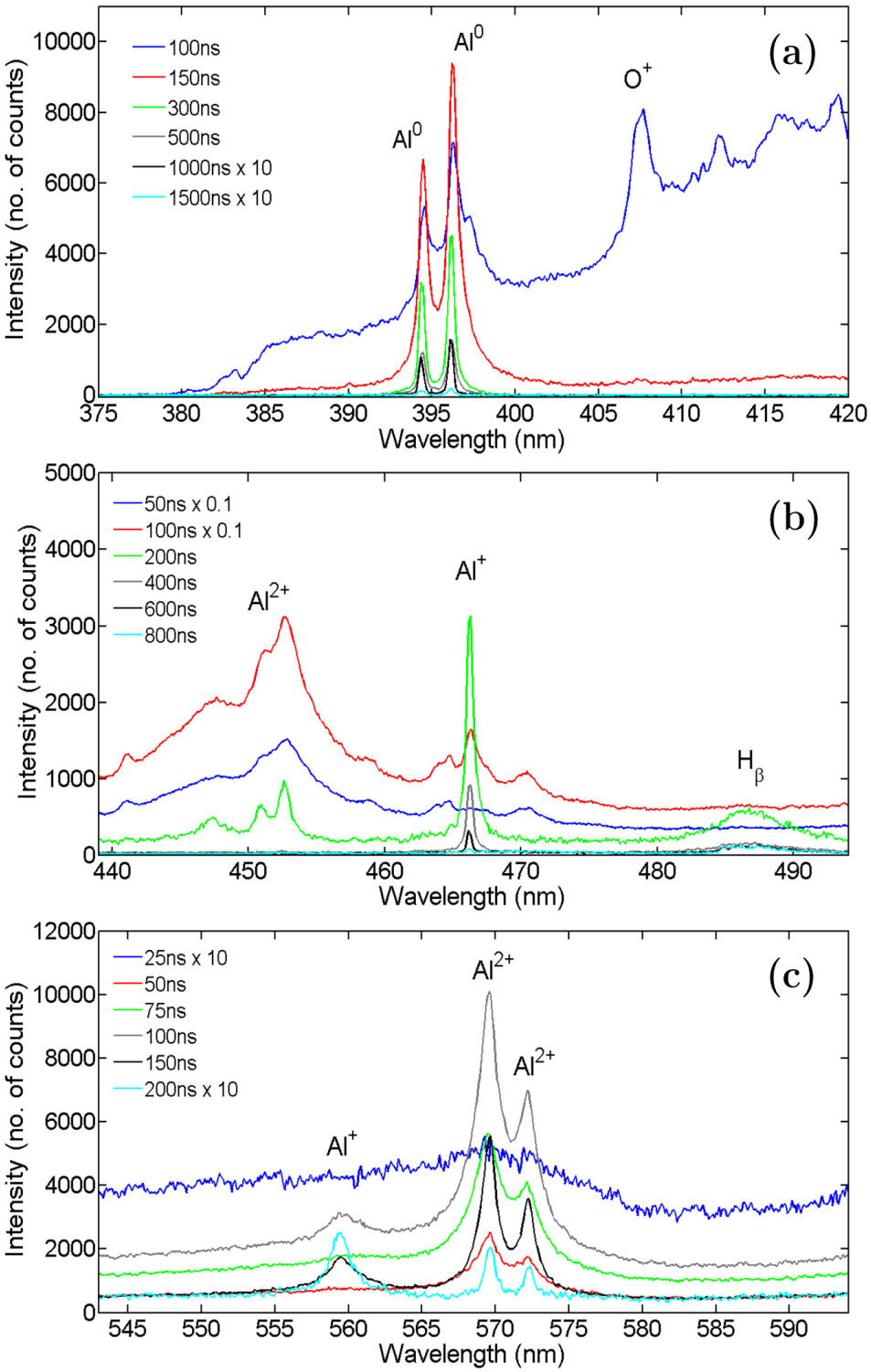

Figure 7.27: Time resolved spectra recorded with a 25 ns ICCD gate width of (a) aluminium neutral (b) aluminium singly ionised and (c) aluminium double ionised spectral regions. The time delays are with respect to the arrival time of the reheating pulse (532 nm, 52 mJ) which was delivered 200 µs after the original 1064 nm, 52 mJ plasma formation pulse.

Initially broadband continuum emission is observed. Within the first 100 ns this broadband emission becomes supressed and line emission begins to dominate the spectra. Figure 7.27 (a) shows the emission of the neutral aluminium doublet lines Al(I) $3p(^2P^0_{1/2,\ 3/2}) - 4s(^2S_{1/2})$ (396.15 nm and 394.4 nm) appearing from the continuum. The appearance of oxygen emission lines are also observed within the first 100 ns of spectra recorded. The oxygen lines contributing to this feature are singly ionised lines O(II) $3p(^4D^0_{7/2})$ - $3d(^4F_{9/2})$, O(II) $3d(^4F_{3/2})$ - $4f(D[2]_{3/2})$ and O(II) $3p(^4D^0_{3/2})$ - $3d(^4F_{3/2})$ at wavelengths of 407.58 nm, 407.7 nm and 407.88 nm respectively. Emission of neutral aluminium lines were observed for a duration of 1.5 µs after the arrival of the second laser pulse (532 nm, 52 mJ). In figure 7.27 (b) the singly ionised aluminium emission line Al(II) $3p^2(^1D_2) - 4p(^1P^0_1)$ at 466.3 nm appears following the suppression of broadband continuum emission. The observance of a broad profile is noted at a centre wavelength of ~486 nm. This emission feature appears to correspond in wavelength range and profile to the H_β emission profile at 486.13 nm reported in several studies of laser produced plasmas in air and other background gases [31], [32]. The appearance of distinct spectral features around 450 nm are comprised of two doubly ionised aluminium emission lines Al(III) $4p(^2P^0_{1/2,\ 3/2}) - 4d(^2D_{3/2})$ occurring at wavelengths of 451.26 nm and 452.92 nm respectively. An additional broader peak can be seen around 448 nm and is attributed to contributions from the two emission lines Al(II) $4f(^2F^0_{5/2}) - 5g(^2G_{7/2})$ at 448.99 nm and Al(III) $4f(^2F^0_{7/2}) - 5g(^2G_{9/2})$ at 448.0 nm. Figure 7.27 (c) shows considerable Al^{2+} emission. The presence of strongly emitting Al(III) lines $4s(^2S_{1/2}) - 4p(^2P^0_{3/2,\ 1/2})$ at wavelengths of 569.66 nm and 572.27 nm are observed in addition to the Al(II) emission line $4p(^1P^0_1) - 4d(^1D_2)$ at 559.33 nm.

While neutral line emission was similar to that recorded in air, notable differences were found for other species. Comparing to spectral emission recorded in ambient air, ionic emission observed within the cavitation bubble exhibited a narrower line profile than in the case of air. Also evidence of additional peaks was found. Moreover, the presence of the doubly ionised 569.66 nm line is quite clear in water ambient but was difficult to observe in air. An additional doubly ionised line at 572.27 nm was also observed quite

strongly in the cavitation bubble, but was not present in air. The profiles of aluminium ions lines recorded in atmosphere were broad and noisy whereas smooth narrow emission is observed from within the bubble. This would suggest that the conditions within the cavitation bubble appear to be that of a low pressure environment, lower than atmospheric pressure. This is consistent with the imaging data recorded within the bubble where a rapid expansion of the plasma plume was observed, more similar to expansion into a low pressure background or into vacuum.

Investigation of the bubble formation and collapse regions were carried out by studying the neutral aluminium species. The times corresponding to formation, maximum expansion and collapse were deduced from the shadowgraphy measurements presented earlier (figure 7.15) to occur at delays of 20 µs, 120 µs and 220 µs with respect to the initial pulse. Here the pre-pulse and reheating pulse were 1064 nm, 8 mJ and 532 nm, 8 mJ. Figure 7.28 shows the spectra recorded in the bubble formation region (a), the stable region of maximum expansion (b), and in the region of collapse (c).

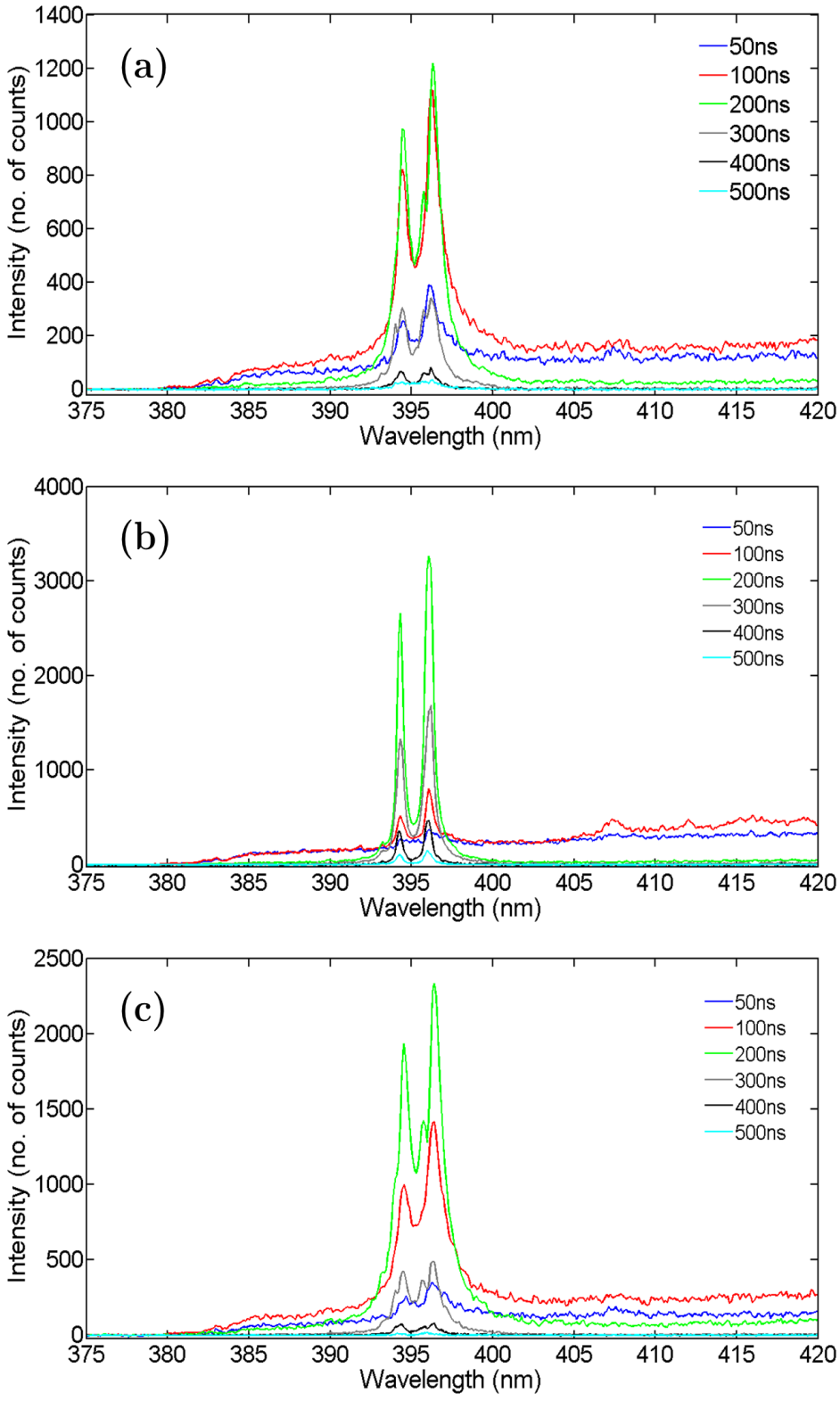

Figure 7.28: Aluminium neutral spectra recorded at times corresponding to (a) bubble formation 20 µs (b) bubble centre 120 µs and (c) bubble collapse 220 µs. Data was obtained using a 8 mJ, 1064 nm pulse for the formation of the plasma and a second pulse of 8 mJ, 532 nm which was used to probe the cavitation bubble.

From figure 7.28 the typical neutral doublet is observed. Figures 7.28 (a) and (c) demonstrate the typical spectra recorded at the cavitation bubble formation (20 µs) and collapsing times (220 µs) while figure 7.28 (a) corresponds to the point of maximum spatial expansion of the cavitation bubble (120 µs). Distinctive differences in the recorded spectra of the neutral doublet are apparent in the three cases. Evidence of self-reversal is noted at times corresponding to bubble formation and collapse where distinct dips in the peak of the emission lines are observed indicating self-absorption of the neutral emission at these times.

Self-absorbed line profiles are characterised by a saturation at the emission peak distorting the FWHM or even the appearance of a dip at the peak position (self-reversal) [33]. Plasma radiation is often considered to consist of two separate regions, a hot dense central plasma core surrounded by a cold outer layer at the periphery of the expanding plasma. The plasma radiation from within the hot core may be absorbed by this cooler region, predominantly consisting of atoms and ions in the ground state. Both regions are considered to exist in a state of local thermodynamic equilibrium [36]. As the outer layer of the plasma is highly populated by atoms in the ground state configuration, a high probability of self-absorption exists for ground state transitions as radiation is emitted from the inner core. As a result line emission can be strongly absorbed by the lower level atoms and become optically thick [37]. At times where the cavitation bubble is of a small volume, a high pressure environment is created which causes the self-absorption observed in the emission spectra. Similar phenomena have been reported for these neutral aluminium lines in air [33].

Figure 7.29 provides a closer look at the self-reversed neutral doublet spectra in the region of formation at 30 µs obtained using 52 mJ pulses (both plasma formation and reheating pulses). Spectra of the aluminium neutral doublet obtained in the formation region are compared to those obtained around 200 µs where the cavitation bubble is most stable.

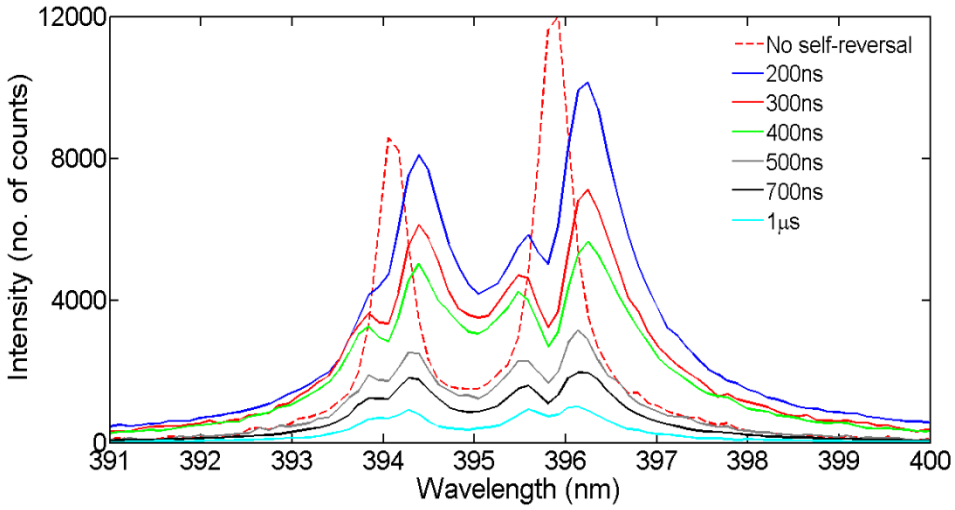

Figure 7.29: Spectra of neutral aluminium measured using an ICCD gate width of 25ns at a range of time delays from the second laser pulse focussed into the cavitation bubble 30 μs after initial plasma breakdown in water. A 1064 nm, 52 mJ pre-pulse and a 532 nm, 52 mJ reheating pulse were used. Spectra are obtained at delays of 200 ns, 300 ns, 400 ns, 500 ns, 700 ns and 1 μs with respect to the second pulse. A comparison to a typical spectra observed at 200 μs is also shown in the dashed red line for a time delay of 200 ns. Evidence of self-reversal is apparent.

.

For 52 mJ pulses, self-absorption was observed for the two neutral lines at 394.4 nm and 396.15 nm up to *ca.* 1 μs after the 532 nm pulse was delivered to the target and *ca.* 500 ns for the 8 mJ case. A broadening of the emission lines is also apparent suggesting a higher density at times corresponding to the formation and collapse of the cavitation bubble. This is intuitively what one might expect to observe due to plasma compression at the formation and collapsing phases of bubble evolution where the pressure within the cavitation bubble is greatest [5]. No distortion in profile was observed in ionic aluminium emission spectra. A broadening of the emission lines is also evident from figure 7.29 suggesting a higher density at times corresponding to the formation and collapse of the cavitation bubble. This is intuitively what one might expect to observe due to plasma compression at the formation and collapsing phases of bubble evolution where the pressure within the cavitation bubble is greatest [5].

7.4 Temperature and Density Calculations within the Cavitation Bubble

In order to investigate further the cavitation bubble, some plasma parameters were extracted from the time resolved spectroscopy data. Electron temperatures and densities within the cavitation bubble were calculated using the techniques described in chapter 2. As a brief reminder, electron densities may be deduced from the Stark width of the line profile and electron temperatures were calculated using the ratio of line intensities from consecutive charge states. Voigt profiles were fitted to the experimental lines of interest and this data was then used to extract temperature and density information.

Electron densities were calculated using the Stark-broadened profile of Al(II) 466.3 nm. The lifetime of the line was observed to occupy a time window from 25 ns up to 800 ns after the arrival of the second reheating laser pulse. For the calculations of the electron temperatures, the relative line intensity of the two spectral lines Al(II) 466.3 nm ($3p^2(^1D)$-$3s4p(^1P^0)$) and Al(I) 396.15 nm ($3s^23p(^2P_{3/2})$-$3s^24s(^2S_{1/2})$) were used. The lifetime of the doubly ionised lines recorded was deemed too short for a reliable trend to be observed; i.e., in the 100-300 ns window and hence for a 25 ns increment only 9 data points could be obtained for temperature calculations using the Al(III)/Al(II) ratio.

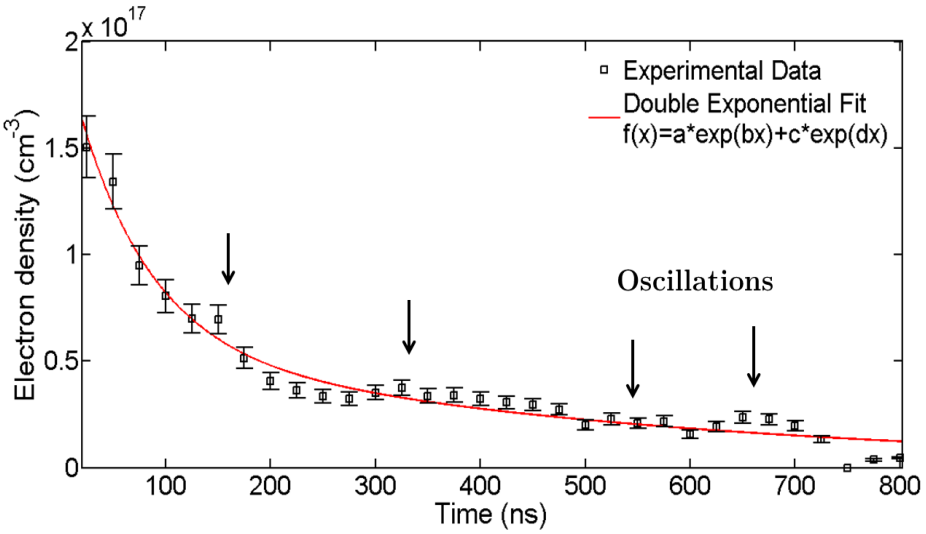

Figure 7.30: Electron density measured as a function of delay time from the Al^+ 466.3 nm line profile. Evergies of 52 mJ for the plasma pulse and 52 mJ for the second pulse were used. A double exponential fit is applied to the data with an adjusted $\overline{R^2}$ value of 0.97 obtained. Fitting parameters extracted from fit were a = 1.43 ± 0.18×10^{17} (cm^{-3}), b = -0.0147 ± 0.004 (ns^{-1}), c = 6.02 ± 1.77×10^{16} (cm^{-3}), d = -0.0020 ± 0.0006 (ns^{-1}).

An electron density in the order of $10^{17}\,cm^{-3}$ was observed. This is an order of magnitude lower than in the case of air where an average electron density of $10^{18}\,cm^{-3}$ was revealed in chapter 4. The rate of decay of the electron density is rapid at the initial stages, i.e., in the first 200 ns and then is seen to decay at a more gradual rate. It is postulated that the electrons and ions may travel freely away from the target surface and move outwards to fill the cavitation bubble forming a diffuse plume of lowered electron density. However, without spatial resolution this is not verifiable from present measurements. A double exponent was used as a best fit to the experimental data. Comparing the coefficients of rate decay (terms "b" and "d") a rapidly decaying term and a slowly decaying term are revealed from the fit. These fast and slow components have been observed in multiple studies of plasma expansion into background gases and are attributed to strong plasma confinement [38]. As the pressure of the background gas increases, an increase in the collision frequency of electron and ions occurs with the background gas [39]. This increased number of collisions results in an increase in ionisation, recombination and plasma emission [40], [41]. Hence, at higher background pressures, a slower decay rate is observed in the electron density [42]. The relatively fast

decay rate observed may constitute further evidence that the environment within the cavitation bubble is that of a low pressure gas. The electron density appears to exhibit an oscillatory behaviour as a function of time. These periodic increases in electron density may be attributed to re-excitations due to the confined nature of the cavitation bubble.

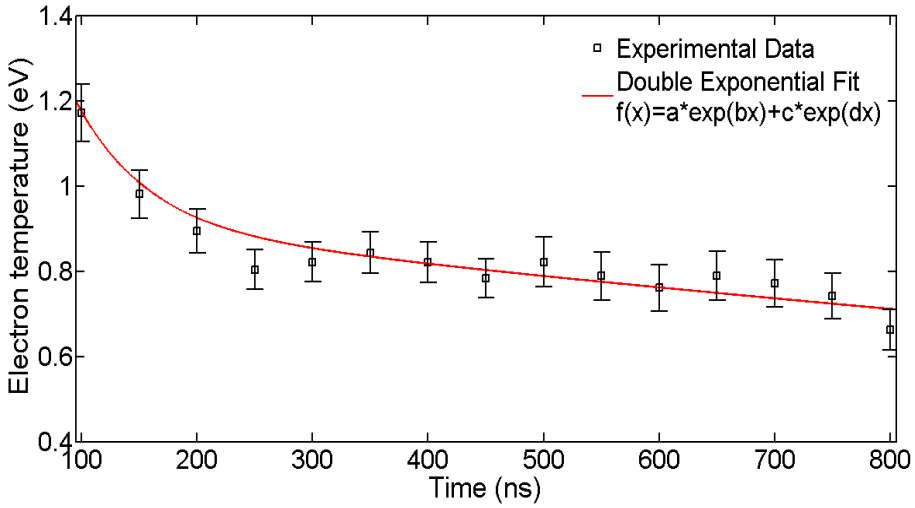

Figure 7.31: Results of electron temperature as a function of time calculated from the intensity ratio of Al^{+} 466.3 nm and Al^{0} 396.15 nm lines. Energies of 52 mJ for the plasma pulse and 52 mJ for the second probe pulse were used. A double exponential was used as a best fit to the experimental data resulting in an adjusted $\overline{R^2}$ of 0.97. Fitting parameters obtained were a = 1.41 ± 0.40 (eV), b = -0.0165 ± 0.0037 (ns^{-1}). c = 0.94 ± 0.06 (eV), d = -0.0003 ±0.0001 (ns^{-1}).

The results of electron temperature calculations are shown in figure 7.31. The electron temperature appears to follow a similar trend to the electron density showing best agreement to a double exponential decay fit. The temperature decreases rapidly in the first 200 ns and declines then at a more gradual rate up to 800 ns. A peak value of 1.17 ± 0.07 eV was found for the electron temperature within the cavitation bubble occurring at the earliest possible measurement at 100 ns which drops to 0.89 ± 0.05 eV after 200 ns. The plasma proceeds to cool at a more gradual rate eventually reaching an electron temperature of 0.66 ± 0.05 eV at 800 ns. A comparison of the decay terms obtained by the double exponential fit shows a brief initial period of rapid decay followed by a much more gradual decay rate. To within experimental error the

temperature remains approximately constant after 200 ns for the remaining observable measurements. A more rapid decrease in temperature was found in ambient air for the same timescale (see chapter 4). A decrease of 0.23 ± 0.10 eV compared to 0.22 ± 0.09 eV is observed between 200-800 ns in air and in the cavitation bubble respectively. The fast and slow components of the decay terms observed in both electron density and electron temperature measurements are likely due to the restricted physical dimensions of the cavitation bubble [38]. An increased number of collisions may take place within the confines of the bubble resulting in prolonged plasma emission, analogous to findings reported during plasma studies carried out in background gases [39]. A number of small elevations in the electron temperature are observed (*ca.* 500 ns and 650 ns) similar to electron density measurements and may again be attributed to confinement of the plasma within the boundaries of the cavitation bubble.

7.5 Summary

This chapter reports the main findings on optical emission studies of laser produced plasmas formed in liquid ambient. A range of experiments were performed using time resolved imaging and spectroscopy to investigate the plasma that forms in a high pressure background such as water using several techniques. Additional plasma probing techniques performed on the underwater plasma included shadowgraphy and interferometry. Information about shockwave formation, electron density distributions and the cavitation bubble that forms were ascertained from these techniques. Double pulses experiments were carried with the intention to detect ionic line emission from a sample submerged in a liquid medium by probing the bubble-target interface. All experiments were performed in single-shot mode.

Single pulse studies revealed information on the dynamic evolution of the plasma formed in a liquid environment. A strong confinement of the plasma is observed in water compared to free expansion typically observed in the more well-studied case of

plasma expansion into a gas or vacuum ambient. Data extracted from single pulse imaging data reveals that the dynamic behaviour of an underwater plasma proceeds very differently depending on the wavelength of the laser pulse used to create the plasma. In the case of a plasma generated using 532 nm laser pulses, an initial expansion of the plasma occurs on a timescale of ~400 ns after which time the plasma plume appears to remain at a fixed expansion diameter of ~0.4 mm. Broadband emission is observable for ~10 µs. Using the 1064 nm laser a distinctly different behaviour was observed where a rapid expansion of the plasma, over a period of 100 ns, followed by an apparent contraction of the plume was observed. The physical expansion of the plume to ~1 mm in the initial stages appears more aggressive than in the 532 nm case for the same amount of energy delivered to the target surface. Although emission was only detectable for ~500 ns the plume appears to reach roughly 0.5 mm after the initial expansion phase. As a hotter plasma is expected in the case of 1064 nm laser pulses, it is proposed that after expansion the very hot plasma reaches an equilibrium with the temperature of the surrounding water medium and eventually is forced to contract due to the pressure exerted by the surrounding liquid. Whereas for the relatively cooler plasma created using the 532 nm laser, a more gradual exchange of energy occurs between excited species and the cold surrounding liquid medium.

Spectroscopic data indicated that a very hot and dense plasma is formed during laser-matter irradiation of metal targets submerged in water where broadband continuum emission was the main observation. The plasma that forms is rapidly quenched by the surrounding liquid. The absence of line emission suggests the origin of the emission to be predominantly due to the deceleration of electrons. This was attributed to the short duration of the laser pulses of ~6 ns in agreement with similar works reported in the literature where pulse lengths of ~100 ns duration are shown to produce intense line emission [43], [44]. It is proposed in these works that the use of a long pulse length facilitates coupling of radiation to the nascent plasma via the trailing pulse edge exciting the plume efficiently by avoiding energy delivery to the target surface [45]. Some slight evidence of neutral line emission was observed for single 532 nm pulses.

This may be an indication that the 1064 nm laser energy is being more strongly absorbed by the water resulting in less energy delivery to the target surface. However, higher pulse energies than those reported here were attempted during experimentation (5-200 mJ) and no line emission was observed using 1064 nm pulses.

Shockwaves were studied as a function of laser pulse energy in water from shadowgraphy measurements. The velocity of the shockwave appeared from the results to be independent of the laser pulse energy having an average velocity of 1464 ± 14 ms^{-1}. This is remarkably close to the reported value for the speed of sound in water which is 1482 ms^{-1} at 20 °C. Some evidence of non-linear velocity was observable at early shockwave expansion times however due to the spatial and temporal resolution of the recorded data a definitive conclusion could not be arrived at. In order to verify the early shockwave behaviour, an increment of 10 ns instead of the 50 ns used in present measurements should be applied resulting in a greater number of data points for a more reliable observation of a non-linear trend. As the shock-front expands into the liquid it will lose energy to the surroundings. This energy loss however appears to be insufficient to reduce the velocity of the shockwave which proceeds at a constant velocity. As the shock-front expands it displaces the fixed column of water and hence the pressure on the plasma declines with time. So it appears that the loss in energy as the plasma expands is balanced by the decreasing pressure experienced by the expanding shockwave resulting in a roughly constant velocity. The shock-front velocity was not observed to vary with target material. The appearance of numerous sound waves were also observed following the leading shock-front in water. The speed of these horizontal shock-fronts was found to vary with the target material and was related to the acoustic velocity of sound in the given metals.

Some microseconds after the laser pulse is delivered to the target submerged in water the formation of a cavitation bubble is observable from the shadowgraphy data. The dynamic evolution of the cavitation bubble was tracked using shadowgraphy measurements which were subsequently used to inform the timing of double pulse experiments. The evolution of the bubble was monitored as a function of time for two

different pulse energies. For a higher pulse energy the bubble was found to reach a greater maximum radius and persists for a longer time. The appearance of secondary and tertiary bubbles was also observed in particular for the high pulse energy case. These subsequent bubbles had a reduced diameter and were irregular in form. Their existence is thought to be related to the dampened nature of energy loss and recovery in the system as the bubble collapses and reforms in an analogous fashion to a bouncing ball eventually expending its mechanical energy.

Double pulse experiments were performed by probing the target at times corresponding to the appearance of the cavitation bubbles that were studied with the shadowgraphy setup. Imaging studies were performed during the growth and maximum expansion phases of the cavitation bubble life-cycle. In contrast to the single pulse case, the second plasma that forms within the cavitation bubble is seen to physically expand away from the target surface. Expansion occurs very rapidly within the first 150-250 ns and appears to stop at roughly the same distance as the expansion radius of the cavitation bubble. After roughly 1 µs the plasma plume then appears to retreat back towards the target surface and become more diffuse. Emission is observed up to 10 µs after which time emission is very diffuse, the plume appearing to have dispersed in all directions apparently expanding to within the confines of the cavitation bubble dimensions. A qualitative interpretation was proposed to explain the physical displacement of the plasma plume from the target surface observed within the confines of the bubble volume. Here the behaviour of the plume was qualitatively described by a moving point concept where the effective mass velocity of the plasma plume travelling in the flowing velocity field of the water vapour is considered. The hypothesis predicts that the effective mass velocity of the plasma plume should move at a higher velocity than the expansion velocity of the plume, which agrees with experimental findings.

Strong ionic emission was observed by firing a second laser pulse onto the target at times corresponding to the maximum in radius and stability of the bubble. In comparable studies to those performed in air, ionic line emission was spectrally narrow and several additional lines were observed. From the time resolved spectroscopic data

obtained, important plasma parameters such as electron temperatures and densities were ascertained. The electron density was found to be roughly an order of magnitude lower in the bubble than in air. The density decay appeared to consist of a fast and a slow component. Experimental data were fitted to a double exponential curve which was found to be the best fit to the data. A rapid decay of the electron density was observed for early times followed by a more gradual decay rate. Similar temperatures to those of air were found within the bubble with a maximum temperature of 1.17 ± 0.07 eV occurring for the earliest possible measurement at 100 ns. Evidence of self-reversal was observed in the neutral emission lines recorded at times corresponding to the formation and collapse of the cavitation bubble. As this absorption of line emission was not observed at times where the bubble was stable it may indicate that self-absorption is occurring at the bubble-water interface.

The nature of the bubble is hypothesised to be of a gaseous phase. Spectra recorded within the cavitation bubble reveal multiple doubly ionised emission lines not present in spectra recorded in ambient air. This suggests the nature of the bubble to be of a low pressure gaseous phase due to the spectral profile and presence of highly charged aluminium ion emission lines. A faster decay rate for the electron density is observed within the cavitation bubble giving further support to the assumption that the environment appears comparable to a low pressure gas ambient.

References

[1] M. Dell′Aglio, R. Gaudiuso, O. De Pascale, and A. De Giacomo, "Mechanisms and processes of pulsed laser ablation in liquids during nanoparticle production," *Appl. Surf. Sci.*, vol. 348, pp. 4–9, Sep. 2015.

[2] A. De Giacomo, M. Dell'Aglio, A. Santagata, R. Gaudiuso, O. De Pascale, P. Wagener, G. C. Messina, G. Compagnini, and S. Barcikowski, "Cavitation dynamics of laser ablation of bulk and wire-shaped metals in water during nanoparticles production," *Phys Chem Chem Phys*, vol. 15, no. 9, pp. 3083–3092, 2013.

[3] B. Kumar and R. K. Thareja, "Synthesis of nanoparticles in laser ablation of aluminum in liquid," *J. Appl. Phys.*, vol. 108, no. 6, p. 64906, 2010.

[4] D. Colombant and G. F. Tonon, "X-ray emission in laser-produced plasmas," *J. Appl. Phys.*, vol. 44, no. 8, p. 3524, 1973.

[5] A. De Giacomo, M. Dell'Aglio, O. De Pascale, and M. Capitelli, "From single pulse to double pulse ns-Laser Induced Breakdown Spectroscopy under water: Elemental analysis of aqueous solutions and submerged solid samples," *Spectrochim. Acta Part B At. Spectrosc.*, vol. 62, no. 8, pp. 721–738, Aug. 2007.

[6] S. Eliezer, *The interaction of high-power lasers with plasmas*. Bristol: Institute of Physics Pub., 2002.

[7] W. B. Zel'dovich and Raizer, Y.P., *Physics of Shock Waves and High-Temperature Hydrodynamic Phenomena*, Academic Press, New York. 1966.

[8] L. Martí-López, R. Ocaña, J. A. Porro, M. Morales, and J. L. Ocaña, "Optical observation of shock waves and cavitation bubbles in high intensity laser-induced shock processes," *Appl. Opt.*, vol. 48, no. 19, p. 3671, Jul. 2009.

[9] T. T. P. Nguyen, R. Tanabe, and Y. Ito, "Effects of an absorptive coating on the dynamics of underwater laser-induced shock process," *Appl. Phys. A*, vol. 116, no. 3, pp. 1109–1117, Sep. 2014.

[10] R. Fabbro, J. Fournier, P. Ballard, D. Devaux, and J. Virmont, "Physical study of laser-produced plasma in confined geometry," *J. Appl. Phys.*, vol. 68, no. 2, p. 775, 1990.

[11] R. Tanabe, T. T. P. Nguyen, T. Sugiura, and Y. Ito, "Bubble dynamics in metal nanoparticle formation by laser ablation in liquid studied through high-speed laser stroboscopic videography," *Appl. Surf. Sci.*, vol. 351, pp. 327–331, Oct. 2015.

[12] T. Tsuji, Y. Okazaki, Y. Tsuboi, and M. Tsuji, "Nanosecond Time-Resolved Observations of Laser Ablation of Silver in Water," *Jpn. J. Appl. Phys.*, vol. 46, no. 4A, pp. 1533–1535, Apr. 2007.

[13] A. Vogel, "Acoustic transient generation by laser-produced cavitation bubbles near solid boundaries," *J. Acoust. Soc. Am.*, vol. 84, no. 2, p. 719, 1988.

[14] L. I. Sedov, "Propagation of strong shock waves," *J. Appl. Mat. Mech.*, vol. 10, pp. 241–250, 1946.

[15] G. Taylor, "The Formation of a Blast Wave by a Very Intense Explosion. I. Theoretical Discussion," *Proc. R. Soc. Math. Phys. Eng. Sci.*, vol. 201, no. 1065, pp. 159–174, Mar. 1950.

[16] D. A. Freiwald and R. A. Axford, "Approximate spherical blast theory including source mass," *J. Appl. Phys.*, vol. 46, no. 3, p. 1171, 1975.

[17] P. Hough, T. J. Kelly, C. Fallon, C. McLoughlin, P. Hayden, E. T. Kennedy, J. P. Mosnier, S. S. Harilal, and J. T. Costello, "Enhanced shock wave detection sensitivity for laser-produced plasmas in low pressure ambient gases using interferometry," *Meas. Sci. Technol.*, vol. 23, no. 12, p. 125204, Dec. 2012.

[18] T. T. P. Nguyen, R. Tanabe, and Y. Ito, "Laser-induced shock process in under-liquid regime studied by time-resolved photoelasticity imaging technique," *Appl. Phys. Lett.*, vol. 102, no. 12, p. 124103, 2013.

[19] A. Nath and A. Khare, "Size induced structural modifications in copper oxide nanoparticles synthesized via laser ablation in liquids," *J. Appl. Phys.*, vol. 110, no. 4, p. 43111, 2011.

[20] W. Lauterborn, *Cavitation and Inhomogeneities in Underwater Acoustics Proceedings of the First International Conference, Göttingen, Fed. Rep. of Germany, July 9-11, 1979*. Berlin, Heidelberg: Springer Berlin Heidelberg, 1980.

[21] P. Giovanneschi and D. Dufresne, "Experimental study of laser-induced cavitation bubbles," *J. Appl. Phys.*, vol. 58, no. 2, p. 651, 1985.

[22] T. T. P. Nguyen, "Dynamics of Under-liquid Laser-induced Shock Process Studied by Time-resolved Photoelasticity Imaging Technique," Nagaoka University of Technology, Japan, 2013.

[23] A. Prosperetti, "Nonlinear bubble dynamics," *J. Acoust. Soc. Am.*, vol. 83, no. 2, p. 502, 1988.

[24] R. Löfstedt, B. P. Barber, and S. J. Putterman, "Toward a hydrodynamic theory of sonoluminescence," *Phys. Fluids Fluid Dyn.*, vol. 5, no. 11, p. 2911, 1993.

[25] A. Casavola, A. De Giacomo, M. Dell'Aglio, F. Taccogna, G. Colonna, O. De Pascale, and S. Longo, "Experimental investigation and modelling of double pulse laser induced plasma spectroscopy under water," *Spectrochim. Acta Part B At. Spectrosc.*, vol. 60, no. 7–8, pp. 975–985, Aug. 2005.

[26] A. Pearson, E. Cox, J. R. Blake, and S. R. Otto, "Bubble interactions near a free surface," *Eng. Anal. Bound. Elem.*, vol. 28, no. 4, pp. 295–313, Apr. 2004.

[27] M. Duocastella, J. M. Fernández-Pradas, J. L. Morenza, and P. Serra, "Time-resolved imaging of the laser forward transfer of liquids," *J. Appl. Phys.*, vol. 106, no. 8, p. 84907, 2009.

[28] A. E. Pichahchy, D. A. Cremers, and M. J. Ferris, "Elemental analysis of metals under water using laser-induced breakdown spectroscopy," *Spectrochim. Acta Part B At. Spectrosc.*, vol. 52, no. 1, pp. 25–39, Jan. 1997.

[29] S. S. Harilal, C. V. Bindhu, M. S. Tillack, F. Najmabadi, and A. C. Gaeris, "Internal structure and expansion dynamics of laser ablation plumes into ambient gases," *J. Appl. Phys.*, vol. 93, no. 5, p. 2380, 2003.

[30] S. S. Harilal, C. V. Bindhu, M. S. Tillack, F. Najmabadi, and A. C. Gaeris, "Plume splitting and sharpening in laser-produced aluminium plasma," *J. Phys. Appl. Phys.*, vol. 35, no. 22, pp. 2935–2938, Nov. 2002.

[31] C. G. Parigger, L. D. Swafford, A. C. Woods, D. M. Surmick, and M. J. Witte, "Asymmetric hydrogen beta electron density diagnostics of laser-induced plasma," *Spectrochim. Acta Part B At. Spectrosc.*, vol. 99, pp. 28–33, Sep. 2014.

[32] C. G. Parigger, "Measurements of Laser-Induced Plasma and Optical Breakdown Spectra of Aluminium," 2006, vol. 874, pp. 101–111.

[33] H. R. Pakhal, R. P. Lucht, and N. M. Laurendeau, "Spectral measurements of incipient plasma temperature and electron number density during laser ablation of aluminum in air," *Appl. Phys. B*, vol. 90, no. 1, pp. 15–27, Jan. 2008.

[34] J. Bengoechea, J. A. Aguilera, and C. Aragón, "Application of laser-induced plasma spectroscopy to the measurement of Stark broadening parameters," *Spectrochim. Acta Part B At. Spectrosc.*, vol. 61, no. 1, pp. 69–80, Jan. 2006.

[35] R. D. Cowan and G. H. Dieke, "Self-Absorption of Spectrum Lines," *Rev. Mod. Phys.*, vol. 20, no. 2, pp. 418–455, Apr. 1948.

[36] H. Amamou, A. Bois, B. Ferhat, R. Redon, B. Rossetto, and M. Ripert, "Correction of the self-absorption for reversed spectral lines: application to two resonance lines of neutral aluminium," *J. Quant. Spectrosc. Radiat. Transf.*, vol. 77, no. 4, pp. 365–372, Apr. 2003.

[37] H. R. Griem, *Plasma Spectroscopy*. Mc Graw-Hill, 1964.

[38] P. Hough, C. McLoughlin, T. J. Kelly, S. S. Harilal, J. P. Mosnier, and J. T. Costello, "Time resolved Nomarski interferometery of laser produced plasma plumes," *Appl. Surf. Sci.*, vol. 255, no. 10, pp. 5167–5171, Mar. 2009.

[39] S. Amoruso, J. Schou, and J. G. Lunney, "Multiple-scattering effects in laser ablation plume propagation in gases," *Europhys. Lett. EPL*, vol. 76, no. 3, pp. 436–442, Nov. 2006.

[40] J. Gonzalo, F. Vega, and C. N. Afonso, "Plasma expansion dynamics in reactive and inert atmospheres during laser ablation of Bi(2)Sr(2)Ca(1)Cu(2)O(7−y)," *J. Appl. Phys.*, vol. 77, no. 12, p. 6588, 1995.

[41] R. K. Singh, A. Kumar, B. G. Patel, and K. P. Subramanian, "Role of ambient gas and laser fluence in governing the dynamics of the plasma plumes produced by laser blow off of LiF–C thin film," *J. Appl. Phys.*, vol. 101, no. 10, p. 103301, 2007.

[42] C. Colón, G. Hatem, E. Verdugo, P. Ruiz, and J. Campos, "Measurement of the Stark broadening and shift parameters for several ultraviolet lines of singly ionized aluminum," *J. Appl. Phys.*, vol. 73, no. 10, p. 4752, 1993.

[43] T. Sakka, H. Oguchi, S. Masai, K. Hirata, Y. H. Ogata, M. Saeki, and H. Ohba, "Use of a long-duration ns pulse for efficient emission of spectral lines from the laser ablation plume in water," *Appl. Phys. Lett.*, vol. 88, no. 6, p. 61120, 2006.

[44] B. Thornton, T. Sakka, T. Takahashi, A. Tamura, T. Masamura, and A. Matsumoto, "Spectroscopic Measurements of Solids Immersed in Water at High Pressure Using a Long-Duration Nanosecond Laser Pulse," *Appl. Phys. Express*, vol. 6, no. 8, p. 82401, Aug. 2013.

[45] T. Sakka, S. Masai, K. Fukami, and Y. H. Ogata, "Spectral profile of atomic emission lines and effects of pulse duration on laser ablation in liquid," *Spectrochim. Acta Part B At. Spectrosc.*, vol. 64, no. 10, pp. 981–985, Oct. 2009.

Chapter 8

Conclusions

During the work reported here an investigation of the laser produced plasma formed in water has been undertaken and compared to the case of ambient air. This was achieved by the full characterisation of the plasma formed in each ambient. The main findings and conclusions of the thesis are summarised in this final chapter. A general perspective is offered on the relevance of the work for the scientific community in general in addition to the perceived importance of these findings in the context of potential applications. Suggestions on potential future work are also outlined.

8.1 Summary and Conclusions

A comprehensive study of laser produced aluminium plasmas was carried out in ambient air using 1064 nm and 532 nm laser pulses. Time resolved spectroscopic studies were carried out to extract the plasma parameters (temperatures and densities) for the two different laser wavelengths. Evidence of Stark-shifting of emission lines were found using the 532 nm laser pulses suggesting a higher electron density for plasmas formed using this shorter wavelength. Stark analysis of the emission lines confirmed these findings where average densities of approximately 2× were found for plasma formed using 532 nm pulses. A rapid rate of decay was observed initially, followed by a more

gradual decay rate in the mid to late stages of the atomic emission lifetime. For the case of 1064 nm pulses, a more gradual rate of decay was observed than in the case of 532 nm pulses. The results of plasma temperature measurements carried out using line intensity ratios from successive ion stages revealed that a hotter plasma is formed using the 1064 nm pulses. A slightly higher rate of cooling is revealed from the double exponential decay fits to the 532 nm plasma temperature data.

In the laser produced plasma, radiation is absorbed via two main processes; inverse Bremsstrahlung (IB) and photoionisation. For a higher photon energy, an increase in the probability of photoionisation is expected which explains the higher electron densities observed in the plasmas formed using 532 nm pulses. As a higher density plasma is formed using the 532 nm pulses, a higher rate of collisions and hence de-excitation should be expected in line with findings. Although a higher density plasma is formed, the plasma temperature is found to be less than that found in the 1064 nm pulse case. This result was attributed to the strong wavelength dependence of the IB process since the IB coefficient is proportional to λ^3. These observed trends in the plasma parameters are in line with similar studies carried out in atmospheric air [1], [2], [3].

In chapter 5, the aluminium plasma formed in air was studied at the mid to late phases of the plasma emission lifetime, i.e., several microseconds post plasma ignition. During this period, condensation of plasma species begins to take place and molecules begin to form. Plasma parameters such as electron densities and temperatures may be ascertained from the molecular emission spectra available at these late time delays. The availability of a plasma diagnostics at such late plasma lifetimes alleviates the pressing requirement of fast gating systems and has particular relevance for LIBS measurements. Optical emission spectroscopy of molecular AlO was studied over the observable emission lifetime of *ca.* 50 µs. The trends in the formation and dissociation rates were explained from a thermodynamic perspective where a strong temperature dependence was found. A series of re-heating experiments were then performed using a wavelength tuneable optical parametric oscillator (OPO). At a wavelength of 484 nm the delivery of

the OPO pulse to the plasma sees a significant enhancement in the Al(II) emission line in addition to the appearance of several Al(III) emission lines. These observations were attributed to the high temperature of the plasma expected using a 484 nm re-heating pulse and consequently, a higher population of Al^{2+} ions. Tuning the OPO wavelength to 466 nm, a strong enhancement in both the Al(II) and the Al(III) emission lines were observed. At this particular wavelength, resonance-enhanced multi-photon absorption was thought to account for the observed behaviour. Re-heating of the AlO molecule was carried out at a range of different inter-pulse delay times. For late inter-pulse delays a significant effect was observed in the AlO emission spectra where an enhancement in the emission strength was observed several microseconds after the delivery of the re-heating pulse. The main conclusion drawn from this series of experiments was that effective re-heating of molecular AlO occurs at some time delay with respect to the pre-pulse due to the strong temperature dependence of the different formation/dissociation pathways.

Chapter 6 presented a comparison between the laser produced plasma formed using a single laser pulse in air and water ambient. From time resolved imaging measurements the plume front expansion was compared in both environments for a range of laser pulse energies. In air, the plume expansion was found to be best described by the drag force model which takes into account the deceleration of the plasma plume due to collisional events. In water, a different behaviour was observed where initial expansion was followed by an apparent contraction phase. This contraction was concluded to occur via heat conduction as a faster rate of cooling was observed using a higher pulse energy.

The behaviour of the shockwave formed in air ambient was found to be consistent with the point explosion model. Expansion velocities tended towards an approximately linear expansion in the late stages of observable measurements several microseconds after plasma ignition due to deceleration caused by collisions with air molecules. The shockwave associated with the plasma formed in water showed an approximately linear behaviour with some evidence of a high velocity component appearing at early delay times (< 400 ns). At later times, the shockwave is shown to transition to a linear expansion at a velocity close to the speed of sound in water.

In chapter 7 a full characterisation of the laser produced plasma in water is presented. The results of imaging and spectroscopy using a single laser pulse reveal a strongly confined plasma and corresponding broadband continuum emission. Shadowgraphy measurements were performed to examine the dynamic behaviour of the cavitation bubble that eventually forms post plasma ignition. These measurements were used to inform subsequent investigations designed to probe the bubble environment. The conditions within the bubble during each phase of its life-cycle were also outlined. The results of time resolved imaging from within the cavitation bubble using a second laser pulse reveal for the first time the full dynamic evolution of the plasma formed in such an environment. Rapid displacement of the plasma plume in a direction normal to the target surface followed by a diffusive outwards expansion was observed and a qualitative model was proposed to explain the observed behaviour. Here the behaviour of the plume was qualitatively described by a moving point concept where the effective mass velocity of the plasma plume travelling in the flowing velocity field of the water vapour is considered. The hypothesis predicts that the effective mass velocity of the plume should move at a higher velocity than the expansion velocity of the plume, which agrees with experimental findings.

Atomic line emission from within the cavitation bubble is observed using the double pulse method. This allows for time resolved determination of temperatures and densities, using the line ratio method and Stark broadening, which are of critical importance in LIBS measurements. Evidence of self-reversal of neutral emission lines was observed at times corresponding to formation and collapsing phases of the cavitation bubble suggesting a high population of ground state atoms during these times. Optical emission measurements reveal a more stable environment within the cavitation bubble during the phase of maximum expansion in line with the more uniform pressure conditions expected from calculations. A plasma formed during this époque of maximum bubble expansion does not appear homogenous until *ca.* 2 µs after plasma formation which is again of potential interest for LIBS applications. Many LIBS measurements, including ones made with the double-pulse method on submerged

targets, are made with relatively long gate-widths compared to the laser pulse width and thus are subject to the criterion that the plasma be homogenous over the measurement time. Time-resolved measurements are therefore useful in establishing the transient nature of the plasma and yet are relatively unexplored for the case of submerged targets.

8.2 Future Work

Through time-resolved optical emission and diagnostic studies a thorough characterisation of the submerged plasma has been carried out. Using a double-pulse arrangement the plasma created by the second pulse is formed within the gaseous environment of the cavitation bubble circumnavigating the challenges associated with the single pulse setup. Imaging within the cavitation bubble has provided new insights into the plasma formed in such an environment which is of fundamental interest as well as from a LIBS measurement perspective. Due to time restraints, only one configuration was used; formation of the cavitation bubble using the 1064 nm pulse and plasma formation within the bubble environment using the 532 nm pulse. For future studies, different probe laser wavelengths should be used to investigate the effect of laser wavelength on the dynamic evolution of the plasma formed inside the cavitation bubble. By forming the plasma at different phases during the bubble life-cycle some interesting new phenomenon may be discovered by varying the plasma conditions via the laser wavelength and pulse energy. Spatially resolved measurements would be of interest for the full characterisation of plasma conditions within the cavitation bubble. These types of fundamental experiments may prove useful for the optimisation of LIBS-type measurements in aqueous environments for such applications as environmental monitoring [4], underwater geology [5], and marine research [6].

Kumar *et al.* report in situ growth of nanoparticles in air and water environments using the technique of Raleigh scattering [7]. Nanoparticles are predicted to nucleate in the

plasma on a sub-nanosecond timescale [7] and become ejected into solution upon collapse of the cavitation bubble [8]. This would be an interesting experiment to undertake within the cavitation bubble where in theory the dynamic evolution of nanoparticle growth could be investigated. As the cavitation bubble effectively acts as a variable pressure and temperature environment, nanoparticles formed during the different stages of the bubble life-cycle should allow for tunability of particle size in the subsequent colloidal suspension, one of the highly advantageous properties of nanoparticle formation in a liquid environment [9].

Laser surgery has been in widespread practice since the invention of the ruby laser [10] highlighting the relevance of such fundamental studies in terms of potential real-world applications. The nanosecond pulses produced by the Nd:YAG laser are known to result in thermal damage to surrounding tissue [11] and as a result, the use of femtosecond lasers is now widespread in clinical areas such as ophthalmology [12]. As the formation of bubbles is known to be the key mechanism for collateral damage in cell surgery, the study of laser produced plasmas in a liquid environment using ultra-short pulses may provide some important insights. In recent times, attention has turned to the development of femtosecond LIBS systems [13] due to its high sensitivity and superior spatial resolution. During optical breakdown, the plasma generated by a femtosecond pulse is very different from that formed using a nanosecond pulse. Use of a pulse duration shorter than the thermal coupling time (~1 ps) leads to lower plasma temperatures and densities, a repression of continuum emission and hence an improvement in the signal-to-background ratio. and high spatial resolution. For detection of trace elements in water for geo-chemical and environmental analysis, the limits of detection provided by nanosecond LIBS are insufficient and femtosecond measurements are required [14]. As the study of laser produced plasmas in liquids using femtosecond pulses is relatively unexplored to date, much work remains to be done which, owning to the numerous applications, may make this an interesting area of future research.

References

[1] H. Hegazy, E. AlAshkar, H. H. Abou-Gabal, M. N. Aly, and N. Hamed, "Spectroscopic Evolution of Plasma Produced by Nd-YAG Laser," *IEEE Trans. Plasma Sci.*, vol. 42, no. 6, pp. 1674–1684, Jun. 2014.

[2] N. M. Shaikh, S. Hafeez, B. Rashid, and M. A. Baig, "Spectroscopic studies of laser induced aluminum plasma using fundamental, second and third harmonics of a Nd:YAG laser," *Eur. Phys. J. D*, vol. 44, no. 2, pp. 371–379, Aug. 2007.

[3] O. Barthélemy, J. Margot, M. Chaker, M. Sabsabi, F. Vidal, T. W. Johnston, S. Laville, and B. Le Drogoff, "Influence of the laser parameters on the space and time characteristics of an aluminum laser-induced plasma," *Spectrochim. Acta Part B At. Spectrosc.*, vol. 60, no. 7–8, pp. 905–914, Aug. 2005.

[4] G. Arca, A. Ciucci, V. Palleschi, S. Rastelli, and E. Tognoni, "Trace Element Analysis in Water by the Laser-Induced Breakdown Spectroscopy Technique," *Appl. Spectrosc.*, vol. 51, no. 8, pp. 1102–1105, 1997.

[5] B. Thornton, T. Sakka, T. Takahashi, A. Tamura, T. Masamura, and A. Matsumoto, "Spectroscopic Measurements of Solids Immersed in Water at High Pressure Using a Long-Duration Nanosecond Laser Pulse," *Appl. Phys. Express*, vol. 6, no. 8, p. 82401, Aug. 2013.

[6] C. Fabre, M.-C. Boiron, J. Dubessy, M. Cathelineau, and D. A. Banks, "Palaeofluid chemistry of a single fluid event: a bulk and in-situ multi-technique analysis (LIBS, Raman Spectroscopy) of an Alpine fluid (Mont-Blanc)," *Chem. Geol.*, vol. 182, no. 2–4, pp. 249–264, Feb. 2002.

[7] B. Kumar and R. K. Thareja, "Growth of titanium nanoparticles in confined plasma," *Phys. Plasmas*, vol. 19, no. 3, p. 33516, 2012.

[8] C. X. Wang, P. Liu, H. Cui, and G. W. Yang, "Nucleation and growth kinetics of nanocrystals formed upon pulsed-laser ablation in liquid," *Appl. Phys. Lett.*, vol. 87, no. 20, p. 201913, 2005.

[9] H. Zeng, X.-W. Du, S. C. Singh, S. A. Kulinich, S. Yang, J. He, and W. Cai, "Nanomaterials via Laser Ablation/Irradiation in Liquid: A Review," *Adv. Funct. Mater.*, vol. 22, no. 7, pp. 1333–1353, Apr. 2012.

[10] T. H. Maiman, "Stimulated Optical Radiation in Ruby," *Nature*, vol. 187, no. 4736, pp. 493–494, Aug. 1960.

[11] T. Juhasz, G. A. Kastis, C. Suárez, Z. Bor, and W. E. Bron, "Time-resolved observations of shock waves and cavitation bubbles generated by femtosecond laser pulses in corneal tissue and water," *Lasers Surg. Med.*, vol. 19, no. 1, pp. 23–31, 1996.

[12] H. K. Soong and J. B. Malta, "Femtosecond Lasers in Ophthalmology," *Am. J. Ophthalmol.*, vol. 147, no. 2, p. 189–197.e2, Feb. 2009.

[13] S. Harilal, "Comparison of nanosecond and femtosecond LIBS," 2013, p. CTu2H.8.

[14] S. S. Golik, O. A. Bukin, A. A. Il'in, E. B. Sokolova, A. V. Kolesnikov, M. Y. Babiy, Y. N. Kul'chin, and A. A. Gal'chenko, "Determination of detection limits for

elements in water by femtosecond laser-induced breakdown spectroscopy," *J. Appl. Spectrosc.*, vol. 79, no. 3, pp. 471–476, Jul. 2012.

List of Publications

[1] N. Walsh, T. J. Kelly, and J. T. Costello, "Optical diagnostics of laser produced aluminium plasmas under water," 2016. [In Press].

[2] M. Ilchen, T. Mazza, E. T. Karamatskos, D. Markellos, S. Bakhtiarzadeh, A. J. Rafipoor, T. J. Kelly, N. Walsh, J. T. Costello, P. O'Keeffe, N. Gerken, M. Martins, P. Lambropoulos, and M. Meyer, "Two-electron Processes in Multiple Ionization under Strong Soft X-ray Radiation," *Phys. Rev. A*, 2016. [In Press].

[3] T. J. Kelly, T. Butler, N. Walsh, P. Hayden, and J. T. Costello, "Features in the ion emission of Cu, Al, and C plasmas produced by ultrafast laser ablation," *Phys. Plasmas*, vol. 22, no. 12, p. 123112, Dec. 2015.

[4] C. Fallon, P. Hayden, N. Walsh, E. T. Kennedy, and J. T. Costello, "Target geometrical effects on the stagnation layer formed by colliding a pair of laser produced copper plasmas," *Phys. Plasmas*, vol. 22, no. 9, p. 93506, Sep. 2015.

[5] T. Mazza, A. Karamatskou, M. Ilchen, S. Bakhtiarzadeh, A. J. Rafipoor, P. O'Keeffe, T. J. Kelly, N. Walsh, J. T. Costello, M. Meyer, and R. Santra, "Sensitivity of nonlinear photoionization to resonance substructure in collective excitation," *Nat. Commun.*, vol. 6, p. 6799, Apr. 2015.

Conferences Attended

ICGEE & INSPIRE Business and Innovation workshop. Dublin, Sept 2011.

SWISS Summer School. Bern, Switzerland, Sept 2012.

Communication Skills Workshop for Research Students, Dublin, Nov 2013.

NCPST Plasma/Nanoscience Conference. Dublin, March 2014.

PIRE Annual Meeting. Dublin, Jul 2015.

Photonics Ireland. Cork, Sept 2015.

8th EMSLIBS Conference. Linz, Austria, Sept 2015.

List of Courses Taken

PH5094	Introduction to Nanoscience
PH502	Scientific Programming Concepts
UE6005	Nanoelectronics
CS507A	Multivariate Statistical Analysis
GS604	Research Ethics
EE506	Fundamentals of Photonic Devices